

# Journal of Research of the National Bureau of Standards

Volume 89	Number 1	January-February
Note From the Board of Editors. <i>John W. Cooper</i> .....		1
Surface Roughness Studies with DALLAS—Detector Array for Laser Light Angular Scattering. <i>T. V. Vorburger, E. C. Teague, F. E. Scire, M. J. McLay, and D. E. Gilsinn</i> .....		3
Microstructural Characterization of Ceramic Materials by Small Angle Neutron Scattering Techniques. <i>K. Hardman-Rhyne, N. F. Berk, and E. R. Fuller, Jr.</i> .....		17
Characterization of Creep Damage in Metals Using Small Angle Neutron Scattering. <i>E. R. Fuller, Jr., R. J. Fields, T.-J. Chuang, and S. Singhal</i> .....		35
Impedance of a Coil in the Vicinity of a Crack. <i>Arnold H. Kahn</i> .....		47
Theory of Acoustic Emission From Phase Transformations. <i>J. A. Simmons and H. N. G. Wadley</i> .....		55
Reconstructing Internal Temperature Distributions From Ultrasonic Time-of-Flight Tomography and Dimensional Resonance Measurements. <i>S. J. Norton, L. R. Testardi, and H. N. G. Wadley</i> .....		65
Acoustic Emission: Establishing the Fundamentals. <i>D. G. Eitzen and H. N. G. Wadley</i> .....		75
List of Publications of the National Bureau of Standards .....		101

The Journal of Research of the National Bureau of Standards features advances in measurement methodology and analyses consistent with the NBS responsibility as the nation's measurement science laboratory. It includes reports on instrumentation for making accurate and precise measurements in fields of physical science and engineering, as well as the mathematical models of phenomena which enable the predictive determination of information in regions where measurements may be absent. Papers on critical data, calibration techniques, quality assurance programs, and well characterized reference materials reflect NBS programs in these areas. Special issues of the Journal are devoted to invited papers in a particular field of measurement science. Survey articles appear periodically on topics related to the Bureau's technical and scientific programs. As a special service to subscribers each issue contains complete citations to all recent NBS publications in NBS and non-NBS media.

#### David T. Goldman, Editor

Executive Editors  
Donald R. Johnson  
(Natl. Measurement Lab.)  
John W. Lyons  
(Natl. Engineering Lab.)

#### Board of Editors

John W. Cooper (Physics)      Harold J. M. Hanley  
Sharon G. Lias (Chemistry)      (Boulder Laboratory)  
Donald G. Eitzen (Engineering)      John W. Cahn (Materials)

Issued six times a year. Annual subscriptions: domestic \$18.00; foreign \$22.50. Single copy, \$5.50 domestic; \$6.90 foreign.

Order all publications from the Superintendent of Documents  
U.S. Government Printing Office, Washington, DC 20402

The Secretary of Commerce has determined that the publication of the periodical is necessary in the transaction of the public business required by law of this Department. Use of funds for printing this periodical has been approved by the Director of the Office of Management and Budget through April 1, 1985.

# About This Topical Issue...

In the industrial society in which we live there is a growing need for rather complex measurement techniques to characterize the properties of materials and manufactured articles and their defects both during production and in actual use. Successful implementation of these techniques requires both a basic understanding of the physical processes involved in such measurements and theoretical models which relate measured quantities to actual material properties.

Current NBS efforts in this area are represented by the seven papers of this topical issue on "Scientific Aspects of Non-Destructive Evaluation." These papers reflect three different types of research. Three of them deal with new experimental techniques. Laser light scattering (Vorburger *et al.*) provides an attractive alternative technique to stylus measurements as a probe of surface roughness. Small angle neutron scattering (Hardman-Rhyne *et al.*, Fields *et al.*) may be used as a unique probe of the internal structure of materials which can provide reference standards for intercomparison with more conventional non-destructive evaluation techniques. Three articles (those by Kahn, Simmons and Wadley and Norton *et al.*) are not concerned directly with measurement but deal with the development of mathematical models which will relate observed signals in electromagnetic, acoustic emission and ultrasonic measurement systems to internal properties or defects in materials. The development of such models is an important part of the science of measurement. The last article (Eitzen and Wadley) is of yet a different type. It is concerned with the problem of acquiring a basic understanding of the acoustic emission technique.

The seven papers in this issue, although they are representative, reflect only a small fraction of current research activities at NBS in the areas of non-destructive evaluation. Other articles will appear in following issues.

John W. Cooper  
for the Board of Editors

# Surface Roughness Studies with DALLAS-Detector Array for Laser Light Angular Scattering

T. V. Vorburger, E. C. Teague, F. E. Scire, M. J. McLay, and D. E. Gilsinn  
National Bureau of Standards, Washington, DC 20234

Accepted: October 14, 1983

An instrument has been developed to study surface roughness by measuring the angular distributions of scattered light. In our instrument, a beam from a He-Ne laser illuminates the surface at an angle of incidence which may be varied. The scattered light distribution is detected by an array of 87 fiber optic sensors positioned in a semicircular yoke which can be rotated about its axis so that the scattered radiation may be sampled over an entire hemisphere. The output from the detector array is digitized, stored, and analyzed in a laboratory computer. The initial experiments have concentrated on measurements of stainless steel surfaces which are highly two-dimensional and which yield scattering distributions that are localized in the plane of incidence. The results are analyzed by comparing the angular scattering data with theoretical angular scattering distributions computed from digitized roughness profiles measured by a stylus instrument. The theoretical distributions are calculated by substituting the roughness profiles into the operand of an integral equation for electromagnetic scattering developed by Beckmann and Spizzichino. This approach directly tests the accuracy of the basic optical theory.

Key words: angular distribution; diffraction; diffuse scattering; electromagnetic scattering; fiber optics; light scattering; optical fiber; optical scattering; roughness; surface roughness; texture; topography.

## 1. Introduction

Optical scattering techniques have been used for a long time to monitor the surface roughness of industrial parts ranging from crankshaft bearings [1]<sup>1</sup> to x-ray mirror prototypes [2]. These techniques lend themselves to on-line surface inspection in industry because they are intrinsically area-averaging, high-speed methods. A single measurement can yield a quantity that is closely related to some average property of the surface roughness [3]. However, optical scattering methods are almost exclusively used in an empirical way because the quantitative deduction

of roughness parameters from optical measurements is extremely difficult because of the complexity of optical scattering itself. Empirical approaches [1,4] have been developed which rely on the use of a number of calibration surfaces with known roughness parameters that are similar to the unknown surfaces to be measured. These calibration standards enable the operator to calibrate the surface measuring instrument empirically. Although this comparator approach is effective, we attempt here to derive optical scattering quantities from more basic principles. Then perhaps, optical methods could be applied to surface roughness problems more generally and with a higher degree of confidence.

---

**About the Authors, Paper:** T. V. Vorburger, E. C. Teague, F. E. Scire, M. J. McLay, and D. E. Gilsinn are with the Mechanical Production Metrology Division in NBS' Center for Manufacturing Engineering. The work on which they report was supported by NASA and the NBS Office of Nondestructive Evaluation.

---

This difficulty of understanding is particularly acute for engineering surfaces where the roughness heights are typically in the range between 0.1 and 1.0  $\mu\text{m}$ . He-Ne lasers with wavelength  $\lambda=0.6328 \mu\text{m}$  are commonly used in such applications because of their relative safety, good stability, ease of alignment, and other features. However, this means that the roughness heights are on the same order of magnitude as the wavelength of light [5]. The mathematical description is much more complicated in this regime

---

<sup>1</sup> Figures in brackets indicate literature references at the end of this paper.

than it is for optically smooth surfaces [6,7] where the effect of surface roughness is a small perturbation on the basic phenomenon of specular optical scattering, i.e., where the surface basically functions like a mirror.

The present work is an attempt to develop a better mathematical description of optical scattering phenomena for engineering surfaces. The ultimate goal of this work is an optical scattering apparatus for reliable and routine measurements of roughness parameters without resorting to specially fabricated comparator standards.

After a brief experimental overview in section 2, we discuss the apparatus in detail in section 3. There follows an outline of the theory in section 4. Section 5 deals with the experimental results, and section 6 (Analysis) compares the experimental and theoretical scattering distributions. In section 7 we discuss the limitations of the present work as well as previous work and probable future directions. Some experimental notes are included as an appendix.

## 2. Experimental Overview

When a beam of laser light is reflected by a rough surface, the radiation is scattered into an angular distribution (fig. 1) according to the laws of physical optics. The intensity and the pattern of the scattered radiation depend on the roughness heights, the roughness spatial wavelengths, and the wavelength of the light [6-8]. In general, small spatial wavelength components diffract the light into large angles relative to the specular direction, and long spatial wavelength components diffract the light into small angles. Most surfaces have a broad range of spatial wavelengths,

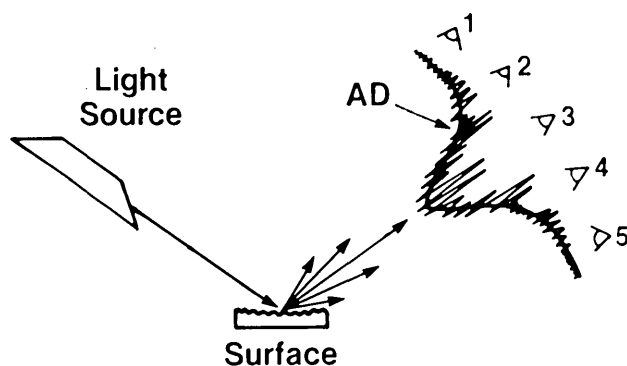


Figure 1—Schematic diagram of a laser beam scattered by a rough surface. The pattern consists of the overall angular distribution envelope (AD) and a fine structure known as speckle. A simple optical detection system is also shown. Detector 3 measures the intensity in the specular direction. Detectors 1, 2, 4, 5 measure other components of the angular distribution.

and the light is therefore diffracted over a range of angles.

For very smooth surfaces, most of the reflected light propagates in the specular direction. As the roughness increases, the intensity of the specular beam decreases while the diffracted radiation increases in intensity and becomes more diffuse. In addition, the angular distribution of diffuse radiation consists of a fine grainy structure called speckle [9], which shows up as intensity contrast between neighboring points in the scattered field. Finally, the light wave may undergo a change in its polarization state upon reflection from the surface.

In this work, we study how the angular distribution is related to the detailed topography of engineering surfaces. In particular we explore the following fundamental question: If the detailed surface topography were perfectly known, could the angular scattering distribution be predicted from available optical scattering theories? If so, that basic knowledge might lead to optical techniques for measuring the roughness of surfaces without resorting to calibration artifacts. If one cannot relate optical scattering to surface roughness in this very straightforward way, then it is likely that metrologists will be limited to empirical approaches for the characterization of engineering surfaces by optical scattering.

Our approach uses an optical instrument called DALLAS (detector array for laser light angular scattering), a stylus profiling instrument interfaced to a minicomputer for accurate characterization of surface topography, and a fairly elementary optical scattering theory. Surface profiles measured by the stylus instrument are substituted into the scattering theory to generate angular distributions which may be compared with those directly measured by DALLAS for the same surfaces. We report here some preliminary results with this equipment.

## 3. Apparatus

A block diagram of the twofold apparatus is shown in figure 2. In the DALLAS experiment, a beam of laser light illuminates the rough surface under test and the scattered radiation is collected by an array of 87 detectors. The signals are sequentially routed by a scanner to a digital voltmeter which functions as an analog-to-digital converter. The resulting angular distribution is stored in a desktop microcomputer and may be compared with distributions generated from the stylus experiment. In the latter system, a commercial stylus instrument measures surface profiles and stores them on a magnetic disk on a large

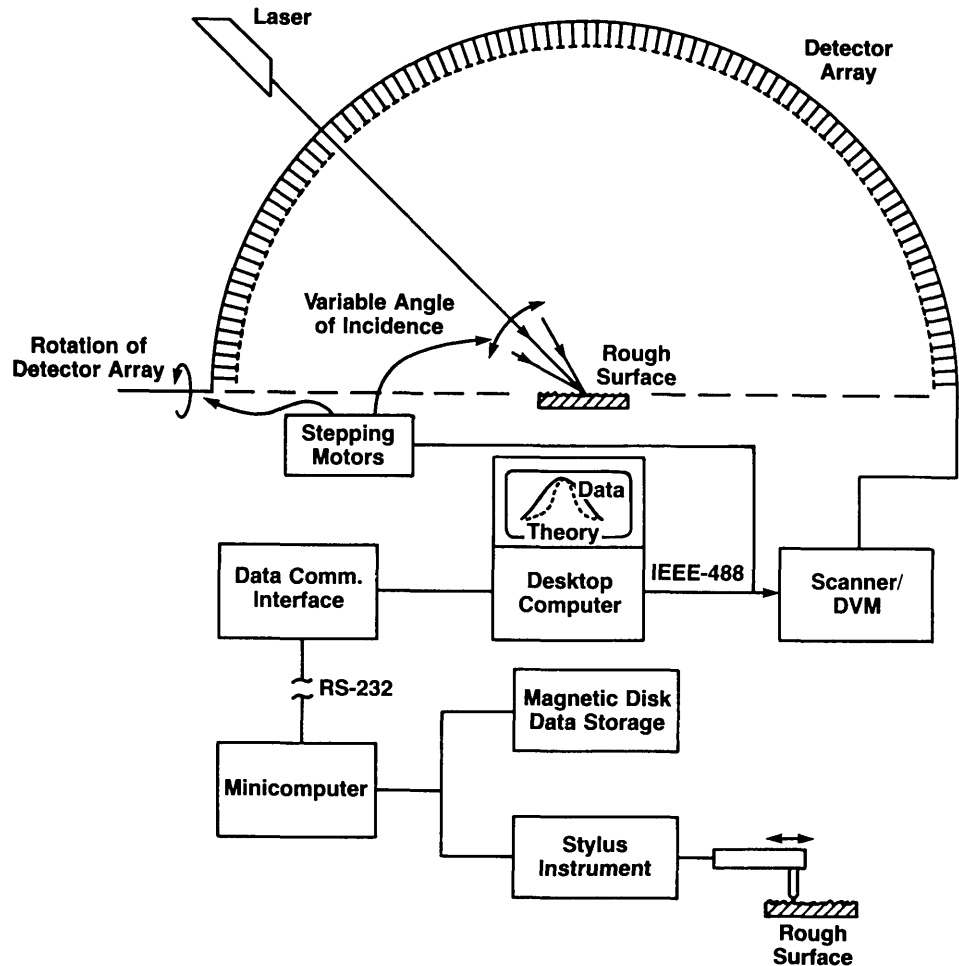


Figure 2-Block diagram of the apparatus. The optical experiment, DALLAS, is shown at the top, and the stylus system, at the bottom. Experimental and theoretical angular distributions may be compared on the desktop microcomputer shown near the center.

minicomputer. Optical scattering distributions are then calculated from these profiles and the results may be transmitted to the microcomputer by a hardwired RS-232 interface.

### 3.1 Optical Apparatus

The apparatus for measuring intensity distributions as a function of scattering angle from surfaces is shown in figure 3 and consists of an illumination system and a detection system.

The illumination system consists of a 5 mW He-Ne laser with linear polarization, a quarter-wave plate to produce circular polarization, an automatic shutter, and a rotating assembly of two mirrors, M1 and M2, to direct the laser beam onto the specimen surface. The angle of incidence may be varied by a stepping motor which controls the angular position of M1 and M2. The illuminated region of the specimen is a spot approximately 2 mm × 3 mm, depending on the angle of incidence. The detection system consists of an array of 87 detectors spaced 2° apart in a semicircular yoke

(diam=164 mm) which is centered on the illumination spot on the specimen. The yoke can be rotated about one axis by a stepping motor so that the detectors can sample practically the entire hemisphere of radiation scattered from the surface.

Each detector consists of a lens, an optical fiber, and a PIN Si photodiode with an integral op-amp circuit. Each lens has a diameter of 4.4 mm and subtends an angle of about 1.5° in the yoke. It collects the radiation and focuses it onto the fiber which transmits the radiation to the photodiode. The output voltage signals from the op-amps are scanned by a 100-channel scanner, digitized, and stored in the desktop microcomputer using BASIC language software. At present, a single angular scan of the 87 detectors takes about 10 s and yields intensity distributions which span over 5 orders of magnitude in intensity. That is, the rms noise of the apparatus is approximately 50 μV, and the saturation voltage of the detectors is about 9 V. The nonlinearity of two typical detectors was measured by comparing their voltage outputs with that of a highly linear, standard Si detector. Over a

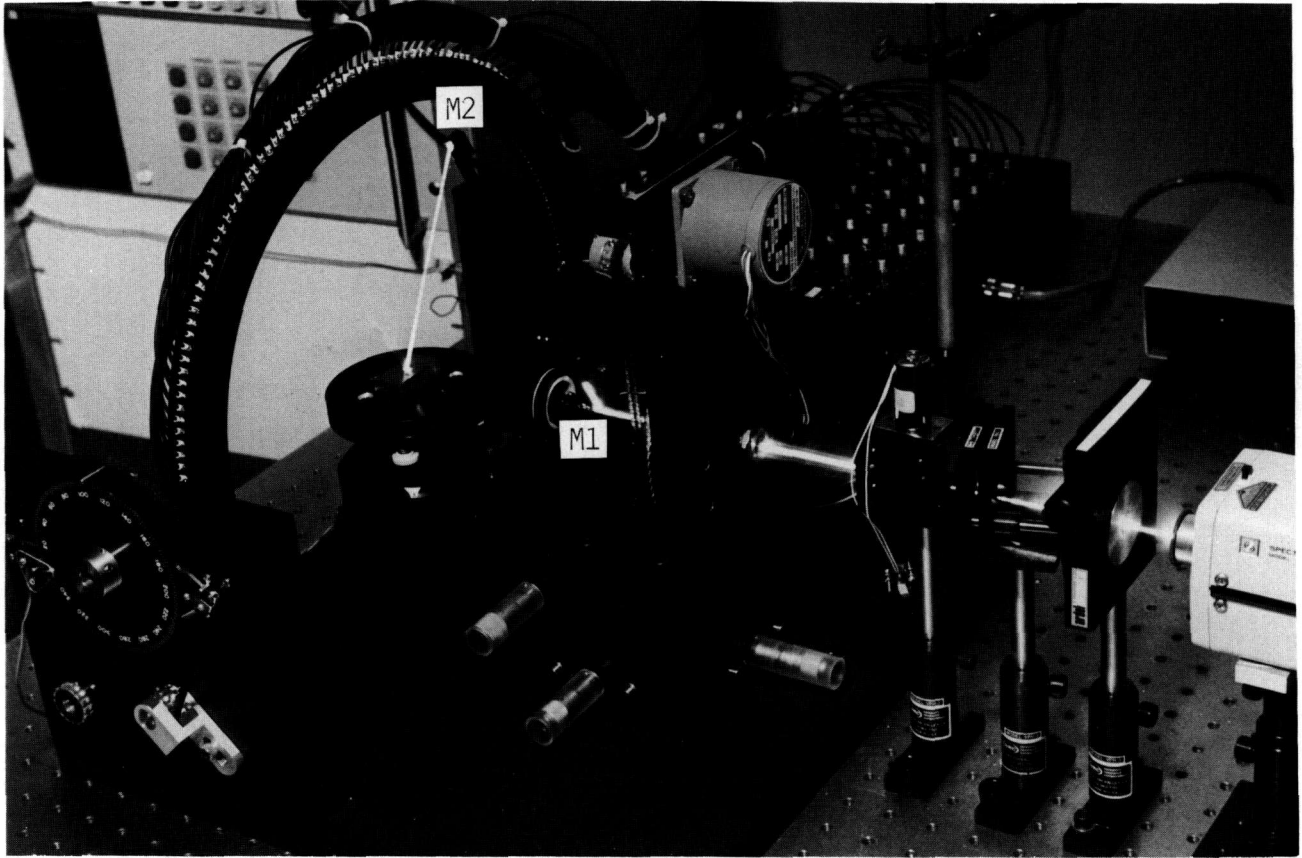


Figure 3-DALLAS in operation. Mirrors (M1 and M2) direct laser beam onto the surface of the specimen located under semicircular yoke supporting the detection system.

dynamic range of  $10^5$  in input light intensity, the nonlinearity of the output voltage was less than 2% or  $50 \mu\text{V}$ , whichever is greater. The relative linearity of the 87 detectors with light intensity (tracking) has also been checked. Over  $3 \frac{1}{2}$  orders of magnitude of light intensity, the output voltages track one another with a standard deviation of 2% or 2.5 times the rms noise, whichever is greater.

The 87-point angular distributions may be stored permanently on magnetic tape cassettes or plotted on the CRT of the microcomputer for comparison with the angular scattering calculations predicted from stylus data. Additional notes on the detection system are given in section 8.

### 3.2 Stylus Apparatus

The stylus system has been described previously [10-12]. It consists of a Talystep<sup>2</sup> stylus instrument

<sup>2</sup> Certain kinds of commercial equipment are identified in this article to specify adequately the experimental procedure. In no case does such identification imply recommendation or endorsement by the National Bureau of Standards, nor does it imply that the equipment identified is necessarily the best available for the purpose.

interfaced to a minicomputer. As the stylus traverses the peaks and valleys of the surface, the vertical motion is converted to a time-varying electrical signal which undergoes 12-bit A/D conversion. The result is a roughness profile consisting of 4000 digitized points that may be permanently stored on the magnetic disk. The horizontal length of the profile is approximately 1.84 mm, and the point spacing is  $0.46 \mu\text{m}$ . The horizontal resolution of the instrument is approximately  $1 \mu\text{m}$ , limited by the high frequency falloff of the stylus response function.

The ultimate vertical resolution of the stylus instrument is approximately 0.3 nm over the length of the stylus profile. The vertical resolution of the digitized profile may also be limited by the quantization increment of the 12-bit A/D converter, which depends on the magnification scale of the stylus instrument controller. For the rougher surfaces, the controller was set at a low magnification; the smallest quantization increment was approximately 1.2 nm.

Each surface was sampled with 10 stylus traces evenly distributed over an area approximately  $3 \text{ mm} \times 6 \text{ mm}$ . Hence, the total amount of topography

information amounts to 40,000 digitized points for each surface.

### 3.3 Specimens

A commercial set of four surface specimens [13] was studied with both the stylus and DALLAS techniques. Three of the specimens were specially machined to produce highly two-dimensional roughness specimens; that is, each surface has a fairly random roughness profile in one direction and an essentially smooth profile in the perpendicular direction. The fourth specimen was very smooth in all directions on the surface. The two-dimensional nature of the three rougher specimens was quite important.

The specimens were oriented in the DALLAS apparatus so that the roughness direction was in the plane of incidence of the light; therefore, essentially all of the scattered light was in the plane of incidence as well. This arrangement has two beneficial effects: 1) all of the scattered light may be detected by a single scan of the detectors without having to rotate the yoke, and 2) the complex, vector electromagnetic scattering problem reduces to a scalar problem [14–16]. Therefore, the use of these specimens reduces a three-dimensional problem that is both theoretically and experimentally complex to a two-dimensional problem without any approximation. The basic approximations of the optical scattering theory may be tested in a fairly straightforward way.

## 4. Theory

The formulas used to predict the angular scattering distributions involve a basic scalar theory of light scattering which has been investigated by Beckmann and Spizzichino [14] as well as others [17,18]. The theory assumes that a plane wave of uniform intensity illuminates the specimen surface and that the electric field on the surface and its normal derivative can be expressed in terms of a surface reflection coefficient [14] independent of the local surface topography. The geometry of this scattering problem is shown in figure 4. The surface is assumed to be two dimensional, i.e., rough in the  $x$  direction and smooth in the  $y$  direction. The incoming plane wave is represented by the wave vector  $\mathbf{K}_i$  with angle of incidence  $\theta_i$  with respect to the normal vector  $\mathbf{n}$  of the mean plane of the surface. The functional form for the incident electric field  $E_i$  is given by  $\exp(j\mathbf{K}_i \cdot \mathbf{r})$ . The scattered electric field is to be evaluated for an angle  $\theta_s$  with corresponding outgoing vector  $\mathbf{K}_s$ . The vector  $\mathbf{r}$  extends from some nearby origin 0 to a point on the surface.

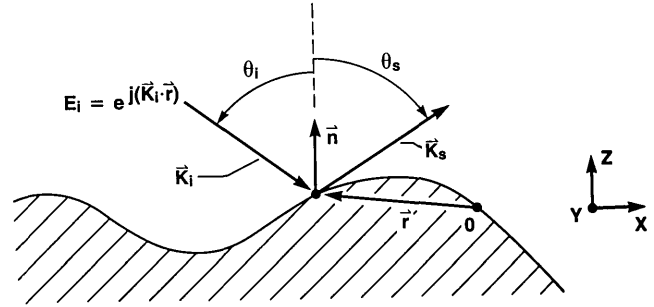


Figure 4—Schematic diagram of the scattering geometry showing the incoming plane wave with wave vector  $\mathbf{K}_i$  and angle of incidence  $\theta_i$ , and an outgoing wave vector  $\mathbf{K}_s$  with scattering angle  $\theta_s$ .  $\mathbf{r}$  is the vector from the origin 0 to the point under consideration. (Vector symbols are arrowless [and bold-faced] in the text; arrows are used with such symbols in the caption to match the arrowed symbols of the figure.)

With the foregoing considerations and assumptions, the scattered electric field  $E$  can be calculated as a function of scattering angle  $\theta_s$  in the Fraunhofer zone of the scattered radiation field. It is given by the phase integral over the surface profile  $z(x)$ :

$$E(\theta_s) = C_0 \frac{(1 + \cos(\theta_i - \theta_s))}{\cos\theta_i + \cos\theta_s} \int_0^L e^{j\mathbf{V} \cdot \mathbf{r}} dx = C_0 F, \quad (1)$$

where  $\mathbf{V} = \mathbf{K}_i - \mathbf{K}_s$ ,  $L$  is the length of the illuminated region along the  $x$  direction, and  $\mathbf{r} = x\hat{\mathbf{i}} + z(x)\hat{\mathbf{k}}$ . The vectors  $\hat{\mathbf{i}}$  and  $\hat{\mathbf{k}}$  are unit vectors in the  $x$  and  $z$  directions, respectively, and  $\mathbf{r}$  contains all of the information concerning the surface profile, and in detail,

$$\begin{aligned} \mathbf{V} \cdot \mathbf{r} &= V_x x + V_z z \\ &= 2\pi/\lambda [(\sin\theta_i + \sin\theta_s)x + (\cos\theta_i + \cos\theta_s)z(x)]. \end{aligned} \quad (2)$$

The sign convention here is such that  $\theta_s = -\theta_i$  in the specular direction.  $C_0$  is a quantity which depends on a number of factors such as  $\theta_i$  and  $E_i$ , but is independent of  $\theta_s$ . The quantity  $F$  contains all of the information concerning the shape of the angular scattering distribution.

The plan of the experiment is as follows: measure a surface profile  $z(x)$  point by point, then substitute this profile into the integral, eq (1), to calculate a theoretical angular scattering distribution. This distribution may be compared with the one measured in the DALLAS apparatus for the same surface. In this way the adequacy of the scattering theory can be tested. If the theory is inadequate, then one can remove the various approximations one by one that

have entered into it and perform the calculation with a more elaborate integral.

## 5. Experimental Results

### 5.1 Optical Scattering

A typical set of angular distribution measurements for one of the four surfaces is shown in figure 5. For all of the surfaces the angle of incidence (AI) was  $\pm 30^\circ$  with respect to the mean surface normal. We assumed that the mean plane of the surface was the one that gave rise to the specular beam in the angular distribution. This consideration enables one to determine the angle of incidence and the angles of scattering with respect to the mean surface normal in eq (1) if the angle of incidence and scattering angles in the laboratory coordinate system are known. Figure 5 shows pairs of distributions for both  $+30^\circ$  and  $-30^\circ$  AI. The difference between the members of a pair is a rotation of the specimen of  $180^\circ$  about the normal. The deep holes in the distributions occur at the backscattering angle where the mirror M2, which directs the incident light towards the surface, also

shadows the detector array from the scattered light. The close match between the members of each pair suggests that there is very little directionality to the roughness peaks and valleys and that the surface is well aligned in the instrument. Two pairs of distributions like these were taken for each of the four specimens.

Distributions for the four specimens are shown in figure 6. These were all taken with an angle of incidence of  $+30^\circ$ . The values given for roughness average  $R_a$  were calculated from the stylus data (sec. 5.2). The roughness average is defined as the average deviation of the profile about the mean line [19]. There are obvious changes in these distributions as the roughness increases. The AD for the smoothest surface has a strong specular beam at  $\theta_s = -30^\circ$  and very little scattered light. For  $R_a = 0.20 \mu\text{m}$ , the specular beam appears to have vanished but the distribution still peaks strongly at the specular angle. The results for the two roughest surfaces differ significantly from the first two but are quite similar to each another. This is to be expected since at high roughness values ( $R_a \gtrsim \lambda$ ), the effect on the distribution due to increasing roughness should approach saturation.

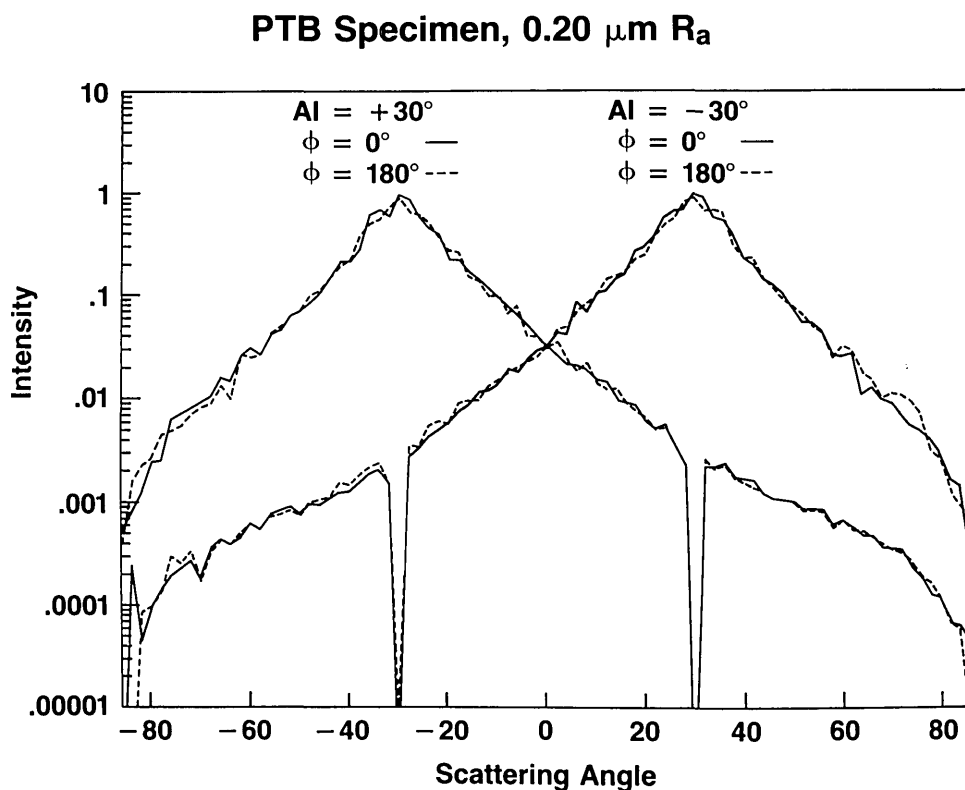


Figure 5—Four angular scattering distributions for a commercial roughness specimen. The measured  $R_a$  was  $0.20 \mu\text{m}$ . For each angle of incidence, AI =  $+30^\circ$  or  $-30^\circ$ , distributions were measured with the specimen oriented at rotation angles  $\phi = 0^\circ$  and  $180^\circ$  about the normal axis to the specimen.

## PTB Roughness Specimens; $\text{AI} = +30^\circ, \phi = 0^\circ$

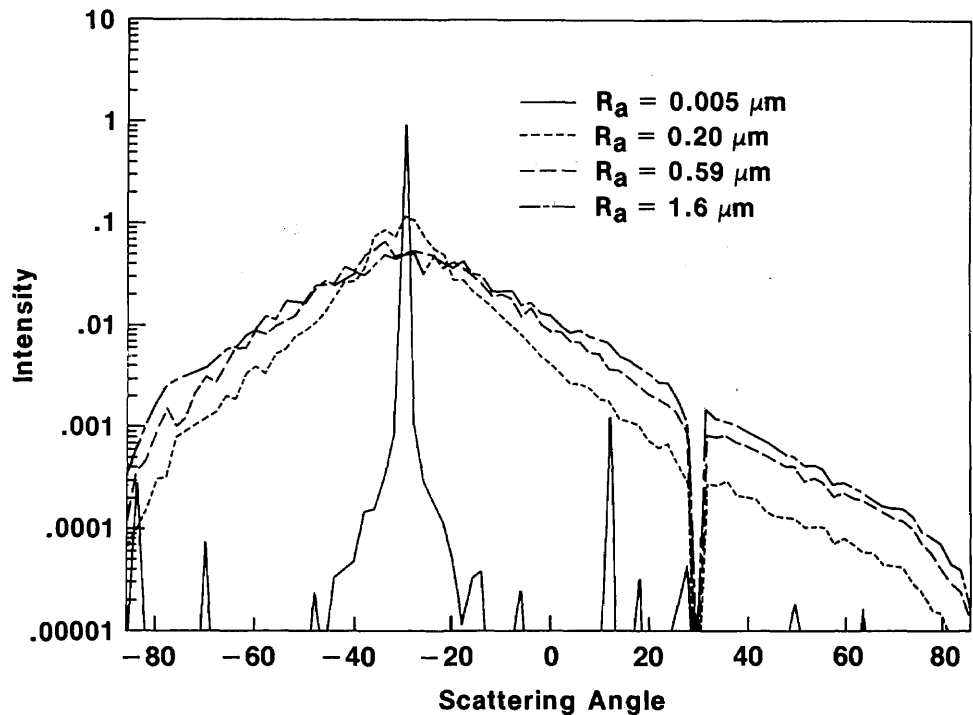


Figure 6—Angular scattering data for the set of four commercial roughness specimens. Those with  $R_a=0.20, 0.59,$  and  $1.6 \mu\text{m}$  are highly two-dimensional, i.e., the surface is essentially smooth perpendicular to the plane of incidence. The angular distributions are normalized so that each has the same total intensity, which is obtained by summing the signals from all the detectors. Note that the intensities are plotted on a logarithmic scale.

### 5.2 Stylus

Portions of the stylus traces taken for each specimen are shown in figure 7. The traces were measured without any electronic long-wavelength cutoff, and the profiles are thus undistorted except for the high-frequency cutoff of the instrument and convolution of the profile with the stylus tip, which has a measured width of less than  $1 \mu\text{m}$ .

The quoted  $R_a$  values were calculated as the average deviation of the profile around a least squares straight line. For this calculation, the 1.84 mm trace length was not divided into shorter sampling lengths as is often done in surface metrology. Hence the  $R_a$  values include effects due to spatial wavelengths limited only by the trace itself.

The three rough specimens were manufactured so that the 2-D "random" roughness pattern repeats itself. This is not evident in the profiles since the periods of the patterns are 1.3, 4, and 4 mm, respectively. Such a periodicity gives rise to very closely spaced diffraction peaks in the angular distribution, but this structure is not resolved by the  $1.5^\circ$  angular resolution of the detectors. Therefore, the long periodic structure of the surface does not significantly affect the measured angular distributions.

### 6. Analysis

The least squares straight line was subtracted from the stored profile data from the stylus instrument to yield a new digitized profile  $z(x)$ . It was assumed that the least squares line was equivalent to the  $x$ -direction of integration in eq (1) and lay in the mean plane that gave rise to the specular beam in the optical experiment.

The profile data  $z(x)$  were substituted into eq (1) and the value for the relative field strength  $F$  was calculated for each angle  $\theta_s$ . It was not necessary to determine the constant  $C_0$  to determine the shape of the scattering distribution. The value of  $|F|^2$  was calculated to derive a quantity proportional to light intensity. This quantity  $|F|^2$  was then averaged in two ways to develop good statistics in the result:

*Speckle Average.* Figure 8 shows a close-up view of a segment of the angular distribution projected on the wall of the laboratory. The distribution consists of a complex pattern of fine speckles [9] that vary greatly in intensity from one point to the next. In our apparatus, the average size of the speckles is roughly 0.1 mm or  $0.04^\circ$  [20] at the front surfaces of the detector lenses. The lenses themselves span an angle of  $1.5^\circ$  (about 40% of the length of figure 8); therefore,

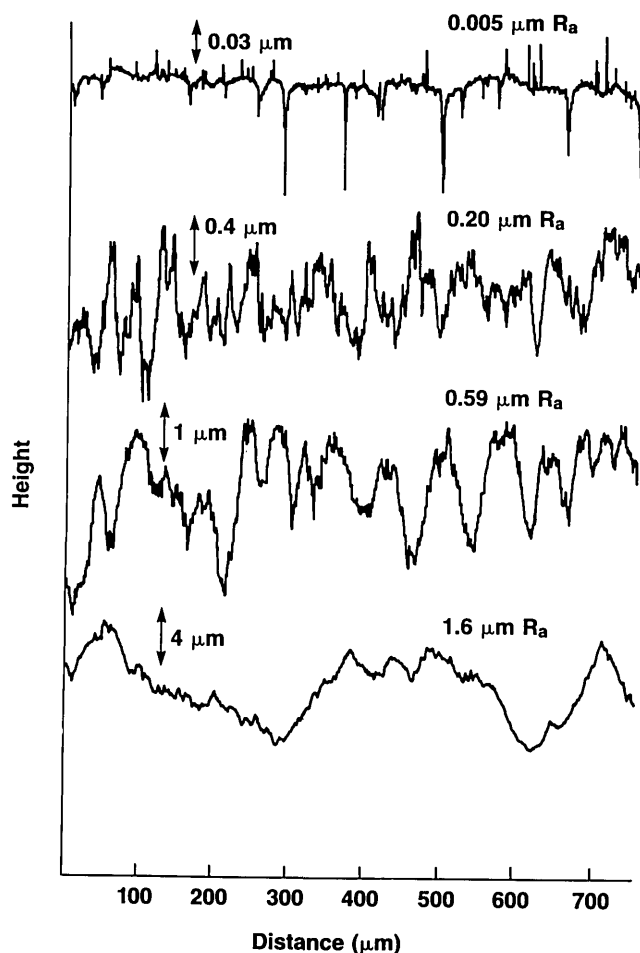


Figure 7—Stylus profiles for the specimens which were studied by the angular scattering measurements shown in figure 6. Note the differences in the vertical scales.

each detector averages the intensity of a large number of speckles. A single calculation of  $|F|^2$  from eq (1) would only yield the intensity of a single point. Hence for each detector angle  $\theta_s$ , it is necessary to average over several closely spaced angles to derive reasonable statistics for the overall pattern. In the present experiment, we used seven angles in the plane of incidence separated from one another by  $0.05^\circ$  and centered about the nominal angle  $\theta_s$ .

*Profile Average.* The intensity distributions resulting from the speckle average were then averaged over 10 surface profiles in order to achieve some measure of area average which simulates the area averaging of the light scattering approach. In the case of the  $1.6 \mu\text{m } R_a$  surface, only nine surface profiles were used because we subsequently discovered that one of the profiles had anomalies in the data in several places. To improve the statistics for this case, nine speckle values were calculated instead of seven.



Figure 8—A segment of the angular distribution projected on the wall of the laboratory. The specimen had  $R_a=0.20 \mu\text{m}$ . The photograph spans an angle of about  $3.5^\circ$  from top to bottom. The fine speckle structure is clearly shown.

As a result of the averaging procedure, the relative intensity calculated for each value of  $\theta_s$  is an average of 70 integrals represented by eq (1) and takes approximately 9 hours on a Perkin Elmer 3230 minicomputer. The resulting distributions are shown by the dotted lines in figures 9–12 and are compared with the measured angular distributions (solid lines). The phase integral calculations successfully reproduce the changes in the experimental distributions from one surface to the next. The specular beam dominates the pattern for the smoothest surface in figure 9. Both the theory and experiment show the same amount of sharp curvature near the specular direction in figure 10 and the same rounded structure in figures 11 and 12. The major difference between the model and the data is that in all cases, the theoretical distribution falls below the experimental one on the wings. The ratios between the curves are as high as an order of magnitude at some places. Nevertheless, it is gratifying that for these regimes of roughness, the simplified theory can predict much about the distributions.

## 7. Discussion

### 7.1 Limitations in the Present Work

A large number of approximations has entered into the simplified theory of eq (1). Improvements to the preliminary analysis will involve removing each of

Figure 9—Data vs. calculation for the mirror-like surface with  $R_a=0.005 \mu\text{m}$ . The distributions are normalized in the same way as those in figure 6.

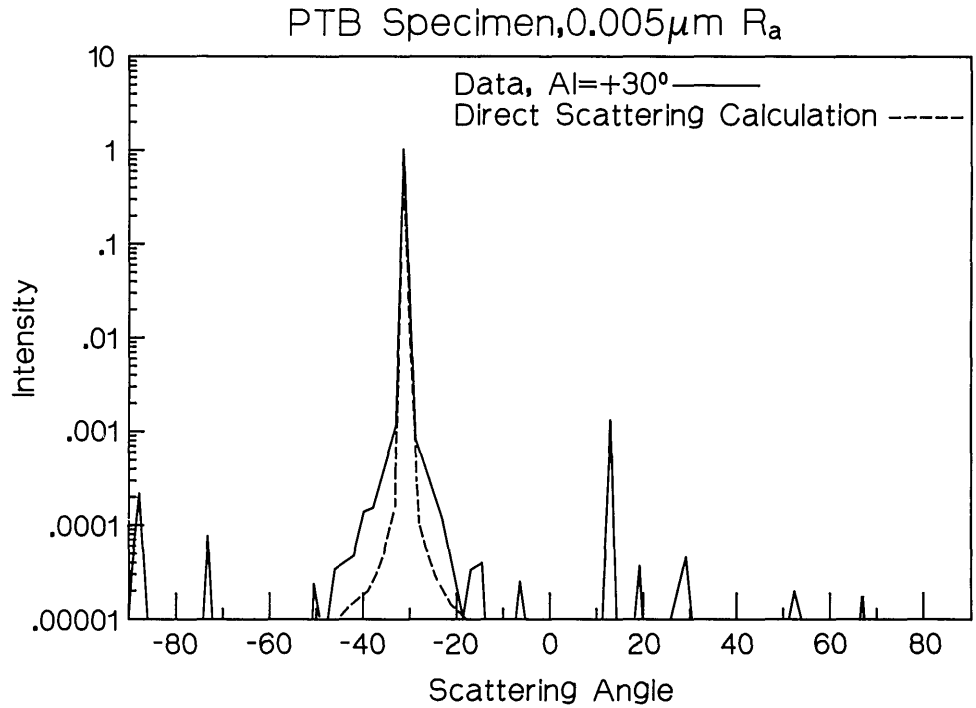
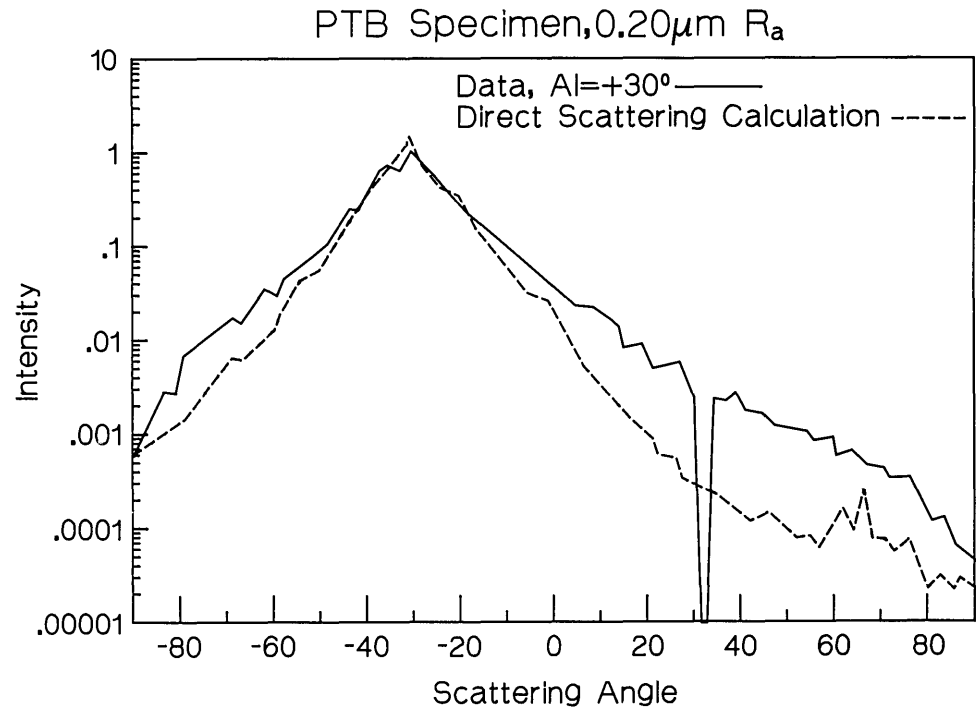


Figure 10—Data vs. calculation for the  $R_a=0.20 \mu\text{m}$  surface.



these approximations and observing how the agreement with the data is affected. We outline some of these possibilities below in terms of one experimental limitation and three model limitations:

1) It is possible that the stylus profiles should be taken with better horizontal resolution, i.e., there may be structures in the true surface profile with spatial

wavelengths between  $0.4$  and  $1.5 \mu\text{m}$  that were not sufficiently resolved by the stylus instrument with its high spatial frequency cutoff of  $1 \mu\text{m}$ . These structures may contribute significantly to the optical scattering. In fact, they would tend to increase the scattering on the outer wings, since short spatial wavelengths scatter light into large angles.

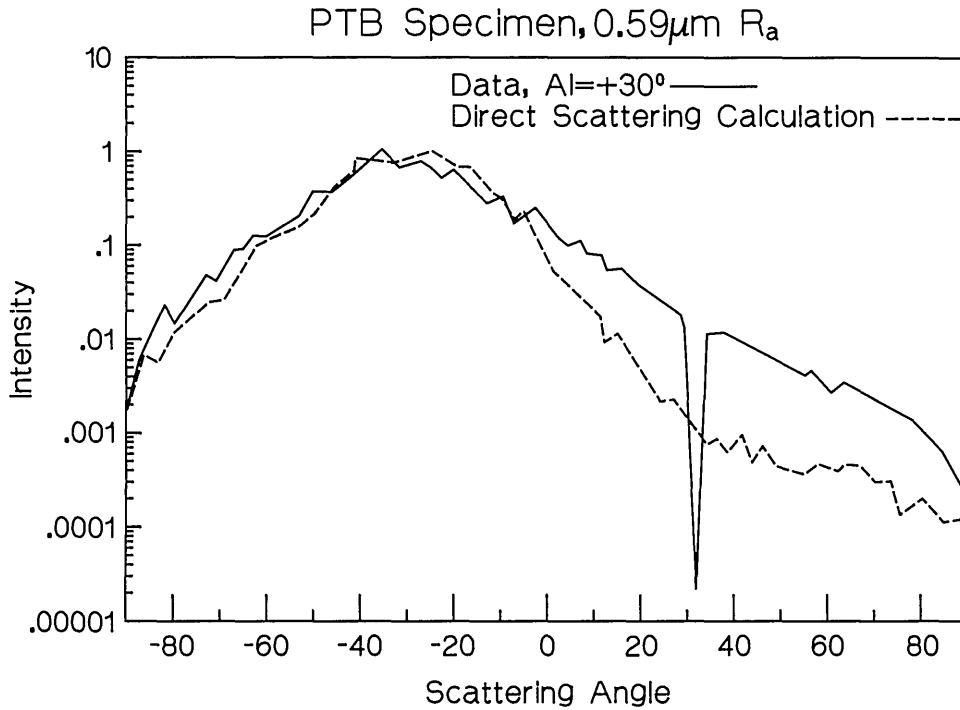


Figure 11—Data vs. calculation for the  $R_a=0.59 \mu\text{m}$  surface.

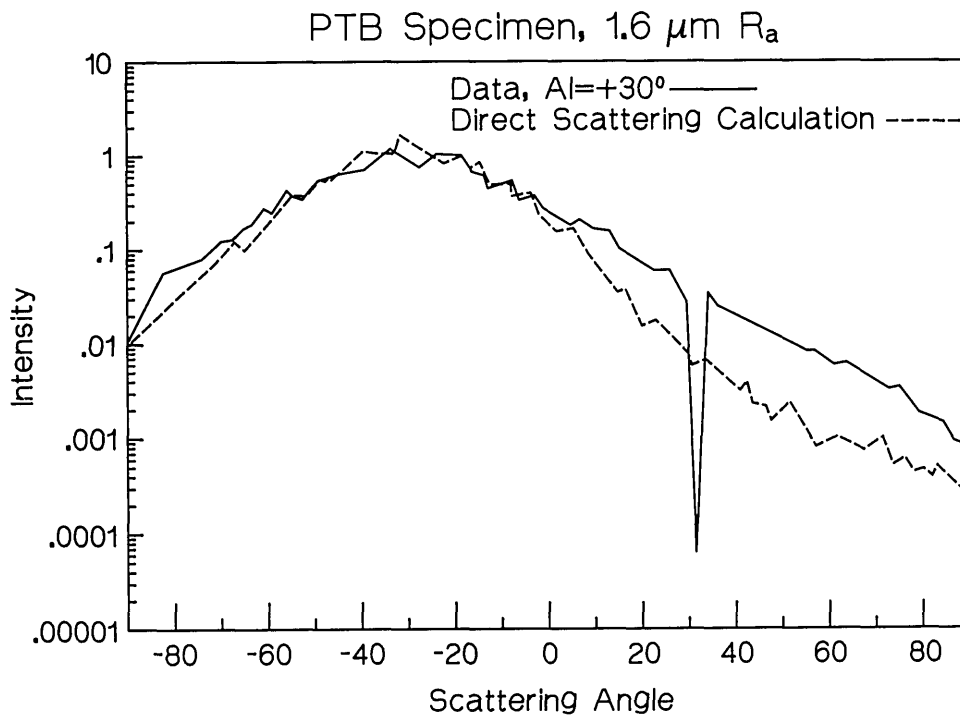


Figure 12—Data vs. calculation for the  $R_a=1.6 \mu\text{m}$  surface.

2) Equation (1) is the result of an integration by parts [21]. It neglects an additive contribution from the end points, 0 and  $L$ . This approximation seems valid provided the length  $L$  is much greater than  $\lambda$ , but perhaps the approximation fails at low scattering intensities, where destructive interference due to phase

cancellation effects in the scattering pattern is very high.

3) The preliminary analysis neglects any contribution from shadowing. It assumes that every point on the surface profile is illuminated with uniform intensity and contributes to the scattering at every

angle  $\theta_s$ . However, it is likely that at grazing scattering angles, the outgoing wave from certain valleys is blocked by the peaks, and it is also possible that some of these valleys are shadowed from the incoming beam as well. The former effect probably tends to reduce the radiation scattered into the wings of the distribution, whereas the latter probably broadens the angular distribution by adding a degree of amplitude modulation to the already phase modulated outgoing wave.

4) It has been assumed in eq (1) that the electric field quantities on the surface are not functions of the local surface topography. This assumption implies several other assumptions, for example, that the reflection coefficient is not a function of either local slope or local curvature and that the electric field at each point on the surface is not affected by scattering from other points. All of these simplifications seem to be good ones for metallic surfaces where the reflection coefficients are fairly high, the surface slopes and curvatures small, and the significant roughness wavelengths much greater than  $\lambda$ . If some of the approximations were invalid, that might result in significant polarization effects in the angular scattering distributions. We have done experiments with linearly polarized light on the 0.59 and 0.20  $\mu\text{m}$  surfaces and have found no significant differences between the angular distributions for *s*- and *p*-polarized incident beams, further suggesting that the simple theory may be valid for these surfaces. However, in view of the current differences between data and calculation, the breakdown of these simplifications and assumptions must be more carefully investigated, and more rigorous theories of electromagnetic scattering [22–23] should be applied to the roughness regime studied here.

## 7.2 Previous Work

Our experiment is a direct test of the Beckmann-Spizzichino optical scattering theory for engineering surfaces where the roughness heights are the same order of magnitude as the wavelength of light. With the capabilities for measuring angular scattering distributions and storing and analyzing surface profiles, we have all the components for determining the level of complexity needed for a valid description of the optical scattering from these surfaces. Several previous studies on engineering surfaces [24–27] have correlated optical scattering measurements with roughness parameters such as  $R_q$  or the rms roughness  $R_q$  [19] obtained from stylus instruments, but they have not investigated the effects of the surface profiles

directly. Chandley [28] and Thwaite [29] took a middle approach by comparing optical results with statistical functions generated from stylus profiles. Chandley compared the autocorrelation functions predicted from optical scattering distributions with those measured by stylus; Thwaite compared the power spectral densities calculated from stylus profiles with optical scattering distributions directly. However, both approaches involved theoretical assumptions that are not needed in the present work.

Experiments involving measured and calculated scattering distributions have been done for optical surfaces by Elson, Bennett, and Rahn [30,31]. Their work differs from ours in that the theory they used is more straightforward. Since the rms roughness  $R_q$  was much less than  $\lambda$  in the optical regime, first order Rayleigh theory could be used to analyze the optical scattering effects due to surface roughness. On the other hand, their experiments posed different kinds of difficulties from the present work. Optical surfaces generally produce low-intensity angular distributions that are strongly peaked in the forward direction near the specular beam, so the angular resolution and signal resolution requirements for their apparatus were high. Despite these differences, the agreement between theory and experiment for the previous studies is comparable to that observed here.

## 7.3 Future Directions

Our work is a preliminary step in the study of engineering surfaces by optical scattering. Once this direct scattering approach produces agreement with experiments for ideal, two-dimensional surfaces, its validity must be tested for real, anisotropic surfaces produced by many kinds of processes such as milling, grinding, and lapping. For these surfaces, there is a certain amount of light scattered slightly out of the plane of incidence, so the geometrical problem is only approximately two-dimensional. Highly isotropic surfaces such as those produced by shot blasting or electron-discharge machining must also be studied. In those cases, the scattering problem is truly three-dimensional.

Finally, in order to use the optical scattering techniques for characterizing surfaces, comparisons with direct scattering methods are not sufficient. The inverse scattering problem must be solved adequately so that surface parameters such as  $R_q$  may be derived in a reliable way solely from optical scattering data. This is where the speed and resulting economic benefits of on-line optical methods will be realized.

## 8. Appendix: Experimental Notes

### 8.1 Calibration

The calibration of the 87 detectors is an important part of the operation of the apparatus. The relative sensitivity can vary by as much as a factor of 3 from one detector to the next. Therefore, at the beginning of each day's run, the system is calibrated in the following way. The specimen table is dropped below the center of the yoke, and a fixture with a flat mirror is inserted into the rotating mirror assembly. The surface of this mirror is located at the center of the yoke, but the mirror rotates with the M1, M2 assembly. This setup allows a laser beam of constant intensity to illuminate each of the detectors in turn as the mirror assembly is rotated. The 87 signals from the detector array are collected in this way and stored as a set of normalization data. The signals collected in the subsequent data runs are then normalized by dividing each detector reading by the corresponding normalization datum. The relative sensitivities of the detectors, when normalized in this way, are equal to within approximately  $\pm 2\%$  (1 standard deviation), a figure which includes the variation in sensitivity from one day to another.

In addition to the variation of sensitivity among the detector channels, there is an offset voltage signal at

zero light level, which is constant with time but which varies from one detector to the next. Since the magnitudes of these offset signals are between 20 and 100 mV, and measurements are made which may be as small as  $10 \mu\text{V}$ , these light-off signals must be subtracted from those measured with the light on. Therefore, each calibration run or data run actually consists of taking the difference between two scans of the detectors, a background scan measured with the laser beam diverted by a shutter, and a signal scan measured with the laser beam turned on.

### 8.2 Stray Light

A certain amount of stray light enters the detectors due to reflection from the ends of the optical fibers themselves. Approximately 1% of the light entering each lens is reflected from the fiber located at the focal point and refocused back to the surface. For a sharply peaked angular distribution, the effect influences the signals in the backscattered direction as shown in figure 13. The dotted line was taken under conditions which allow the light reflected from the detectors near  $-30^\circ$ , the specular direction, to propagate to the detectors located near the backscattering angle of  $+30^\circ$ . The solid line was taken by placing a dark mask to block the detectors near

PTB Specimen,  $0.20 \mu\text{m } R_a$ ,  $\text{Al} = +30^\circ$

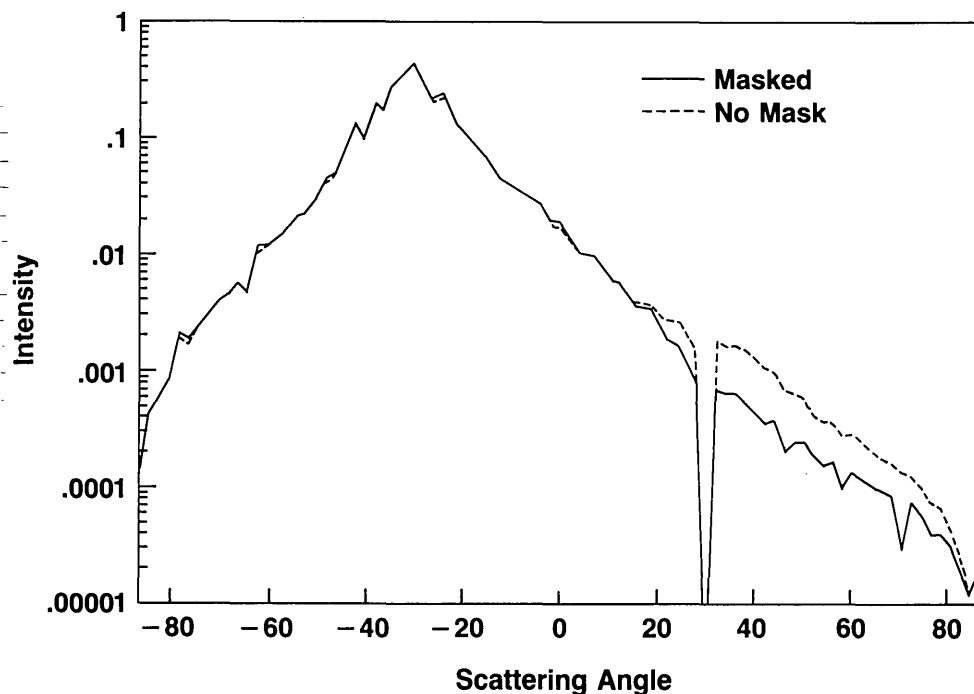


Figure 13—Two angular distributions that show the effects of reflected stray light. The data shown by the solid line were taken with a dark shield masking the detectors around the specular beam when the backscattered detectors were scanned. The data represented by the dotted line were taken without masking and show a small shoulder in the backscattered direction.

-30° as those near +30° were being scanned. The solid line represents a true angular distribution whereas the dotted line includes a shoulder around +30° due to the reflected stray light. All of the experimental distributions shown in figures 9-12 were measured with the masking approach. The difference between the curves of figure 13 is approximately a mirror image of the angular distribution itself but lower in intensity by about 2 1/2 orders of magnitude.

It is important to note that this effect is significant only when the yoke is positioned vertically, when the angular distribution is sharply peaked, and when the surface is highly two-dimensional, so that most of the stray light is scattered by the surface back into the plane of incidence again.

In future experiments, we plan to model the effect of this reflected light on the detector signals and perform the appropriate subtractive massage on the measured angular distributions to correct for it.

---

The authors are grateful to K. M. Kunz, D. Medved, A. W. Hartman, J. Geist, E. F. Zalewski, and W. Gladden for key contributions during the construction and testing of DALLAS, and to members of the Fabrication Technology Division, particularly C. Summers and R. Lach, for the construction of a number of components. We would also like to thank S. A. Holliday for assistance during the early stages of the project, H. M. Helfer for photography of the apparatus and the angular distribution patterns, S. Morris for assistance in the preparation of the manuscript, and E. Marx, G. Blessing, and D. R. Flynn for valuable suggestions while the manuscript was in review.

## 9. References

- [1] Gardner, C. S.; Alster, L. G. Electro-optic gauge for measuring the surface roughness of crankshaft bearings, presented at the 2nd Int. Prec. Eng. Seminar (National Bureau of Standards, Gaithersburg, MD, May 1983); Gardner, C. S.; Streight, W. E. U.S. Patent No. 4,364,663, 12/82.
- [2] Zombeck, M. V.; Wyman, C. C.; Weisskopf, M. C. High resolution x-ray scattering measurements for Advanced X-ray Astrophysics Facility (AXAF), in *Radiation Scattering in Optical Systems*. Proc. SPIE 257, 230 (1980).
- [3] Vorburger, T. V.; Teague, E. C. Optical techniques for on-line measurement of surface topography. *Prec. Eng.* 3, 61 (1981).
- [4] Corey, H. S. Surface finish from reflected laser light, in *Advances in Optical Metrology*. Proc. SPIE 153, 27 (1978).
- [5] Teague, E. C.; Vorburger, T. V.; Maystre, D. M. Light scattering from manufactured surfaces. *CIRP Annals* 30, 563 (1981).
- [6] Elson, J. M.; Bennett, J. M. Vector scattering theory, *Opt. Eng.* 18, 116 (1979).
- [7] Church, E. L.; Zavada, J. M. Residual surface roughness of diamond-turned optics. *Appl. Opt.* 14, 1788 (1975).
- [8] Stover, J. C.; Serati, S. A. Calculation of surface statistics from light scatter, in *Precision Surface Metrology*. Proc. SPIE 429, 96 (1983).
- [9] Dainty, J. C., ed. Laser speckle and related phenomena, *Topics in Applied Physics*, Vol. 9 (Springer-Verlag, Berlin, 1975).
- [10] Teague, E. C. Evaluation, revision, and application of the NBS stylus/computer system for the measurement of surface roughness. *Natl. Bur. Stand. (U.S.) Tech. Note* 902; 1976.
- [11] Vorburger, T. V.; Teague, E. C.; Scire, F. E. Fast facility available for engineering needs. *Dimensions/NBS* 62, No. 11, 18 (Nov. 1978).
- [12] Vorburger, T. V. FASTMENU: A set of FORTRAN programs for analyzing surface texture. *Natl. Bur. Stand. (U.S.) NBSIR* 83-2703; 1983.
- [13] Similar specimens are discussed by Häsing, J., *Herstellung und Eigenschaften von Referenznormalen für das Einstellen von Oberflächenmessgeräten*. *Werksattstechnik* 55, 380 (1965).
- [14] Beckmann, P.; Spizzichino, A. *The Scattering of Electromagnetic Waves from Rough Surfaces* (Pergamon, New York, 1963). Refs. 14,17,18 cite many other works dealing with the theory of optical scattering from rough surfaces.
- [15] Azzam, R. M. A.; Bashara, N. M. Polarization characteristics of scattered radiation from a diffraction grating by ellipsometry with application to surface roughness. *Phys. Rev.* B5, 4721 (1972).
- [16] Vorburger, T. V.; Ludema, K. C. Ellipsometry of rough surfaces, *Appl. Opt.* 19, 561 (1980).
- [17] Bass, F. G.; Fuks, I. M. *Wave Scattering from Statistically Rough Surfaces* (Pergamon, London, 1979).
- [18] Wirgin, A. Scattering from sinusoidal gratings: An evaluation of the Kirchoff approximation. *J. Opt. Soc. Am.* 73, 1028 (1983).
- [19] American National Standards Institute B46.1-1978, *Surface Texture* (American Society of Mechanical Engineers, New York, 1978).
- [20] Francon, M. *Laser Speckle and Applications in Optics* (Academic Press, New York, 1979), p.25.
- [21] Ref. 14, p. 24f.
- [22] Petit, R., ed. Electromagnetic theory of gratings, *Topics in Current Physics*, Vol. 22 (Springer-Verlag, Berlin, 1980).
- [23] Maystre, D. Electromagnetic scattering from perfectly conducting rough surfaces in the resonance region. *IEEE Trans.* AP-31, 885 (1983).
- [24] A few representative articles on light scattering experiments are given in refs. 4 and 25-31 below. A number of other articles are cited in ref. 3.
- [25] Bennett, H. E.; Porteus, J. O. Relation between surface roughness and specular reflectance at normal incidence. *J. Opt. Soc. Am.* 51, 123 (1961).
- [26] Tanner, L. H. A comparison between Talysurf 10 and optical measurements of roughness and surface slope. *Wear* 57, 81 (1979).
- [27] Smith, T. F.; Hering, R. G. Comparison of the Beckmann

- model with bidirectional reflectance measurements, presented at the ASME-AICH Heat Transfer Conf. (Atlanta, 1973), ASME publ. 73-HT-11.
- [28] Chandley, P. J. Determination of the autocorrelation function of height on a rough surface from coherent light scattering. *Opt. Quant. Elect.* **8**, 329 (1976).
  - [29] Thwaite, E. G. The direct measurement of the power spectrum of rough surfaces by optical Fourier transformation. *Wear* **57**, 71 (1979), and A quantitative comparison of the wavelength spectrum of a surface obtained by optical Fourier transformation with calculations from profile measurements. *Wear* **83**, 181 (1982).
  - [30] Elson, J. M.; Bennett, J. M. Relation between the angular dependence of scattering and the statistical properties of optical surfaces. *J. Opt. Soc. Am.* **69**, 31 (1979).
  - [31] Elson, J. M.; Rahn, J. R.; Bennett, J. M. Light scattering from multilayer optics: comparison of theory and experiment. *Appl. Opt.* **19**, 669 (1980).

# Microstructural Characterization of Ceramic Materials by Small Angle Neutron Scattering Techniques

K. Hardman-Rhyne, N. F. Berk, and E. R. Fuller, Jr.

National Bureau of Standards, Washington, DC 20234

Accepted: December 1, 1983

The use of small angle neutron scattering (SANS) techniques for ceramic materials is discussed. Two areas are emphasized: 1) diffraction for microstructural phenomena of less than 100 nm, and 2) beam broadening for microstructural phenomena greater than 90 nm.

Key words: ceramic materials; green compact  $\text{YCrO}_3$ ; porosity;  $\text{Si}_3\text{N}_4$ ; small angle neutron scattering.

## Introduction

Small angle neutron scattering (SANS) techniques are used to study microstructural phenomena in the range of 1 to  $10^4$  nm in size. Since they cover a wide range of sizes, these techniques are particularly useful in studies of ceramic processing and distributed damage in ceramics. While many metal and alloy systems have used SANS techniques, few experiments have been published on ceramic materials. This is not surprising considering the difficulties inherent in analyzing SANS data on these materials. Often ceramics have several microstructural components such as residual voids from the sintering process, inclusions or impurities from starting materials, second phases, and microcracks or cavities from temperature and/or pressure treatments, as well as dislocations present in the material. All these effects produce small angle neutron scattering. It is important to either eliminate all effects except the one of interest or to identify the effects through complementary studies

that use other techniques such as electronic or optical microscopy. While these complementary techniques can identify defects, voids, and second phases, SANS can quantify these effects throughout the bulk of the materials in a nondestructive way due to the general nature of neutrons.

Neutrons are an excellent nondestructive probe of microstructure because the thermal neutron energies are very low and neutrons are not absorbed in most materials. Since the neutrons primarily interact with the nucleus of the atoms, the neutron beam is highly penetrating without disturbing the sample. This allows us to examine the bulk of the material whereas x-ray and other techniques are more sensitive to surface phenomena. One strength of neutron scattering is its dependence on the chemical elements present in the material through a quantity called the coherent scattering length,  $b$  [1]<sup>1</sup>. Since  $b$  values vary in an unsystematic way from one element to another, differences between elements with similar atomic numbers can be detected, e.g., aluminum and magnesium or iron and manganese (see table 1).

Magnetic and isotope behavior can be studied with SANS techniques. Neutrons have a magnetic moment which interacts with the electrons in the material. The magnetic and structural properties of many ferrites and rare earth garnets have been examined with neutron scattering. Isotope studies involving hydrogen

---

**About the Authors, Paper:** K. Hardman-Rhyne, a chemist, and N. F. Berk and E. R. Fuller, Jr., physicists, are with the NBS Center for Materials Science. The work reported on here was supported in part by the Army Materials and Mechanics Research Center with funds provided by the Department of Energy under Interagency Agreement DOE/AMMRC (DOE-1A No. DE-A101-77-CS5-1017).

---

<sup>1</sup> Numbers in brackets indicate references at the end of this paper.

**Table 1.** Bound values of coherent scattering length, incoherent scattering cross-section and absorption cross-section for elements and isotopes (from Ref. [1])

Atomic number	Element or isotope	Nucl. spin	Scattering length <sup>a</sup> $b(10^{-12} \text{ cm})$	Incoherent scattering cross-section $\sigma_{\text{inc}}(\text{barn})$	Absorption cross section for $\lambda = 1.8 \text{ \AA}$ $\sigma_{\text{abs}}(\text{barn})$
1	<sup>1</sup> H	1/2	-0.3740 (1)	79.7	0.33
	<sup>2</sup> H=D	1	0.6674 (6)	2.0	0.00046
	<sup>3</sup> H=T	1/2	0.50 (3)		
2	<sup>3</sup> He	1/2	0.62	1.2	5500
	<sup>4</sup> He	0	0.30 (2)	0	<0.007
3	Li		-0.203 (5)	0.7	71
	<sup>6</sup> Li	1	0.18+0.025 <i>i</i>		945
	<sup>7</sup> Li	3/2	-0.233	0.7	
4	Be	3/2	0.78 (4)	0.005 (1)	0.010
5	B		0.535 (6)+0.021 <i>i</i>	0.7 (2)	755
	<sup>10</sup> B	3	0.14+0.11 <i>i</i>		3813
	<sup>11</sup> B	3/2	0.60		
6	C		0.66484 (13)	<0.018	0.0033
	<sup>12</sup> C	0	0.665	0	
	<sup>13</sup> C	1/2	0.60	1.0	
7	N		0.936 (2)	0.46 (12)	1.88
	<sup>14</sup> N	1	0.94		
	<sup>15</sup> N	1/2	0.65		
8	O		0.5803 (5)	<0.015	<0.0002
	<sup>16</sup> O	0	0.580	0	
	<sup>17</sup> O	5/2	0.578		
	<sup>18</sup> O	0	0.600	0	
9	F	1/2	0.566 (2)	0.0004	<0.01
10	Ne		0.46	<0.11	<2.8
11	Na	3/2	0.363 (2)	1.75 (3)	0.505
12	Mg		0.5375 (4) <sup>b</sup>	0.04 (3)	0.063
	<sup>24</sup> Mg	0	0.55	0	
	<sup>25</sup> Mg	5/2	0.36		
	<sup>26</sup> Mg	0	0.49	0	
13	Al	5/2	0.3446 (5)	<0.01	0.230
14	Si		0.41491 (10)	<0.017	0.16
15	P	1/2	0.513 (1)	<0.23	0.2
16	S		0.2847 (1)	0.012 (4)	0.52
17	Cl		0.95792 (8)	5.9 (3)	33.6
	<sup>35</sup> Cl	3/2	1.18		
	<sup>37</sup> Cl	3/2	0.26		
18	A		0.18 (2)	0.27 (12)	0.66
	<sup>36</sup> A	0	2.43	0	
19	K		0.371 (2)	0.38 (11)	2.07
	<sup>39</sup> K	3/2	0.37		
20	Ca		0.490 (3)	<0.06	0.46
	<sup>40</sup> Ca	0	0.49	0	
	<sup>44</sup> Ca	0	0.18	0	
21	Sc	7/2	1.215 (13)	0.446 (23)	24

and deuterium are also possible because the neutron scattering behavior of these elements is very different. This capability is often used in biological or polymer research.

This paper will discuss several NBS experiments on ceramic materials with a greater emphasis on SANS techniques rather than the actual pertinent values obtained. The main intention here is to emphasize the advantages and limitations of these techniques and to

spark interest in further SANS ceramic research studies. We will divide the measurement discussion into three parts, as follows: 1) the diffraction limit which includes small particles or defects in the range of 1 to 100 nm, 2) the multiple refraction limit which includes large particles and defects, usually 20  $\mu\text{m}$  or greater, and 3) the beam broadening region which lies between these two limits. However, preceding this discussion are two sections, one on the SANS

Table 1 (Continued)

Atomic number	Element or isotope	Nucl. spin	Scattering length <sup>a</sup> $b(10^{-12} \text{ cm})$	Incoherent scattering cross-section $\sigma_{\text{inc}}(\text{barn})$	Absorption cross section for $\lambda = 1.8 \text{ \AA}$ $\sigma_{\text{abs}}(\text{barn})$
22	Ti		-0.337 (2)	2.71 (22)	5.8
	<sup>46</sup> Ti	0	0.48	0	
	<sup>47</sup> Ti	5/2	0.33		
	<sup>48</sup> Ti	0	-0.58	0	
	<sup>49</sup> Ti	7/2	0.08		
	<sup>50</sup> Ti	0	0.55	0	
23	V		-0.0385 (1)	4.97 (5)	4.98
	<sup>51</sup> V	7/2	-0.038		
24	Cr		0.3532 (10)	1.90 (3)	3.1
	<sup>52</sup> Cr	0	0.490	0	
25	Mn	5/2	-0.373 (2)	0.6 (2)	13.2
26	Fe		0.954 (6)	0.22 (16)	2.53
	<sup>54</sup> Fe	0	0.42	0	
	<sup>56</sup> Fe	0	1.01	0	
	<sup>57</sup> Fe	1/2	0.23		
	<sup>58</sup> Fe	0	1.54 (68)		
27	Co	7/2	0.278 (4)	5.22 (8)	37
28	Ni		1.03 (1)	5.0 (6)	4.8
	<sup>58</sup> Ni	0	1.44	0	
	<sup>60</sup> Ni	0	0.28	0	
	<sup>61</sup> Ni	3/2	0.76		
	<sup>62</sup> Ni	0	-0.87	0	
	<sup>64</sup> Ni	0	-0.037	0	
29	Cu		0.7689 (6)	0.51 (4)	3.77
	<sup>63</sup> Cu	3/2	0.67		
	<sup>65</sup> Cu	3/2	1.11		
30	Zn		0.5686 (3)	0.08 (1)	1.10
	<sup>64</sup> Zn	0	0.55	0	
	<sup>66</sup> Zn	0	0.63	0	
	<sup>68</sup> Zn	0	0.67	0	
31	Ga		0.72 (1)	<0.5	2.80
32	Ge		0.81858 (36)	<0.2	2.45
33	As	3/2	0.673 (2)	<1.6	4.3
34	Se		0.795 (4)	0.27	12.3
35	Br		0.677 (2)	<0.5	6.7
36	Kr		0.791 (15)		31
37	Rb		0.708 (2)	<0.4	0.7
	<sup>85</sup> Rb	5/2	0.83		
38	Sr		0.69 (1)	4.0	1.21
39	Y	1/2	0.775 (2)	0.15 (1)	1.31
40	Zr		0.70 (1)	<0.3	0.18
41	Nb	9/2	0.7050 (3)	0.0063 (6)	1.15
42	Mo		0.695 (7)	<0.6	2.7
43	<sup>99</sup> Tc	9/2	0.68 (3)		122
44	Ru		0.721 (7)	<0.1	2.56
45	Rh	1/2	0.588 (4)	1.2	156
46	Pd		0.60	0.093 (9)	8.0

instrument at NBS and the other on the theory, that will provide some background.

### Instrument

The SANS instrument at the National Bureau of Standards is described in detail elsewhere [2];

however, a schematic of the major components is shown in figure 1. The characteristics of the SANS instrument are given in table 2. The wavelength,  $\lambda$ , can be varied from 0.4 to 1.0 nm by selecting the appropriate speed of a rotating helical-channel velocity selector. This is particularly important in beam broadening experiments because the wavelength

Table 1 (Continued)

Atomic number	Element or isotope	Nucl. spin	Scattering length <sup>a</sup> $b(10^{-12} \text{ cm})$	Incoherent scattering cross-section $\sigma_{\text{inc}}(\text{barn})$	Absorption cross section for $\lambda = 1.8 \text{ \AA}$ $\sigma_{\text{abs}}(\text{barn})$
47	Ag		0.602 (2)	0.49 (4)	63
	<sup>107</sup> Ag	1/2	0.83		
	<sup>109</sup> Ag	1/2	0.43		
48	Cd		0.37+0.16i		2450
	<sup>113</sup> Cd	1/2	-1.5+1.2i		20000
49	In		0.408 (4)		196
50	Sn		0.6223 (4)	0.022 (5)	0.625
	<sup>116</sup> Sn	0	0.58	0	
	<sup>117</sup> Sn	1/2	0.64		
	<sup>118</sup> Sn	0	0.58	0	
	<sup>119</sup> Sn	1/2	0.60		
	<sup>120</sup> Sn	0	0.64	0	
	<sup>122</sup> Sn	0	0.55	0	
	<sup>124</sup> Sn	0	0.59	0	
	51	Sb		0.5641 (12)	
52	Te		0.543 (4)	0.6 (4)	4.7
	<sup>120</sup> Te	0	0.52	0	
	<sup>123</sup> Te	1/2	0.57		
	<sup>124</sup> Te	0	0.55	0	
	<sup>125</sup> Te	1/2	0.56		
53	I	5/2	0.528 (2)	~0	7.0
54	Xe		0.488 (3)		74
	<sup>135</sup> Xe				$2.7 \times 10^6$
55	Cs	7/2	0.542 (2)	4.6	29
56	Ba		0.528 (5)	2.5	1.2
57	La		0.827 (5)	1.87 (17)	9.3
	<sup>139</sup> La	7/2	0.83		
58	Ce		0.483 (4)	~0	0.77
	<sup>140</sup> Ce	0	0.47	0	
	<sup>142</sup> Ce	0	0.45	0	
59	Pr	5/2	0.445 (5)	1.6	11.6
60	Nd		0.780 (7)	11 (2)	46
	<sup>142</sup> Nd	0	0.77	0	
	<sup>144</sup> Nd	0	0.28	0	
	<sup>146</sup> Nd	0	0.87	0	
62	Sm				5600
	<sup>149</sup> Sm	7/2	-1.9+4.5i		41000
	<sup>152</sup> Sm	0	-0.5	0	210
	<sup>154</sup> Sm	0	0.96	0	5.5
63	Eu		0.68		4300
	<sup>153</sup> Eu	5/2			450
64	Gd		1.5		49000
	<sup>157</sup> Gd	3/2	4.3+4i		~254000
	<sup>160</sup> Gd	0	0.91	0	0.77
65	Tb	3/2	0.738 (3)		46

dependency of the neutron scattering is a necessary part of the analysis. Longer wavelengths are also useful in diffraction measurements where larger sizes ( $>0.5 \text{ nm}$ ) of particles or voids are being examined and when multiple Bragg scattering from the crystal structure of the material is to be avoided. A cold source is important in SANS facilities because measurements can be obtained at higher wavelengths

in a reasonable time interval. The function of a cold source is to lower the neutron thermal equilibrium temperature in the reactor, which shifts the peak intensity to higher wavelengths. Therefore  $\lambda$  values of 1.5 to 1.8 nm can be used routinely and data can be collected at  $\lambda=1.0 \text{ nm}$  more quickly. The SANS facility at NBS is adding a cold source and will increase the power of the reactor to 20 MW (June

Table 1 (Continued)

Atomic number	Element or isotope	Nucl. spin	Scattering length <sup>a</sup> $b(10^{-12} \text{ cm})$	Incoherent scattering cross-section $\sigma_{\text{inc}}(\text{barn})$	Absorption cross section for $\lambda=1.8 \text{ \AA}$ $\sigma_{\text{abs}}(\text{barn})$
66	Dy		1.71 (3)		950
	<sup>160</sup> Dy	0	0.67	0	55
	<sup>161</sup> Dy	5/2	1.03		585
	<sup>162</sup> Dy	0	-0.14	0	200
	<sup>163</sup> Dy	5/2	0.50		140
	<sup>164</sup> Dy	0	4.94	0	2300
67	Ho	7/2	0.85 (2)	4	65
68	Er		0.803 (3)	7	173
69	Tm	1/2	0.705 (5)		127
70	Yb		1.262 (12)		37
71	Lu		0.73 (2)		112
72	Hf		0.777 (14)		105
73	Ta		0.691 (7)	0.020 (4)	21
74	W		0.477 (5)	1.86 (12)	19.2
	<sup>182</sup> W	0	0.83	0	
	<sup>183</sup> W	1/2	0.43		
	<sup>184</sup> W	0	0.76	0	
	<sup>186</sup> W	0	-0.12	0	
75	Re		0.92		86
76	Os		1.08	0.5	15.3
	<sup>188</sup> Os	0	0.78	0	
	<sup>189</sup> Os	3/2	1.10		
	<sup>190</sup> Os	0	1.14	0	
	<sup>192</sup> Os	0	1.19	0	
77	Ir		1.06 (2)		440
78	Pt		0.95 (3)	0.60 (4)	8.8
79	Au	3/2	0.763 (6)	0.36 (4)	98.8
80	Hg		1.266 (2)	6	375
81	Tl		0.889 (2)	0.1	3.4
82	Pb		0.94003 (14)	0.0013 (5)	0.17
87	Bi	9/2	0.8495 (12)	0.0072 (6)	0.036
			0.85256 (14)		
90	<sup>232</sup> Th	0	1.008 (4)	0	7.56
91	<sup>231</sup> Pa		1.3		200
92	U		0.861 (4)		7.68
	<sup>235</sup> U	7/2	0.98		694
	<sup>238</sup> U	0	0.85	0	2.71
93	<sup>237</sup> Np		1.06		170
94	<sup>239</sup> Pu		0.75		1026
	<sup>240</sup> Pu	0	0.35	0	295
	<sup>242</sup> Pu	0	0.81	0	
	<sup>243</sup> Am	5/2	0.76		
96	<sup>244</sup> Cm	0	0.7	0	

<sup>a</sup> Coherent scattering lengths for the elements are mostly best values recommended by Koester (1977). Complex scattering lengths relate to  $\lambda=1 \text{ \AA}$ . All entries without quoted errors are to be considered with caution as their accuracy is uncertain. Incoherent scattering cross sections for nuclei with zero spin have been set equal to zero.

1984). Both of these additions will increase the neutron flux at the sample significantly and will result in shorter measurement times.

There are two types of collimating apertures which define the beam direction and divergence. One type consists of a pair of cadmium pin hole irises, one after the velocity selector and another before the sample chamber. The other collimation system is for higher

resolution measurements and consists of a set of channels in cadmium masks which effectively converge the neutron beam to a point at the center of the detector. The multiple sample chamber is computer controlled and can be used under vacuum. Single samples can be studied as a function of temperature from 12 to 1600 K. Horizontal and vertical field electromagnets are also available. Sample

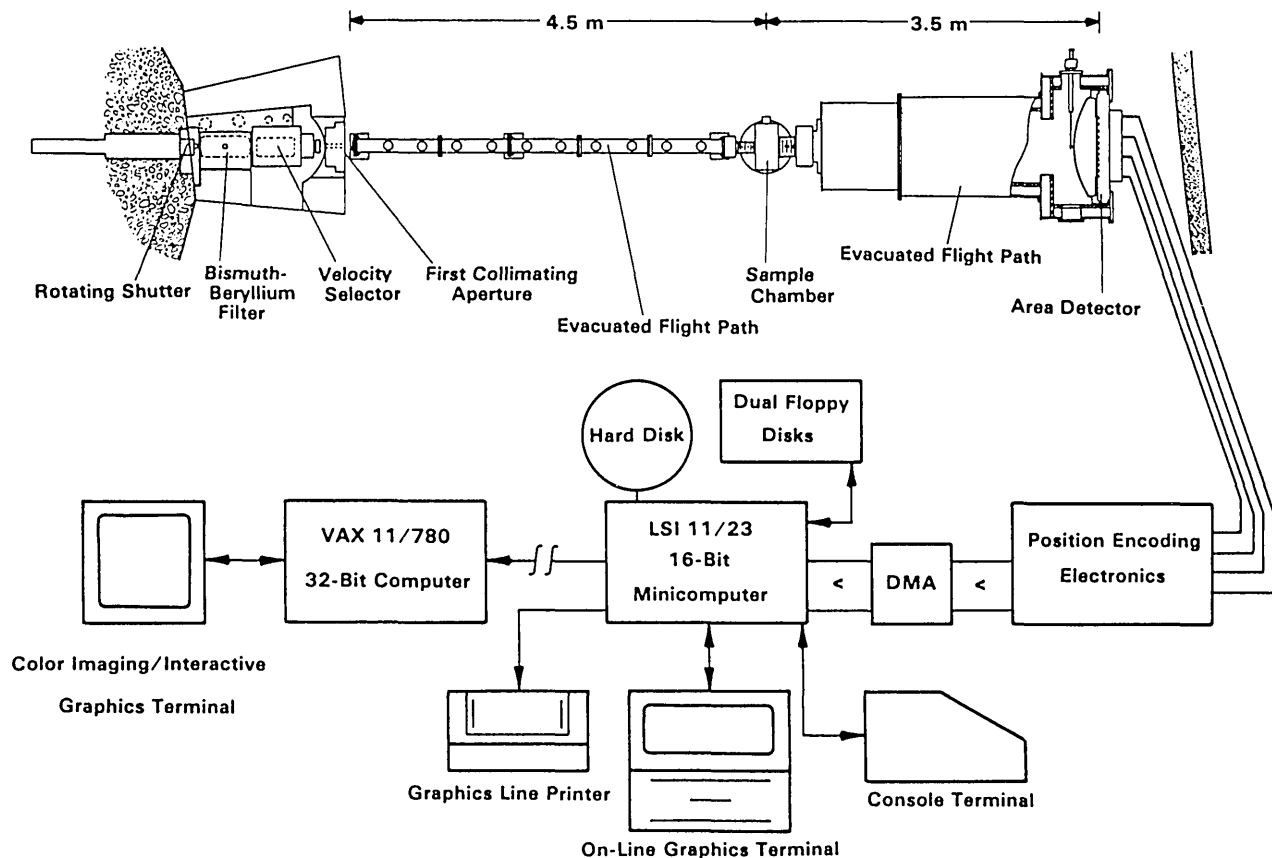


Figure 1—A diagram of the NBS small angle neutron scattering facility including computer capabilities (Ref. [2] is source).

Table 2. Characteristics of the SANS instrument at 10 MW reactor power

Wavelength:	Variable from 0.48 to 1.0 nm, $\Delta\lambda/\lambda=0.25$
Collimation:	Single pair of circular irises or 7 to 9 channel converging beam collimation
Minimum Q:	$0.006 \text{ \AA}^{-1}$ at $\lambda=0.6 \text{ nm}$ ; $0.004 \text{ \AA}^{-1}$ at $\lambda=0.9 \text{ nm}$
Q range:	$0.004 \text{ \AA}^{-1}$ to $0.5 \text{ \AA}^{-1}$
Sample size:	0.4 to 2.0 cm pin-hole collimation; $1.6 \text{ cm} \times 1.6 \text{ cm}$ or 2.2 cm diameter—converging collimation 1–30 mm thickness (uniform)
Flux at sample:	$10^4$ to $2 \times 10^5 \text{ n/cm}^2\text{-sec}$ depending on slit sizes and wavelength
Detector:	$64 \text{ cm} \times 64 \text{ cm}$ position sensitive counter with $8 \times 8 \text{ mm}^2$ resolution

sizes are usually 1.0 to 2.5 cm in diameter and 2 to 30 mm thick. Uniform thickness is essential for analyzing the results. The scattered neutrons are detected on a  $64 \text{ cm} \times 64 \text{ cm}$  position-sensitive proportional counter with a spatial resolution of 8 mm in each direction and is divided into 128 columns and 128 rows. A dedicated minicomputer processes the signals from the detector and stores the data. The data are recorded on floppy disks for archival storage and are transferred to a larger computer for analysis, and they can be viewed

on an interactive color graphics terminal as well. The angle between the incident beam and the scattered beam is the scattering angle,  $\epsilon$ , (see fig. 2). The magnitude of the scattering vector  $Q$  is  $(4\pi/\lambda)\sin \epsilon/2$  which is approximated  $2\pi\epsilon/\lambda$  in the small angle limit.

## Theory

This section is a very brief discussion of some of the theoretical considerations that are particularly germane to ceramics applications of SANS. Excellent reviews [3–5] of SANS formalism and practice exist for the interested reader.

The nature of small angle scattering from a monodisperse population of spherical particles or voids is determined by the phase shift  $\rho$  that a plane wave suffers in traversing a single particle;

$$\rho = (4\pi/\lambda)\Delta nR, \quad (1)$$

where  $\lambda$  is the neutron wavelength,  $R$  is the particle radius, and

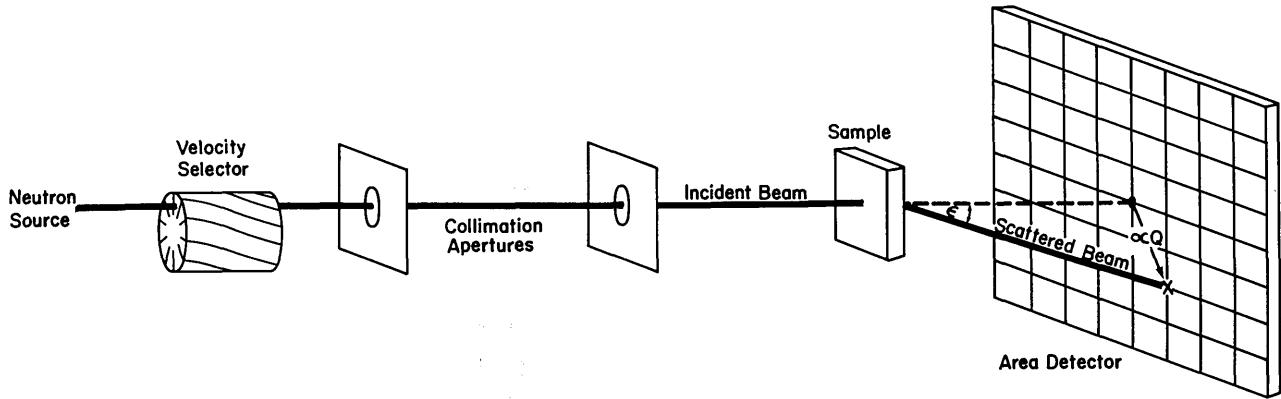


Figure 2—A schematic diagram of key components used for the small angle scattering measurements.

$$\Delta n = \Delta b \lambda^2 / 2\pi, \quad (2)$$

is the index of refraction of the particle or void relative to the matrix medium, which is assumed to be homogeneous and thus, acting alone, to produce no angular divergence in the neutron beam. In eq (2),  $\Delta b$  is the relative scattering length density or contrast of the particle (or void) with that of the matrix material:

$$\Delta b = \sum_{\text{cell}} b_i / V_{\text{cell}} - b_{\text{matrix}}, \quad (3)$$

where the sum is over the coherent scattering lengths  $b_i$  of the material formula unit for a crystalline unit cell,  $V_{\text{cell}}$  is the unit cell volume, and where  $b_{\text{matrix}}$  is defined by the analogous average for the matrix material. Thus combining eqs (1) and (2) the phase shift parameter  $\rho$  can be written in the useful form

$$\rho = 2\Delta b R \lambda, \quad (4)$$

which shows the three independent factors on which it depends: 1) material contrast  $\Delta b$ , 2) particle size  $2R$ , and, 3) neutron wavelength  $\lambda$ .

In the limit of small phase shift,  $\rho \ll 1$ , single-particle scattering is described by the Born approximation, or equivalently, the Rayleigh-Gans model, which in SANS is identified with small angle diffraction. In this limit the neutron differential cross-section—i.e., the relative probability for scattering into angle  $\epsilon$  which is equal to  $2\theta$ —is exactly expressed as the Fourier transform of the single-particle density self-correlation function, which is sensitive to the details of particle shape and size. The diffractive regime theory and measurement are usually described in terms of the scattering wavevector

$$Q = 2\pi\epsilon/\lambda, \quad (5)$$

which absorbs *all* of the  $\lambda$ -dependence of the scattering; in particular the width of the scattering in the  $Q$ -representation is inversely proportional to particle radius but independent of  $\lambda$ , so that in the angular representation, the root mean square, rms, angular deviation of scattered neutrons is proportional to  $\lambda$  and is inversely proportional to the particle radius. Moreover, as  $\rho$  approaches zero, the single-particle *total* cross-section  $\sigma$ ,—i.e., the integral of the differential cross-section over all angles—becomes proportional to the particle geometrical cross-sectional area multiplied by  $\rho^2$  and thus also tends rapidly to zero. As a result, the mean-free-path length

$$l = 1/D\sigma, \quad (6)$$

where  $D$  is the number of scatterers per unit volume, becomes much larger than sample dimensions—except for very dense systems or for very thick samples. This has two important (related) consequences: 1) the relative probability for scattering becomes small so that the observed intensity is the sum of an unscattered “incident” beam, broadened only by instrumental resolution, and a much weaker scattered beam which contains the particle size and shape information; and 2) incident neutrons effectively have only one opportunity to be scattered by individual particles while traversing the sample so that the scattered component of the observed neutron intensity is simply the  $N$ -fold multiplication of the single-particle scattering from  $N$  particles—i.e., contributions from multiple scattering and coherent interparticle interference are negligible. (We simply note here that interparticle interference *can* be an important effect in small angle diffraction from dense systems of scattering particles or voids.) Typically, the diffractive regime is considered to apply to particles of radius less than  $0.1 \mu\text{m}$ , and  $\sigma = \pi R^2 \rho^2 / 2$ .

In the opposite limit,  $\rho \gg 1$ , the scattering from a single particle is well described by ray optics with each particle *refracting* neutrons as a lens. In this regime the rms angular deviation of the neutron beam produced by a particle is independent of its size and determined only by the relative index of refraction which, recalling eq (2), is proportional to  $\lambda^2$ . Moreover, the total cross-section  $\sigma$  approaches the geometrical limit  $2 \times$  cross-sectional area ( $\sigma = 2\pi R^2$ ), so that the mean-free-path length becomes comparable to the average interparticle spacing. In probabilistic terms every particle scatters, and as a result: 1) the observed intensity is *not* separable into an unscattered “incident-beam” and a weak, scattered part—in effect the incident beam is broadened beyond instrumental resolution without “residual” scattering; and 2) multiple scattering effects dominate this “beam broadening” which means that the particle size influences the measurement indirectly—but substantially—through its influence on the macroscopic configuration of scatterers (e.g., the mean particle spacing for fixed volume fraction). Generally, the refractive regime is reached by particles larger than 10  $\mu\text{m}$ .

For intermediate values of the phase shift,  $\rho \sim 1$ , the scattering is not well described in terms of either limiting case or as a simple combination of diffractive and refractive effects. A plot of  $\sigma/\pi R^2$  vs  $\rho$  in figure 3 suggests the effective extent of the intermediate or “cross-over”  $\rho$ -regime connecting these extremal behaviors. The diffractive regime is confined to the immediate neighborhood of the origin while the refractive asymptote, defined by the dotted line, is approached only slowly for large  $\rho$ . In work described elsewhere [6] we have developed a synthesis of a general formal expression for the single-particle scattering cross-section, for unrestricted  $\rho$ , as derived by Weiss [7] with the multiple-scattering formalism of Snyder and Scott [8], modified for the relevant “pin-hole” geometry of the typical SANS instrument. We find that for  $\rho \sim 1$ , the relevant regime for many ceramics applications, the predicted neutron intensity as a function of scattering angle is approximately Gaussian, an informal characteristic of multiple-scattering phenomena, with a standard deviation estimated by  $\Delta\epsilon$

$$\Delta\epsilon = [T/l(\lambda)]^{1/2} \epsilon_0(\lambda) \quad (7)$$

where  $T$  is the sample thickness,  $l$  is the mean-free-path length as defined in eq (6), and  $\epsilon_0$  is a measure of the rms angular deviation produced by a single particle. In eq (7) we have indicated the implicit wavelength

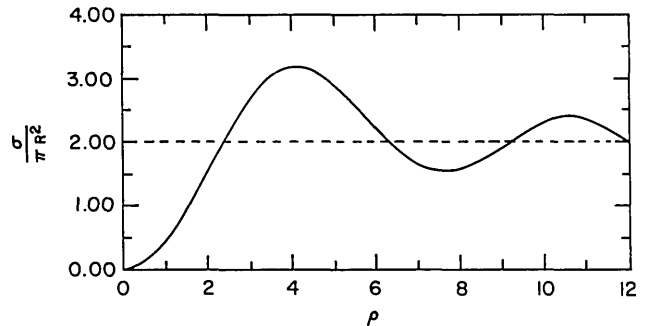


Figure 3—The oscillatory variation of the total neutron cross-section scattering  $\sigma$  as a function of the phase shift  $\rho$ . In the multiple refraction limit  $\rho = 2\pi R^2$  (Ref. [7] is source).

dependence since a plot of measured  $\Delta\epsilon$  vs  $\lambda$  is the most effective means of determining the nature of beam broadening. In this regime  $l$  is inversely proportional to  $\lambda^2$  and  $\epsilon_0$  is approximately linear in  $\lambda$  (the  $\epsilon_0$  behavior thus suggesting the approach to the single-particle diffractive limit), so that the overall variation of  $\Delta\epsilon$  is approximately quadratic in  $\lambda$ . A similar expression applies to the refractive regime,  $\rho \gg 1$ , where  $l$  becomes independent of  $\lambda$  while  $\epsilon_0$  varies approximately as  $\lambda^2$ , thus giving  $\Delta\epsilon$  a similar wavelength dependence as for  $\rho \sim 1$  but one that arises from a different “mechanism” and which depends in a very different way on  $R$ . An application to experiment is discussed below.

## Experiment

Diffraction and beam broadening measurements are quite different and are usually obtained in different configurations of the SANS instrument. Diffraction experiments probe for microstructural phenomena in the range of 1 to 100 nm. The SANS detector is usually located directly behind the sample so that the incident beam is centered in the middle of the detector. The experiment generally requires 6 to 12 hours and a beamstop is used to eliminate scattering from the incident beam. Sample thickness (2 to 6 mm) is kept small to minimize multiple scattering effects. Absorption and incoherent neutron scattering should be reduced for best results in most SANS experiments with ceramic materials.

The beam broadening effect is wavelength ( $\lambda$ ) dependent and the resulting widths are most sensitive to  $\lambda$  at  $\lambda$  greater than 0.7 nm. Typical experiments require only 3 minutes to 2 hours depending on  $\lambda$ , the void or particle size, density and thickness of the sample and are similar to transmission measurements.

It is important to determine the exact center of the neutron scattering; therefore, the incident beam is set off to one side of the detector without a beamstop. This can be done without harming the detector because the peak intensity is greatly reduced in the broadened state. Cadmium foil can be used to reduce the scattered beam intensity over the entire detector to further ensure the safety of the detector; nevertheless, care should be taken when obtaining data without a beamstop. The samples should be measured at three wavelengths or more for best results. Also thicker samples, 5 to 30 mm, are desirable to increase the number of scattering events.

Hydrogen and  $B^{10}$  or naturally occurring boron are generally undesirable in elastic neutron scattering experiments so that deuterium and  $B^{11}$  are often substituted for these elements respectively.  $B^{10}$  absorbs neutrons and can be used to stop the chain reaction in nuclear reactors. Therefore SANS measurements of boron containing ceramic materials should have less than 10% B and be 3 mm or less in thickness. If these conditions are not possible then the materials can be made with  $B^{11}$  which is relatively inexpensive and easy to obtain. Hydrogen has a large incoherent scattering component that reduces the signal-to-noise ratio in the data. Ceramic binders containing hydrogen and ceramics containing water are difficult to measure. Usually heavy water ( $D_2O$ ) can be used if water is required in the sample. The coherent scattering lengths ( $b$ ), incoherent scattering cross-sections, and absorption cross-section values for the elements and isotopes can be found in table 1, taken from Kostorz [1]. It is worthwhile to avoid elements or isotopes with high neutron absorption or high incoherent scattering cross-section values.

### Diffraction Region

Most SANS experiments are in the diffraction region and in ceramics are concerned with inhomogeneities such as voids, cavities, microcracks, precipitates, sintered porosity, inclusions, nucleation, and growth of second phases. In principle it is possible to determine quantitatively particle size, shape, size distribution, surface area and other microstructural values. Examples of SANS experiments with ceramic materials include the following: formation and growth of heterogeneities in glass by A. W. Wright [9], creep cavitation in sintered alumina by R. A. Page and James Lankford [10], growth and coarsening of pure and doped  $ZrO_2$  by A. F. Wright, S. Nun and N. H. Brett [11], microcracks in sintered  $YCrO_3$  by E. D.

Case and C. Glinka [12], and Fe and W inclusions in hot pressed  $Si_3N_4$  by K. Hardman-Rhyne, N. F. Berk and N. Tighe [13]. The results of the two last-named works will be discussed briefly.

It is preferable to have a two-component system such as the matrix material and precipitates or voids. One way to avoid multiple component systems is to run a control sample which was done in the  $YCrO_3$  microcrack experiment [12].  $YCrO_3$  is a material which is sintered around 1750 °C, thereby establishing its microstructure (porosity, grain size, etc.) but which undergoes an apparent phase transition around 1100 °C. Thus if the material is quenched from above 1100 °C, microcracks as well as pores are present in the final material. However if the material is annealed at 1050 °C the microcracks can heal and only the pores remain. Thus by subtracting the neutron scattering data of a healed  $YCrO_3$  sample from that of a microcracked sample, a third scattering distribution, due only to the microcracks in the material called  $I_{DIFF}$ , can be obtained. These data are analyzed to determine several microstructural parameters.

Both SANS and elasticity measurements were collected on these samples which allowed the mean crack radius and crack number density to be calculated. The total surface area of the microcracks was estimated by using high  $Q$  data which was normalized to the scattering from water. Figure 4 shows the logarithmic function of  $I_{DIFF}$  versus the scattering vector  $Q$ . The solid line is a Porod [14] functional fit which describes the data at large

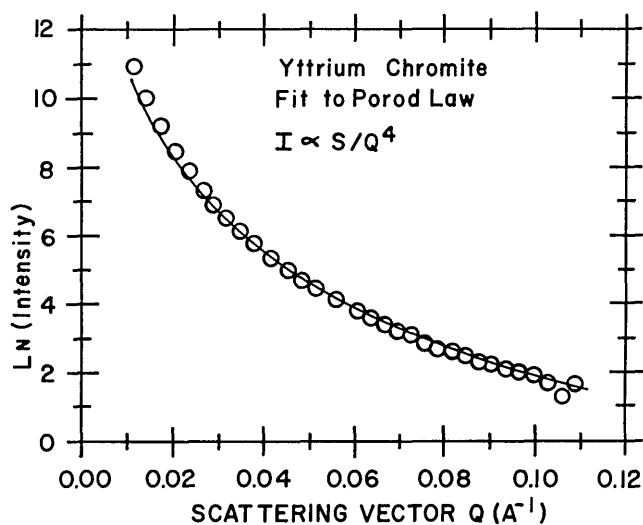


Figure 4—Open circles are the net scattering due to microcracks from a 7 mm thick specimen of  $YCrO_3$  plotted on a logarithmic scale versus the scattering vector  $Q$ . The curve is a least-square fit of a Porod law (Ref. [12] is source).

$Q(Q > 0.03 \text{ \AA}^{-1})$  and can be expressed in the following form:

$$I \propto \frac{d\Sigma}{d\Omega} \sim \frac{2\pi(\Delta b)^2}{V} \frac{S}{Q^4} \quad (8)$$

where  $d\Sigma/d\Omega$  is the macroscopic cross-section,  $V$  the sample volume seen by the neutron beam and  $S$  the total surface area of the scattering centers.

Because the Porod function does not apply to low  $Q$  region, other functional forms of the scattering cross-section must be used. For sharp-edged, randomly oriented scattering centers of any given geometry, a Guinier [15] function can be used at small  $Q$  values;

$$\frac{d\Sigma}{d\Omega} \sim (\Delta b)^2 V_p^2 \exp(-R_G^2 Q^2/3) \quad (9)$$

where  $V_p$  is the volume of the particle (or scattering center) and  $R_G$  is the particle's radius of gyration with respect to its center of gravity. However a better functional fit to the data can be obtained by assuming that the scattering from microcracks is modeled after randomly oriented thin disks [14] of thickness  $2H$ , diameter  $2a$ ;

$$\frac{d\Sigma}{d\Omega} = \frac{V_p^2 N_p^2 (\Delta b)^2}{V} \frac{2}{Q^2 a^2} \exp(-Q^2 H^2/3) \quad (10)$$

where  $N_p$  is the number of microcracks and  $QH < 1 \ll Qa$ . This low  $Q$  fit to the data ( $I_{\text{DIFF}}$ ) can be seen in figure 5. Various microcrack parameters have been calculated and agree well with other similar parameters in the literature [12] and are as follows: crack number density ( $4.7 \times 10^8 \text{ cm}^{-3}$ ), surface area ( $1.5 \text{ cm} \times 10^3 \text{ cm}$ ), crack aspect ratio ( $1.5$  to  $3.5 \times 10^{-3}$ ), volume fraction ( $2.6 \times 10^{-3}$ ), and crack opening displacement ( $250 \text{ \AA}$ ). The mean crack radius is  $5.7 \text{ \mu m}$  which corresponds well with the measured grain size of  $6 \text{ \mu m}$  and is consistent with a model of localized stress induced microcracks.

Although optical and electron microscopy can identify small defects ( $< 10 \text{ \mu m}$ ) in advanced ceramic materials, SANS can quantify the size, shape and distribution of these defects in the bulk of the material. Hot pressed, MgO doped  $\text{Si}_3\text{N}_4$  is an example of a complementary study with SANS and transmission electron microscopy, TEM. TEM studies of this material clearly showed small, approximately spherical inclusions in  $\text{Si}_3\text{N}_4$  that were identified as Fe and W. There was no evidence of pores, microcracks or

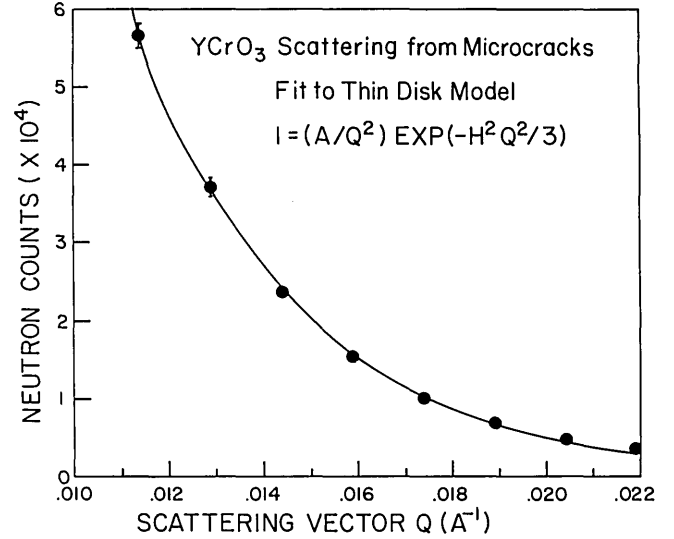


Figure 5-The data points are the low  $Q$  scattering from microcracks in a 7 mm thick specimen of  $\text{YCrO}_3$ . The curve is a least-squares fit to the data of the scattering function for randomly oriented thin disks of thickness  $2H$  (Ref. [12] is source).

microvoids from the TEM observations, but the sample had not been temperature treated where voids are more likely to appear.

Pores larger than  $90 \text{ nm}$  can be detected by examining transmission data collected at two or more wavelengths remembering that the higher wavelengths are more sensitive to porosity effects. Focussing collimation was used to examine the wavelength dependency of the neutron scattering as shown in figure 6 and no wavelength-dependent beam broadening was observed. This is consistent with observations from TEM and other characterization methods which suggest that this sample of  $\text{Si}_3\text{N}_4$  is fully dense with little or no porosity. Therefore we assume the SANS data reflect information relevant to the Fe and W inclusions that are present.

The small angle neutron scattering of the inclusions at  $\lambda = 0.9 \text{ nm}$  is plotted as exponentially spaced intensity contour lines for the two dimensional detector (see fig. 7). There is a beamstop located in the center of the detector (solid circle) where the intensity is greatest and decreases as the distance away from the center increases. The intensity of the scattering is usually expressed as a function of  $Q$ , given in units of inverse angstroms ( $10 \text{ \AA} = 1 \text{ nm}$  and  $1 \text{ \AA}^{-1} = 10 \text{ nm}^{-1}$ ). Background and transmission corrections must be made to the raw data. Since the contour plot (fig. 7) indicates the scattering is isotropic we have circularly averaged the corrected data and plotted logarithm of intensity versus  $Q$  for the Fe and W inclusions in  $\text{Si}_3\text{N}_4$  (see fig. 8).

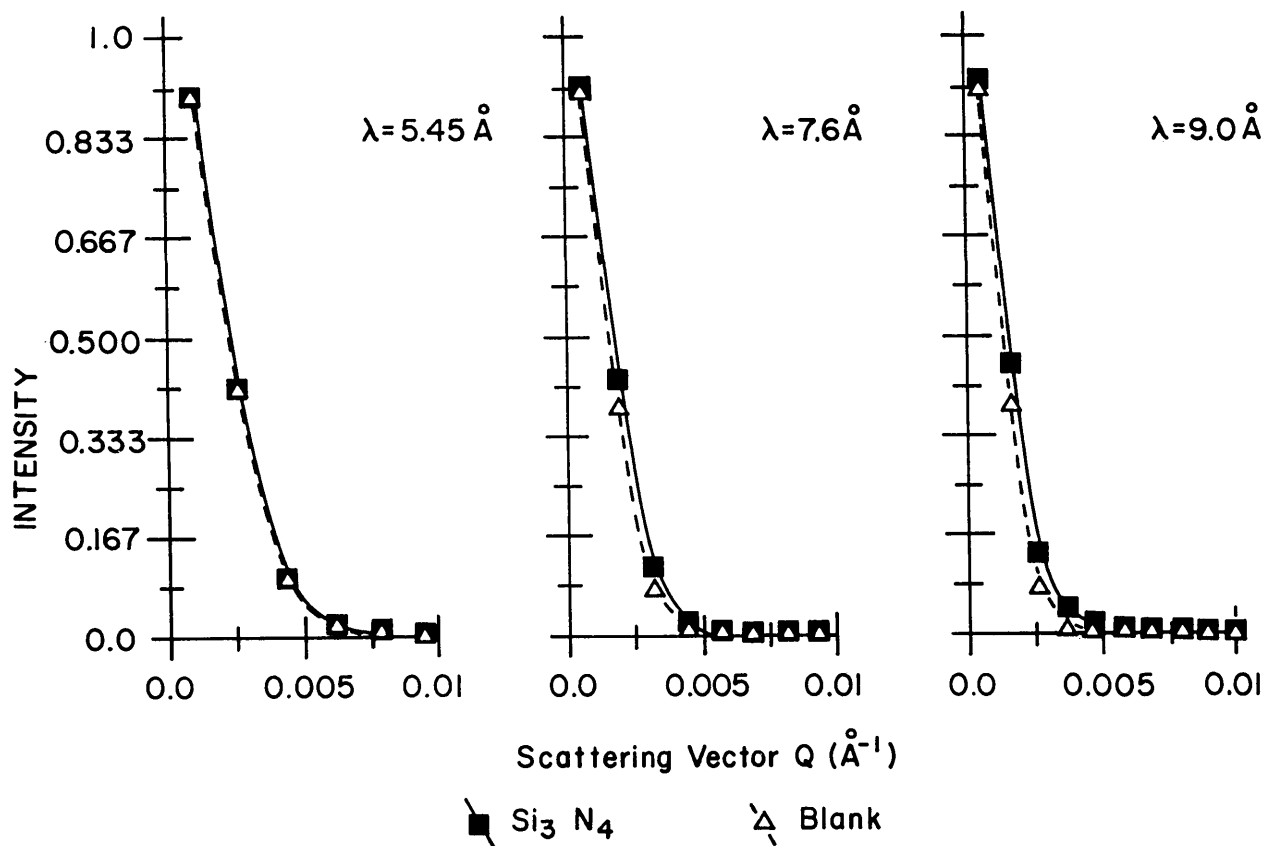


Figure 6—Comparison of direct beam scattering (blank sample) with the scattering from the  $\text{Si}_3\text{N}_4$  sample at several wavelengths.

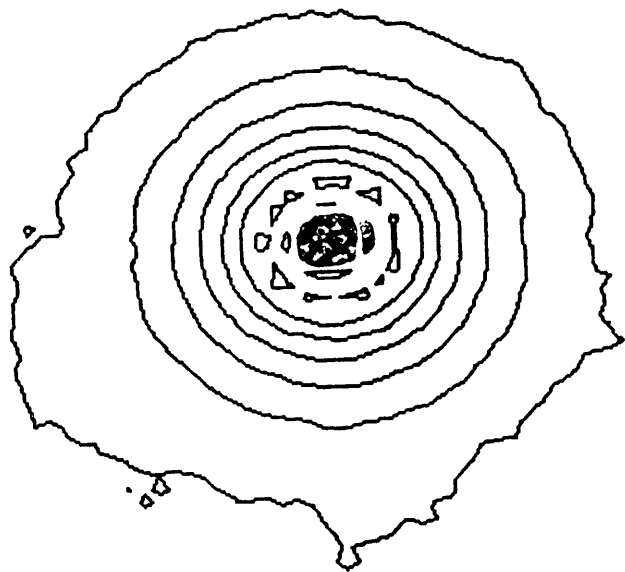


Figure 7—Exponentially spaced intensity contour plots from the two-dimensional SANS detector of the  $\text{Si}_3\text{N}_4$  sample at  $\lambda = 0.9$  nm.

Most SANS analyses include one or both regions indicated in figure 8. Often the intermediate region will be included in one of these regions or treated

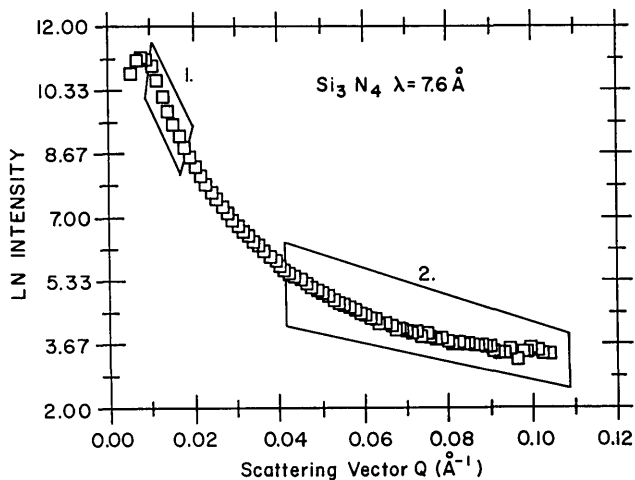


Figure 8—Logarithm of neutron scattering intensity of Fe and W inclusions in  $\text{Si}_3\text{N}_4$  versus scattering vector,  $Q$ , in reciprocal angstroms. The two regions (1 and 2) denote the Guinier and Porod regions, respectively.

separately as was the case in the thin disk model for  $\text{YCrO}_3$  microcracks. Region 1, shown in figure 8 and expanded in figure 9, is the Guinier region where the logarithm of the intensity has a  $Q^2$  behavior. A

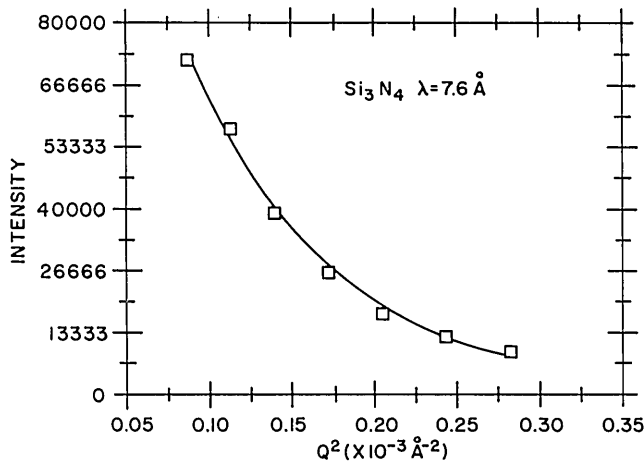


Figure 9-Plot of the Guinier fit (solid line) to the data (squares) at  $\lambda=0.76$  nm.

Guinier fit (solid line in fig. 9) to the data (squares) at  $\lambda=0.76$  nm yields a radius of gyration (from eq (9)) of 18.6 nm which is related to the average radius of the Fe and W inclusions. If we assume the inclusions are monodispersed and spherical in shape,  $R_G=(3/5)^{1/2} R_S$  so that the average particle radius is 24.0 nm. In this scattering region the neutron intensity is limited by the larger dimensions of the scattering particles. The Guinier approximation is valid over a range of  $Q_{MAX}R_G \leq 1.2$ . In our case the maximum  $Q$  is  $0.017 \text{ \AA}^{-1}$  and  $Q_{MAX}R_G \sim 3$  which extends outside the Guinier approximation range although the logarithm of the intensity has  $Q^2$  behavior in this region.

Region 2 in figure 8 is called the Porod region and has a  $Q^{-4}$  dependence. The Porod region is more sensitive to smaller dimensions of the scattering centers and results in a characteristic Porod length which measures a surface to volume ratio if absolute intensities can be determined. Since the Porod region is valid for high  $Q$  values only, other similar functional forms have been used to extend the Porod region to lower  $Q$  values. One such form is the Debye *et al.* model [16] which assumes scattering from a two phase material. The particles or voids can be random in size, shape, and distribution throughout the material. The scattering cross-section from this model is given by

$$\frac{d\Sigma}{d\Omega} = \frac{8\pi V a^3 (\Delta b)^2}{(1+Q^2 a^2)^2} \quad (11)$$

The correlation length  $a$  is equal to Porod's inhomogeneity length [14],  $l_p=4V/S$  where  $V/S$  is the volume to surface ratio of the total interface

separating the two phases. Thus, for a population of spheroidal particles  $a$  is a characteristic of average particle size ( $a=4/3 R_S$ ). A Debye *et al.* fit (solid line) to the data (squares) at  $\lambda=0.55$  nm is shown in figure 10. The correlation length  $a$  for the Fe and W inclusions in  $\text{Si}_3\text{N}_4$  is 21.2 nm. A complicating factor in this study is the wide distribution of inclusion sizes and the difference in  $\Delta b$  of Fe and W.

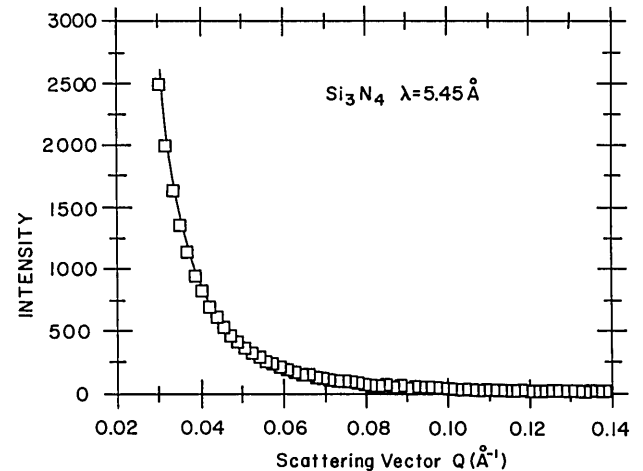


Figure 10-Plot of a Debye fit (solid line) to the data (squares) at  $\lambda=0.55$  nm.

Further SANS diffraction experiments of distributed damage due to stress and temperature are expected as this technique becomes familiar in ceramic research. These results, coupled with failure tests, optical and electron microscopy, can help in understanding and improving the structural reliability of advanced ceramic materials.

## Multiple Refraction Region

A few experiments have been published on multiple refraction effects in nonmagnetic materials, yet it remains unclear if these effects have been observed. Nevertheless, two papers discuss these phenomena in some detail. Weiss [7] studied the neutron beam broadening effect of several materials including bismuth, magnesium, and carbon black. Moreover he demonstrated the full width at half maximum as a function of scattering angle, called  $\Delta\epsilon$ , from neutron beam broadening depends on  $T^{1/2}$ ,  $\lambda^2$ ,  $\Delta b$ , and  $s$ , where  $T$  is the thickness of the sample and  $s$  is a parameter describing the particle or void shape, and is independent of  $R$  the radius of the particle or void. The experimentally determined  $\Delta\epsilon$  was compared to theoretical values obtained using the von Nardroff multiple scattering formula for spheres and for random

surfaces [17]. The von Nardroff formula assumes the measured angular distribution to be Gaussian. But this is true only if the single particle scattering angle distribution falls off faster than Porod behavior ( $\epsilon^{-4}$ ), which generally is not the case. This is consistent with the behavior of the observed intensity which one approximates as Gaussian at small angles, but which falls off much more slowly at large angles.

P. Pizzi [18] collected neutron scattering measurements of  $\text{Si}_3\text{N}_4$  materials at various densities and heat treatments to detect microvoids from multiple refraction effects. Two samples were reaction bonded with densities of 2.28 and 2.49  $\text{gm}/\text{cm}^3$  and several were hot pressed with densities from 3.03 to 3.19  $\text{g}/\text{cm}^3$ . Plots of intensity versus  $Q$  (or  $K$ ) for the reaction bonded and hot pressed  $\text{Si}_3\text{N}_4$  at two wavelengths (fig. 11) reveal wavelength dependency suggesting the presence of multiple refraction neutron scattering. Results for three  $\text{Si}_3\text{N}_4$  samples with densities of 2.28, 2.46 and 3.18  $\text{gm}/\text{cm}^3$  give radius values for the voids of 3, 5 and 2.7  $\mu\text{m}$  respectively. This would indicate phase shifts,  $\rho$  of 4.6 to 8.6 (see fig. 2) which probably fall within the intermediate

beam broadening region between the diffraction and multiple refraction limits.

### Beam Broadening Region

Porosity is a critical aspect in the densification process of a sintered ceramic material. To elucidate the extent of such porosity, a quantitative study with SANS has been conducted at NBS to determine average pore size. Rather than restricting the SANS measurements to the typical 1 to 100 nm size regime of SANS diffraction, we have explored the neutron beam broadening region by extending the SANS characterization into the tens of micrometer size regime. This extension of SANS technique to larger sizes is an important result because it allows a greater overlap of SANS characterization with other NDE techniques.

Two samples of  $\text{YCrO}_3$  were fabricated from pure powders by isostatic pressing at 207 MPa (30,000 psi); one sample was then sintered [19]. The density of the "green" compact (the unfired ceramic) was approximately 57% of theoretical density and that of the sintered material was approximately 94%. The starting ceramic powder, with approximately 30% of theoretical density, was also examined. Since beam broadening measurements are wavelength dependent, SANS experiments were taken at six or seven wavelengths of the following: 0.485, 0.545, 0.625, 0.70, 0.80, 0.90, 0.95, 1.0 nm. The results reveal a striking difference between the samples as illustrated in figures 12 and 13 which are SANS spectra for the sintered and "green" compact specimens respectively. The sintered material (fig. 12) shows little wavelength dependence but the "green" compact reveals dramatic beam broadening which is strongly wavelength dependent (see fig. 13). This dependence is illustrated in figure 14 by plotting the normalized intensity versus scattering vector  $Q$  for five wavelengths.

The direct beam is wavelength independent with respect to the scattering angle,  $\epsilon$  and is defined in part by the instrumental collimation. Beam broadening data can resemble a Gaussian distribution at low  $Q$  values where the full width at half maximum,  $\Delta\epsilon$  can be determined by the Gaussian standard deviation parameter  $\sigma_G$  as shown below:

$$I = I_0 \exp(-Q^2/2\sigma_G^2) \quad (12)$$

$$\text{For full width at half maximum } \Delta Q = 2.355 \sigma_G \quad (13)$$

$$\text{Since } Q = 2\pi\epsilon/\lambda, \text{ the } \Delta\epsilon = 0.3748 \lambda \sigma_G \quad (14)$$

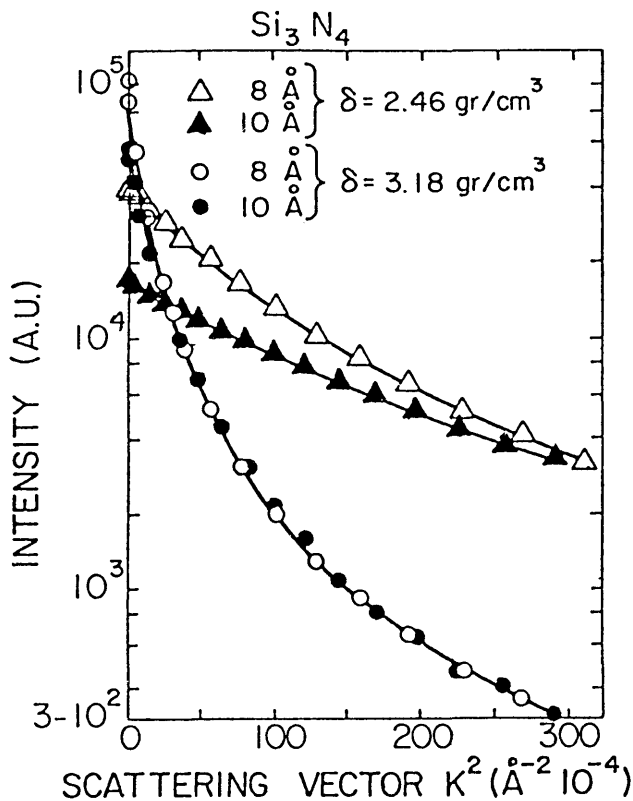


Figure 11-SANS from two samples of  $\text{Si}_3\text{N}_4$  measured at  $\lambda=0.8$  and 1.0 nm. The scattering vector  $K$  is the same as  $Q$  in this paper. Densities of the two samples were  $2.46 \times 10^3$  and  $3.18 \times 10^3 \text{ kg}/\text{m}^3$ , respectively (Ref. [18] is source).

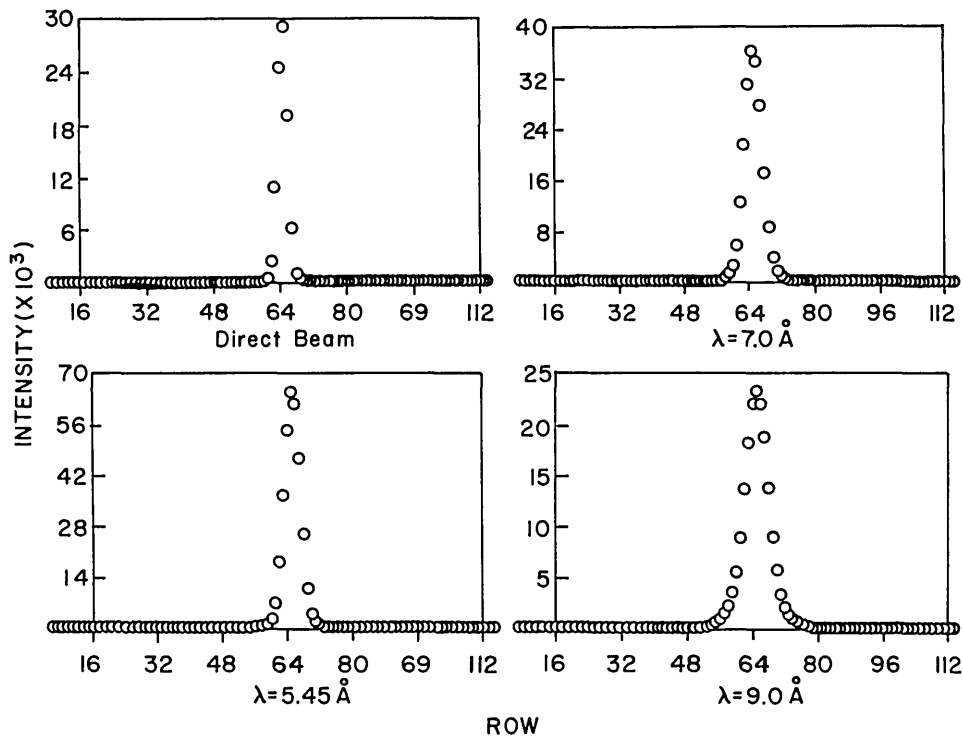


Figure 12-SANS spectra for a sintered compact of  $\text{YCrO}_3$  at three wavelengths: 0.545, lower left, 0.7, and 0.9 nm. Plotted is the scattering intensity versus a linear column slice through the center of the neutron scattering plane (as indicated by the row number).

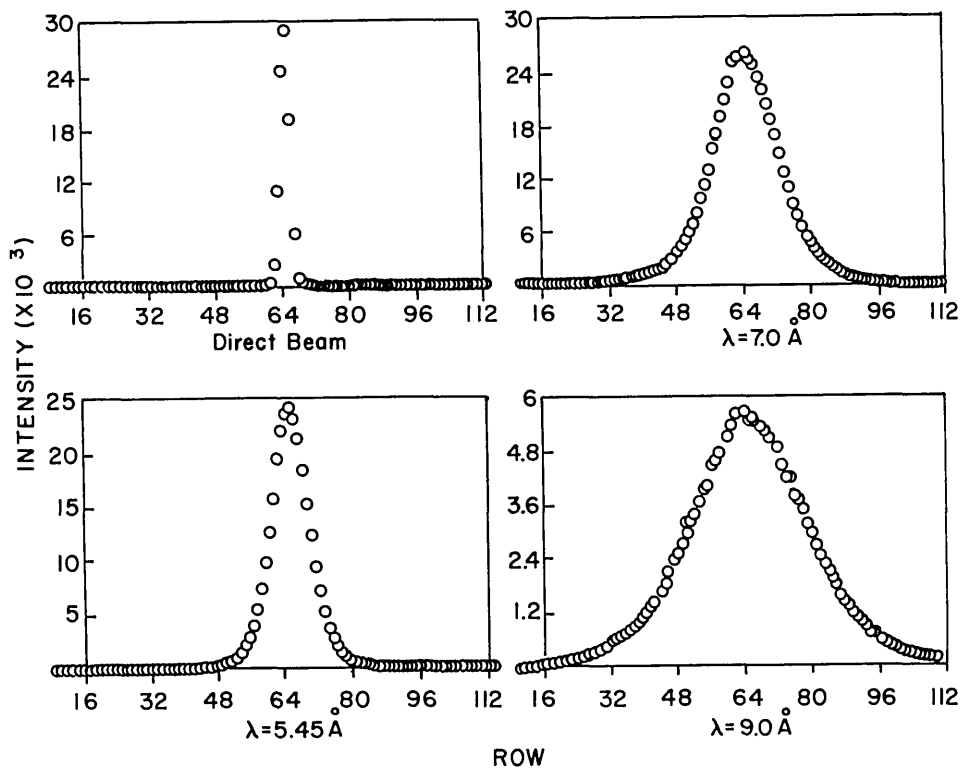
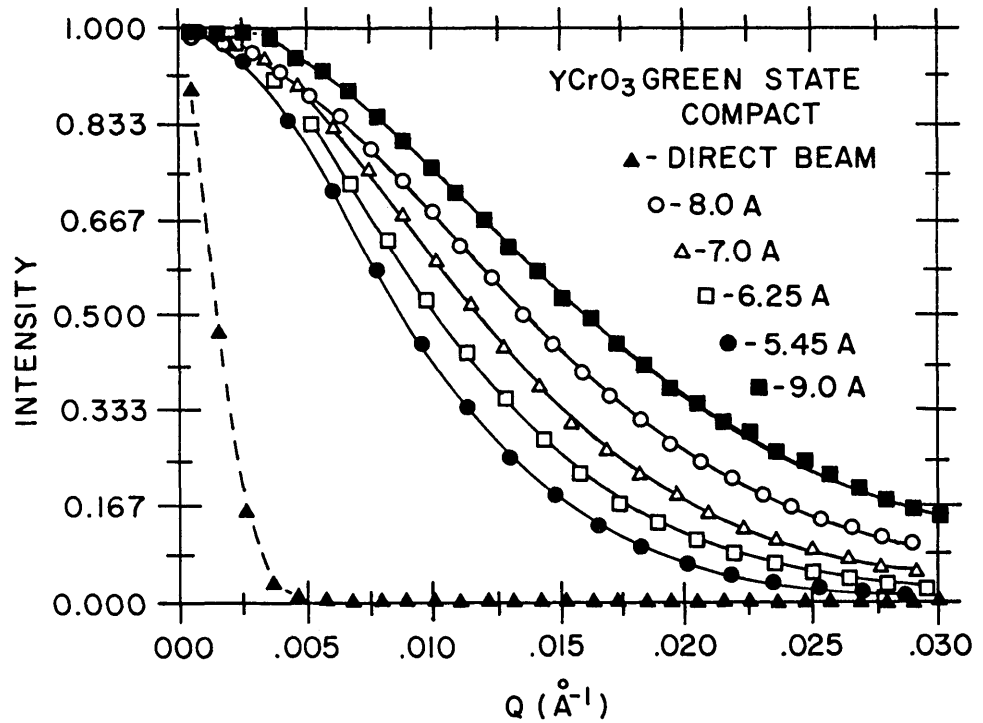


Figure 13-SANS spectra for a "green" compact of  $\text{YCrO}_3$  at three wavelengths: 0.545, 0.7, and 0.9 nm. Plotted is the scattering intensity versus a linear column slice through the center of the neutron scattering plane (as indicated by the row number).

Figure 14—Normalized scattering intensity versus scattering vector,  $Q$ , for neutron scattering from a “green”  $\text{YCrO}_3$  compact at five wavelengths.



The full width at half maximum for the direct beam,  $\epsilon_b$ , was determined for two different collimating conditions. In the fine pin-hole geometric configuration (12 and 8 mm) the  $\epsilon_b$  is  $4.62 \times 10^{-3} \pm 10^{-5}$  radians which was used in the  $\text{YCrO}_3$  materials. The beam broadening experiment of  $\text{Si}_3\text{N}_4$  shown in figure 6 was obtained under focussed collimation conditions and the  $\epsilon_b$  is  $3.882 \times 10^{-3}$  rad.  $\pm 10^{-6}$ . The  $\Delta\epsilon$  value contains both the beam broadening scattering and that due strictly to the direct beam, thus the direct beam,  $\epsilon_b$ , must be subtracted from the experimentally determined value,  $\epsilon$ .

$$\Delta\epsilon = [\epsilon^2 - \epsilon_b^2]^{1/2} \quad (15)$$

An example of the data (squares) and Gaussian fit (dashed line) for the “green” compact of  $\text{YCrO}_3$  at  $\lambda = 0.625$  nm is shown in figure 15.

Although the qualitative aspects of the data clearly demonstrate a strong effect of ceramic processing on the neutron scatterers population in these materials, quantitative measures of the particle or void size, shape and size distribution are less straightforward. Moreover the  $\Delta b$ ,  $\lambda$  and probably  $R$  values correspond to phase shifts well within the intermediate range of values for which the neutron scattering is not expected to be analyzable by multiple refractive behavior alone. Therefore, a generalized beam

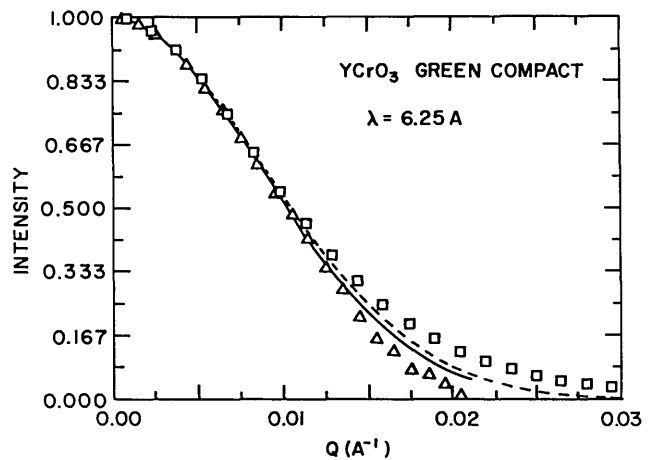


Figure 15—Normalized intensity versus  $Q$  from a “green”  $\text{YCrO}_3$  compact at  $\lambda = 0.625$  nm. The squares are the data with the direct beam and the dashed line represents the Gaussian fit to the low  $Q$  region. The triangles are the theoretically derived beam broaden data points which do not include the direct beam. The solid line is the Gaussian fit through this data fit.

broadening theory [6] relevant for this region and multiple refraction has been developed to quantitatively analyze the SANS data for densified ceramics and other distributed defects in this size regime. Figure 15 contains a generated data set from the theory (triangles) and the Gaussian fit to these data points (solid line). The  $\Delta\epsilon$  does not contain the direct beam

portion. The radius, void (or particle) density ratio and shape factor can be obtained from this theory, which can be expanded to consider particle packing, polydispersivity and various shapes of particles and voids other than spheres. Excellent agreement of data and theoretical values for  $\Delta\epsilon$  can be seen in figure 16 and table 3. The average radius void size in the  $\text{YCrO}_3$  "green" compact material is  $0.17 \mu\text{m}$  and has a void density ratio of 0.42 compared to the overall density ratio of 0.43.

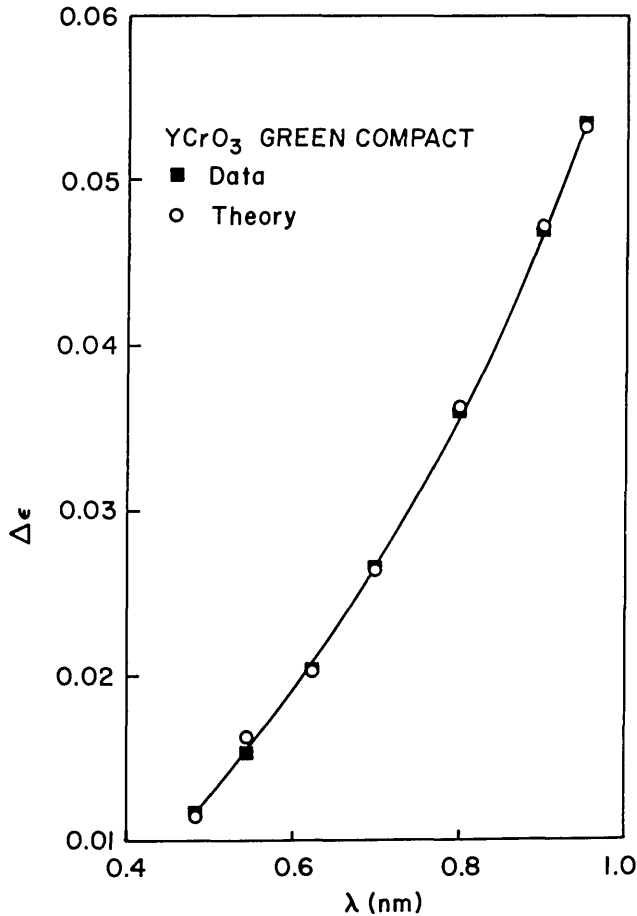


Figure 16—Full width at half maximum,  $\Delta\epsilon$  (in radians) versus the wavelength,  $\lambda$ , for voids in the "green" compact of  $\text{YCrO}_3$ . The squares are the data and the circles are the  $\Delta\epsilon$  values derived from theory.

A powder sample of  $\text{YCrO}_3$  was examined to compare previously determined average particle size values with that obtained from SANS experiments. The  $\text{YCrO}_3$  powder particles were ultrasonically dispersed and magnetically stirred at a temperature of  $32^\circ\text{C}$  [20]. A plot of the cumulative mass percent versus the equivalent spherical diameter in  $\mu\text{m}$ , determined by sedimentation methods, is shown in

Table 3.  $\Delta\epsilon$  values for  $\text{YCrO}_3$  "green" compact where  $\Delta b = 5.277 \times 10^{-4} \text{ nm}^{-2}$ , void density ratio = 0.42,  $T = 12.2 \text{ mm}$ ,  $R = 0.17 \mu\text{m}$

$\lambda$ (nm)	$\Delta\epsilon$ (radians)	
	Data	Theory
0.485	0.01156	0.01137
0.545	0.01525	0.01611
0.625	0.02038	0.02028
0.7	0.02660	0.02645
0.8	0.03598	0.03617
0.9	0.04700	0.04711
0.95	0.05338	0.05322

figure 17. The two runs were reproducible with an apparent small distribution of powder sizes present. The average diameter value is approximately  $1.4 \mu\text{m}$  (or  $R = 0.7 \mu\text{m}$ ) and agrees well with the  $R$  value obtained from the SANS analysis of  $0.74 \mu\text{m}$ . The data (squares) and theory values (circles) for  $R = 0.74 \mu\text{m}$  are shown in figure 18. If we assume that multiple refraction effects only are present, then a fairly good fit to the data using von Nardroff formula for random spheres can be obtained (triangles and dashed line in fig. 18). However the number of scattering events determined from this fit is 33.4 which requires  $R$  to be  $62 \mu\text{m}$ . This is clearly outside the range of possible radius values for this material.

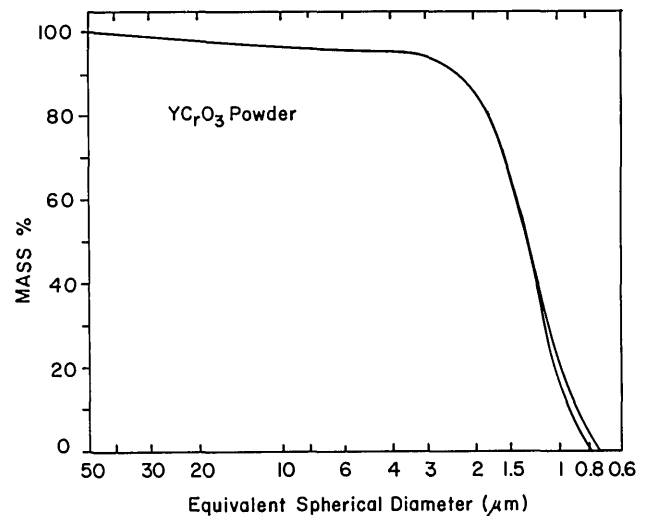


Figure 17—Size distribution of  $\text{YCrO}_3$  powder particles. A plot of cumulative mass percent versus the equivalent spherical diameter by ultrasonic dispersion technique.

The general beam broadening theory and SANS technique allows us to study the densification process in a nondestructive way. It is being extended to study the sintering of spinels ( $\text{MgAl}_2\text{O}_4$ ) as a function of

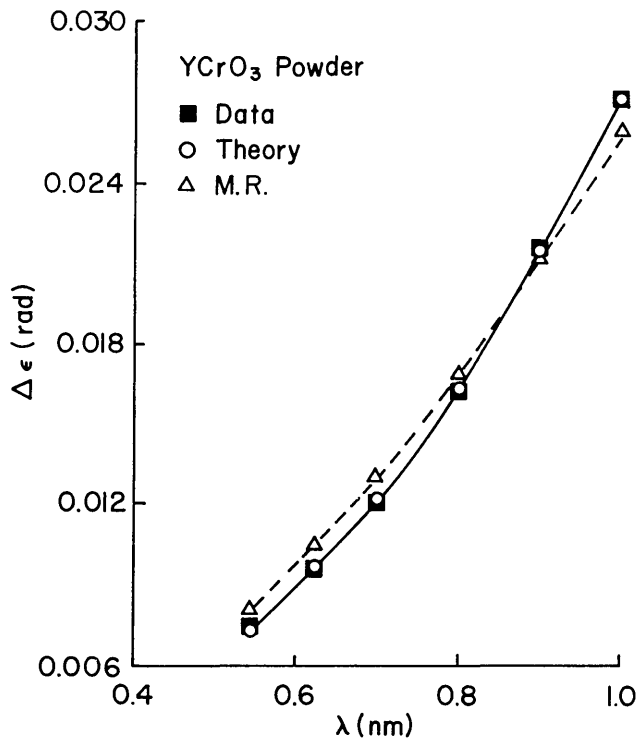


Figure 18—Full width at half maximum,  $\Delta\epsilon$  (in radians) versus  $\lambda$  for  $\text{YCrO}_3$  powder particles. The data (squares) theoretically derived values (circles) and multiple refraction results (triangles) are given.

temperature. Although the spinel powders have been heated at  $1300^\circ\text{C}$  for 12 hours, very little sintering has occurred (fig. 19) but sintering effects are apparent after only 3 hours at  $1500^\circ\text{C}$ . Nevertheless the material is not fully sintered in that the  $\epsilon_b$  of the direct beam (the blank) is significantly smaller than the  $\epsilon$  of the spinel at  $1500^\circ\text{C}$ . In situ as well as other ceramic processing experiments are expected to fully develop the capabilities of this new approach in SANS. It should be of interest to other material disciplines such as magnetic broadening effects, pores in metal alloys and colloidal chemistry.

## References

- [1] Kostorz, G. *Treatise on Materials Science and Technology*, Vol. 15, ed., G. Kostorz, Academic Press, New York: 5-8; 1979.
- [2] Glinka, C. J. AIP Conference Proceedings No. 89, J. Faber, ed., Neutron Scattering-1981, p. 395.
- [3] Weertman, J. R. *Nondestructive Evaluations: Microstructural Characterization and Reliability Strategies*, eds., O. Buck and S. M. Wolf, American Institute of Mining, Metallurgical, and Petroleum Engineers, New York: 147-168; 1981.
- [4] Kostorz, G. *Treatise on Materials Science and Technology*, Vol. 15, ed., G. Kostorz, Academic Press, New York: 227-289; 1979.
- [5] Herman, H. *Non-Destructive Evaluation of Materials with Cold Neutron Beams*, report to Naval Air Systems Command, Contract No. N00019-77-M-0418, Washington, DC: Dec. 1977.

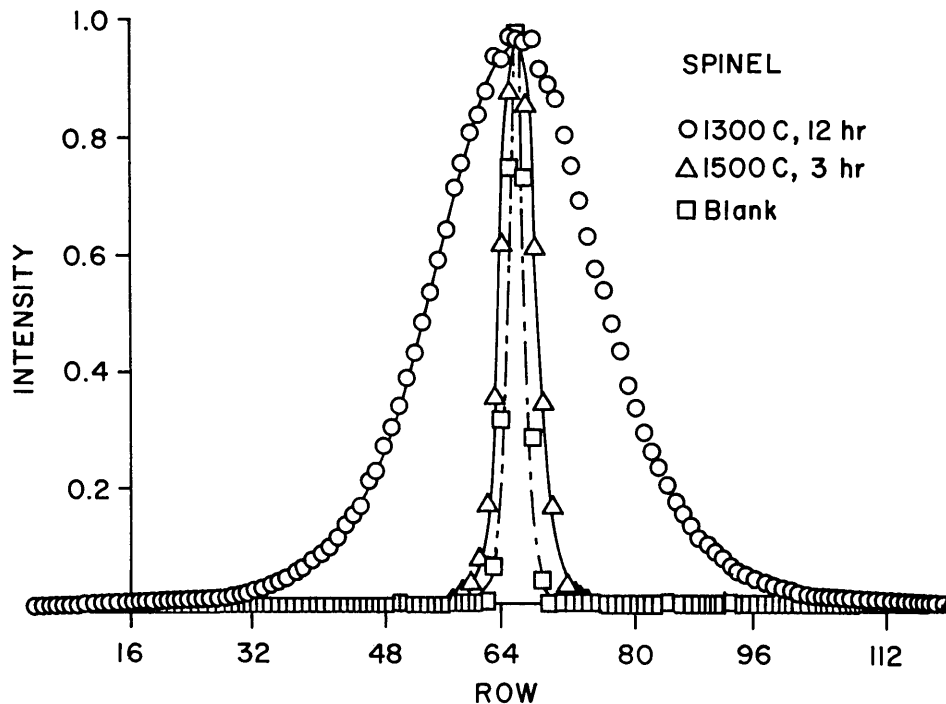


Figure 19—SANS spectra for a spinel ( $\text{MgAl}_2\text{O}_4$ ) at  $\lambda=0.9$  nm. The circles represent the SANS spectra of the spinel with 12 hours of heat treatment at  $1300^\circ\text{C}$ . After 3 hours of  $1500^\circ\text{C}$  temperature (triangles) the spinel is partially sintered but slight neutron beam broadening can be seen from that of the direct beam (squares).

- [6] Berk N. F.; Hardman-Rhyne, K., to be published.
- [7] Weiss, R. J. Phys. Rev. **83**: 379; 1951.
- [8] Snyder, H. S.; Scott, W. T. Phys. Rev. **76**: 220; 1949.
- [9] Wright, A. F. Neutron Scattering 1981 AIP Conference Proceedings, ed., J. Faber: 359; 1982.
- [10] Page, R. A.; Lankford, J. Communications of the American Ceramic Society: C-146; 1983.
- [11] Wright, A. F.; Nunn, S.; Brett, N. H., to be published in the proceedings of the conference on zirconia in Stuttgart: 1983.
- [12] Case, E. D.; Glinka, C. J., to be published in the J. of Matl. Sci.
- [13] Hardman-Rhyne, K.; Berk, N. F.; Tighe, N., to be published.
- [14] Porod, G. Acta Phys. Austriaca **2**: 255; 1948.
- [15] Guinier, A. *X-ray diffraction*, Chapter 10, W. H. Freeman and Company, San Francisco: 1963.
- [16] Debye, P.; Anderson, H. R.; Brumberger, H. J. Appl. Phys. **28**: 679; 1957.
- [17] von Nardroff, R. Phys. Rev. **28**: 240; 1926.
- [18] Pizzi, P. *Symposium on Fracture Mechanics of Ceramics*, Vol. 3, eds., R. C. Bradt, D. P. H. Hasselman and F. F. Lange, Penn. State; Plenum Press, New York: 85; 1978.
- [19] Negas, T.; Domingues, L. P., private communication: 1983.
- [20] Robbins, C., private communications: 1983.

# Characterization of Creep Damage in Metals Using Small Angle Neutron Scattering

E. R. Fuller, Jr., R. J. Fields, T.-J. Chuang, and S. Singhal  
National Bureau of Standards, Washington, DC 20234

Accepted: December 1, 1983

Creep damage in polycrystalline metallic materials can be attributed to cavitation and cracking along the grain interfaces. Theories of creep cavitation that have been developed in recent years are reviewed. Further evaluation and/or refinement of these theories has been retarded by a lack of an experimental counterpart. Small angle neutron scattering studies (SANS) provide one experimental tool which is complementary to others. SANS done at NBS and elsewhere have shown that this technique is suitable for studying nucleation and early stage of growth of creep cavities. This would provide the impetus to further progress in this area.

Key words: creep cavitation; creep crack growth; creep damage; creep fracture; high temperature failure of metals; small angle neutron scattering.

## 1. Introduction

At high temperatures and low stresses, metals often fail with an elongation of only a few percent and only a small reduction in area [1]<sup>1</sup>. This phenomenon occurs even in normally ductile materials like copper and nickel [2]. When metals which have fractured under the above conditions are examined microscopically, it is found that they have cavities and cracks distributed throughout the specimen along grain boundaries as shown in figure 1. The failure mechanism associated with these cavities is therefore referred to as intergranular creep fracture. It is the dominant

mechanism of long-term fracture of both 304 stainless steel and 2-1/4 Cr-1 Mo steel, as shown in figure 2 [1,3-7], and of many other commercial alloys.

The cavities usually contain inclusions or second phase particles, apparently having nucleated on them. The cavities, once nucleated, grow by the diffusive movement of atoms from the cavity onto and along the grain boundary [8] as shown schematically in figure 3. This mechanism is equivalent to the stress-directed condensation of vacancies on the cavity. The migration of atoms (or of vacancies) results in the extension of the specimen—allowing the applied force to do work. Most of this work is dissipated by the diffusive fluxes associated with the redistribution of matter [9]; some, however, is stored as the energy associated with the newly created surface area of the cavities. If the load were removed, the specimen would contract as the cavities shrink by sintering. However, it is the nucleation and growth of these cavities that is of interest here as more and more of the grain boundaries are consumed and fracture eventually occurs.

As will be shown, theoretical progress in modeling creep cavitation has greatly outstripped the experimental advances or measurements in this field. At present, there are several viable models that can predict the

---

**About the Authors, Paper:** All four authors are members of organization units within NBS' Center for Materials Science. E. R. Fuller, Jr. and T.-J. Chuang are with the Inorganic Materials Division, R. J. Fields is with the Fracture and Deformation Division, and S. Singhal is a member of the Center's Reactor Radiation Division. The work on which they report was supported by the NBS Office of Nondestructive Evaluation.

---

<sup>1</sup> Numbers in brackets refer to references at the end of this paper.

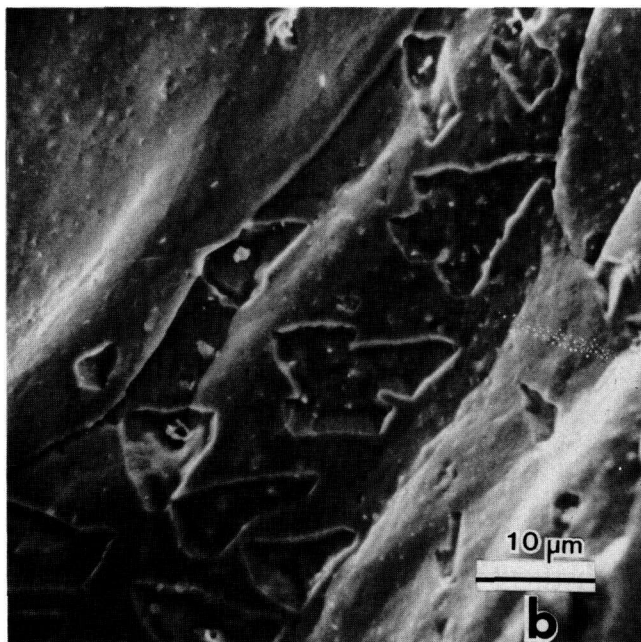
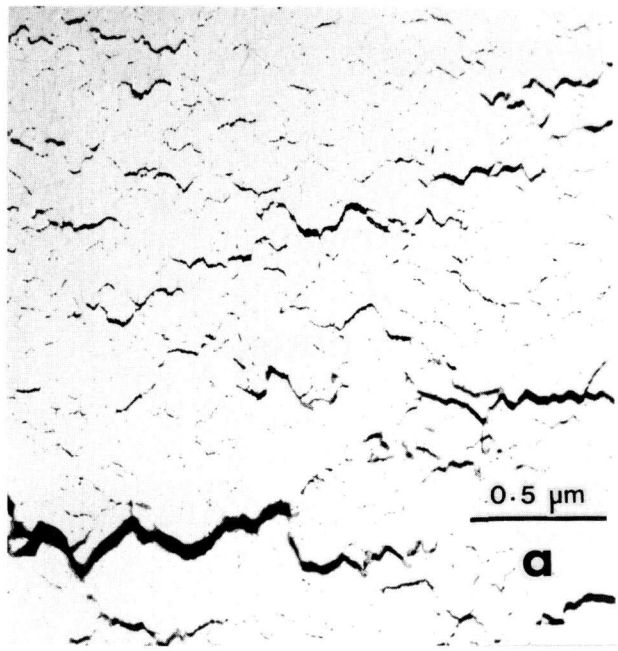


**Figure 1**-(a) Intergranular cavitation in copper tested at 600 °C viewed edge-on in an optical microscope. (b) Intergranular cavitation in iron tested at 600 °C, viewed in a scanning electron microscope on a grain boundary which is exposed by a low temperature fracture.

accumulation of damage and the time-to-fracture. Experimental measurements clearly supporting one model or, at least, rationalizing the differences between models, have not been available. Indeed, most experiments have focused on the stress dependence of the time-to-fracture (an integrated result), and have

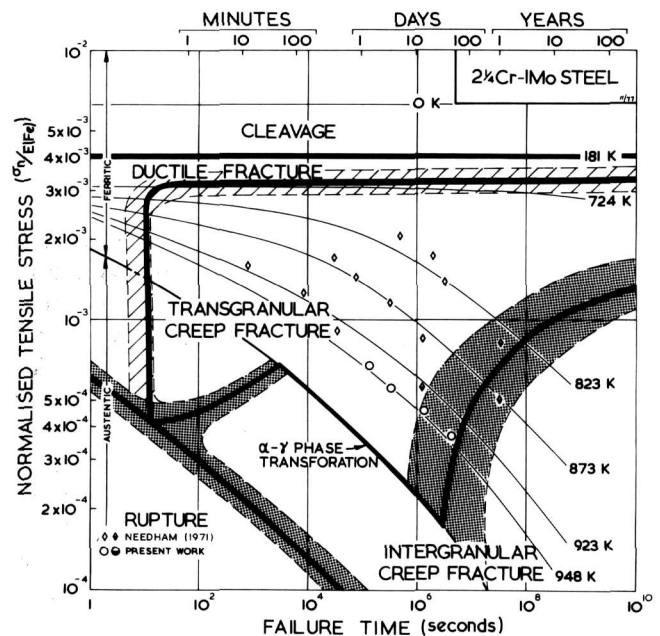
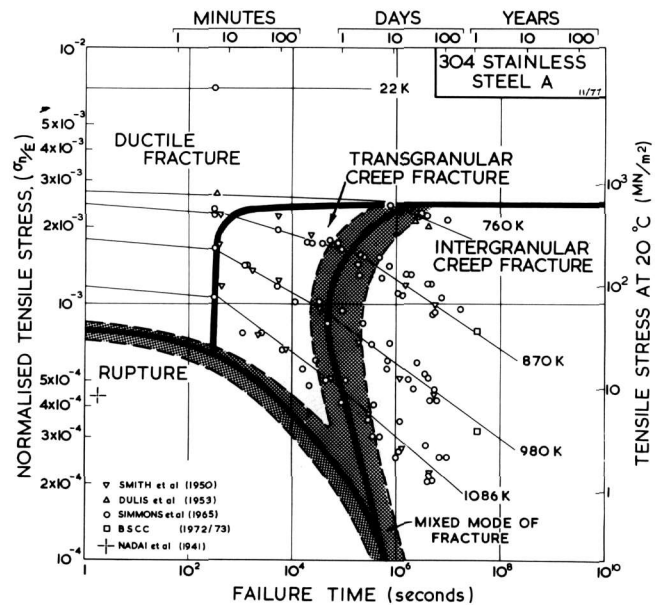


**Figure 2**-Fracture mechanism maps for 304 stainless steel and 2 1/4 Cr-1 Mo steel showing the regions of stress and temperature in which intergranular cavitation occurs.

given little attention to size distributions of cavities and their time dependence. Furthermore, this lack of experimental measurements for small cavity size distributions has hindered refinement of the various theoretical models.

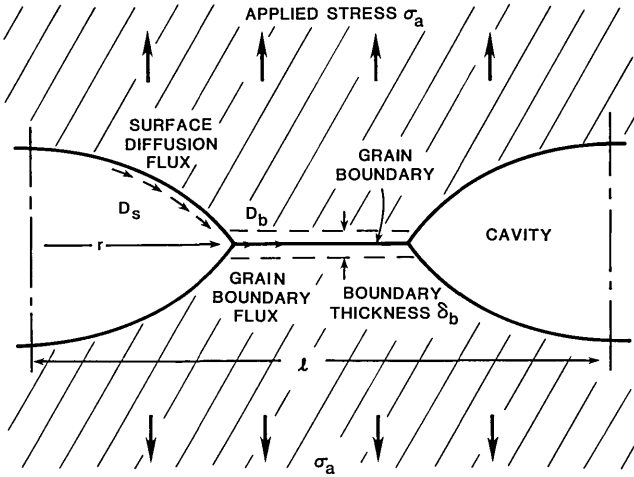


Figure 3—Schematic illustration of the stress-directed flow of material from the cavity surface onto the grain boundary.

In this paper, we present small angle neutron scattering (SANS) results which show that SANS is quantitatively sensitive to these small cavities. These results indicate that SANS may be the new technique to answer many of the pressing questions arising from existing theoretical treatments of creep cavitation. To understand what these questions are and how they have arisen, we first give a brief review of the theoretical developments in this area of fracture.

Historically, developments in creep cavitation have focused primarily on the stress dependence of the time-to-fracture, which, unfortunately, is not directly related to the cavity size information obtained by SANS. To indicate this connection, we demonstrate for several of these models how cavity size varies with time under stress. Following this review, we briefly discuss several experimental techniques for obtaining information on creep cavitation damage and conclude with a section describing our SANS measurements for a 304 type stainless steel.

## 2. Modeling of Creep Cavitation

On the basis of the few available experimental observations, Hull and Rimmer [10] developed a basic model for creep cavitation. They assumed that the cavities are spherical and that diffusion of matter away from them is achieved predominantly by grain boundary diffusion. According to Fick's first law, the flux,  $J$ , of matter from the cavity to the grain boundary is

$$J = -(D_b/kT\Omega)\nabla\mu \quad (1)$$

where  $D_b$  is the grain boundary diffusivity,  $\Omega$  is the atomic volume, and  $\nabla\mu$  is the gradient of chemical potential. To obtain this last quantity, Hull and Rimmer assumed that the chemical potential is  $-\sigma_a\Omega$  midway between cavities and  $-2\gamma_s\Omega/r$  at the periphery of a cavity, where  $\sigma_a$  is the applied stress,  $\gamma_s$  is the surface energy, and  $r$  is the radius of the cavity. By assuming a linear variation in chemical potential between these two points, they obtained the following expression for the flux:

$$J = (D_b/kT) \left\{ \frac{\sigma_a - 2\gamma_s/r}{l/2} \right\} \approx 2D_b\sigma_a/kTl \quad (2)$$

where  $l$  is the distance between voids and  $2\gamma_s/r$  is assumed to be much less than the applied stress. The area through which this flux occurs is  $2\pi r\delta_b$ , where  $\delta_b$  is the effective grain boundary thickness. Since each atom that leaves the cavity increases the cavity's volume by  $\Omega$ , the total flux results in a net volume flow of matter,

$$dV/dt = 4\pi r D_b \delta_b \sigma_a \Omega / kTl \quad (3)$$

away from the cavity and onto the grain boundary.

If the cavities are spherical, this volume flow of matter results in a size rate of cavity growth of

$$dr/dt = D_b \delta_b \sigma_a \Omega / kTlr \quad (4)$$

Integrating this result, the time development of the cavity size is given by

$$\begin{aligned} r &= [(2D_b\delta_b/l)(\sigma_a\Omega/kT)t + r_i^2]^{1/2} \\ &\approx [(2D_b\delta_b/l)(\sigma_a\Omega/kT)]^{1/2} t^{1/2} \end{aligned} \quad (5)$$

where  $r_i$  is the initial cavity radius, which here is assumed to be much smaller than the current cavity size,  $r$ , at time  $t$ . Hull and Rimmer bypassed this result, eq (5), and calculated directly the time-to-fracture,  $t_f$ , as the time for the cavities to grow to one-half their separation,  $l/2$ , where they coalesce and failure ensues. Thus, their final result was

$$\begin{aligned} t_f &= (l^3/8D_b\delta_b)(kT/\sigma_a\Omega) \\ &= \beta^3(\rho^{-3/2}/8D_b\delta_b)(\sigma_a\Omega/kT)^{-1} \end{aligned} \quad (6)$$

where  $\rho(=\beta^2/l^2)$  is the number of cavity nuclei per unit area of grain boundary and  $\beta$  is a geometric factor related to the coordination number of nearest-neighbor cavities (for example,  $\beta=1$  for a square array and  $\beta=(4/3)^{1/4}$  for an hexagonal array). Although the time-to-fracture and its stress dependence are the important parameters from an engineering perspective, the intermediate result of cavity size as a function of time, and also of cavity size distributions, are the important quantities when making a nondestructive assessment of creep damage for remaining lifetime.

Speight and Harris [11] objected to the assumption of a linear variation in chemical potential which is a direct consequence of performing the above, one-dimensional calculation. Since the cavitation occurs in one plane, a two-dimensional calculation is required and this does not lead to a linear variation. Actually, Hull and Rimmer [10] realized this and had carried out an elegant calculation for the time-to-fracture in the appendix of their pioneering paper. In that appendix, they assumed a two-dimensional, square array of equal-sized, spherical nuclei. The solution for this geometry did not result in a linear gradient of chemical potential. Despite this modification, the calculated time-to-failure differed from the above equation, eq (6), only by a constant factor.

A further modification to the above model was suggested by Vitovek [12] who pointed out that as the cavities cover the boundaries, the stress on the remaining ligaments goes up. Then the assumption that the chemical potential is determined at all times by the applied stress must be dropped in favor of a stress that increases as the internal, loadbearing area decreases. Harris *et al.* [13] make this adjustment as well as that suggested by Speight and Harris [11] earlier, and find that the Hull and Rimmer model predicts<sup>2</sup>

<sup>2</sup> In deriving the equation which ultimately leads to their form of eq (7). Speight and Harris [11] assumed that the stress midway between cavities is given by the remote stress, or by an adjusted ligament stress [13]. This is a valid approximation for small cavities; but as their results show, the stress can vary substantially across the grain boundary ligament for larger cavity sizes. Accordingly, in this regime the remote stress should be equated to the average stress on the grain-boundary ligament. This modification was first suggested by Raj and Ashby [14] and their model equates the remote stress to the average stress in the circular catchment area surrounding each cavity. This idea should be extended over the entire grain boundary area which includes the area excluded by the close packing of circles. We have made this modification in writing both eqs (7) and (9).

$$t_f = t_{HR}(15\pi^2 - 140 - \pi\beta^2)/60$$

$$\approx t_{HR}/13.6 \quad (\text{for a hexagonal array}) \quad (7)$$

where  $t_{HR}$  is the combination of material parameters ( $D_b$ ,  $\delta_b$ ,  $l$ ,  $\Omega$ ) and experimental variables ( $\sigma_a$  and  $T$ ) that represent the time-to-failure in the simple Hull-Rimmer calculation presented above [see eq (6)]

$$t_{HR} = (l^3/8D_b\delta_b)(kT/\sigma_a\Omega) \quad (8)$$

In addition to the integrated result of eq (7), Harris *et al.* [13] also give a cavity growth relationship, which for short times has the form

$$t/t_{HR} = (2/3)x^3 \ln(1/x) \quad (9)$$

where  $x$  is the normalized cavity size ( $2r/l$ ). Although this relationship cannot be inverted analytically to give the time dependence of the cavity size, one can easily demonstrate that initial cavity growth rates and cavity sizes are faster for this modified Hull-Rimmer model than for the simple calculation, eq (5).

One fault of the Hull-Rimmer model, whether in its simple or modified form, is that the cavities are assumed to be spherical. Only very small cavities are ever observed to be spherical. Usually, they are ellipsoidal or lenticular in cross-section. As the cavities grow, their shape frequently becomes more eccentric and they sometimes resemble long, thin cracks. An ellipsoidal cavity consumes more grain boundary than a spherical cavity for the same volume flux. This means that the above model, which assumes spherical cavities, will generally overestimate the time-to-fracture.

The reason for crack-like cavities is apparent. The shape of a growing cavity is determined by the interaction between volume or boundary diffusion (the growth mechanism) and surface, volume, or vapor diffusion (spheroidizing mechanisms). Surface diffusion is generally the dominant rounding influence, while grain boundary diffusion is the principal growth mechanism. As the cavities enlarge, spheroidizing mechanisms become less effective and the cavities become more eccentric or penny-shaped.

Chuang and Rice [15] consider a crack-like creep cavity advancing at a steady state velocity  $v$  along the interface between two grains by the diffusive transport of atoms into the boundary ahead of the tip. They assume that spheroidization of the cavity is accomplished by surface diffusion, and that the cavity

grows under steady-state conditions so that it retains a constant profile which is described by a crack-tip radius of curvature,  $r_{tip}$ , and a crack opening width,  $2w$ , a few radii back from the crack tip. Solving the surface diffusion problem they find that the crack half-thickness is given by

$$w \approx 0.98 \sqrt{2-\gamma_b/\gamma_s} [D_s \delta_s \gamma_s \Omega / kT v]^{1/3} \quad (10)$$

where  $\gamma_s$  and  $\gamma_b$  are the surface free energy and grain-boundary free energy, respectively;  $D_s$  is the surface diffusivity; and  $\delta_s$  is the thickness of the surface diffusion layer (i.e., the surface density of diffusing atoms times the atomic volume). The radius of curvature adjacent to the crack tip is given by

$$\begin{aligned} r_{tip} &\approx 0.93 [D_s \delta_s \gamma_s \Omega / kT v]^{1/3} / \sqrt{2-\gamma_b/\gamma_s} \\ &\approx 0.95 w / (2-\gamma_b/\gamma_s). \end{aligned} \quad (11)$$

Since  $\gamma_b$  is usually about one-half  $\gamma_s$  (corresponding to a dihedral angle of about  $76^\circ$ ), eq (11) becomes approximately

$$\begin{aligned} w &\approx 1.57 r_{tip} \\ &\approx 1.20 [D_s \delta_s \gamma_s \Omega / kT v]^{1/3}. \end{aligned} \quad (12)$$

This shows that the faster a crack grows, the thinner it becomes. Alternatively, the crack velocity at a given temperature is inversely proportional to the third power of the crack thickness. Hence, the time-to-fracture for thin cracks or cavities is much less than that for spherical cavities. Chuang *et al.* [16] extend this analysis to calculate the time-to-fracture when the life is determined by the growth of cavities whose shape is determined by the interaction of spheroidizing and growth mechanisms. They find that

$$t_f \approx \left( \frac{kT l \gamma_s^2}{35 D_s \delta_s \Omega \sigma_a^3} \right) (2-\gamma_b/\gamma_s)^{3/2} \left( \frac{\bar{F}}{\sqrt{(1+\bar{F})-1}} \right)^3 \quad (13)$$

where

$$\bar{F} = \frac{4\sigma_a l (D_s \delta_s / D_b \delta_b)}{3\gamma_s \sqrt{2-\gamma_b/\gamma_s}} \bar{q} \quad (14)$$

and  $\bar{q} \approx 0.6$  is the average value of a slowly varying function of the cavity size [16]. Equation (13) has two

limiting forms which depend on the relationship between a combination of material properties and the applied stress level. At one extreme, failure time is independent of grain-boundary diffusion and varies as the inverse third power of stress

$$t_f \approx \left( \frac{8kT l \gamma_s^2}{35 D_s \delta_s \Omega \sigma_a^3} \right) (2-\gamma_b/\gamma_s)^{3/2} \quad (15a)$$

when  $\sigma_a < 0.8(\gamma_s/l)(D_b \delta_b / D_s \delta_s)$ ; whereas at the other limit, failure time is controlled by both surface and grain-boundary diffusion and varies as the inverse 3/2 power of stress

$$t_f \approx \left( \frac{kT}{35 D_s \delta_s \Omega} \right) \left[ \left( \frac{64 \bar{q}^3}{27} \right) \left( \frac{l^5 \gamma_s}{\sigma_a^3} \right) \left( \frac{D_s \delta_s}{D_b \delta_b} \right)^3 \right]^{1/2} \quad (15b)$$

$$\text{when } \sigma_a > 150 \left( \frac{\gamma_s}{l} \right) \left( \frac{D_b \delta_b}{D_s \delta_s} \right).$$

This concern over the stress dependence of the time-to-fracture arises from a discrepancy between the theoretical predictions and experimental fact. The Hull and Rimmer model [10], and Speight and Harris modifications [11,13], predict that the time-to-fracture should vary inversely with the first power of stress. Indeed, experiments by Raj [17] have indicated that this may be the case in bicrystal specimens. However, as shown above, the Chuang *et al.* model [16], which considers cavity shape, predicts that under certain conditions the fracture lifetime will be inversely proportional to a power of applied stress between 3/2 and 3. Thus, cavity shape can play an important part in determining how quickly a component will fracture by grain-boundary cavitation. By pre-nucleating cavities in silver and other metals, Goods and Nix [18] found times-to-failure that varied inversely with approximately the third power of stress, thus providing extremely strong experimental support for the theory of Chuang *et al.* [16].

Despite this support for the Chuang-Rice model [15,16] by creep lifetime measurements on pre-cavitated metals, the situation is not as clear-cut for the case where cavities are nucleated naturally on the grain boundaries. Experimental creep fracture work generally indicates a stronger inverse power-law stress dependence than given by either the Hull-Rimmer model or the Chuang-Rice model. To illustrate this dependence, creep fracture results for various metals and alloys [19-22] have been analyzed and are

presented in table 1. The stress exponent,  $n$ , given in this table is defined by the equation

$$t_f = B\sigma_a^{-n} \quad (16)$$

where  $B$  is a constant of proportionality. The weakest stress dependences occur for the longest tests or at the highest temperatures, where  $n$  is found to be about 3 or 4; but for shorter times-to-fracture,  $n$  becomes quite large.

**Table 1.** Stress dependence of time-to-fracture for selected metals.

Metal	$T/T_M^1$	$t_f$	$n$	Reference
316 S.S.	0.54	4–20 yr	3.6	Simmons and van Echo [5]
	0.60	2 w–6 mo	3.8	
	0.54	1 d–6 mo	6.3	
	0.60	1 d–2 w	5.3	
	0.54	$\frac{1}{2}$ h–3 h	14.3	
	0.60	$\frac{1}{4}$ h– $\frac{3}{4}$ h	12.5	
304 S.S.	0.52	1–3 yr	3.8	Simmons and van Echo [5]
1Cr $\frac{1}{2}$ Mo Steel	0.45	1–10 yr	3.7	Bennewitz [19]
Lead	0.50	1–5 yr	3.0	Gohn et al. [20]
Tungsten	0.83	1–10 d	4.4	Conway et al. [21]
Iron	0.48	10 h–1 w	10.1	Fields et al. [1]
	0.54	3 h–1 w	9.0	
Copper	0.31	3–9 w	13.5	Carreker and Hibbard [22]
	0.52	2 d–1 w	4.1	

<sup>1</sup>  $T/T_M$  is the homologous temperature, where  $T_M$  is the melting temperature; and the stress exponent  $n$  is defined by  $t_f \propto \sigma^{-n}$ .

Although, as discussed above, the predominance of experimental evidence is related to the power of the stress dependence, there are at least two other important distinctions between the two models that are amenable to experimental investigation. The first is the density of cavities on the grain boundary, as defined, for example, by  $\rho (\propto 1/l^2)$ . In the Hull-Rimmer model, both the time-to-failure and the time required to grow to a given cavity size are proportional to  $\rho^{-3/2}$  (see eqs (6) and (9), respectively); whereas in the Chuang-Rice model, this dependence varies from  $\rho^{-1/2}$  to  $\rho^{-5/4}$  depending upon the applied stress and the material properties as defined by the two limiting cases (see eq (15)). The other distinction between the two models is the cavity growth rate. The Hull-Rimmer model predicts a complex time dependence as prescribed by eq (9); whereas for small cavities, the Chuang-Rice model predicts a constant cavity growth

rate or a linear time dependence of the normalized cavity size<sup>3</sup>,

$$(2r/l) \approx 16t/35t_{CR} \quad (17)$$

where  $t_{CR}$  is the time-to-failure as given by either eq (13) or one of its limiting forms, eq (15).

Based on these differences, alternative experimental techniques, such as small angle neutron scattering measurements, might help to elucidate the nature of cavity nucleation kinetics and cavity growth rates by providing information about cavity size distributions and how they evolve with time.

Returning, however, to the concern over the high powers of the stress dependence, Dyson [23], Rice and Needleman [24], and Rice [25] introduced the idea of constrained cavity growth to explain this. At high growth rates, the atoms diffusing away from the cavities cannot be distributed uniformly along the grain boundary. This effect locally unloads the regions around the cavities. Growth then requires the time dependent plastic straining of the matrix (i.e., creep) to counteract this load-shedding. Using this idea, the constrained cavity growth model predicts the Monkman-Grant [26] relation:

$$t_f \dot{\epsilon}_{ss} = \text{constant} \quad (18)$$

where  $\dot{\epsilon}_{ss}$  is the steady state creep rate. This relation is a commonly found experimental result. The high powers listed in table 1 might then be explained by this constrained cavity growth model.

The above models all assume that all nucleation occurs at the onset of loading and that all the nuclei begin to grow at the start of the test. Greenwood [27] shows that most experimental data are consistent with a model in which the number of cavities is a linear function of strain, i.e., nucleation occurs throughout the life of a specimen. Indeed, the fact that Goods and Nix [18] had to pre-nucleate cavities to obtain the Chuang result indicates that nucleation is an important step in the creep fracture of some metals. This is another area where a technique such as small angle neutron scattering can be expected to provide vital information regarding this creep failure mechanism.

To include continuous nucleation in their analyses, Raj and Ashby [14] consider quantitatively two

<sup>3</sup> This equation is derived in the same spirit as Chuang *et al.* [16] calculated the time-to-failure.

models for nucleating new cavities throughout a test: one without grain boundary sliding, and one with grain boundary sliding. Without grain boundary sliding, subcritical or embryonic cavities can become stable and grow by being thermally activated over the nucleation barrier. In this case, they applied classical nucleation theory. The change in free energy on forming a cavity is calculated by balancing the energy released when the applied forces do work against the energy absorbed by the creation of new interfacial area:

$$\Delta G = -r^3 F_v(\psi) \sigma_a + r^2 [\gamma_s F_s(\psi) - \gamma_b F_b(\psi)] \quad (19)$$

where  $F_s$  and  $F_b$  are the functions that relate the surface area of the cavity and the grain-boundary area, respectively, to the cavity radius squared;  $F_v$  is a similar function for the cavity volume; and  $\psi$  is the cavity dihedral angle given by  $\arccos(\gamma_b/2\gamma_s)$ . Using the definitions of the functions  $F_v$ ,  $F_s$ , and  $F_b$ , eq (19) has been shown to have a maximum at a critical radius [14]

$$r_c = 2\gamma_s/\sigma_a \quad (20)$$

below which cavities tend to shrink and above which they tend to grow. Substituting this critical radius into eq (19), gives the activation energy for nucleation:

$$\Delta G_c = r_c^3 F_v(\psi) \sigma_a / 2 = 4\gamma_s^3 F_v(\psi) / \sigma_a^2 \quad (21)$$

The area density of critical nuclei, i.e., those that prefer to neither shrink nor grow, on the grain boundary is

$$\rho_c = \rho_{\max} \exp[-\Delta G_c/kT] \quad (22)$$

where  $\rho_{\max}$  is the maximum density of possible nucleation sites there. The nucleation rate can be obtained from  $\rho_c$  by multiplying eq (22) by the time-dependent probability,  $P(t)$ , of adding one vacancy to a critical nucleus. Raj and Ashby [14] derive  $P(t)$  from the vacancy jump frequency and from the probability of finding a vacancy at the perimeter of a critical nucleus. They obtain

$$P(t) = (4\pi\gamma_s/\sigma_a\Omega)(D_b\delta_b/\Omega^{1/3}) \exp[\sigma_a\Omega/kT] \quad (23)$$

By combining eqs (21), (22), and (23), the nucleation rate is found to be

$$\dot{\rho} = (4\pi\gamma_s D_b \delta_b / \sigma_a \Omega^{4/3}) (\rho_{\max} - \rho) \times \exp[(\sigma_a \Omega - 4\gamma_s^3 F_v(\psi) / \sigma_a^2) / kT] \quad (24)$$

The dominant term in the above equation is  $\exp(-1/\sigma_a^2)$ . How does this term in the nucleation rate affect the time-to-fracture? To obtain the time-to-fracture, it is necessary to perform a double integration over time because nucleation occurs simultaneously with cavity growth. Since exponential arguments are unaffected by integration, the strong stress dependence of nucleation will be carried into the time-to-fracture. Such an exponential dependence on stress can mimic any power-law dependence of the form

$$t_f = B \sigma_a^{-n} \quad (\text{see eq (16)}),$$

regardless of the value of  $n$ , over certain ranges of stress.

The second type of nucleation mechanism examined by Raj and Ashby [14] is based on grain boundary sliding. If there is an inclusion on a sliding grain boundary, then this sliding is either accommodated by flow of atoms around the particle or else a gap opens up. Accommodation is possible at low stresses leading to low sliding rates, but as the stress and sliding rate increase the flow intensification at the inclusion also increases until cavity nucleation occurs. Thus, the nucleation rate and the number of nuclei are dependent on strain and strain rate. Since the rate of fracture is proportional to the rate of nucleation, an additional stress dependence similar to that for the strain rate will enter the expression for the time-to-fracture. In this way, nucleation considerations can be used to predict the Monkman-Grant relation.

### 3. Experimental Techniques to Study Creep Cavitation

We have discussed four theories: Hull and Rimmer [10], coupled grain boundary and surface diffusion controlled growth [15], constrained cavity growth [23], and continuous cavity nucleation [14]. Of the numerous theoretical works on creep cavitation, the models discussed above are the ones supported by experiment. To some extent, the above models are mutually exclusive. While it is likely that under different experimental circumstances, different models are appropriate, the situation is confusing. Most often, support for one model over another is determined

from the stress dependence of the time-to-fracture. Considerably more persuasive support would come from direct measures of cavity nucleation rates and subsequent cavity growth rates.

Attempts to experimentally measure these two quantities have not been conclusive. The two most common techniques are metallography and density. Metallographic techniques include microscopy techniques ranging from optical measurements on polished surfaces to transmission electron microscopy (TEM) measurements on thin foils. The optical techniques suffer from a lack of resolution and the difficulties inherent in preparing a surface without grossly altering the cavities. The TEM studies usually have had difficulty finding any cavities due to the limited material volume which is sampled in each TEM specimen. When a cavity is found, it is not clear that it is representative of typical cavities in the material. Another metallographic technique is to fracture a specimen along its grain boundaries at low temperature after it has been crept at elevated temperature, and to measure the cavitation in a scanning electron microscope (SEM). This is the most successful of the metallographic techniques. It is always a concern, however, that the low temperature fracture surface has selected the most heavily cavitated boundaries and may not be representative of the overall cavitation.

High precision density measurements usually employ Archimedes' principle. Since the buoyant fluid will probably penetrate surface cracks, this technique will be mainly sensitive to bulk cavitation. This technique can only tell the total volume of cavities. For this reason, it cannot be used to study continuous nucleation, which requires a knowledge of cavity size distributions.

Two new techniques for studying the cavitation phenomenon are small angle neutron scattering (SANS) and x-ray topography or x-radiography. SANS work has already been performed at NBS and other laboratories. These initial studies have demonstrated that SANS is very sensitive to cavitation and may be the most powerful technique yet tried for studying nucleation of creep cavities. X-ray techniques have not been tried yet, but they may provide information concerning the shape and growth rate of creep cavities measured in-situ.

SANS is performed by measuring the angular dispersion of an initially collimated beam of monochromatic neutrons. This dispersion can be related to the size and size distribution of scattering particles, or cavities, by using elements of established diffraction theory. In addition to the present studies,

SANS studies have been carried out on creep-damaged stainless steel [28], superalloys [29], and copper [30]. In every case, the scattering was observed to increase as the damage increased. The interpretation of the results for the stainless steel and the superalloys was clouded by changes in the precipitate size distribution that occurred during the test. Furthermore, the scattering in the stainless steel was attributed to cavities although other techniques, such as TEM, never revealed the presence of creep cavities. SANS studies of creep cavitation at NBS to date have centered on 304 stainless steel. As will be discussed below, the use of unstressed reference specimens and a carbide stabilizing heat treatment have virtually eliminated the ambiguities arising from precipitate redistribution during the test. Also, microscopic studies have revealed intergranular cavities in specimens that have been tested long enough to grow the cavities to resolvable sizes. Therefore, it is valid to attribute the neutron scattering to cavitation.

#### **4. SANS Study of Cavitation in 304 Stainless Steel**

304 stainless steel used in high temperature applications consists mainly of austenite grains and grain-boundary metal carbides. The carbide-austenite interface at the grain boundary is a preferential site for cavity nucleation, which at high temperatures can be readily activated with low applied stresses by creep deformation and/or grain-boundary sliding. The resulting cavities then grow, link, and ultimately cause failure. The early stages of this process are extremely slow and the creep cavities, due to their small size, are not easily detectable or quantifiable. It is these early stages of nucleation and cavity growth that are examined here through the use of small angle neutron scattering.

The structure after cavitation consists of grain-boundary cavities and two material phases (austenite and carbides). The unequivocal determination of cavity size, or size distribution, from a SANS spectra requires that the creep-induced changes in the carbide volume fraction, size distribution, and spacial distribution do not contribute significantly to the scattered intensity. By adopting special experimental procedures, the effects due to the carbides could be minimized. The following two procedures were employed:

1. All samples were given a stabilizing heat treatment of 40 h at 775 °C prior to creep

testing. This resulted in a very coarse and stable carbide distribution.

2. A heat-treated, but unstressed, reference sample was placed in the furnace with each creep specimen. In each case, the SANS spectra of the unstressed sample was subtracted from that of the stressed specimen to obtain the SANS spectra of the creep damage.

The SANS studies were carried out at the NBS reactor facility using a converging collimation and a neutron wavelength of 0.625 nm. With this choice of collimation and wavelength parameters, a scattering vector ( $\mathbf{Q}$ ) range of 0.05 to 1.5 nm<sup>-1</sup> (0.005 to 0.15 Å<sup>-1</sup>) could be measured in these experiments. This  $\mathbf{Q}$  range measures the scattering contribution of the inhomogeneities in the size range of 4 to 120 nm. Detailed theory and procedures for analyzing SANS data have been described by Kortorz [31]. A few relevant features will be discussed here. If the scattered intensity is denoted by  $I$ , the differential scattering cross-section is given by

$$d\Sigma/d\Omega = cI/MTd \quad (25)$$

where  $d$  is the sample thickness,  $M$  is the total monitor count (or scattering time),  $T$  is the sample transmission, and  $c$  is a combination of experimental constants related to the SANS facility. Creep damage is related to the difference in differential scattering cross-sections between the crept sample (C) and the reference sample (R):

$$\left[ \frac{d\Sigma_C}{d\Omega} - \frac{d\Sigma_R}{d\Omega} \right] = c \left[ I_C/M_C T_C d_C - I_R/M_R T_R d_R \right]. \quad (26)$$

Accordingly, all intensities in the following discussion have been normalized by sample thickness, transmission, and scattering time. We now assume that the entire difference in scattering is due to creep cavities alone. This is justified by the use of the special procedures described above. Figure 4 shows a scattering pattern for one set of creep and reference samples. This figure shows, as did all the samples, that the crept sample scatters more strongly than the reference sample. This result supports the assumption that cavities are the predominant scattering feature, because carbide coarsening would show up as decreased scattering. The data are replotted in figure 5 as the difference spectra.

One parameter of major interest is the growth of average cavity size as a function of time under load. A

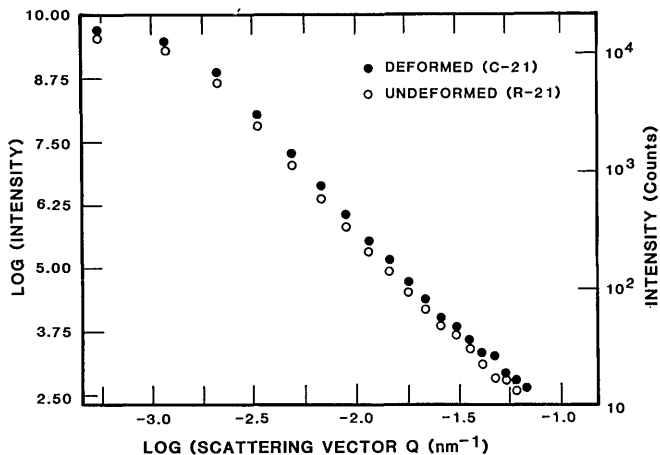


Figure 4—SANS spectra for a 304 stainless steel specimen which was deformed under a 145 MPa tensile stress at 600 °C for 1493 h (specimen C-21) and for an undeformed reference specimen (specimen R-21).

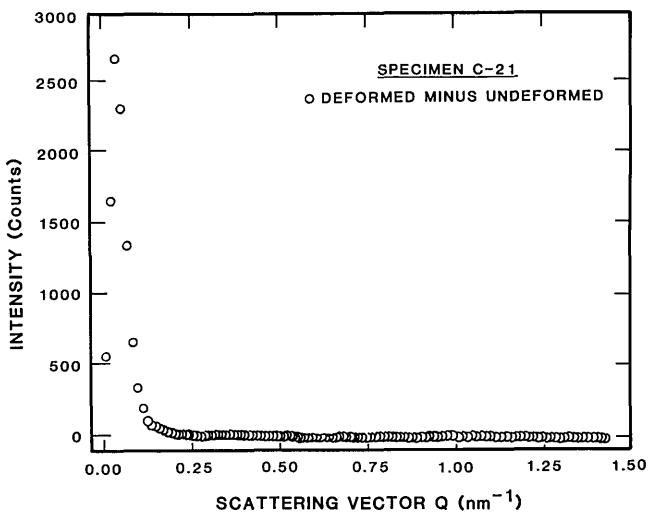


Figure 5—SANS difference spectra from figure 4 showing the scattering due to creep-induced cavities.

Guinier analysis [31] was performed on spectra like figures 4 and 5 to obtain an average cavity size. Guinier showed that for a randomly distributed monosized, spherical heterogeneity, the intensity ( $I$ ) and scattering vector ( $\mathbf{Q}$ ) relationship can be described by the equation

$$I = I_0 \exp[-R_g^2 \mathbf{Q}^2/3]. \quad (27)$$

Here  $R_g$  is the radius of gyration of the cavities and for spherical cavities it is related to the cavity radius ( $R$ ) by the equation

$$R = \sqrt{5/3} R_g. \quad (28)$$

If the cavities are not of one size, then the utility of the Guinier approximation is limited to a very small  $Q$  range near zero. Figure 6 is a Guinier plot ( $\log I$  versus  $Q^2$ ) for the difference spectra of figure 5 giving information about the creep cavitation damage. It is clear from this plot that cavities in this material must have a nonuniform size distribution, as a straight line in these plots can be fitted only over a narrow  $Q$  region near the peak. The cavity diameter obtained by this procedure normally overestimates the contribution of large cavities, yet it is a very useful parameter to study cavity growth as a function of creep time while degradation is in progress. Using a least square fit subroutine, the above equation for  $I$  was fit to the

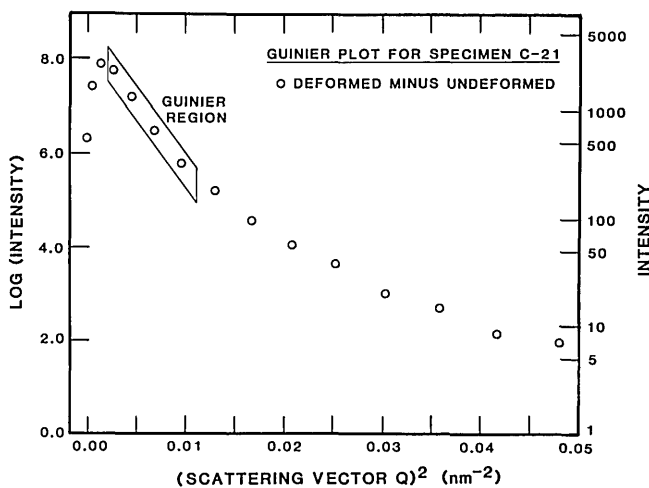


Figure 6—Plot of the Guinier region for the difference spectrum of figure 5 showing the creep damage in specimen C-21.

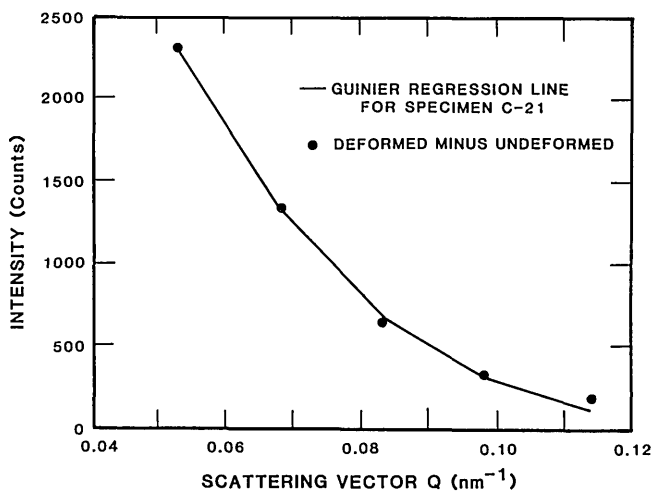


Figure 7—Least squares regression analysis of the linear Guinier region in figure 6 and the fitted, appropriate data points.

Table 2. Growth of creep cavities as a function of time at constant stress in 304 stainless steel.

Sample	Creep parameters		Average cavity diameter—Guinier approximation (nm)
	Applied stress	Time (h)	
C-21	145 MPa (21 ksi)	745	34.6
		1493	77.0
C-18	124 MPa (18 ksi)	789	26.6
		1537	76.3

data points in the relevant  $Q$  range. A set of experimental data points and the regression lines are shown in figure 7. (Note that this figure is plotted as  $I$  versus  $Q$ , so that the regression line is not straight.) A reasonably accurate fit was obtained in the selected  $Q$  range for this specimen as well as for the other creep specimens. The average cavity sizes derived for the various stresses and times under load at 600 °C are shown in table 2.

Table 2 shows that doubling the creep time at the same stress apparently doubles the average cavity size, apparently in agreement with the Chuang-Rice model, which predicts a constant cavity growth rate. Figure 8 shows cavity size as a function of creep time. If we include a point at the origin, the linear time dependence in the growth rate of the cavities is again apparent, but in the absence of more data points, only a limited significance can be attached to the trend in figure 8. Specimens have been tested to intermediate times and their SANS spectra will be determined shortly.

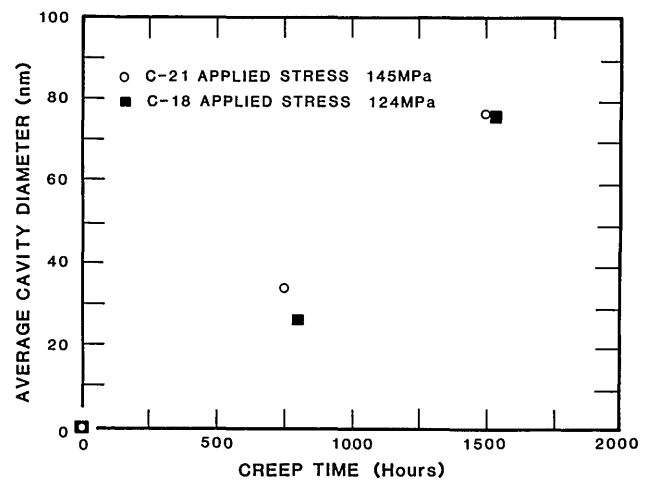


Figure 8—Average cavity diameter for 304 stainless steel specimens at 600 °C as a function of time and stress.

From table 2, we see that specimen C-21, which was stressed at 145 MPa (21 ksi), has a higher average cavity size after 750 h than specimen C-18 which was stressed at 124 MPa (18 ksi). After 1500 h, we find that the average cavity size at these two stress levels is not too different. This could indicate that for longer creep times the size growth of cavities is less sensitive to small changes in applied stress. A more likely possibility, as noted by Weertman [30], is that when a sizable fraction of cavities grows large enough to scatter at  $Q$  values below the minimum resolvable  $Q$  in the experiments, the average size and volume fraction deduced from the standard SANS analysis are highly underestimated. Recent efforts have been made to extend SANS measurements to larger size ranges [32], for which other techniques have enough resolution to be effective. In this overlapping size range, SANS and these other techniques can be compared with each other to provide some assessment of their validity in the nonoverlapping size ranges.

The most important development demonstrated here is that we are capable of measuring cavities at early times when they are only 20 to 30 nm in diameter. This must be close to the nucleation event. No other technique, that we know of, is capable of resolving this initiation phenomenon. Further work should provide direct experimental information that will test the assumptions of the models discussed previously. Since these models are to be used for predictive purposes, they must be verified. SANS currently appears to be the best technique to characterize creep damage in order to test these theories.

## 5. Conclusion

Numerous theories of creep cavitation have developed over the years. The evaluation and further refinement of these theories has been impeded by a lack of experimental research in this area. Small angle neutron scattering studies at NBS and elsewhere have shown that this technique may provide the necessary tool for studying nucleation and early growth of cavities. Such a development would provide the impetus to further progress in this field.

---

We wish to thank S. M. Wiederhorn and T. R. Shives for reviewing this paper and for their helpful suggestions.

## References

- [1] R. J. Fields, T. Weerasooriya, and M. F. Ashby, *Met. Trans.* **11A**, 333 (1980).
- [2] M. F. Ashby, C. Gandhi, and D. M. R. Taplin, *Acta Met.* **27**, 699 (1979).
- [3] G. V. Smith, E. J. Dulis, and E. G. Houston, *Trans. ASME* **42**, 935 (1950).
- [4] E. J. Dulis, G. V. Smith, and E. G. Houston, *Trans. ASME* **45**, 42 (1953).
- [5] W. J. Simmons and J. A. van Echo, *ASTM Data Series Publication DS5-s1* (1965).
- [6] B.S.C.C., British Steel Corporation, p. 11, ISO/TC17 /SC10/ETP-SG (Secretariat 104) 138- MT/QF/54/74 (1972-73).
- [7] A. Nadai and M. J. Manjoine, *J. Appl. Mech.* **63**, A-77 (1941).
- [8] R. K. Varma and B. F. Dyson, *Scripta Met.* **16**, 1279 (1982).
- [9] T.-J. Chuang, *Int. J. Fracture* **23**, 229 (1983).
- [10] D. Hull and D. E. Rimmer, *Phil. Mag.* **4**, 673 (1959).
- [11] M. V. Speight and J. E. Harris, *J. Metal Science* **1**, 83 (1967).
- [12] F. H. Vitovek, *J. Materials Science* **7**, 615 (1972).
- [13] J. E. Harris, M. O. Tucker, and G. W. Greenwood, *Metal Science* **8**, 311 (1974).
- [14] R. Raj and M. F. Ashby, *Acta Met.* **23**, 653 (1975).
- [15] T.-J. Chuang and J. R. Rice, *Acta Met.* **21**, 1625 (1973).
- [16] T.-J. Chuang, K. I. Kagawa, J. R. Rice, and L. B. Sills, *Acta Met.* **27**, 275 (1979).
- [17] R. Raj, *Acta Met.* **26**, 341 (1978).
- [18] S. H. Goods and W. D. Nix, *Acta Met.* **26**, 739 (1978).
- [19] J. H. Bennet, *Joint International Conf. on Creep* (Inst. of Mech. Engineers, London, 1963).
- [20] G. R. Gohn, S. M. Arnold, and G. M. Boulton, *Proc. ASTM* **46**, 990 (1946).
- [21] J. B. Conway and P. N. Flagella, *Creep Rupture Data for the Refractory Metals to High Temperatures* (Gordon and Breach Publishers, New York, 1971).
- [22] R. P. Carreker, Jr. and W. R. Hibbard, Jr., *Acta Met.* **1**, 654 (1953).
- [23] B. Dyson, *Metal Science*, 349 (1976).
- [24] A. Needleman and J. R. Rice, *Acta Met.* **28**, 1315 (1980).
- [25] J. R. Rice, *Acta Met.* **29**, 675 (1981).
- [26] F. C. Monkman and N. J. Grant, *Proc. ASTM* **56**, 593 (1956).
- [27] G. W. Greenwood, *Phil. Mag.* **19**, 423 (1969).
- [28] M. H. Yoo, J. C. Ogle, J. H. Schneibel, and R. W. Swindeman, in *Proc. 6th International Conf. on Strength of Metals and Alloys*, Melbourne, Australia, Aug. 16-20, 1982 (Pergamon Press).
- [29] H. Walther and P. Pizzi, *SANS for Nondestructive Testing in Research Techniques in Nondestructive Testing*, Vol. IV, Edited by R. S. Sharpe (Academic Press, 1980).
- [30] J. R. Weertman, M. Yang, and M. Roth, *Grain Boundary Cavitation in Copper Subjected to High Temperature Creep*, Annex to Annual Report, Institut Laue-Langevin, Grenoble, France, p. 263.
- [31] G. Kostorz, *Neutron Scattering in Materials Science*, Chapter 5 in *Treatise in Materials Science and Technology*, Vol. 15, Edited by H. Herman (Academic Press, New York, 1979).
- [32] K. Hardman-Rhyne, N. F. Berk and E. R. Fuller, Jr., *J. Res. Natl. Bur. Stand. (U.S.)* **89**(1): 00-00; 1984 January-February.

# Impedance of a Coil in the Vicinity of a Crack

Arnold H. Kahn  
National Bureau of Standards, Washington, DC 20234

Accepted: November 16, 1983

Calculations are presented for the impedance of a coil as it is moved in the vicinity of a v-groove crack in the surface of a metallic slab. The coil is modeled as a pair of parallel wires, oriented parallel to the crack, carrying equal and opposite currents. The inhomogeneous electromagnetic fields in the air above the slab and in the metal are determined by the boundary integral equation (BIE) method. This approach leads to a pair of coupled integral equations for the tangential components of the electric and magnetic field vectors on the surface of the slab containing the crack. The solutions, which are obtained by standard methods of discretization, are valid for arbitrary ratio of crack or coil dimensions to skin depth. Illustrations are presented of the Poynting vector distribution over the surface of the metal, including the crack faces. A plot of the complex impedance is given in the form of a coil scan across the crack.

Key words: boundary integral equations; crack detection; eddy currents; electromagnetic NDE; nondestructive evaluation.

## 1. Introduction

In the design of electromagnetic NDE systems for the detection and examination of cracks or other defects in conducting materials, it is necessary to have a quantitative description of the electric and magnetic fields in the vicinity of the defect. In practice, the fields are produced by an exciting coil, the impedance of which is used to provide the detection signal. (The voltage induced in a secondary pickup coil may also be used.) In previous work by the author [1,2]<sup>1</sup>, the fields in the vicinity of a crack were calculated for models based on excitation by a spatially uniform applied ac magnetic field such as would be found in the interior of a solenoid. The present work offers an improved description of the fields through the introduction of nonuniformity of the applied field due to finite coil size and the inclusion of coil position relative to the crack.

Recently there has been significant activity in the development of theoretical modeling in electromagnetic NDE. The finite element method has been applied by Ida and Lord [3] to the cylindrical geometry of reactor tubing. Studies have been presented by Auld *et al.*, Kincaid *et al.*, Bahr, and others [4] on experimental and theoretical considerations of crack detection and coil design. A principal difficulty is the calculation of signals when the electromagnetic skin depth and crack size are of comparable magnitude, which is the domain of greatest sensitivity. The two-dimensional model of this paper represents a contribution toward the solution of this problem. A full three-dimensional treatment may be possible as new computing capabilities are developed [3].

## 2. Description of the Model and Theoretical Formulation

The calculations described in this paper are based on the following model: We consider a flat surface with an infinitely long, symmetrical v-groove representing a surface crack in a slab of metal. Below the surface, the material is homogeneous and uniform in conductivity. A pair of wires carrying equal and opposite currents is located above the slab and is oriented parallel to the crack. The wires are infinitesimal in thickness and infinite in extent. This

---

**About the Author, Paper:** Arnold H. Kahn, a physicist, is part of the Nondestructive Characterization Group in the NBS Metallurgy Division. The work on which he reports was supported in part by the NBS Office of Nondestructive Evaluation.

---

<sup>1</sup> Figures in brackets indicate literature references at the end of this paper.

simplified model of an eddy-current testing configuration allows a two-dimensional calculation of the impedance signals due to the crack. The calculation will allow for the effect of crack dimensions; coil dimensions, elevation, and displacement; and the material parameters of the metal. This is an improvement over calculations in which the exciting field is spatially uniform.

By solving for the electromagnetic fields first on the surface of the metal and then at the exciting wires, we obtain the impedance due to the presence of the metallic region. If the problem is solved for a plane surface without the crack, then the additional impedance due to the crack may be obtained by subtraction. Also, by solving for different positions of the wires representing the detection coils, we may obtain the impedance signal on traversing the crack and also the signal due to liftoff effects.

The model is illustrated in figure 1. The circles above the surface represent the wires, with + and - indicating the direction of the impressed current  $I_0 e^{-i\omega t}$ , where  $\omega$  is the angular frequency and  $t$  the time. The current is held at fixed amplitude  $I_0$ , according to the usual procedure for eddy-current NDE. In the figure additional parameters are shown:  $A$  is the separation between the wires,  $H$  is the height of the coil above the plane,  $P$  is the center position of the coil relative to the crack,  $D$  is the depth of the crack, and  $F$  is the half-width of the crack opening.

Because of the symmetry of this two-dimensional model, the electric and magnetic fields may be derived from a vector potential,  $A$ , which has only one component,  $A_z$  [5], where the  $z$ -direction is parallel to the wires and the crack. If the wires were not parallel to the crack, a full three-dimensional analysis would be

necessary. The vector potential is thus of the form  $A(x,y)e^{-i\omega t}$ , where  $A$  is complex to represent phase relations with respect to the exciting current.

In the region above the conductor the vector potential satisfies a Helmholtz equation. However, at the frequencies of eddy current testing the transit time for wave propagation across the region of the crack is negligibly small and a quasi-static approximation is satisfactory. Thus, in the region above the metal slab the vector potential satisfies the Laplace equation,

$$\nabla^2 A = 0, \quad (1)$$

except for the singularities at the wires. Below the surface, in the metallic region, the Helmholtz equation is obeyed,

$$(\nabla^2 + k^2)A = 0, \quad (2)$$

where

$$k^2 = i\sigma\omega\mu \quad (3)$$

is the square of the propagation constant,  $\sigma$  is the electrical conductivity, and  $\mu$  is the magnetic permeability. Here too, displacement currents are neglected, in this case because the ohmic currents represented by the  $k^2$  term are so much larger. At the boundary surface, including the faces of the crack, the

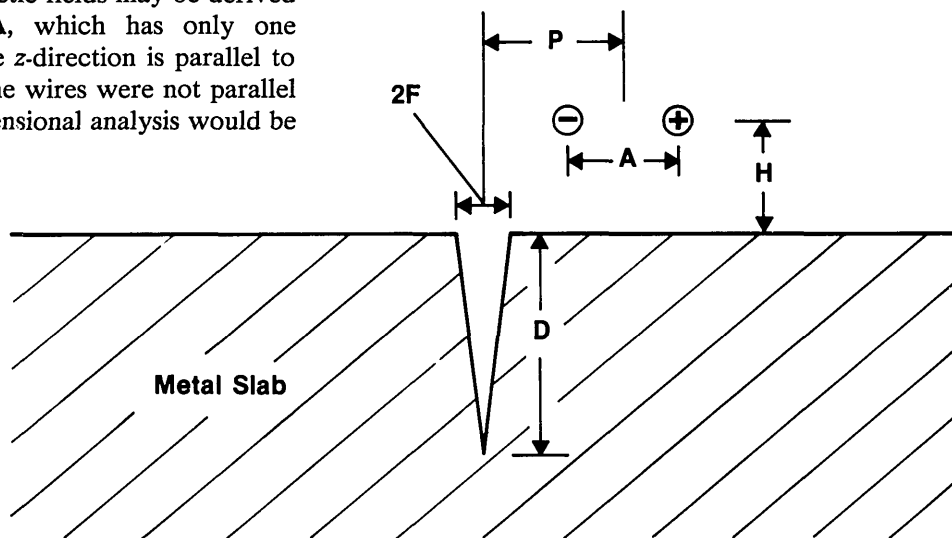


Figure 1—Configuration of model and parameters for the calculation of the impedance signal due to a crack.

- |           |                      |          |  |
|-----------|----------------------|----------|--|
| <b>D</b>  | <b>Crack Depth</b>   | <b>A</b> | <b>Wire Separation</b>                 |
| <b>2F</b> | <b>Crack Opening</b> | <b>H</b> | <b>Wire Elevation</b>                  |
|           |                      | <b>P</b> | <b>Wire Position Relative to Crack</b> |

usual conditions of continuity of tangential  $E$  and  $H$ , and normal  $B$  and  $D$  must hold. In terms of the vector potential, these conditions are equivalent to the continuity of  $A$  and  $1/\mu \partial A/\partial n$ , where  $\partial A/\partial n$  is the normal derivative of  $A$  at the interface. To summarize, the vector potential must satisfy the Laplace equation in the upper region, the Helmholtz in the lower region, and conditions of continuity at the interface, and it must approach the known form of the impressed field in the vicinity of the source wires.

The method of solution selected in this paper is an extension of the boundary integral equation (BIE) approach [6,7]. This method, usually applied to a single region, has been used by the author [2] in eddy-current problems involving excitation by a uniform ac field. In the present application the method leads to a pair of coupled Fredholm integral equations of the first kind, as follows:

By application of Green's theorem we express the vector potential in the upper region in terms of the source fields and the values of  $A$  and its normal derivative  $\partial A/\partial n$  on the bounding curve:

$$A(r) = \mathcal{S}(r) + \int \frac{\partial G(r, S')}{\partial n'} A(S') dS' - \int G(r, S') \frac{\partial A(S')}{\partial n'} dS' \quad (4)$$

in which  $dS'$  is an element of arc in a planar cross-section normal to the surface of the metal. In the above,  $\mathcal{S}$  is the vector potential due to the source wires as if the metallic region were absent. The two integrals give the change due to the induced currents below the boundary. They are taken over the boundary  $\hat{n}$  is the unit normal vector pointing out of the upper region. The remaining boundary closure at infinity makes no contribution since the fields decay with sufficient rapidity. Green's function for the Laplace operator is given by

$$G(r, r') = -1/2\pi \log|r-r'|; \quad (5)$$

it satisfies

$$\nabla^2 G(r, r') = -\delta(r-r'), \quad (6)$$

where  $\delta$  is the two-dimensional Dirac delta function. For the two-wire case treated in this paper, the source field  $S$  has the form

$$S(r) = I_0 [G(r, r_+) - G(r, r_-)],$$

where  $r_+$  and  $r_-$  are the positions of the wires which

carry the exciting current,  $I_0$ , parallel and anti-parallel to the z-direction, respectively. In the metallic region

$$A(r) = - \int \frac{\partial \mathcal{G}(r, S')}{\partial n'} A(S') dS' + \int \mathcal{G}(r, S') \frac{\partial A(S')}{\partial n'} dS', \quad (7)$$

where  $\mathcal{G}$  is now the two-dimensional Helmholtz Green's function,

$$\mathcal{G}(r, r') = (i/4) H_0^{(1)}(k|r-r'|), \quad (8)$$

where  $H_0^{(1)}$  is the Hankel function of the first kind, order zero. It, too, has a logarithmic singularity and satisfies the Helmholtz equation with a source,

$$(\nabla^2 + k^2) \mathcal{G}(r, r') = -\delta(r-r'). \quad (9)$$

This latter Green's function contains the complex  $k$  and represents a damped outgoing cylindrical wave at large values of  $r-r'$ . In eq (7) we have retained the same direction of the normal vector  $\hat{n}$ ; hence the unusual sign convention on the right hand side.

The BIE method prescribes letting  $r$  approach the surface to obtain the fields on the bounding surface. When we let  $r=S$ , a well-defined expression is obtained if we use the Cauchy principal values for the singular integrals and replace  $A$  on the boundary by  $A/2$ . For nonmagnetic materials  $A$  and  $\partial A/\partial n$  are both continuous across the boundary, and we shall so restrict the present calculations. The resulting BIE's are

$$\frac{1}{2}A(S) - \int \frac{\partial G(S, S')}{\partial n'} A(S') dS' + \int G(S, S') \frac{\partial A(S')}{\partial n'} dS' = \mathcal{S}(S) \quad (10)$$

$$\frac{1}{2}A(S) + \int \frac{\partial \mathcal{G}(S, S')}{\partial n'} A(S') dS' - \int \mathcal{G}(S, S') \frac{\partial A(S')}{\partial n'} dS' = 0 \quad (11)$$

This is a coupled pair of equations for unknowns  $A(S)$  and  $\partial A(S)/\partial n$  on the interface. We may look on the

inhomogeneous term  $\mathcal{S}(S)$  as the driving force for the system. When  $A$  and  $\partial A/\partial n$  are found on the boundary, then the field  $A$  may be constructed at any point above the interface by application of eq (4), or below the interface by application of eq (7).

The ultimate objective is the determination of the impedance per unit length induced in the wires by the presence of the metallic region. The time-average of the power per unit length delivered by the exciting wires is given by the complex expression

$$P = \frac{1}{2} \int E' \cdot J^* da,$$

where  $J$  is the (constant) current density in the wires,  $E'$  is the electric field at the wires produced by the induced currents, and  $da$  is an element of cross-sectional area normal to the wires.  $E'$  is derived from the vector potential  $A'$  of the induced currents,

$$A' = A - \mathcal{S},$$

by the usual relation

$$E' = i\omega A'.$$

Hence, for a set of idealized line-wires, denumerated by the index  $i$ , we have

$$P = \frac{1}{2} \sum I_i^* i\omega A'_i.$$

Connection with conventional circuit parameters can be made by expressing  $P$  in terms of the currents, voltages per unit length, and impedance per unit length of the wires. Under the constant current assumption of eddy current testing, we have

$$P = \frac{1}{2} \sum V_i I_i^* = \frac{1}{2} \sum I_i I_i^* Z_i,$$

where  $V_i$  is the voltage per unit length induced in the  $i$ th wire and  $Z_i$  is the extra impedance in the  $i$ th wire due to induced currents in the metallic region. Finally we obtain

$$Z_i = i\omega A'_i / I_i,$$

for the impedance per unit length in the  $i$ th wire, caused by the induction. Now  $A_i$  is evaluated at the  $i$ th wire and can be computed by use of Green's theorem after  $A$  and  $\partial A/\partial n$  have been found on the interface. Thus we have a method of computing the extra impedance seen by each wire due to the presence of the metal below. These impedances may now be calculated with and without a crack being present.

### 3. Numerical Treatment

The coupled integral equations are solved by an application of the method of moments [8]. The solution is expressed as a linear combination of a finite set of basis functions with unknown coefficients. The coefficients are determined by requiring that the integral equations be satisfied at a number of points equal to the number of unknown coefficients; i.e., point-matching is used.

For the basis functions, the elements  $F$  shown in figure 2 were used, after the method of Harrington [8].

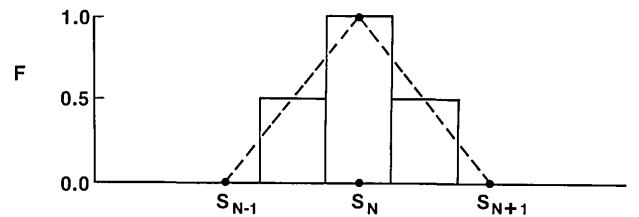


Figure 2—Triple-pulse hat function  $F$  used in the numerical calculations. The illustration shows the function  $F(S-S_n)$ . The dashed line is the common triangular hat-function.

We approximate the solution for the vector potential and its normal derivative on the interface by the finite sums:

$$A(S) = \sum A_i F(S-S_i) \quad (12)$$

and

$$\frac{\partial A(S)}{\partial n} = \sum N_i F(S-S_i) \quad (13)$$

These expansions are introduced into the integral equations, eqs (10) and (11). The integration over each element is carried out by use of the midpoint rule for the entire integrand of each flat section of the fundamental element, except when the Green's function is singular, i.e., when  $S_i = S_j$ .

When a singular integrand occurs in the evaluation of eq (10), the integration of the logarithmic Green's function is performed exactly. When a singular integrand occurs in eq (11), the dominant logarithmic part of the Hankel function is used for the evaluation.

The width of the elements is not restricted. It was found practical to use a fine grid where the solution

was large or varying rapidly, and a coarse grid elsewhere. With these approximations and the point-matching, the coupled integral equations are reduced to a linear algebraic system of the form:

$$\sum \left[ \frac{1}{2} \delta_{ij} - \left( \frac{\partial G}{\partial n} \right)_{ij} \right] A_j + \sum G_{ij} \left( \frac{\partial A}{\partial n} \right)_j = \mathcal{S}_i \quad (14)$$

$$\sum \left[ \frac{1}{2} \delta_{ij} + \left( \frac{\partial G}{\partial n} \right)_{ij} \right] A_j - \sum \mathcal{S}_{ij} \left( \frac{\partial A}{\partial n} \right)_j = 0 \quad (15)$$

In these equations, each doubly-subscripted term corresponds to that part of the integrations of eqs (10) and (11) connecting element  $j$  and matching-point  $i$ .

The calculations were first attempted with square pulse functions as the basis set. It was found that the solutions were unstable in the vicinity of the crack corners and near the location of a grid-size change. The use of the triple pulse element is equivalent to doubling the number of points in a pulse function calculation, but applying the constraint that the solution at each point be averaged with its two nearest neighbors. In addition to reducing the dimensions of the needed matrices, this has a smoothing effect and leads to solutions which are stable as the grid size is decreased. The triple pulse basis function may be looked upon as an approximation to the common triangular hat-function, shown in figure 2 by the dashed line. The hat-function yields a piecewise trapezoidal approximation to the solution which would be superior to the present form, but its application is precluded because of nonintegrability

when multiplied by the Hankel functions of the integrand. The solution of the linear equations was obtained by Gaussian elimination without pivoting. The logarithmic singularities of the Green's functions associated with the diagonal elements of the matrices allow this economical simplification. The solutions were considered to have converged when further refinement produced an insignificant change in the physical results, usually about 1 percent. Typically the dimension of the square matrices ranged from 200 to 300.

#### 4. Coil Impedance in the Absence of a Crack

The radiation field of an oscillating dipole above a conducting earth was a problem first attacked successfully by Sommerfeld [9]. Analytical solutions have been given for finite coils by Dodd *et al.* [10,11]. These solutions are in the form of integrals over various Bessel function arguments. Numerical evaluation is possible; analytic evaluation is in terms of asymptotic series. The same methods can be applied to this problem of a pair of parallel wires over a plane. However, the approach of this publication is readily applicable in the absence of a crack. Solving an integral equation requires a greater computing effort than evaluating an integral solution for the lesser problem. However, it is quite useful to have the programs available as a byproduct of the crack case. In this section we examine the results of calculations for the parallel wire coil above a flat conducting half-space, calculated by the boundary integral equation method.

In figure 3 we show the results of a typical calculation. For this case, and all others reported here,

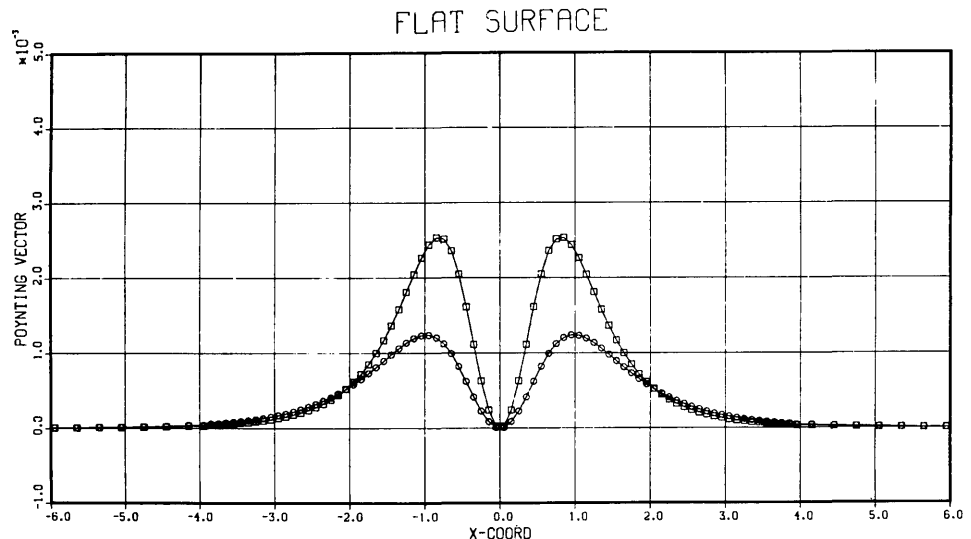


Figure 3—Poynting vector on the surface of a metallic slab in the absence of a crack. The coordinate  $x$  is along the flat surface of the metal. Distances are in units of the skin-depth and the Poynting vector is in units of  $\mu_0 \omega 10^{-3}$ . The exciting wires are located at  $\pm 0.5 \delta$  and are at an elevation of  $0.5 \delta$ .

lengths are in units of the skin depth  $\delta$ , where

$$\delta = \sqrt{2/\sigma\omega\mu_0}, \quad (16)$$

and the symbols under the radical are the same as before. The complex Poynting vector  $\bar{S}$ , represents the time average of the complex energy flux, in our application, across the surface of the conductor. In the units we are using, we have

$$\begin{aligned} \bar{S} &= \frac{1}{2} \bar{E} \times H^* \\ &= -\frac{i}{2} \frac{\mu_0\omega}{\delta} \left| I_0 \right|^2 A \frac{\partial A^*}{\partial n'}, \end{aligned} \quad (17)$$

where  $A$  and  $\partial A/\partial n'$  are calculated by solving the coupled boundary integral equations. While our principal interest is in the impedance change of the exciting wires, the Poynting vector plots show a detailed picture of the radiation field. The plots are useful for assessing the convergence of the calculations as well as for showing the regions of the test material where the significant absorption and field penetration take place.

## 5. Coil Impedance With a Crack

The presence of the crack adds two more parameters to the required inputs to the calculation. We treat only a symmetric v-groove crack which we specify by its depth and the half-width at its mouth. The calculations are performed in the same way as without the crack, with the only difference being that

the needed matrices are larger in dimension and somewhat more complex in preparation. The algorithms for the solution are identical to those of the previous case. The output of the program is the impedance per unit length of the wires, with the crack present. In addition we may inspect the complex Poynting vector on the surface of the crack as well as on the flat surface of the test material.

For the initial investigations we selected a crack depth of  $2.0 \delta$  and an opening of half-width  $0.25 \delta$ . The coil wires were taken as having a separation of  $1.0 \delta$  and at an elevation of  $1.0 \delta$  above the plane. These dimensions correspond to the physical situation of a No. 30 AWG wire insulated pair in close contact, elevated one radius above the contact with the plane, and driven at a frequency of 110 kHz. The relevant parameters for this model applied to aluminum are given in table 1.

Table 1. Parameters for model calculation based on aluminum at 110 kHz.

Resistivity	$\rho$	$2.82 \times 10^{-8} \Omega \cdot m (20^\circ C)$
Conductivity	$\sigma (= 1/\rho)$	$3.54 \times 10^7 \Omega^{-1} m^{-1}$
Skin depth	$\delta$	0.255 mm
Crack depth ( $= 2\delta$ )		0.51 mm
Crack half-opening ( $\delta/4$ )		0.064 mm
Wire radius ( $\delta/2$ )		0.13 mm

The calculations were performed for a range of values of the parameter  $P$ , the location of the coil center relative to the crack. Figures 4, 5, and 6 show the Poynting vector for the values  $P=2.5 \delta$ ,  $0.5 \delta$ , and  $0.0$

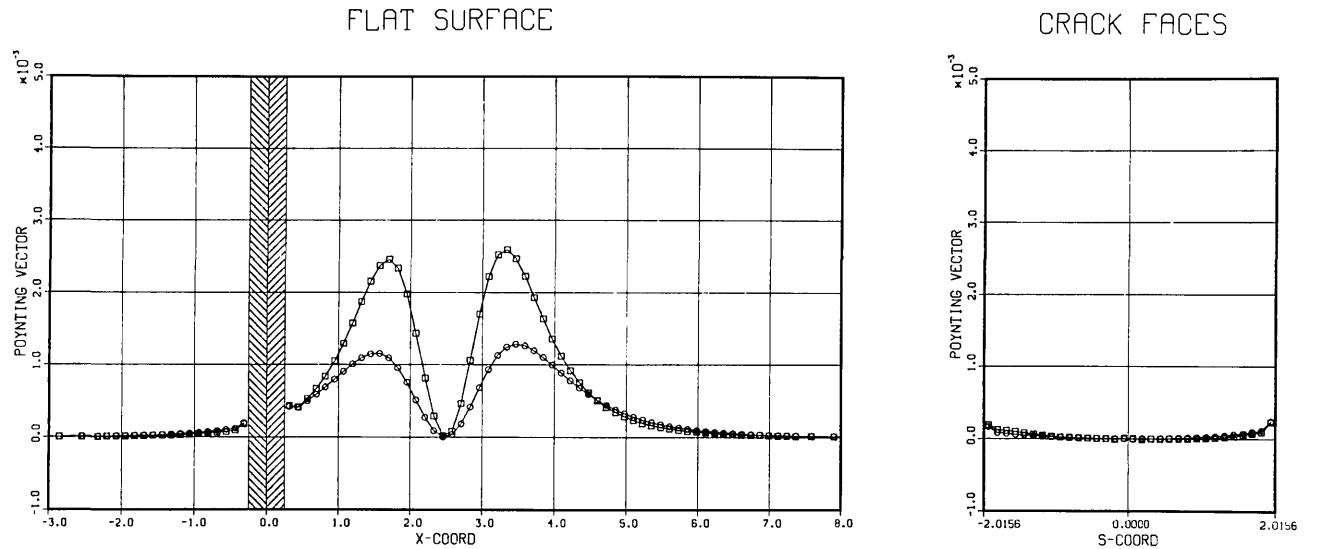


Figure 4—Poynting vector on the surface of a metallic slab with a crack. The coordinate  $S$  is along the faces of the crack, which is shown as folded open in the right-hand figure. The shaded band indicates the location of the v-groove crack. The lateral distance between the coil and the crack,  $P$ , is  $2.0 \delta$  and the half-opening,  $F$ , is  $0.25 \delta$ . All other parameters are as in figure 3.

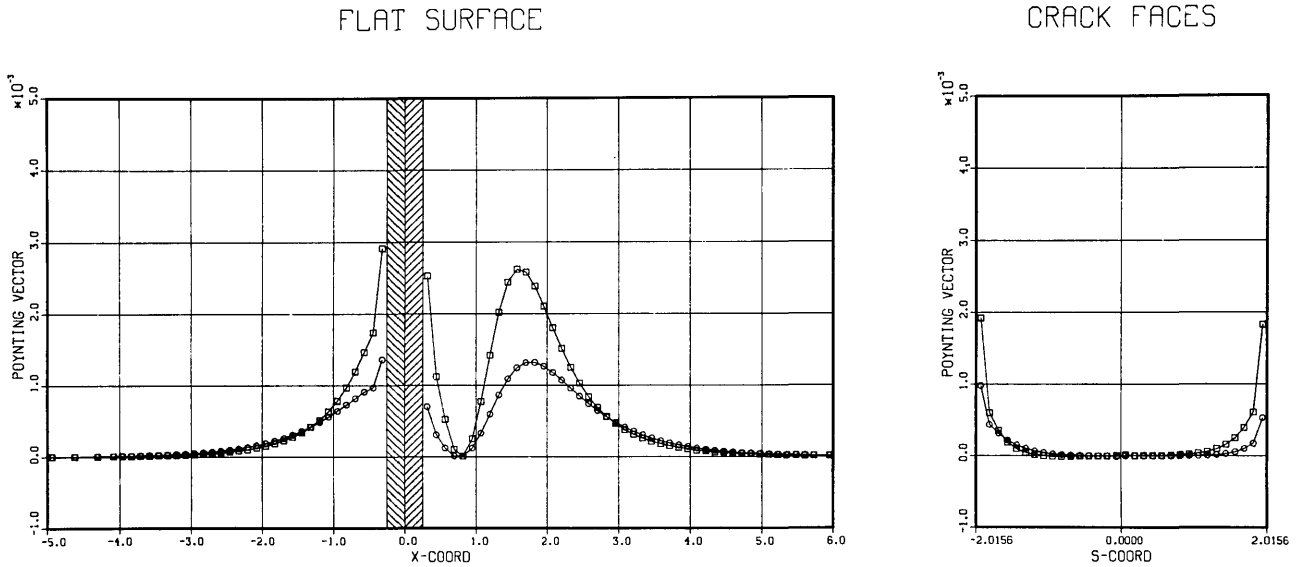


Figure 5—Poynting vector on the surface of a metallic slab with a crack. The lateral distance between the coil and the crack,  $P$ , has the value of  $0.80 \delta$ ; all other parameters are as in figure 4.

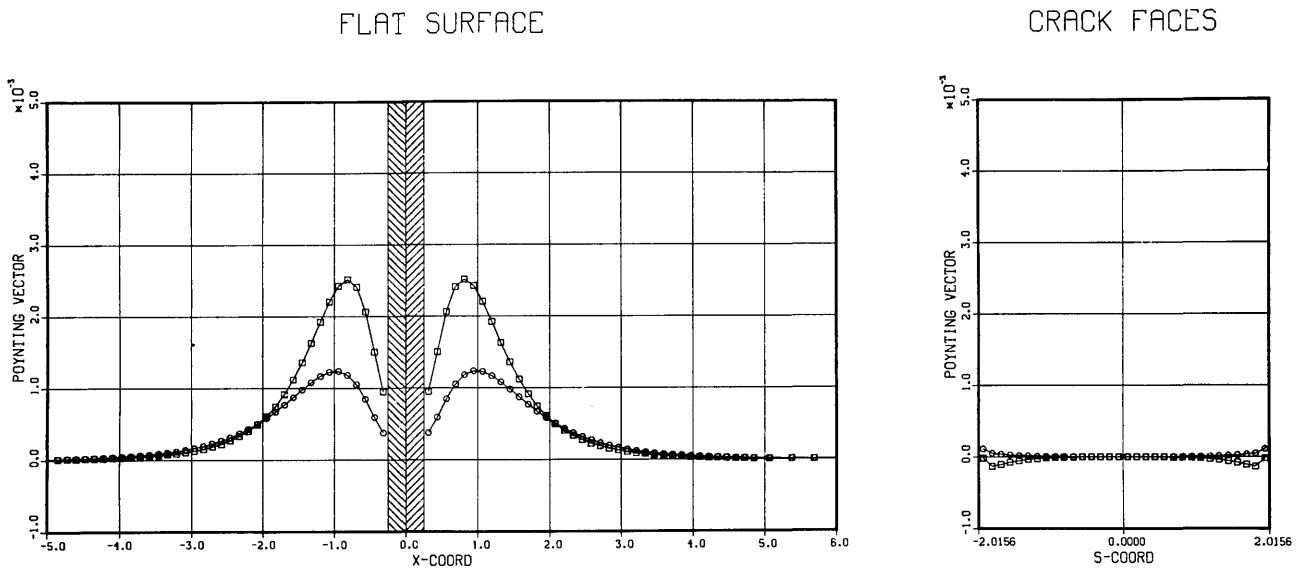


Figure 6—Poynting vector on the surface of a metallic slab with a crack. The lateral distance between the coil and the crack,  $P$ , has the value  $0.0 \delta$ ; all other parameters are as in figure 4.

$\delta$  respectively, illustrating the deformation of the fields as the coil is brought up to the crack. These figures correspond to the same wire separation and elevation as in figure 3, the case with no crack.

Qualitative examination of the figures shows that in the presence of a crack, a portion of the integrated Poynting flux is “stolen” from the nearer of the peaks in the field distribution. The Poynting flux at the corners is somewhat increased over the value that would occur at that position if no crack were present.

Inside the crack, the Poynting flux decays to zero in approximately one skin-depth. This is quite the opposite behavior to that which occurs in the case of a uniform  $H$ -field parallel to the crack [2]. In that case, the Poynting vector is greatest at the tip and vanishes at the corners.

From a series of calculations like these, the coil impedance per unit length was obtained for numerous positions of the coil. The phase and magnitude of the impedance are shown in the plots of figure 7, in the

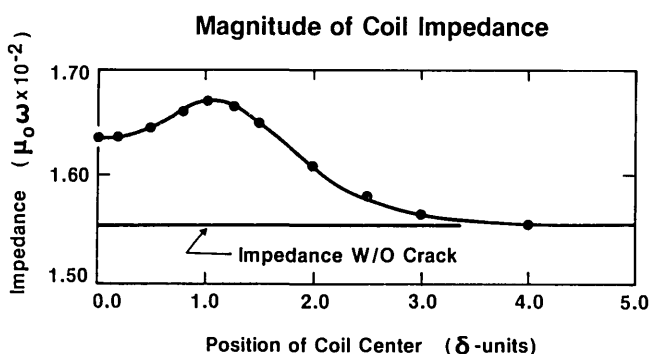
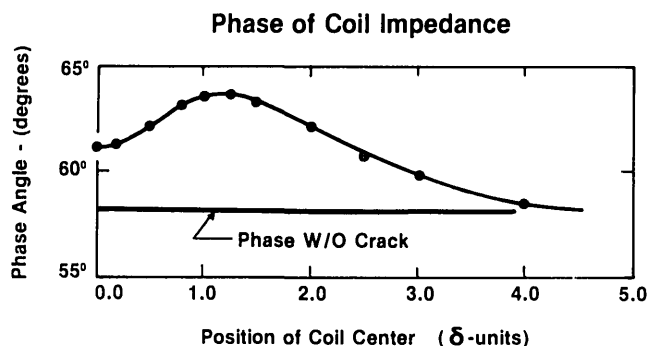


Figure 7—Plots of the phase and magnitude of the crack impedance signal as a function of the lateral displacement of the coil center relative to the crack. Parameters are as in figure 4.

form of a scan across the surface of the slab. These curves would be extended symmetrically for negative values of the coil displacement. The asymmetric signal obtained from an opposed pair of coils [12] can be

obtained from these curves by computing a differential scan corresponding to the coil pair separation.

The author wishes to express his thanks to Dr. B. Auld and Dr. C. Fortunko for most valuable discussions concerning crack detection. He is also grateful to Dr. S. Gershovits for interesting suggestions.

## References

- [1] Kahn, A. H.; Spal, R.; Feldman, A. *J. Appl. Phys.* **48**, 4454 (1977).
- [2] Kahn, A. H. in *Review of Progress in Quantitative Nondestructive Evaluation 1*, D. O. Thompson and D. E. Chimenti, eds., Plenum Press, New York, NY, p. 369.
- [3] Ida, N.; Lord, W. *IEEE Computer Graphics and Appl.* **3**, 21 (1983).
- [4] *Review of Progress in Quantitative Nondestructive Evaluation 2*, D. O. Thompson and D. E. Chimenti, eds., (1983).
- [5] Landau, L. D.; Lifshitz, E. M. *Electrodynamics of Continuous Media*, Pergamon Press, New York, NY (1960), p. 121.
- [6] Rizzo, F. J. in *The Boundary-Integral Equation Method: Computational Applications in Applied Mechanics*, T. A. Cruse and F. J. Rizzo, eds., American Society of Mechanical Engineers, 1975, p. 1.
- [7] Jaswon, M. A.; Symm, G. T. *Integral Equation Methods in Potential Theory and Electrostatics*, Academic Press, London (1977).
- [8] Harrington, R. F. *Field Computation by Moment Methods*, Macmillan, New York, NY (1968).
- [9] Sommerfeld, A. *Partial Differential Equations in Physics*, Academic Press, New York, NY (1949), p. 236 *et seq.*
- [10] Dodd, C. V.; Deeds, W. E. *J. Appl. Phys.* **39**, 2829 (1968).
- [11] Dodd, C. V.; Deeds, W. E.; Luquire, J. W. *Int. J. Nondestructive Testing* **1**, 29 (1969).
- [12] Fortunko, C. M.; Padget, S. A. *Technical Activities 1982*, Office of Nondestructive Evaluation, NBSIR 82-2617, p. 57 *et seq.*

# Theory of Acoustic Emission From Phase Transformations

J. A. Simmons and H. N. G. Wadley  
National Bureau of Standards, Washington, DC 20234

Accepted: December 1, 1983

A theoretical framework is developed within which it is possible to predict the dynamic elastic displacement field (acoustic emission) for a phase transformation in which there is a change of both crystal structure (elastic constants) and shape (density). An integral equation is presented for the acoustic emission displacement field due to formation of inhomogeneous inclusions. This integral equation is solved by expressing the source in multipolar form and using the Eshelby equivalent inclusion method to estimate the dynamic multipolar coefficients. Expressions for the source of elastic radiation are explicitly calculated for small isotropic spherical and ellipsoidal inclusions embedded in an isotropic matrix. These expressions are used for qualitative interpretation of recent experiments on martensitic transformations in steels and for identifying the information that may be deduced about transformation dynamics from quantitative measurements of acoustic emission.

Key words: acoustic emission; martensitic phase changes; twinning.

## 1. Introduction

Acoustic emission (AE) is the term used for the elastic waves generated by abrupt localized changes of stress in a solid [1]<sup>1</sup>. The waves propagate from the source of stress change to cause transient (nano-millisecond) surface displacements of a sample. These transient displacements may be detected with ultrasonic transducers and are known as acoustic emission. Acoustic emission is then a method for observing rapid dynamic material processes with elastic waves. The slower, quasi-static changes of stress are not usually considered sources of acoustic emission even though their surface displacements are incorporated (as a limiting case) in theoretical formulations of acoustic emission [2]. These static displacements, normally measured with extensometers, are the basis of routine mechanical property measurements.

Acoustic emission has begun to be extensively explored as a tool for the investigation of the micromechanisms of deformation and fracture during mechanical testing [3]. It has also found increasing application as a nondestructive evaluation (NDE) technique for detecting and locating flaws in mechanical structures that are subjected to stress and the premature failure of which would have catastrophic consequences [4]. More recently, it is being considered a candidate technique for in-situ monitoring of materials processing because acoustic emission signals are emitted through some of the mechanisms by which a material responds to process variables [5]. These mechanisms may include both benign processes (e.g., phase transformations) and malevolent processes (e.g., cracking).

---

**About the Authors, Paper:** J. A. Simmons is a research mathematician and H. N. G. Wadley a metallurgist in the NBS Center for Materials Science. The work on which they report was supported by the Defense Advanced Research Projects Agency under DARPA Order No. 4275.

---

<sup>1</sup> Figures in brackets indicate the references at the end of this paper.

It has been speculated that the measurement of acoustic emission from benign mechanisms during materials processing could provide much needed in situ information about materials processing. There is current interest in using this information in tandem with recently developed process models to develop improved feedback-controlled systems for materials processing. (The malevolent mechanisms of acoustic emission, e.g., cracking, have already received and continue to attract attention as potential quality control indicators [6]).

As an example of the possible use of AE for phase transformation monitoring, consider some system where above a temperature  $T_1$  phase A is the stable phase and below  $T_1$  phase B is stable. Then, for  $T < T_1$  material composed of the A-phase may lower its free energy by undergoing a phase change to B. Usually, the new phase has a different crystal structure so that there are changes of elastic modulus and density as well as a shape change associated with the rearrangement of atoms in the transforming volume. These changes may generate acoustic emission or internal stresses which give rise to local plastic flow and subsequent acoustic emission. If a transducer is used to detect the acoustic emission from such phase transformations, useful information may be obtained about the temperature, pressure, etc. at which the phase change occurred [7]. Furthermore, the dynamics and crystallography of the phase change are also contained—convolved with the sample and instrumentation impulse response—in the signal. The use of appropriate analysis methods may enable the measurement of hitherto unobserved aspects of phase changes. Such measurements would, because of the passive nature of this monitoring technique, emanate from phase changes unmodified by our attempts to observe them.

The majority of phase transformations occurs at a rate controlled by diffusion. This, unfortunately, is sufficiently slow (compared with the time for elastic waves emitted by the transformation to communicate with the sample boundaries) that no detectable acoustic emission is observed. Thus, diffusion-controlled phase changes, while often resulting in significant stress changes, cause mainly quasi-static surface displacement and no direct acoustic emission (as is usually the case with bainite and pearlite formation during cooling of low alloy steels [8]). In these cases acoustic emission is not a viable candidate for microstructure control during processing.

There is, however, an important class of phase transformations for which atomic diffusion is not rate controlling. These include the martensitic transformations in which the change of crystal structure is accommodated by a so-called “diffusionless” shear transformation. Diffusion, if it occurs, is over a very short range; of the order of the lattice parameter. The velocity at which the transformation may propagate varies enormously from one alloy to the next, but in some systems velocities of  $\sim 1000 \text{ ms}^{-1}$  have been reported [9]. This implies that the formation of a typical  $30 \mu\text{m}$  length of martensite in some alloys is formed in as little as 30 ns. In this time, elastic waves only propagate  $\sim 0.1 \text{ mm}$  and transient sample displacements are observed [8,10] as the sample returns to mechanical equilibrium.

Despite the reporting by several workers [8,10] of intense acoustic emission during some martensitic transformations, effects of micromechanism (transformation velocity, volume, etc.) upon acoustic emission have not been studied. Even during the simpler processes of deformation twinning, there have only been a few tentative correlations made between micromechanism and acoustic emission signal [11,12]. A part of the problem has been the absence of a rigorous theory relating the properties of the dynamic elastic wavefield (acoustic emission radiation) to the dynamics and crystallography of atomic motions during phase transformation or twin growth. It is our purpose here to begin to apply recently developed elastodynamic techniques to the prediction of acoustic emission signals from phase changes and twinning.

## 2. Theoretical Framework

Consider an idealized transformation to consist of a small region of phase A (with density  $\rho$  and elastic moduli  $C$ ) undergoing a change of crystal structure to form a region of phase B with a density  $\rho + \Delta\rho$  and elastic moduli  $C + \Delta C$ . We assume that if the region B could be cut out of the

matrix, its shape would be determined by a linear transformation  $\beta^*$  applied to the original region of phase A. In elastodynamics, a transformation involving both a change of moduli and shape is referred to as an inhomogeneous inclusion. The calculation of the dynamic elastic wavefield for the inhomogeneity problem is complicated by:

- Coupling of the wavefields from density and modulus changes.
- Internal reflection and mode conversion of elastic waves at the inhomogeneity boundary.
- Doppler effects for high transformation velocity ( $\gtrsim 20\%$  speed of sound).

We find the acoustic emission from inhomogeneous inclusions by recourse to certain simplifying assumptions. We make the assumption that the inhomogeneity is small in comparison with the wavelengths of interest.<sup>2</sup> Thus, reverberations within the inhomogeneity are at frequencies above those of interest. It is also assumed that the linear velocity at which the transformation progresses through the austenite is  $\lesssim 20\%$  of the shear wave speed so that a sub-sonic approach may be used. Complications, such as transformation stress induced plastic deformation, twinning of martensite, autocatalytic phenomena, and polycrystalline anisotropy of the matrix are, for the present, put aside.

The theoretical framework we use is based upon the equivalent inclusion problem studied by Eshelby [13] and applied first to acoustic emission by Simmons and Clough [14]. As our starting point we use eq (A32) from ref. [14] to express the farfield elastic displacement field for an ellipsoidal inhomogeneity undergoing a self-similar (constant aspect ratio) change of shape. The ellipsoid volume is  $V_\Omega(t)$  where  $\Omega(r)$  denotes the region transformed ( $\Omega$  has the value one inside the inhomogeneity and zero elsewhere), as shown in figure 1.

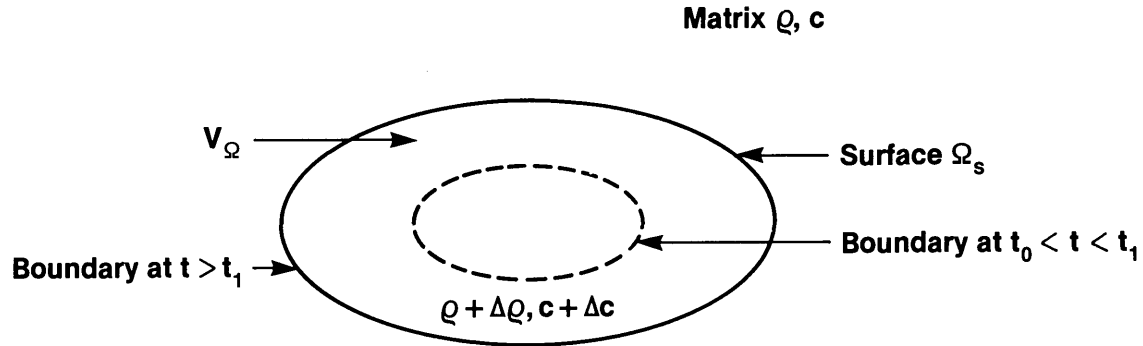


Figure 1—An ellipsoidal inhomogeneity undergoing a self-similar change of shape.

An elegant and simple way to consider the phase transformation problem is to generalize the stress and strain tensors to contain both space and time coordinates. We thus have four dimensional stress and strain tensors:

$$[\sigma_{\bar{ij}}] = \begin{bmatrix} \sigma_{11} & \sigma_{12} & \sigma_{13} & -\rho v_1 \\ \sigma_{21} & \sigma_{22} & \sigma_{23} & -\rho v_2 \\ \sigma_{31} & \sigma_{32} & \sigma_{33} & -\rho v_3 \end{bmatrix} \quad \text{and} \quad [u_{i\bar{j}}] = \begin{bmatrix} u_{1,1} & u_{1,2} & u_{1,3} & v_1 \\ u_{2,1} & u_{2,2} & u_{2,3} & v_2 \\ u_{3,1} & u_{3,2} & u_{3,3} & v_3 \end{bmatrix}$$

<sup>2</sup> We believe this to be reasonable. For example, if a region  $10 \mu\text{m}$  in dimension transforms, its fundamental resonance frequency will be  $\sim 300 \text{ MHz}$ . The upper frequency of acoustic emission measurement is normally  $\lesssim 10 \text{ MHz}$ .

where  $v_i$  is the velocity in direction  $x_i$  and  $\rho v_i$  is dynamic momentum. A hat ( $\hat{\phantom{x}}$ ) above a subscript indicates the subscript runs from 1 to 4 where 4 represents the time dimension. The four dimensional stiffness is denoted in the matrix by:

$$\sigma_{ij} = C_{ijkl} u_{k,l} \quad \text{for } i, j, k, l = 1, 2, \text{ and } 3$$

and

$$C_{i\hat{j}k\hat{l}} = C_{i4k\hat{l}} = -\rho \delta_{4\hat{j}} \delta_{ik}.$$

For the inhomogeneity it is denoted by:

$$\sigma_{ij} = (C + \Delta C)_{ijkl} u_{k,l} \quad \text{for } i, j, k, l = 1, 2, \text{ and } 3$$

and

$$(C + \Delta C)_{i\hat{j}k\hat{l}} = (C + \Delta C)_{i4k\hat{l}} = -(\rho + \Delta\rho) \delta_{4\hat{j}} \delta_{ik}$$

We use the fact that the difference in moduli ( $\Delta C$ ) between the inhomogeneity and surrounding matrix is constant over  $\Omega(t)$  to write eq (A32) in the form:

$$\begin{aligned} u_m(\vec{r}, t) = & -\int \int G_{mi,j}(\vec{r}, \vec{r}', t-\tau) \Delta C_{ijkl} u_{k,l}(\vec{r}', \tau) \Omega(\vec{r}', \tau) d\vec{r}' d\tau & \text{Term 1} \\ & + \int \int G_{mi,4}(\vec{r}, \vec{r}', t-\tau) \Delta \rho u_{k,4}(\vec{r}', \tau) d\vec{r}' d\tau & \text{Term 2} \\ & + \int \int G_{mi,j}(\vec{r}, \vec{r}', t-\tau) (C + \Delta C)_{ijk\hat{l}} \beta_{k\hat{l}}^*(\vec{r}', \tau) \Omega(\vec{r}', \tau) d\vec{r}' d\tau & \text{Term 3} \\ & - \int \int G_{mi,j}(\vec{r}, \vec{r}', t-\tau) \Delta C_{ijk\hat{l}} \beta_{k\hat{l}}^\circ(\vec{r}', \tau) d\vec{r}' d\tau & \text{Term 4} \end{aligned} \quad (1)$$

where:

$u_m(\vec{r}, t)$  is the displacement at  $\vec{r}$  as a function of time in direction  $x_m$  (valid both inside and outside the inhomogeneity).  $G_{mi}(\vec{r}, \vec{r}', t)$  is the dynamic elastic Green's tensor representing the displacement at  $\vec{r}$  in direction  $x_m$  as a function of time ( $t$ ) due to the application of a force impulse in direction  $x_i$  at  $(\vec{r}', 0)$ . The subscript,  $j$ , denotes partial differentiation with respect to the  $x_j$  coordinate.  $\vec{\beta}^\circ$  is the pre-existing elastic distortion and  $\beta^*$  the stress-free strain for the transformation; in the phase change problem, the term  $\beta_{ik}^*$  (the "plastic velocity" component which contributes to shape change emission but not that due to momentum) is taken to be zero. The new elastic distortion is  $\vec{\beta}^\circ + \vec{\beta}^T - \vec{\beta}^*$  where  $\vec{\beta}^T$  is the total distortion (elastic and plastic).

In eq (1), the acoustic emission is given by the change of stress:

$$\begin{aligned} \Delta \sigma(\vec{r}, t) &= (C + \Delta C)(\vec{\beta}^\circ + \vec{\beta}^T - \vec{\beta}^*) - C \vec{\beta}^\circ \\ &= \begin{cases} (C + \Delta C)(\vec{\beta}^T - \vec{\beta}^*) + \Delta C \beta^\circ & \text{for } \Omega(\vec{r}, t) = 1 \\ C(\vec{\beta}^T - \vec{\beta}^*) & \text{for } \Omega(\vec{r}, t) = 0 \end{cases} \end{aligned} \quad (2)$$

It can be seen in eq (1) that the acoustic emission arises from changes associated with the stress-

It can be seen in eq (1) that the acoustic emission arises from changes associated with the stress-free strain (term 3), and the interaction of the change in modulus with the pre-existing strain (term 4). These sources act upon the modulus changes (static and dynamic) to create further changes (terms 1 and 2). It should be clear that eq (1) is very general and describes both the acoustic emission of the phase transformation and the scattering of elastic waves ( $\vec{\beta}^{\circ}$  now time varying) from inhomogeneities.

A difficulty with eq (1) is that the Green's tensor depends upon  $\vec{r}-\vec{r}'$ . Thus, a different Green's tensor must be used between each source point and the receiver. To overcome this problem we approximate the solution to eq (1)—for inhomogeneous transformations of fixed magnitude in the presence of a relatively constant applied stress—by the use of multipolar expansions. These simplify the dependence of the Green's tensor on  $\vec{r}-\vec{r}'$ . If the source is small in size ( $\lesssim 20\%$  of the shortest wavelength of interest) there is only a small error associated with using a multipolar expansion obtained by representing the Green's tensor in a Taylor's series about  $\vec{r}'_0$ , the centroid position. In this exposition we retain only the first term in the expansion, but higher order terms can easily be incorporated. Equation (1) then becomes:

$$\begin{aligned}
u_m(\vec{r},t) = & -\Delta C_{ijkl} \int_{t_0}^{t_1} G_{mi,j}(\vec{r},\vec{r}'_0,t-\tau) \left[ \int_{\Omega} u_{k,l}(\vec{r}',\tau) d\vec{r}' \right] d\tau \\
& + \Delta\rho \int_{t_0}^{t_1} G_{mi,j}(\vec{r},\vec{r}'_0,t-\tau) \left[ \int_{\Omega} u_{k,4}(\vec{r}',\tau) d\vec{r}' \right] d\tau \\
& + \int_{t_0}^{t_1} G_{mi,j}(\vec{r},\vec{r}'_0,t-\tau) \left[ (C+\Delta C)_{ijkl} \int_{\Omega} \beta_{k,l}^*(\vec{r}',\tau) d\vec{r}' - \Delta C_{ij\kappa\lambda} \int_{\Omega} \beta_{\kappa\lambda}^{\circ}(\vec{r}',\tau) d\vec{r}' \right] d\tau
\end{aligned} \quad (3)$$

In terms of the Heaviside Green's tensor  $G^H$  (displacement at  $\vec{r},t$  due to a stepfunction in force at  $\vec{r}',0$ ) we can express eq (3) as:

$$\begin{aligned}
u_m(\vec{r},t) = & -\int_{t_0}^{t_1} G_{mi,j}^H(\vec{r},\vec{r}'_0,t-\tau) \left[ \frac{d}{dt} \Delta C_{ijkl} \int_{\Omega} u_{k,l}(\vec{r}',\tau) d\vec{r}' \right] d\tau \\
& + \int_{t_0}^{t_1} G_{mi,4}^H(\vec{r},\vec{r}'_0,t-\tau) \left[ \frac{d}{dt} \Delta\rho \int_{\Omega} u_{k,4}(\vec{r}',\tau) d\vec{r}' \right] d\tau \\
& + \int_{t_0}^{t_1} G_{mi,j}^H(\vec{r},\vec{r}'_0,t-\tau) \frac{d}{dt} \left[ (C+\Delta C)_{ijkl} \int_{\Omega} \beta_{k,l}^*(\vec{r}',\tau) d\vec{r}' - \Delta C_{ij\kappa\lambda} \int_{\Omega} \beta_{\kappa\lambda}^{\circ}(\vec{r}',\tau) d\vec{r}' \right] d\tau
\end{aligned} \quad (4)$$

Equations (3) and (4) have the physical interpretation that the acoustic emission at  $\vec{r},t$  is obtained from a dynamic multipolar source (in our truncated expansion considered dipolar) at the inhomogeneous inclusion. When an inhomogeneity is present, the magnitude of the source has a "feedback" component on the right hand side of the equation. It is this feedback component that complicates the inhomogeneity problem.

The solution to this integral equation is still not possible unless recourse is made to a final simplifying approximation. The one commonly used in scattering problems, the Born approximation, consists of replacing  $\vec{u}$  on the right hand side of eq (1) or eq (4) with the values of  $\vec{u}$  obtained from eq (1) without terms 1 and 2 (the homogeneous problem). We feel this weak scattering approximation is less appropriate here because of the large differences in modulus that may occur between the inhomogeneity and matrix.

Once it is recognized that the source appears to be a force multipole located at the centroid of the inclusion, we can use information about the static case and the assumption of ellipsoidal shape, which has not yet been needed to approximate the value of the source strength. To understand how we apply such a quasi-static approximation, consider a point outside but near the ellipsoid  $\Omega$ . Suppose we were to stop the growth of the inhomogeneity at some time  $t^*$ . Then, after a short time, the longitudinal and transverse wavefronts generated by the dipole before  $t^*$  would pass through the point and from then on the point would only experience the static displacement associated with the presence of a static multipolar force combination.<sup>3</sup> Thus, the multipolar density  $\vec{M}(t, t^*)$  describing the dynamic motion must be consistent with that of the static case,  $\vec{M}^\infty(t^*)$ , i.e.:

$$\lim_{t \rightarrow t_1} \vec{M}(t, t^*) = \vec{M}^\infty(t^*)$$

where it is assumed that  $t_1$  is sufficiently greater than  $t^*$  that the process “comes to rest.” The physical distinction between  $\vec{M}(t, t^*)$  and  $\vec{M}^\infty(t^*)$  arises from the feedback effects of the growth dynamics and multiple reflections within the ellipsoid. We shall ignore these dynamic feedback effects and correct only for those feedback effects produced by the static component of the dipole field.<sup>4</sup>

To obtain the static correction, i.e. the value of  $\vec{M}^\infty(t^*)$ , we know that  $\vec{\beta}^*$  has a fixed value throughout  $\Omega(t)$ . We assume  $\vec{\beta}^\circ$  to be fixed and constant in the region of  $\Omega(t)$  and recall that  $\vec{G}^\infty(\vec{r}, \vec{r}_0) = \lim_{t \rightarrow \infty} \vec{G}^H(\vec{r}, \vec{r}_0, t)$ . Then, we replace  $\vec{G}^H$  by  $\vec{G}^\infty$  in eq (4) and integrate the source terms with respect to time to give:

$$u_m^\infty(\vec{r}, t) = G_{mi,j}^\infty(\vec{r}, \vec{r}_0) \left[ (C + \Delta C)_{ijkl} \beta_{kl}^* V_\Omega(t^*) - \Delta C_{ijkl} (\beta_{kl}^\circ V_\Omega(t^*) + \int_\Omega u_{k,l}^\infty(\vec{r}', t^*)) \right] d\vec{r}' \quad (5)$$

The solution to this problem is well known from the equivalent inclusion method of Eshelby [13]. In fact, for an ellipsoidal region,  $u_{k,l}^\infty$  is constant over the ellipsoidal region if  $\vec{\beta}^*$  and  $\vec{\beta}^\circ$  are also constant (it is also true that it is a polynomial in  $\vec{r}'$ , if the strains are polynomials in  $\vec{r}'$ ). The effective dipole density associated with the inclusion can then be easily derived.

Using a six-dimensional vector terminology (such as the Voight convention) where vectors are symmetric  $3 \times 3$  matrices, one can easily show that (now replacing  $t^*$  by  $t$ ):

$$\overline{\Delta \sigma}(t) = [\mathbf{I} + \Delta C \overline{\mathbf{D}}]^{-1} [(C + \Delta C) \vec{\beta}^* - \Delta C \vec{\beta}^\circ] V_\Omega(t) \quad (6a)$$

and

$$\overline{\Delta \sigma}_{ii}(t) = 0 \quad , \quad ^5 \quad (6b)$$

<sup>3</sup> If the body in which this occurs has external boundaries (either free surfaces or regions of different  $\rho$ ) then wavefronts are reflected from the boundaries and will pass through both our chosen point and the surface of the ellipsoid. We ignore the effect of these reflected wavefronts on the acoustic emission from the inhomogeneity.

<sup>4</sup> In ref. [14] a slight extension of this assumption, called the retarded density approximation was developed. In that assumption, the expanding ellipsoid was broken into two regions, an inner region, in which the full static feedback correction is applied, and the outer “shell” region of the ellipsoid, in which no feedback correction is applied.

<sup>5</sup> We have already assumed  $\beta_{kk}^\circ = 0$ . The only term that might then contribute to  $\Delta \sigma_{ii}$  would arise from the term  $\Delta \rho \int_\Omega u_{k,k}(\vec{r}', \tau) d\vec{r}'$  which occurs in eq (3). Here, we have ignored this term, which arises from momentum effects associated to density changes in the inclusion. An alternate approach, analogous to the Born approximation, would be to modify the value of  $\vec{u}$  as calculated from eq (6) by including its own “homogeneous” dynamic density contribution.

where

$$u_m(\vec{r}, t) = \int_{t_0}^{t_1} G_{mi,j'}(\vec{r}, \vec{r}_0, t-\tau) \overline{\Delta\sigma}_{ij}(\tau) d\tau \equiv \int_{t_0}^{t_1} G_{mi,j'}^H(\vec{r}, \vec{r}_0, t-\tau) \overline{\Delta\dot{\sigma}}_{ij}(\tau) d\tau \quad (7a)$$

$$\overline{D}_{ijkl} = \frac{1}{2}(D_{ijkl} + D_{ijlk}) \quad (7b)$$

$$D_{ijkl} = \frac{a_1 a_2 a_3}{8\pi} \int_{|\xi|=1} [\tilde{G}_{ik}(\xi) \xi_j \xi_l + \tilde{G}_{jk}(\xi) \xi_i \xi_l] [a_n^2 \xi_n^2]^{-3/2} ds \quad (7c)$$

$$\tilde{G}_{ik}(\xi) = [C_{ijkl} \xi_j \xi_l]^{-1} \quad (7d)$$

For an elastically isotropic spherical inclusion [15]:

$$D_{ijkl} = \frac{1}{6\mu} \left[ \delta_{ik} \delta_{jl} + \delta_{il} \delta_{jk} - \frac{1}{5(1-\nu)} (\delta_{ij} \delta_{kl} + \delta_{ik} \delta_{jl} + \delta_{il} \delta_{jk}) \right] \quad (7e)$$

and for the disc shaped anisotropic inhomogeneity with disc unit normal  $\vec{\nu}$  [16]:

$$D_{ijkl} = \frac{1}{2} [\nu_i \nu_l \tilde{G}_{jk}(\vec{\nu}) + \nu_j \nu_l \tilde{G}_{ik}(\vec{\nu})] \quad (7f)$$

For an isotropic matrix, eq (7f) becomes:

$$\tilde{D}_{ijkl} = \frac{1}{4} \left[ \frac{\nu_i \nu_l}{\mu \delta_{jk} + (\lambda + \mu) \nu_j \nu_k} + \frac{\nu_i \nu_l}{\mu \delta_{ik} + (\lambda + \mu) \nu_j \nu_k} + \frac{\nu_i \nu_k}{\mu \delta_{jl} + (\lambda + \mu) \nu_j \nu_l} + \frac{\nu_k \nu_j}{\mu \delta_{il} + (\lambda + \mu) \nu_j \nu_l} \right] \quad (8a)$$

so that, for instance, if  $\nu_i = \delta_{i3}$

$$\overline{D}_{ijkl} = \frac{\delta_{i3} \delta_{j3} \delta_{k3} \delta_{l3}}{\lambda + 2\mu}$$

and  $[\mathbf{I} + \Delta\mathbf{C} \overline{\mathbf{D}}]^{-1}$  arises from the inverse of the Voight matrix:

$$\frac{1}{\lambda + 2\mu} \begin{bmatrix} \lambda + 2\mu & 0 & \delta C_{1133} & 0 & 0 & 0 \\ 0 & \lambda + 2\mu & \delta C_{2233} & 0 & 0 & 0 \\ 0 & 0 & \lambda + 2\mu + \Delta C_{3333} & 0 & 0 & 0 \\ 0 & 0 & \delta C_{1233} & \lambda + 2\mu & 0 & 0 \\ 0 & 0 & \delta C_{1333} & 0 & \lambda + 2\mu & 0 \\ 0 & 0 & \delta C_{2333} & 0 & 0 & \lambda + 2\mu \end{bmatrix} \quad (8b)$$

### 3. Discussion

The theoretical framework outlined above has several consequences for those interested in studying the dynamics of twinning and martensitic phase changes. The above model shows that the acoustic emission signal contains information about six properties of a martensitic transformation (or twin):

1. Volume of region transformed (of martensitic lath)
2. Dilatational strain
3. Shear/rotational strain
4. Habit plane
5. Internal stress magnitude (through its interaction with  $\Delta C$ )
6. Duration of the reaction

In fact, from eq (6)

$$\overline{\Delta\sigma}(t)=[\mathbf{I}+\Delta C \overline{\mathbf{D}}]^{-1} [(C+\Delta C)\vec{\beta}^*-\Delta C \vec{\beta}^0]V_{\Omega}(t).$$

Ignoring directionality and concentrating upon the magnitude of the stress components of a dipolar source, we see that acoustic emission is proportional to the volume of material that transforms and is linearly related to the transformation strain and pre-existing (residual) stress. If  $\Delta C$  is sufficiently small we can ignore the terms in  $\Delta C$  leaving the simple relation for acoustic emission in a homogeneous medium:

$$\overline{\Delta\sigma}(t)\simeq C \vec{\beta}^* V_{\Omega}(t). \quad (9)$$

Returning to the example in the introduction, we can now enumerate some potential applications for acoustic emission during the phase transformation: 1) If the transformation is accompanied by cracking one should find it possible to distinguish  $\overline{\Delta\sigma}$  signatures of cracking from those of the transformation itself. 2) It should also be possible for one to distinguish between different morphologies of martensitic (lath, plate or needle) based upon their different  $V_{\Omega}$  distributions. 3) If one monitors a local area in the material one could observe the evolution of residual stress. 4) Under “ideal measurement conditions” one can directly deduce the shape change tensor and habit plane dynamically and perhaps gain a deeper understanding of autocatalytic phenomena in which secondary martensitic transformations (with possibly different habit planes) are stimulated by the first transformation.

Equation (9) can be used to deduce the smallest volume of martensitically transformed material detectable by acoustic emission. It is known that the smallest displacements detectable by an acoustic emission transducer is  $\sim 10^{-14}$  m. This corresponds to a dipole of  $3 \times 10^{-8}$  Nm strength with 30 ns risetime buried 25 mm below the receiver [2]. Using values of  $200 \text{ GNm}^{-2}$  and 0.2 for  $C$  and  $\beta^*$  gives a minimum detectable volume of  $1 \mu\text{m}^3$ .

We can use the above results to comment on the work of Speich and Schwoeble [8] who monitored the acoustic emission of SAE 4300 series steels with systematically varied carbon content during transformation to martensite, as shown in figure 2. They demonstrated that acoustic emission was able to accurately determine the martensitic start ( $M_s$ ) temperature of the steel. In addition, their data shows a distinct correlation between carbon concentration and acoustic emission per unit volume of sample for which they did not account.

From eq (6) we can speculate that the cause of the correlation could be due either to the increase of transformation strain ( $\beta^*$ ) or an increase of individual martensitic nucleations associated with a change of martensite morphology with increasing carbon content. This may be further compounded by a consistent change of bulk residual stress with increasing carbon content or a change in reaction time whose accompanying frequency shift could affect instrument

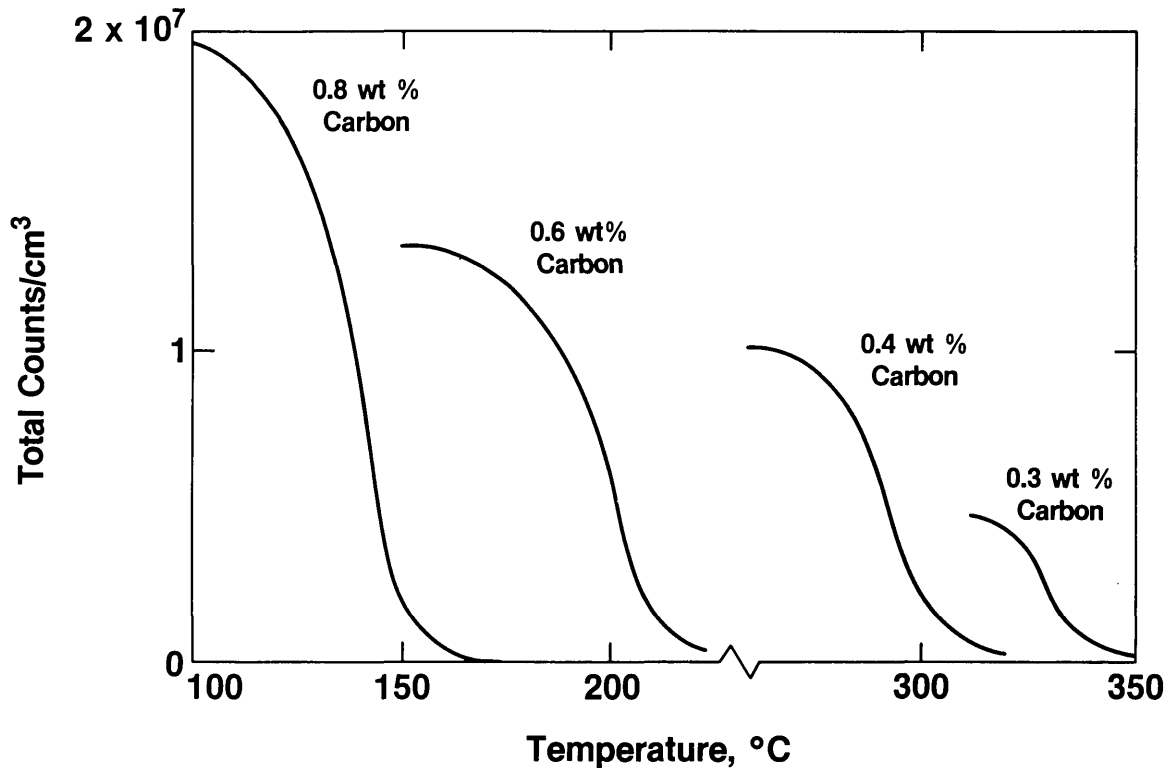


Figure 2—Acoustic emission per unit volume as a function of temperature measured during the cooling of low alloy steels of variable carbon content [8].

sensitivity. Change in lath morphology producing more (but smaller) emissions with increasing carbon content seems the most likely, but detailed metallographic studies are required.

#### 4. Summary

An elastodynamic formulism has been used to obtain a solution for the acoustic emission from dynamic phase transformations where there is a change in the new phase (inclusion) of both shape and elastic constants. Explicit solutions for small ellipsoidal inclusions with anisotropic elastic constants are given for an isotropic matrix. This framework is used to explain how acoustic emission could be used for monitoring martensitic phase changes.

---

We thank J. W. Cahn and J. W. Christian for valuable discussions.

#### References

- [1] Wadley, H. N. G.; Scruby, C. B.; Speake, J. *Int. Metals Rev.* **3**: 41; 1980.
- [2] Scruby, C. B.; Wadley, H. N. G.; Hill, J. J. *J. Phys. D: Appl. Phys.* **16**: 1069; 1983.
- [3] Rusbridge, K. L.; Scruby, C. B.; Wadley, H. N. G. *Mat. Sci. and Eng.* **59**: 151; 1983.
- [4] Scruby, C. B.; Wadley, H. N. G. *Prog. Nucl. Eng.* **11**(3): 275; 1983.

- [5] Wadley, H. N. G.; Mehrabian, R. Proc. Symp. Nondestructive Methods for Material Property Determination, Hershey, PA, April 6-8, 1983.
- [6] Vahaviolos, S. J.; Carlos, N. F.; Siykovje, S. J.; Ternowschck, S. J. Mat. Eval. **39**: 1057; 1981.
- [7] Canelli, G.; Cantelli, R. *Advances in Acoustic Emission* Proc. Int. Conf. on Acoustic Emission, Anaheim, CA; 1979. H. L. Dunegan and W. F. Hartman, eds., Dunhart, 1981.
- [8] Speich, G. R.; Schwoeble, A. J. ASTM STR-571: 40; 1975.
- [9] Fine, M.; Meshi, M.; Wayman, C. Martensitic Transformation, Academic Press, New York; 1978.
- [10] Baram, J.; Rosen, M. Acta Met. **30**: 655; 1982.
- [11] van Doren, S. L.; Pond, R. B.; Green, R. E. J. Appl. Phys. **47**(10): 4343; 1976.
- [12] Tanaka, H.; Horivchi, R. Scripta Met. **9**: 777; 1975.
- [13] Eshelby, J. D. J. Mech. Phys. Solids **17**: 177; 1969.
- [14] Simmons, J. A.; Clough, R. B. *Dislocation Modelling of Physical Systems*, Proc. Int. Conf., Gainesville, FL, June 1980, Pergamon Press, 1981.
- [15] Kneer, G. Phys. Stat. Sol. **9**: 825; 1965.
- [16] Kinoshita, N.; Mura, T. Phys. Stat. Sol. **5**(a): 759; 1971.

# Reconstructing Internal Temperature Distributions From Ultrasonic Time-of-Flight Tomography And Dimensional Resonance Measurements

S. J. Norton, L. R. Testardi, and H. N. G. Wadley

National Bureau of Standards, Washington, DC 20234

Accepted: November 7, 1983

Two ultrasonic techniques for reconstructing the internal temperature distribution in metal bodies—time-of-flight tomography and dimensional resonance profiling—are described. An analysis of the tomographic reconstruction of temperature (including ray refraction effects) in a cylindrical body is presented together with initial experimental results. Dimensional resonance profiling is a new technique that allows the reconstruction of a one-dimensional distribution of temperature in a structure from measurements of its resonant frequencies. While time-of-flight tomography is well suited for measuring temperature in a cylindrical geometry, a combination of dimensional resonance and (a restricted form of) tomography is the best method for measuring temperature profiles in the more practically important rectangular slab geometry.

Key words: dimensional resonance; metals processing; process control; temperature distribution sensor; tomography; ultrasound.

## 1. Introduction

The development of a temperature distribution sensor would be an important step in improving the productivity and quality of metals processing and reducing its energy needs. This has been recognized by the American Iron and Steel Institute [1]<sup>1</sup>, and a collaborative program of research with the National Bureau of Standards has been initiated to develop a sensor capable of providing internal temperature maps (to within 20 °C) with 20 mm spatial resolution or less for a variety of metals processing situations. Anticipated applications include measuring the internal temperature distribution in steel ingots during reheating and monitoring the temperature profile of steel strands as they are withdrawn from a continuous caster. Because of the limited time available for making the measurements, an ideal sensor should be capable of reconstructing temperature reliably with a

minimum of measurements to avoid interfering with production processes.

We report here on two distinct but complementary ultrasonic techniques for reconstructing internal temperature in metals and other materials: time-of-flight tomography and a new method which we call dimensional resonance profiling [2,3]. We identify the experimental and theoretical advantages and limitations of the two techniques for various geometries likely to be encountered in practice, and we propose a combination of the two exploiting their particular strengths for the most important practical geometry, the slab of rectangular cross-section.

The measurement of internal temperature by tomographic or dimensional resonance methods is based on the experimental observation that the velocity of sound in metals varies in a predictable way with temperature [4]. From room temperature to the melting point, the velocity of sound in austenitic steel and aluminum alloys decreases approximately linearly with temperature with a slope on the order of  $-1 \text{ m s}^{-1}/^\circ\text{C}$ . A similar behavior is observed for ferritic steels, although it is somewhat complicated by the bcc to fcc phase change. In the temperature reconstructions reported below, we have assumed for simplicity a linear relation between temperature and velocity

---

**About the Authors:** S. J. Norton, L. R. Testardi, and H. N. G. Wadley are with the Center for Materials Science in NBS' National Measurement Laboratory.

---

<sup>1</sup> Figures in brackets indicate references at the end of this paper.

over the temperature range of interest. However, the use of a piece-wise linear relationship, with a change in slope over a higher range in temperature to approximate the bcc to fcc phase change, was found to introduce no serious complications during reconstruction.

## 2. Time-of-Flight Tomography

The measurement of the time-of-flight (TOF) of an ultrasonic pulse along a path penetrating a steel sample, for example, gives the line integral of the reciprocal sound velocity along that path. The path length divided by the TOF is also the average velocity along the path, and in fact could be used simply to compute the average temperature along that path. However, many TOF measurements over multiple intersecting paths, when employed as input to a tomographic algorithm, can be used to reconstruct a cross-sectional image of the sound velocity within the sample. Using the predetermined velocity-temperature relationship for the metal, the velocity map may then be converted into an image of internal temperature. In this section, we consider the application of tomography to two simple object geometries—cylindrical billets and rectangular slabs—representative of those found in metals processing.

### 2.1 Cylindrical Billet

We have, for simplicity, examined the TOF tomography problem for a cylindrical steel billet under the assumption that the temperature distribution is also cylindrically symmetrical.<sup>2</sup> A crucial advantage of the assumption of circular symmetry is that the number of TOF measurements required for satisfactory spatial resolution is reduced perhaps two orders of magnitude below that of the general case (i.e., under no symmetry assumptions). For the symmetrical case, the unknown temperature reduces to a one-dimensional function of radius. This simplification is important because a hostile measurement environment and time constraints impose severe limits on the

<sup>2</sup> When the shape of the billet is cylindrical and the boundary condition on the surface is symmetrical, this assumption is probably quite reasonable if the billet has been cooling for a short time. This is because heat-flow theory predicts that any initial asymmetrical spatial frequency components of the temperature damp out faster than the low-order symmetrical components [6]. As a result, the temperature tends rapidly toward a symmetrical distribution as the asymmetrical temperature gradients attenuate. (We assume throughout this paper that the thermal conductivity of the body is uniform.)

number of TOF measurements that can be conveniently and reliably performed during processing.

#### 2.1.1 Theory

To measure temperature, our main task is to reconstruct the radial velocity profile  $v(r)$  of the cylindrical billet. The velocity is then converted to a temperature profile  $T(r)$  using, for example, a linear relationship between velocity and temperature of the form

$$T(r) = T_0 + b[v(r) - v_0], \quad (1)$$

where  $T_0$ ,  $v_0$  and  $b$  are experimentally-determined constants.

To recover the radial velocity distribution, a single “fan beam” measurement (i.e., paths radiating outward from one source and ending at an array of receivers) is sufficient. Let  $\tau_m$  denote the measured TOF over a path  $L_m$ , as illustrated in figure 1. Suppose TOF measurements are obtained over  $M$  distinct paths penetrating the cylinder. Then

$$\tau_m = \int_{L_m} \frac{dl}{v(r)}, \quad m = 1, 2, \dots, M. \quad (2)$$

The number  $M$  will be small because of time constraints and the difficulty in making each measurement during processing. Since the angular range over which the TOF data are measured may be limited and sparsely sampled, an important factor in selecting a reconstruction algorithm is how well it performs with only limited data.

With a complete set of path-integral measurements  $\tau_m$ , a variety of tomographic algorithms could be used for recovering  $v(r)$ . Among these are the convolution-backprojection, Fourier inversion, and algebraic reconstruction techniques (ART) [5]. Convolution-backprojection, while computationally fast and well suited for commercial x-ray tomography, was not used here. This algorithm does not generally perform well when the data are limited in angle and/or are sparsely sampled; severe aliasing artifacts often result under these conditions. Fourier inversion is the Fourier-domain equivalent of convolution-backprojection and offers no advantages.

A second disadvantage of these “direct” approaches is that a priori constraints are not easily incorporated. This is undesirable because much a priori information is potentially available in the tomographic temperature problem, such as surface temperature, or a priori bounds on the range of the internal temperature distribution or the smoothness (gradient) of the

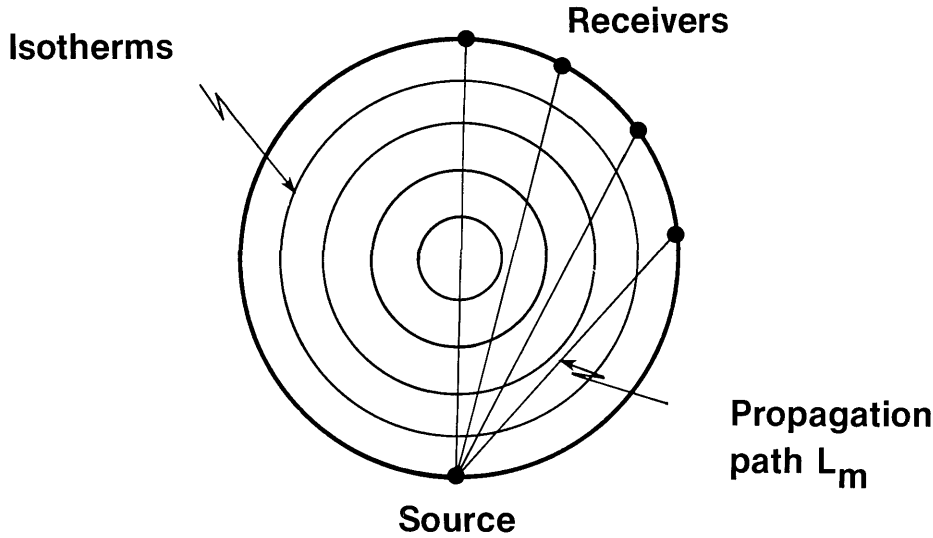


Figure 1—Cylinder cross-section with ray paths diverging from a single ultrasonic source. The temperature distribution is assumed to have cylindrical symmetry.

temperature distribution. Another constraint is imposed by the thermal conductivity equation, which the temperature distribution must obey. Thus, reconstructions obtained at different times are not independent but are coupled by the heat flow equation. If one has a priori information on a temperature distribution at some initial time (e.g., that the temperature was initially uniform), then it might be possible to exploit this information to place bounds on the temperature or its gradient at subsequent times. We mention other beneficial effects of a priori constraints in a later section.

In contrast, the iterative ART algorithms are generally less susceptible to limited-data effects and allow incorporation of a priori information. We have found, however, that for the cylindrically-symmetric problem, for which the number of unknowns is relatively small, the complexity of an iterative technique is unnecessary.

For these reasons, none of the above algorithms is particularly well-suited for the simple cylindrical reconstruction problem. Instead, a “series expansion” algorithm was used and found to be both a natural approach in terms of imposing constraints (such as surface temperature, if known) and an effective way of reducing the number of unknown image pixels (or basis functions; see below) to an absolute minimum. The latter advantage is of fundamental importance because it implies a corresponding reduction in the number of measurements.

The series expansion technique consists of expanding the unknown profile (i.e., the reciprocal velocity) in a suitable set of basis functions, where “suitable” means that a truncated expansion (to, say,  $N$  terms, where  $N$  is small) provides a satisfactory

approximation to the unknown profile. That is, we expand the reciprocal velocity using  $N$  basis functions  $\phi_n(r)$ :

$$\frac{1}{v(r)} = \sum_{n=1}^N a_n \phi_n(r), \quad (3)$$

where  $\{\phi_n(r)\}$  is a basis set orthogonal on the interior of a circle of radius  $R$  (the radius of the cylinder). We consider two choices of basis functions below, although, for an infinite basis set, any choice would suffice to expand  $1/v(r)$ . However, as noted, the choice of  $\{\phi_n\}$  will be dictated (in part) by how well a truncated series can be made to approximate  $1/v(r)$  for  $0 \leq r \leq R$ .

Inserting eq (3) into eq (2) and interchanging orders of summation and integration gives

$$\tau_m = \sum_{n=1}^N a_n \Phi_{mn}, \quad m=1, 2, \dots, M, \quad (4)$$

where

$$\Phi_{mn} = \int_{L_m} \phi_n(r) dl. \quad (5)$$

Once the basis functions  $\phi_n(r)$  are chosen, the matrix elements  $\Phi_{mn}$  can be numerically computed and stored. Our problem then reduces to solving the linear system eq (4) for the unknown coefficients  $a_n$ , where the  $\tau_m$  are measured. Upon solving eq (4) for  $a_n$ , eq (3) gives the reconstruction of the reciprocal velocity  $1/v(r)$ , which in turn can be substituted into eq (1) to obtain

the temperature profile  $T(r)$ . Generally, to mitigate the effect of measurement errors, many more TOF measurements ( $M$ ) than unknowns ( $N$ ) are desirable. In this case, eq (4) will be over-determined, and it is natural to compute the pseudoinverse (the minimum-norm least-mean-square-error solution) of eq (4). To illustrate this, write eq (4) in matrix form:

$$\boldsymbol{\tau} = \Phi \mathbf{a} , \quad (6)$$

where  $\Phi$  is an  $M$  by  $N$  matrix ( $M \geq N$ ),  $\mathbf{a}$  is the  $N$ -component coefficient vector and  $\boldsymbol{\tau}$  is the  $M$ -component measurement vector. Minimizing the mean-square-error  $E = \mathbf{e}^T \mathbf{e}$ , where  $\mathbf{e} = \Phi \mathbf{a} - \boldsymbol{\tau}$ , results in the pseudoinverse of eq (6), given by

$$\hat{\mathbf{a}} = (\Phi^T \Phi)^{-1} \Phi^T \boldsymbol{\tau} , \quad (7)$$

where  $^T$  denotes transpose.

In our work, two candidate basis sets  $\{\phi_n\}$ , Bessel functions and “ring functions,” were studied. Both are orthogonal in the sense that

$$\int_0^R \phi_n(r) \phi_m(r) r dr = N_n \delta_{nm} ,$$

where  $N_n$  is a normalization constant. They are defined as follows:

- 1) Bessel function basis:

$$\phi_n(r) = J_0(k_n r) , \quad (8a)$$

where  $J_0(\cdot)$  is the zero-order Bessel function and  $k_n$  is the  $n$ -th root of  $J_0(kR) = 0$ .

- 2) Ring function basis:

$$\phi_n(r) = \text{ring}_n(r) , \quad (8b)$$

where

$$\text{ring}_n(r) = \begin{cases} 1 & \text{for } r_{n-1} < r \leq r_n \\ 0 & \text{otherwise} , \end{cases}$$

and  $r_n = Rn/N$ ,  $n = 0, 1, \dots, N$ .

The Bessel basis is a particularly interesting choice because Bessel functions are smooth over the circular domain, and we recall that the solution to the thermal conductivity equation in a cylindrical geometry is also given by a Bessel function series [6]. This suggests that the Bessel basis is a natural choice for the temperature reconstruction problem with circular symmetry and that the approximation (3) may even provide a good fit when truncated after the first few terms. This is because the higher-order terms in the series solution to the conductivity equation are exponentially damped with time. As a result, after a relatively short cooling time, the temperature profile increasingly resembles a single Bessel function, in which case only one term in eq (3) may be sufficient to approximate the profile.

The ring basis on the other hand provides a discrete or “staircase” approximation to the temperature profile, and thus does not provide the characteristic smooth temperature profile expected.

## 2.1.2 Simulations and Experiments

In our initial examination of the tomography problem, we performed computer simulations of temperature reconstructions. The following procedure was used: As a first step, we compute a hypothetical temperature profile by solving the thermal conductivity equation for a cooling cylinder. We assume in the simulation a thermal conductivity of 304 stainless steel, a 6-in-diameter cylinder, and an initially uniform temperature of 400 °C. Using the velocity-temperature relation, eq (1), we convert the radial temperature distribution into its corresponding velocity distribution. Given this hypothetical velocity profile, simulated TOF measurements are generated by numerically integrating the reciprocal velocity along  $M$  propagation paths. These simulated TOF values are then used to compute  $M$  values of  $a_n$  by direct inversion of eq (6), i.e.,

$$\mathbf{a} = \Phi^{-1} \boldsymbol{\tau} . \quad (9)$$

In this case, the number of measurements  $\tau_m$  equals the number of unknowns  $a_n$ , and since  $\Phi$  is full rank, direct inversion is possible. The resulting  $\mathbf{a}$  is inserted into eq (3) to obtain the reconstructed velocity profile. The temperature reconstruction is then obtained by substituting the velocity into eq (1). When the Bessel function basis was used, the computed temperature profile was found to be almost indistinguishable from the original temperature distribution for cooling times

longer than several hundred seconds.<sup>3</sup> The values of  $M$  used usually needed to be no larger than 2 or 3 for a good fit, thus confirming our earlier expectation that the Bessel basis is excellent for fitting temperature profiles, at least for an idealized cooling cylinder and after moderate cooling times.

Unfortunately, the matrix inverse  $\Phi^{-1}$  is ill-conditioned, and on introducing random errors into  $\tau_m$  on the order of a few tenths of a microsecond (corresponding to a 1:200 relative error), significant fluctuations in the calculated temperature profile ( $\pm 50^\circ\text{C}$ ) resulted. The ill-conditioning problem became more dramatically apparent when real TOF measurements were obtained from a 6-in-diameter stainless steel cylinder. This cylinder was initially heated to  $400^\circ\text{C}$  and TOF measurements were generated by exciting 25 ns duration elastic wave pulses with a focused 30 mJ pulsed Nd:YAG laser. The received pulses were recorded with a PZT transducer coupled to the cylinder with a fused quartz buffer rod [7].

Eleven TOF measurements were made at increasing angles away from the cylinder diameter (fig. 1). Because of the limits on the accuracy of the measurements in this initial experiment, an attempt at a direct inversion using eq (9) failed for  $M > 2$ . When more measurements were used, thereby increasing the order of the matrix  $\Phi$ , the problem becomes increasingly ill-conditioned.<sup>4</sup> To verify that the reconstructed velocity distribution was consistent with the measured TOF values, we computed numerically the TOF values over each ray path using the reconstructed velocity distribution. The computed TOF values agreed with the measured TOF values to within  $0.001 \mu\text{s}$  or better, thereby confirming that the errors are not of a numerical origin, but arise due to uncertainty in the measurements themselves. Sources of uncertainty include the finite precision in measuring the TOF (about  $\pm 0.05 \mu\text{s}$ ), as well as other sources of error, such as variable grain anisotropy which affects wave propagation in the steel.

<sup>3</sup> The ratio between the coefficients multiplying the second and first Bessel functions in the series expansion of the heat-flow solution is  $\exp(-14.7\alpha t/R^2)$ , where  $\alpha$  is the thermal diffusivity of the metal and  $R$  is the cylinder radius. This number gives us an indication of how fast the second- and higher-order terms attenuate with time relative to the first term, and thus how soon the first term will dominate. In our case,  $\alpha/R^2 = 6.4 \times 10^{-4} \text{ s}^{-1}$ ; letting, for example,  $t = 200 \text{ s}$ , the above ratio is 0.15.

<sup>4</sup> A singular value decomposition of  $\Phi$  shows condition numbers ranging from 3 to  $10^5$  as the number of unknowns varies from 2 to 11 and depending on the choice of basis functions. The condition number provides an upper bound on the amplification of errors in the inversion process.

Another possible source of error is ray bending due to refraction. We show in the Appendix one method of estimating the error in a TOF measurement contributed by ray refraction. For the small temperature gradients encountered in our initial experiment ( $\approx 50^\circ\text{C}/\text{cm}$ ), we found that the TOF errors due to refraction were quite negligible. Longer propagation paths and higher temperature gradients could, however, make ray bending effects significant, in which case some compensation for refraction would be needed for accurate reconstructions. Refraction effects in ultrasonic tomography have been discussed in the literature, and a first-order correction to the TOF due to refraction has been reported [8]. Iterative correction approaches have also been proposed [9].

It was also found that the ring basis set generates a better conditioned matrix  $\Phi$  than the Bessel basis set. Thus, in some sense, the ring functions constitute a more "linearly-independent" set than the Bessel functions, and as a consequence, the measurement errors are generally amplified by a greater factor for the Bessel set than for the ring set. Although the Bessel basis provides a smoother fit, the ring basis evidently has the advantage of improving the numerical conditioning of the inversion problem.

As a next step, the pseudoinverse eq (7) was used to compute a smaller number of unknowns ( $N$ ) than measurements ( $M$ ). Using all 11 measurements and solving for far fewer coefficients reduced the ill-conditioning to some extent, but error amplification still precluded solving for more than three coefficients.

Figures 2a and 2b show reconstructed temperature profiles using the pseudoinverse, eq (7), and all 11 measurements. The squares indicate measured values of the internal temperature ( $\pm 2^\circ\text{C}$  accuracy) obtained with a thermocouple probe.<sup>5</sup> In figure 2a, a Bessel function basis set was used in which the series expansion [eq (3)] was truncated at two terms. In figure 2b, the ring basis set was used, again with only two terms retained. An attempt to use more than two or three terms resulted in a poorer approximation to the true temperature profile.

We suggest two fundamental approaches to reducing the degree of error amplification in the inversion problem. Increasing the precision of the TOF measurement is the first requirement. Faster digitization rates, reduced noise and greater receiver bandwidth should all contribute to an improvement in

<sup>5</sup> The noticeable difference between the temperature at the surface and at the four interior points is probably a consequence of the short cooling time of the cylinder (a few minutes), as well as the failure to heat the cylinder uniformly prior to the measurements.

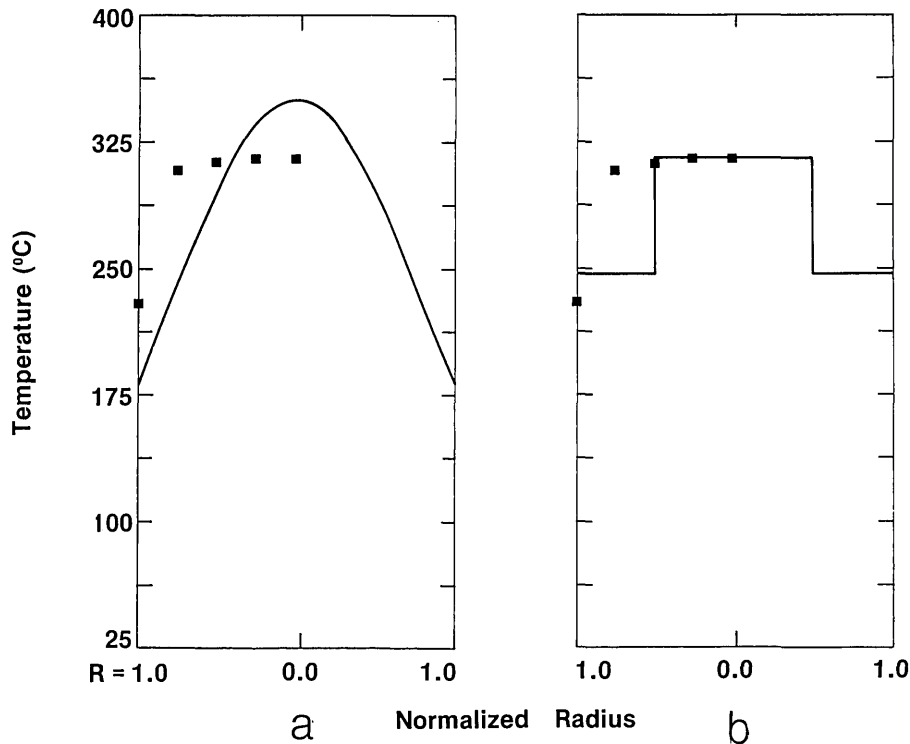


Figure 2-(a) Two-term Bessel function reconstruction of the temperature profile. The squares indicate the measured temperature. (b) Two-term ring function reconstruction of the temperature profile.

the temporal resolution in the TOF measurement. We estimate that a minimum relative accuracy in the TOF measurement of approximately one part in  $10^3$  is needed for acceptable accuracy ( $\pm 20^\circ\text{C}$ ) and resolution ( $\leq 20$  mm) in the tomographic reconstruction. For the 6-in cylinder used in the initial experiment, this represents an error of about 30 ns in the TOF. This TOF error corresponds to a path-length error of 0.15 mm, and so path lengths must also be measured to this sensitivity. Since the relative TOF error decreases in proportion to the length of the path, the longer path lengths expected in larger structures will help ease this exacting path-length precision.

The second approach to reducing error amplification is to use regularization or other numerically-stabilizing methods to reduce ill-conditioning. One such strategy is to impose a priori constraints on the solution. An important example of this is to constrain the boundary value to match the surface temperature, provided the surface temperature can be measured. Simulations demonstrate that such a surface constraint is effective in improving numerical stability. Another approach is to minimize the mean square error subject to a smoothing constraint on the velocity profile, which can be regarded as a form of regularization. A singular value decomposition of the matrix  $\Phi$ , combined with a judicious elimination of the smallest singular values, is also a potentially effective way of

improving the numerical conditioning of the inversion problem [10].

Ill-conditioning of this kind is not peculiar to the series-expansion approach to tomography; in fact, error amplification is characteristic of all inverse problems. In general, when more terms in the series expansion (i.e., more unknowns) are retained, the more ill-conditioned the problem becomes, and the factor by which errors are magnified rapidly increases. This illustrates a fundamental trade-off between spatial resolution and the attainable accuracy in the reconstructed temperature. For a given uncertainty in the TOF measurements, only a finite number of unknowns (i.e., terms in the series) can be reliably computed. An attempt to compute more than this results in an error amplification so large as to seriously degrade the accuracy of the reconstructed temperature.

## 2.2 Rectangular Slab

In this section, we examine the possibility of using TOF tomography to reconstruct the internal temperature of a slab with rectangular cross-section (fig. 3). If the slab thickness is small relative to its height and breadth, the temperature gradient will be predominantly normal to its larger surface (i.e., the isotherms in fig. 3 will run parallel to the  $x$ - $y$  plane

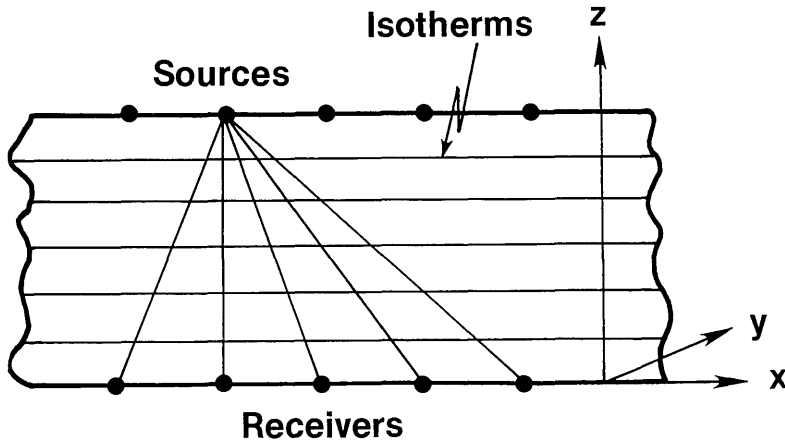


Figure 3—Slab cross-section with sources and receivers on opposite surfaces. The isotherms are assumed parallel to the surface.

with the gradient pointing in the  $z$ -direction). To a first approximation, it is reasonable in this case to regard the temperature as a function of  $z$  only, with negligible variation in the  $x$  and  $y$  directions. This approximation again represents a major simplification in the reconstruction problem, because the unknown temperature profile is now only one-dimensional.

Unfortunately, if the isotherms run truly parallel to the edges, as assumed, a tomographic scheme will be ineffective if the sources and receivers are constrained<sup>6</sup> to lie on either side (fig. 3). Line integrals over different paths intersecting the parallel layers sample the various layers in precisely the same proportion; the resulting system of equations is consequently linearly dependent, and any attempted inversion to recover the different velocities in the parallel layers will fail.

This problem is fundamental, and no tomographic algorithm, whether analytical or iterative, will succeed here. An equivalent interpretation of the “non-invertibility” of the measurements is this: With the sources and receivers on opposite sides, no propagation path lies parallel to the slab surface. In reconstruction-from-projections theory, this condition defines a so-called “limited-angle problem,” and the well-known central slice theorem [5] predicts that the spatial frequency component corresponding to variations in the slab in the  $z$ -direction cannot be recovered from the limited-angle measurements. In particular, propagation along paths parallel to the slab surface are required to retrieve this component.

On the other hand, a limited form of tomography may be used if we restrict the possible temperature profiles to a particular form or shape. If this shape has

one undetermined parameter, one TOF measurement will suffice to compute it. As an example, suppose we assume a symmetrical profile with the shape of a half sine wave. That is, if the slab thickness is  $L$ , we assume a temperature profile of the form

$$T(z) = T(0)[1 + a \cdot \sin(\pi z/L)] , \quad 0 \leq z \leq L ,$$

where  $T(0) = T(L)$  is the surface temperature, which, for simplicity, we assume can be measured. The undetermined parameter,  $a$ , can then be recovered with a single TOF measurement; we see that the center temperature ( $z = L/2$ ) is  $T(0)(1 + a)$ .

Finally, an alternative, or complement, to this approach is the method of dimensional resonance profiling which is capable of recovering the spatial variations in temperature in the  $z$ -direction. This is described next.

### 3. Dimensional Resonance Profiling

This technique represents a novel approach to reconstructing a one-dimensional inhomogeneity in the elastic modulus and density of a body from measurements of its resonant frequencies [2,3]. An analysis reveals a simple relation between the coefficients of a Fourier expansion of the modulus and density and the measured values of the fundamental and overtone frequencies. The theory as developed thus far treats only the one-dimensional problem, and experiments successfully demonstrating the technique have been performed to date on a thin brass rod. For the case of a slab, the dimensional resonance approach should in principle allow one to reconstruct (from thickness resonance frequencies) the thickness variations of the modulus and density, from which the

<sup>6</sup> This statement also applies if the sources and receivers lie on one side of the slab and the paths are defined by reflecting the pulses from the opposite surface.

velocity of sound may then be computed. The thickness velocity profile can then be converted to temperature in the usual way. The theory of dimensional resonance is outlined below; a more complete treatment may be found in [2,3].

### 3.1 Theory

Consider a one-dimensional object of length  $L$  along the  $z$ -axis, where  $0 \leq z \leq L$ . Assume stress-free boundary conditions, and that the variations in the modulus and density are small relative to their dc components. Then the  $n$ -th order normal mode (dimensional resonance) is approximately

$$u(z,t) = \sqrt{2/L} \cos(n\pi z/L) \cos(\omega_n t), \quad (10)$$

where  $u(z,t)$  denotes displacement and  $\omega_n$  is the (perturbed) resonance frequency. Represent the spatial variations of the linear elastic modulus by the Fourier series

$$M^L(z) = M_0^L + \sum_{m=1}^{\infty} M_m^L \cos(m\pi z/L), \quad 0 \leq z \leq L, \quad (11)$$

and the linear density  $\rho^L(z)$  by a similar series (the superscript  $L$  stands for "linear," meaning  $M^L$  and  $\rho^L$  have units of modulus and density per unit length). If the acoustic damping is small, we can equate the time-averaged kinetic energy (KE) and potential energy (PE) of the structure:

$$\text{KE} = \int_0^L \frac{1}{2} \rho^L \overline{\dot{u}^2} dz = \text{PE} = \int_0^L \frac{1}{2} M^L \overline{\epsilon^2} dz \quad (12)$$

where  $\epsilon = \partial u / \partial z$  is the strain and the over-bar denotes time average. Substituting eqs (10) and (11) into eq (12) gives to first order in small quantities

$$\frac{1}{2} \left( \frac{M_{2n}^L}{M_0^L} + \frac{\rho_{2n}^L}{\rho_0^L} \right) = \frac{\bar{\omega}_n^2 - \omega_n^2}{\bar{\omega}_n^2} \quad (13)$$

where  $\bar{\omega}_n = (n\pi/L)(M_0^L/\rho_0^L)^{1/2}$  are the resonant frequencies associated with the dc values of the modulus and density,  $M_0^L$  and  $\rho_0^L$ .

Equation (13) equates the  $2n$ -th Fourier coefficient of the modulus and density to the shift in the resonant frequency of the  $n$ -th mode. We see from eq (13) that by measuring the shifts in the resonant frequencies, we obtain the even-order coefficients of the Fourier expansion of the inhomogeneity in modulus and

density.

One limitation of the dimensional resonance technique is that only the even-order Fourier coefficients are recoverable; i.e., the anti-symmetric part of the variation is not measurable from the resonant frequencies alone. A second limitation is that the dc values of the modulus,  $M_0^L$ , and density,  $\rho_0^L$ , are not directly measurable from eq (13). However, the dc modulus under certain conditions may be obtained from a single TOF measurement along the  $z$ -direction (provided dispersion is properly accounted for), and the dc density can be estimated from the mass of the object [2,3].

The first limitation is potentially the more serious of the two. However, when it is reasonable to assume that the temperature distribution is symmetrical about the center, the dimensional resonance approach is potentially effective in recovering the internal temperature profile through the short dimension of a slab. Dimensional resonance also has the advantage of employing relatively low-frequency standing waves, and is thus less susceptible to signal-to-noise loss arising from high ultrasonic attenuation in hot steel with large grain size. This technique is also exceedingly well-behaved numerically compared to the inherent ill-conditioning of two-dimensional tomography.

### 3.2 Experimental Result

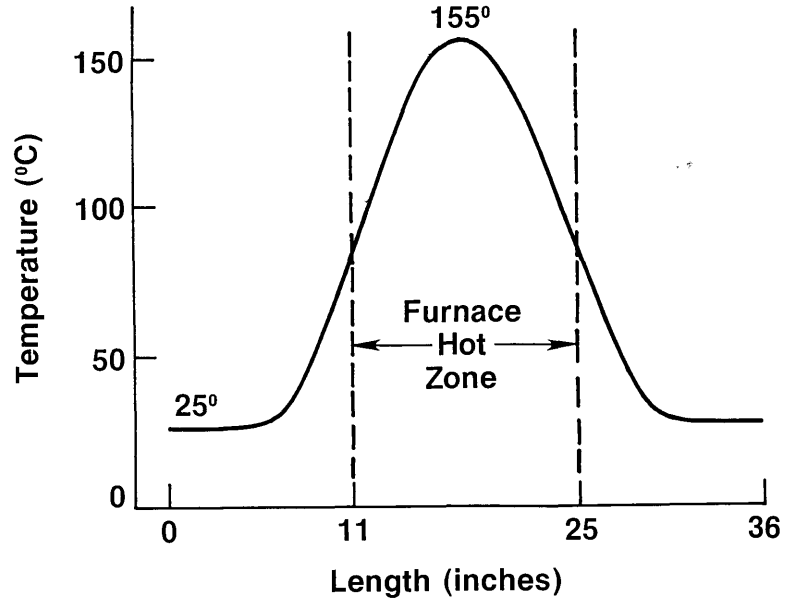
Figure 4 shows the reconstructed temperature distribution along a brass rod (36 in long with a diameter of 0.25 in) heated near its center. In this experiment, extensional waves were excited and detected in the rod using a noncontact, electromagnetic (eddy-current) transducer at one end; a phased-locked loop was used to measure the resonant frequencies to a precision of several parts in  $10^5$ . A more detailed description of this experiment can be found in [3].

The reconstruction in figure 4 was performed using the five lowest dimensional resonances. Because the actual temperature distribution was relatively smooth, the calculated profile from only five terms in the Fourier series agreed with the true temperature profile to within 5% at all points along the rod.

## 4. Discussion

We have seen that time-of-flight tomography represents one approach to reconstructing the radial temperature profile in a cylindrical body. Dimensional resonance, as thus far studied, is a one-dimensional

Figure 4—Dimensional resonance reconstruction of the temperature distribution along a rod heated near its center.



technique, but its generalization to two dimensions is now under study. The successful extension of dimensional resonance to the symmetrical cylinder could provide an alternative to tomography in that geometry. This success will depend particularly on how well the symmetrical resonances can be resolved and the difficulty in separating them from the asymmetrical modes.

Although dimensional resonance has been tested on thin rods, it has not yet been demonstrated on a slab. Owing to diffraction effects within the slab, we expect a reduction in the signal-to-noise ratio and the resolvability of the resonances, but the simple one-dimensional theory should still apply. If these problems are not too serious, dimensional resonance may be the method of choice in this geometry since a conventional tomographic approach to reconstructing the “stratified” slab will fail, as noted earlier.

On the other hand, the limited tomographic approach may be used if we restrict the temperature profile to a simple shape with one undetermined parameter. This approach fails of course to recover the “fine structure” of the temperature profile, if it exists. Often, however, it may be reasonable to assume that the temperature profile is smooth and symmetrical, in which case the limited tomographic approach may be sufficient, particularly if an accurate estimate of the center temperature is all that is needed.

## Appendix

To estimate the error in a TOF measurement due to ray refraction, consider the simple example of a linear

velocity gradient in the  $y$ -direction:

$$v(y) = v_0 + yv_y, \quad (\text{A1})$$

where  $v_y = \partial v / \partial y$  is the velocity gradient and  $v_0$  is the (constant) velocity along the  $x$ -axis. Let the source and receiver lie on the  $x$ -axis separated by the distance  $l$  (fig. 5). In the absence of refraction ( $v_y = 0$ ), the pulse will propagate along the  $x$ -axis with  $\text{TOF}_0 = l/v_0$ .

For the linear velocity gradient, given by eq (A1), the refracted path can be shown to be the arc of a circle intersecting the source and receive points. Defining  $D$  as the radius of the circle and  $\theta_0$  as the angle between the  $x$ -axis and the tangent to the circle at the source point (fig. 5), the ray path is given by

$$y(\theta) = D \cos \theta - D \cos \theta_0 \quad (\text{A2})$$

$$x(\theta) = D \sin \theta + D \sin \theta_0, \quad (\text{A3})$$

for  $-\theta_0 \leq \theta \leq \theta_0$ . Snell's law, for the linear gradient eq (A1), may be written

$$v_0 \cos \theta = v \cos \theta_0. \quad (\text{A4})$$

Substituting eq (A1) into eq (A4) and the resulting expression for  $\cos \theta$  into eq (A2), gives the relation

$$v_0 = D v_y \cos \theta_0. \quad (\text{A5})$$

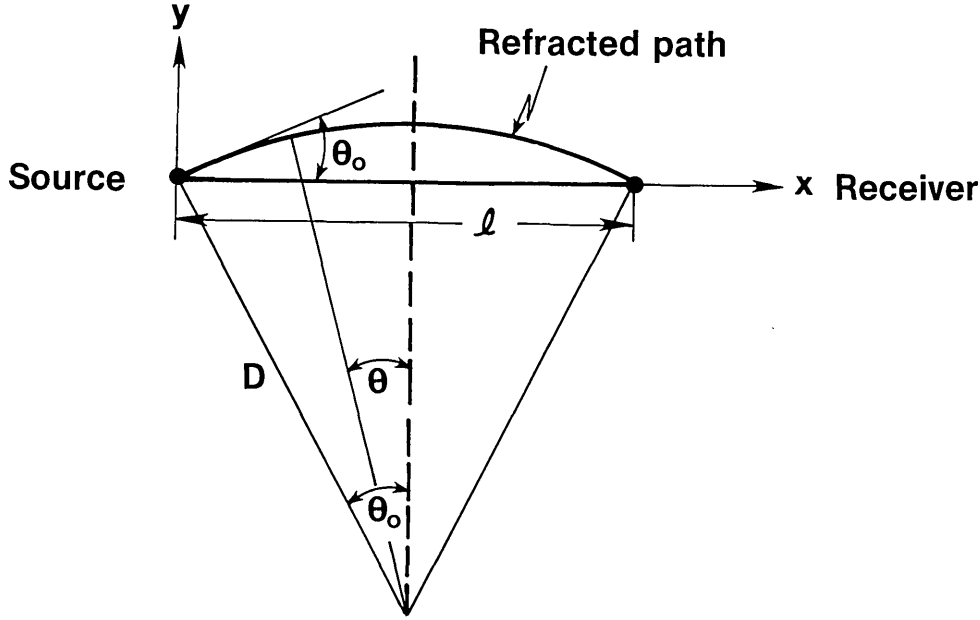


Figure 5—Refracted ray produced by a linear velocity gradient increasing in the y-direction.

From figure 5, we also have

$$l = 2D \sin \theta_0 \quad (\text{A6})$$

The TOF over the refracted path is

$$\text{TOF}_R = \int_{-\theta_0}^{\theta_0} \frac{D d\theta}{v(\theta)}$$

From eqs (A4) and (A5), we have  $v(\theta) = Dv_y \cos \theta$ , so that

$$\begin{aligned} \text{TOF}_R &= \frac{1}{v_y} \int_{-\theta_0}^{\theta_0} \frac{d\theta}{\cos \theta} = \frac{1}{v_y} \ln \left[ \frac{1 + \sin \theta_0}{1 - \sin \theta_0} \right] \\ &= \frac{1}{v_y} \ln \left[ \frac{1 + l/2D}{1 - l/2D} \right] \end{aligned} \quad (\text{A7})$$

Squaring and adding eqs (A5) and (A6) results in

$$D = [(l/2)^2 + (v_0/v_y)^2]^{1/2} \quad (\text{A8})$$

Assuming  $D \gg l$ , we can insert eqs (A8) into (A7) and expand the result to first order in  $l/D$ , giving

$$\text{TOF}_R = \text{TOF}_0 \left[ 1 - \frac{1}{24} (v_y l / v_0)^2 \right] \quad (\text{A9})$$

The second term on the right is the relative TOF error due to refraction (to first order in  $l/D$ ).

## References

- [1] Report of Workshop on Process Control Sensors for the Steel Industry edited by Mehrabian, R., Whitely, R. L., van Reuth, E. C. and Wadley, H. N. G., Natl. Bur. Stand., NBSIR 82-2618 (1982).
- [2] Norton, S. J.; Testardi, L. R. Reconstruction of one-dimensional inhomogeneities in elastic modulus and density using dimensional resonances, *J. Acoust. Soc. Am.*, to be submitted.
- [3] Testardi, L. R.; Norton, S. J.; Hsieh, T. Determination of inhomogeneities of elastic modulus and density for one-dimensional structures using acoustic dimensional resonances. *J. Appl. Phys.*, to be submitted.
- [4] Kurz, W.; Luz, B. Localization of the solid liquid interface in metals by ultrasonic methods. *Z. Metallkunde* 57: 70-73; Jan. 1966.
- [5] Special Issue on Physical and Computational Aspects of 3-Dimensional Image Reconstruction. *IEEE Trans. Nuclear Science* NS-21; 1974.
- [6] Carslaw, H. S.; Jaeger, J. C. *Conduction of Heat in Solids*, 2d Edition (Oxford Univ. Press, 1959).
- [7] Wadley, H. N. G.; Norton, S. J.; Biancaniello, F. S.; Mehrabian, R. *Ultrasonic Measurement of Internal Temperature Distribution*. Proceedings of the 1983 American Society for Metals Congress, Philadelphia.
- [8] Norton, S. J.; Linzer, M. Correcting for ray refraction in velocity and attenuation tomography: a perturbation approach. *Ultrasonic Imaging* 4: 201-233; 1982.
- [9] Schomberg, H. An improved approach to reconstructive ultrasound tomography. *J. Phys. D: Appl. Phys.* 11: L181-L185; 1978.
- [10] Forsythe, G. E.; Malcolm, M. A.; Moler, C. B. *Computer Methods for Mathematical Computations* (Prentice-Hall, Englewood Cliffs, NJ, 1977).

# Acoustic Emission: Establishing the Fundamentals

D. G. Eitzen and H. N. G. Wadley

National Bureau of Standards, Washington, DC 20234

Accepted: January 23, 1984

In the mid-1970's a program of fundamental research was initiated at NBS to improve the scientific understanding of acoustic emission. Many individual results of this research have been reported in the literature and are beginning to be incorporated in a new generation of acoustic emission instrumentation, in improved test methodologies, and in the analysis of data. Here, we summarize the problems faced by acoustic emission midway through the last decade, review the accomplishments of the NBS program and related research programs, and outline the research that will be required in future years.

Key words: acoustic emission; calibration; continuous monitoring; inverse problems; nondestructive evaluation; signal processing; structural integrity; theoretical bases.

## 1. Introduction

Acoustic emission (AE) is the name given to the transient mechanical waves spontaneously generated by abrupt localized changes of strain within a body. Dislocation motion and crack growth are the mechanisms by which these strain changes occur during growth of flaws in materials; even minute crack propagation or plastic deformation results in elastic waves which can cause surface motion of a body. This surface motion is sometimes of sufficient amplitude to be detected by sensors (transducers) attached to the surface; the sensors convert a mechanical disturbance to a voltage-time waveform.

The surface motion due to an AE source contains information about both the location *and* characteristics of the source. Although this has been assumed for

some time, it has been proved only recently [1,2]<sup>1</sup>. Using arrays of transducers and triangulation algorithms based on differences in signal arrival time, AE sources can be detected and located; however, their characterization is much more difficult. Nevertheless, by processing the received signals using newly developed methods, it is possible to extract additional information about the source. The AE technique, then, offers the potential of assessing and monitoring structures such as pressure vessels and piping, aircraft, bridges, etc., where a very high level of integrity is required.

Part of the potential of the AE technique was recognized early in the study of acoustic emission, and the first documented application to an engineering structure was published in 1964 [3], only 11 years after the first major laboratory investigation of the phenomenon by Kaiser [4]. It is important to realize several points. In the mid-1970's industrial experience with AE had been accumulated over a relatively short time compared with established nondestructive evaluation (NDE) techniques. Not until now has sufficient experience been gained to assess the usefulness of AE for NDE. During the early applications of AE, the technique was used without a full understanding of its physical basis. Some mistakes were made and, together with enthusiasm and commercial pressure in the early days, these led to

---

**About the Authors, Paper:** D. G. Eitzen is leader of the Ultrasonic Standards Group in the Mechanical Production Metrology Division, part of the NBS Center for Manufacturing Engineering, while H. N. G. Wadley leads the Nondestructive Characterization Group in the Metallurgy Division, NBS Center for Materials Science. The program on which they report was jointly sponsored by NBS and the Electric Power Research Institute. Additional support was received from the Office of Naval Research.

---

<sup>1</sup> Figures in brackets refer to references at the end of this paper.

extravagant claims for the technique, inappropriate tests and uncritical interpretation of data. In the inevitable disillusionment that followed in the mid-1970's the temptation was to dismiss the technique itself rather than to question the validity of the early experiments. More realistically, there was insufficient reliable evidence to make a valid scientific judgment then.

On the one hand, the technique did successfully solve some very important problems such as leak detection, the determination of regions of structures which require further detailed inspection, and the acceptance testing of glass fiber reinforced structures. Thus, even in its mid-1970's form AE was undoubtedly a cost-effective monitoring technique for certain industrial applications. Table 1 [5] gives some idea of the scope of these successes.

The Electric Power Research Institute and the National Bureau of Standards among others recognized certain key impediments to the development of the AE technique for monitoring the integrity of structures such as nuclear pressure vessels. These impediments included a lack of AE test data interchangeability; lack of a mathematical framework and physical understanding of the AE process; and an inability to determine the characteristics and significance of the AE source event from the processed AE signal.

The NBS program on acoustic emission commenced in November 1975 and had a goal of developing a basis for quantitative AE inspection and monitoring. The purpose of this paper is to describe, in one place, many of the research results that came out of this program (together with supporting results from a similar collaborative project at A.E.R.E. Harwell) and their potential impact on field applications. It is also to point out the remaining (more difficult) problems now limiting the potential of the acoustic emission method of assessing and monitoring the condition and integrity of high performance structures.

## 2. Framework for the Approach and Theoretical Formulation

The sequence of events giving rise to a detected acoustic emission signal can be summarized in the manner shown in figure 1. This figure showing the processes of source generation, evolution, signal transduction and signal processing is also essentially an outline of this paper. An event takes place within, or near, the surface of a structure. This event, considered the AE source, causes a dynamic force (or stress) field at the particular location (Link I). The force field change is propagated as a mechanical disturbance

**Table 1.** Number of production tests monitored by acoustic emission [5]. (Total up to 7.1.79; numbers in brackets 7.1.78-7.1.79 only.)

	Shop hydrotest	Pre-service (installed)	In-service (requalification)	On-line monitoring*
Chemical/petroleum vessels <sup>†</sup>	32 [5]	4 [0]	382 [88]	12 [4]
Chemical/petroleum systems	--	3 [0]	50 [0]	3 [2]
Chemical/petroleum components and piping <sup>‡</sup>	1548 [812]	34 [28]	57 [25]	14 [8]
Nuclear reactor vessels <sup>†</sup>	24 [1]	4 [0]	5 [2]	4 [0]
Nuclear power plant systems	--	22 [0]	9 [0]	--
Nuclear components and piping	8 [0]	22 [1]	1037 [26]	99 [64]
Nonnuclear power plant components	2 [0]	--	5 [2]	17 [16]
FRP vessels <sup>†</sup>	595 [135]	47 [14]	75 [70]	12 [12]
FRP components and piping	23 [23]	303 [300]	12 [12]	--
Storage tanks	46 [1]	29 [6]	68 [14]	1 [0]
Cell liners	--	--	12 [0]	4 [0]
Rocket cases (missiles, etc.)	208 [2]	--	--	--
Autoclaves	2 [0]	1 [0]	33 [18]	11 [3]
Misc. pressure vessels <sup>†</sup>	17 [11]	2 [0]	107 [30]	--
Misc. components	2860 [360]	4 [3]	240 [240]	230 [34]
Structures (bridges, cranes, etc.)	--	14 [12]	85 [14]	4 [1]
Heat exchanger tubing (ft)	231,000	--	500 [500]	--
Liquid and gas pipelines (ft)	58 [5]	1000 [0]	517,000 [46,000]	2002 [2000]
Drill pipe (ft)	961,000 [961,000]			

\*On-line surveillance of operating systems or components.

<sup>†</sup>Excludes experimental vessels.

<sup>‡</sup>Tested separately from a system test.

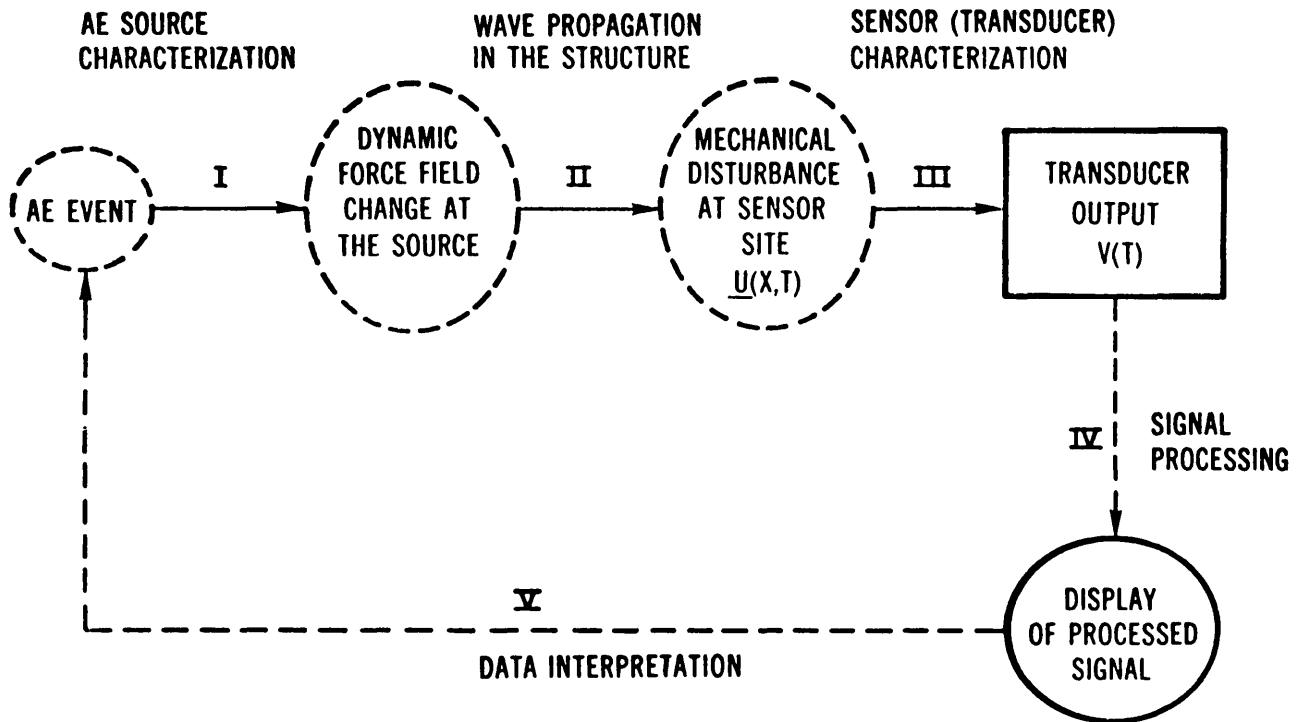


Figure 1—The causal chain of acoustic emission signal analysis.

throughout the structure (Link II). The sensor, usually a piezoelectric transducer mounted at a particular location on the structure, detects the disturbance and produces an output voltage as the detected AE signal (Link III). The goal of AE signal analysis, then, is to identify through a proper choice of signal processing and display (Link IV), the character and significance of the event (Link V).

Achieving this goal is difficult, even though the final output of the detected and amplified signal—a time-dependent voltage—can be recorded and processed, and this is because the characteristics of the source are essentially unknown in as much as they are modified by the structure and sensor. The wave propagation in the structure is affected by interaction with material properties, inhomogeneities, geometrical arrangement of free surfaces, and loading conditions. The complexity of these interactions usually forbids detailed analysis. Furthermore, conventional sensors are made of piezoelectric ceramic materials. Although the electromechanical conversion process of a piezoelectric element is understood in principle, the determination of the mechanical-electrical transfer function of individual transducers has not been possible in the past [6]. In summary, in the mid-1970's the signal flow through the AE system chain was viewed as though completely inside a black box. Only the output signals were available for processing, and

experimentally, only the loads applied and the specific geometry of the specimen were subject to control.

The first requirement of theory was the development of a framework for the quantitative description of acoustic emission from defects and other sources. To begin this, we note that AE consists of elastic waves generated by the release of stored elastic energy. The literature on elastic waves from a dynamic source in an elastic body extends over the fields of dislocation theory [7-9], dynamic fracture [10], and theoretical seismology [11,12]. Since the waves due to AE have the same character as earthquakes except for the scale, the study of acoustic emission is similar to seismology.

## 2.1 The Transfer Function Formalism

The framework for describing the acoustic emission process was developed using a Green's function approach. This approach was specialized to localized, "pseudopoint" sources which admit a transfer function formalism over a restricted bandwidth, called the "informative bandwidth." In essence this permits the replacement of the convolution integral of a Green's function and a stress history in the time domain with the product of a transfer function and the transform of the stress history in the frequency domain. Viewed in the frequency domain, information is transmitted

independently, frequency by frequency, so that filtering and other digital signal techniques can be employed to separate useful signals from noise. The virtues of using a frequency method for source characterization have also been discussed by Stephens and Pollock [13] and by Tatro [14].

After an AE disturbance occurs, the wave character of the disturbance is altered by propagation through the structure, and is further modified when the local wave disturbance is converted to a voltage by a transducer and then processed, figure 2. A prediction of the output voltage in terms of the source and intervening structure is a description of the forward problem (conversely, the inverse problem is the determination of the source from measured voltage waveforms).

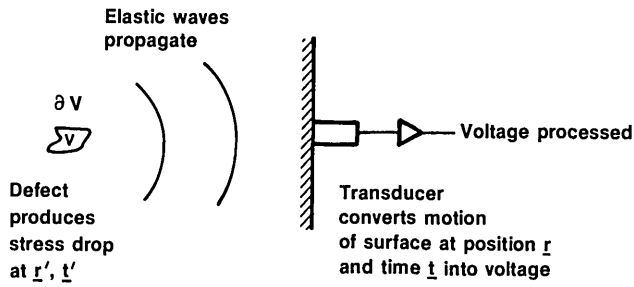


Figure 2-Schematic of AE generation and detection process.

In the time domain, the surface motion due to an AE event is given by the combined effect of the stress rate and traction rate history convolved with the appropriate Green's functions and integrated over the volume and surface of the structure. More formally, given the configuration in figure 2 Simmons and Clough [15] have shown that the displacement vector  $u_i(\underline{r}, t)$  at time  $t$  and position  $\underline{r}$  in a volume  $V$  with boundary  $\partial V$  and surface normal  $\underline{S}'$  due to a source at time  $t'$  and position  $\underline{r}'$  is characterized by a stress rate  $\Delta\dot{\sigma}(r', t')$  and a surface traction rate  $\Delta\dot{\tau}(\underline{r}', t')$ :

$$u_i(\underline{r}, t) = \int d\underline{r}' \int G_{ij,k}^H(\underline{r}, \underline{r}', t-t') \Delta\dot{\sigma}_{jk}(\underline{r}', t') dt' - \int ds'_k \int G_{ij}^H(\underline{r}, \underline{r}', t-t') \Delta\dot{\tau}_{jk}(\underline{r}', t') dt', \quad (1)$$

where the quantities  $G_{ij,k}^H(\underline{r}, \underline{r}', t-t')$  are the partial derivatives at  $\underline{r}'$  in the  $\underline{k}$  direction of the Heaviside elastic Green's tensor<sup>2</sup>. The components of  $G_{ij}^H(\underline{r}, \underline{r}', t-t')$  are the displacements in the  $i$  direction as a function of time,  $t$ , at the point  $\underline{r}$ , due to a step function point force applied in the  $j$  direction at  $(\underline{r}', t')$ .

<sup>2</sup> Capped subscript indices refer to space-time variables ( $k=1,2,3,4$ ) and uncapped indices refer to space variables ( $j,k$ , etc. = 1,2,3).

Equation (1) is more general than need be to describe acoustic emission since it contains within its compass the entire stress history of the structure, both static and dynamic. Acoustic emission sources are generally considered to be sharply limited in spatial extent and are usually measured over some limited frequency range because of noise and instrumentation limitations. Also, it is possible to ignore surface traction changes (although many spurious emission sources, such as frictional slipping of the body or surface oxide cracking, are of this type). Thus, the second term in eq (1) may be omitted to obtain:

$$u_i(\underline{r}, t) = \int d\underline{r}' \int_V G_{ij,k}^H(\underline{r}, \underline{r}', t-t') \Delta\dot{\sigma}_{jk}(\underline{r}', t') dt', \quad (2)$$

which is a convolution of a time varying dipole density ( $\Delta\dot{\sigma}_{jk}$ ) and the spatial derivatives of the Green's tensor. It is still difficult to evaluate this expression in general if  $\Delta\dot{\sigma}$  is extended over a substantial distance since it requires calculation of the Green's tensor between each source and receiver point. It is further complicated by the possibility that, in general, each stress drop (or dipole density) component could, in principle, have a different temporal behavior.

These problems can be avoided by introducing the following simplifications that are expected to be valid for the majority of acoustic emission sources encountered in practice: 1) approximate distributed sources by a Taylor's expansion about a point  $\underline{r}'_0$  (the source centroid position) and 2) assume that all stress drop components have identical temporal behavior (an approximation first developed in seismology). It then follows that:

$$u_i(\underline{r}, \underline{r}_0, t) = \int G_{ij,k}^H(\underline{r}, \underline{r}'_0, t-t') \overline{\Delta\dot{\sigma}_{jk}}(t') dt', \quad (3)$$

where  $\overline{\Delta\dot{\sigma}_{jk}}$  is the space averaged stress drop considered to be distributed on the point  $\underline{r}'_0$ .

In order to complete this derivation, it is necessary to model the response of the transducer and instrumentation. The approximation made was that of a "nondisturbing" transducer monitoring a given area of the body,  $S_T$ . By "nondisturbing" is meant that the change in the waveform caused by the presence of the transducer could be neglected because it is small compared with the magnitude of the waveform itself. If the transducer is considered sensitive to displacement its point-by-point impulse response function can be denoted by  $TP_i(\underline{r}, t)$ ,  $\underline{r} \in S_T$ . This refers to the voltage at time  $t$  produced by a delta-function displacement in the  $i$ -direction at the point  $r$  at time

zero. With this definition, the voltage at time  $t$  due to the emitting source is given by:

$$v(t) = \iint TP_i(\vec{r}, t-t') G_{ij,k}^H(\vec{r}, \vec{r}_0, t-t') \overline{\Delta\sigma}_{jk}(t') d\vec{r} dt'. \quad (4)$$

In the frequency domain, eq (4) becomes the *transfer function formalism*:

$$v(\omega) = T_{jk}(\omega) \overline{\Delta\sigma}_{jk}(\omega) \quad (5)$$

where  $T_{jk}(\omega)$  is defined by combining the transfer tensor of the structure and instrumentation while  $\overline{\Delta\sigma}(\omega)$  is the stress drop (or dipole density) tensor of the source. We note that the integration over the transducer face has a tendency to cancel out “high” frequency components (those with wavelength comparable with the transducer diameter) in the signal; it acts as a (*de facto*) low-pass filter. This transfer function approach, eq (5), has a number of important consequences:

1. By far the most important consequence of the transfer function formalism is that information about the source is passed frequency by frequency to the output through the transfer tensor, a consequence of a linear system. For acoustic emission to be detectable, then, the transfer tensor must have significant components in that frequency band where the signal-to-background noise ratio for the source history is highest. One can expect, then, to gain only the information about the source history that is contained in that frequency band. By maximizing this useful band, one maximizes the possibility of finding enough information about the source to detect its signature. On the other hand, in certain situations no significant information about the source may pass to the output. For instance, in ductile and brittle materials comparable stress drops occur, but since the time scale of the ductile fracture process is longer, most information will be sent at lower frequencies—often below those that are usually measured so that one finds “no acoustic emission” [16,17].
2. Because the complex voltage  $v(\omega)$  consists of the sum of a series of terms, phase interference effects are important. Owing to this, simple amplitude spectrum analysis will be invalid except for single time parameter sources.
3. Because of the number of stress rate components that must be separated from one

another, multichannel measurements generally are needed to find an unknown source. This can mean from six channels, if a point source approximation with six independent components is used, up to 15 channels if the dipole terms, density changes, and surface monopole sources are included.

In the case of multichannel measurements, the transfer function relation can be written as

$$v^\Gamma(\omega) = T_{jk}^\Gamma(\omega) \overline{\Delta\sigma}_{jk}(\omega) \quad (6)$$

where  $v^\Gamma$  is the voltage output of the  $\Gamma$ th transducer and  $T^\Gamma$  is the system transfer function.

If additional information is known about the source (e.g., its orientation and mode) then the number of channels is greatly reduced. For example, quantitative characterizations of acoustic emission have been reported for only a single information channel. The deduction of source properties from acoustic emission signals is referred to as the inverse problem here. An example of the solution of this AE inverse problem was first given by Hsu, Simmons, and Hardy [1]. Further examples were given by Hsu and Hardy [18] and the method was detailed by Hsu and Eitzen [18]. Simmons [20] and Simmons and O’Leary [21] have developed alternative inverse schemes using special decomposition and transform methods.

### 3. The Source

In early applications of AE to pressure vessel testing there was little or no understanding of the origin of acoustic emission signals. Later tests revealed the great weakness of this when it was found that steels used in pressure vessels often failed to give detectable AE even though crack growth clearly occurred.

Laboratory studies have more recently shown that in steels in the conditions likely to be encountered in pressure vessels, the following signal amplitudes could be generated: weak AE signals by plastic deformation, signals of moderate amplitude by the decohesion and/or fracture of inclusions such as sulphides and silicates, and signals with a wide range of amplitudes from crack growth depending upon the local microstructure state [22]. Plastic deformation and inclusion decohesion/fracture can occur during plastic zone formation at the tips of flaws. Using the theoretical formalism developed in Section 2, it is now possible to estimate the AE amplitudes that each type of source would generate.

It has recently [23,24] been shown that the stress change  $\Delta\sigma$  due to the motion of a dislocation is proportional to the distance moved ( $a$ ) and mean velocity ( $v$ ). Using eq (3) it can be concluded that the peak displacement amplitude  $u$  is given by

$$u = \frac{kav}{h} \quad (7)$$

where  $k$  depends on material characteristics and geometry and  $h$  is the distance from the source. For dislocations in steel it has been estimated [23] that  $k \approx 10^{-14}$ . From this it is possible to deduce the weakest detectable source. If a detector is positioned a distance  $h$  from the source, and has a displacement sensitivity threshold of  $x$  then  $av > 10^{14}hx \text{ m}^2\text{s}^{-1}$  for the dislocation to be detected. Measurements of background noise indicate that in the laboratory the smallest detectable displacement is  $\sim 10^{-14}$  m, while in the field it is no better than  $10^{-13}$  m. Then, the smallest detectable dislocation loop at a depth of 100 mm must have  $av \geq 1 \text{ m}^2\text{s}^{-1}$ . Even if the velocity were  $\sim 3000 \text{ ms}^{-1}$  (the theoretical limit is the shear wavespeed,  $\sim 3000 \text{ ms}^{-1}$  in iron and steels), a single dislocation must propagate  $\sim 0.3$  mm for detection. This is much greater than the distance usually moved by a single dislocation [25] and can therefore be discounted as a potential emission source in most structures. However, energetic burst emission during the yield deformation of a number of quenched ferritic steels tempered at 200 to 300 °C has been reported [26]. This has been attributed to the cooperative motion of groups of hundreds or thousands of dislocations. This source, however, occurs over a narrow range of microstructures likely to be encountered only near welds that have been improperly stress relieved. Heavily irradiated metals are susceptible to deformation by dislocation channeling. While the precise mechanisms for this are still not fully resolved, it is possible they may involve a cooperative slip process similar to that of critically tempered material. Thus, irradiated materials undergoing deformation might generate more acoustic emission and this could be why the acoustic emission activity of growing flaws in irradiated material is found to be greater than that of flaw growth in unirradiated material [27].

The fracture (or decohesion) of precipitates and inclusions as a plastic zone sweeps ahead of a flow are candidates for generating detectable emission. Let us suppose that the microfracture event can be approximated by the formation of a "penny-shaped" crack which grows from zero to radius  $a$  at a velocity  $v$  under an applied stress  $\sigma$ . Then for the event to be

detected by a transducer with detection threshold  $x$ , at a distance  $h$  from the source, it can be shown [23]  $\sigma a^2 v > 5 \times 10^{14} hx$  (watts). Thus, for  $h = 100$  mm and  $x = 10^{-13}$  m,  $a^2 v > 5$  watts. Thus detected amplitude is proportional to the rate of release of elastic strain energy. Assuming a local stress of  $500 \text{ MNm}^{-2}$  and an intermediate crack growth velocity of  $100 \text{ ms}^{-1}$ , yields  $a \approx 3 \text{ }\mu\text{m}$ . Carbide particle sizes in steels [25] are  $\leq 1 \text{ }\mu\text{m}$ ; their fracture is therefore below the level of detection unless they fracture at very high velocity. But inclusions are sufficiently large to be detectable.

Inclusion size, volume fraction, and morphology can vary considerably from place to place in large steel structures due to macrosegregation during ingot solidification. These inclusions, initially spheroidal in castings, become extended during rolling into strings with lenticular shapes. In plate material a typical inclusion in the string might be as large as  $1 \text{ mm} \times 100 \text{ }\mu\text{m} \times 10 \text{ }\mu\text{m}$ , the long axis being parallel to the rolling direction. Thus, the fracture of  $100 \text{ }\mu\text{m} \times 10 \text{ }\mu\text{m}$  cross-section of the inclusion would be above a detection threshold of  $10^{-13}$  m. If the inclusions are strongly bonded to the steel matrix the decohesion of a  $1 \text{ mm} \times 100 \text{ }\mu\text{m}$  face is likely to occur at a lower stress. Nevertheless the large surface area is likely to assure detection even at stresses as low as  $1 \text{ MNm}^{-2}$ .

We conclude that, while deformation of unirradiated low alloy steels, or fracture of spheroidal carbides will not be detected, the decohesion and fracture of large inclusions probably is detectable. It is likely to be the single most important emission source during plastic zone development ahead of a flaw in tough low alloy steels.

Applying the above model to the extension of a flaw by microcracking (with the same detection limit of  $10^{-13}$  m displacement and a stress of  $10^9 \text{ Nm}^{-2}$ ), crack advance at the shear wave velocity approximately of  $\sim 3000 \text{ ms}^{-1}$  in steel would be detectable if the new crack area was  $> 2 \text{ }\mu\text{m}^2$ . At a more realistic velocity for a brittle advance ( $v \sim 500 \text{ ms}^{-1}$ ), the minimum detectable crack increment would be  $\sim 10 \text{ }\mu\text{m}^2$ . It might therefore be possible to detect crack advance of about  $1 \text{ }\mu\text{m}$  provided the advance takes place over more than  $10 \text{ }\mu\text{m}$  of crack front, making the acoustic emission technique the most sensitive NDE method available for detecting *growth* of a flaw. During continuous monitoring, ambient noise levels and hence detection thresholds are far higher than in the laboratory. The literature does not provide data on the absolute levels, but assuming for instance an increase by a factor of 100 resulting in a detection threshold of  $10^{-11}$  m, the minimum detectable crack advance becomes  $\sim 1000 \text{ }\mu\text{m}^2$  at a distance of 100 mm

from the receiver (i.e., fracture of a 30  $\mu\text{m}$  diameter grain).

In general, crack advance occurs if the stress at any pre-existing flaw exceeds a critical value determined by the toughness of the material, the local stress and the size and orientation of the flaw. Crack growth will normally occur by the ductile dimple mechanism at temperatures above the ductile-to-brittle transition temperature, and by transgranular (cleavage) or intergranular fracture in the less probable event of crack advance below the transition temperature or in a locally embrittled region. In the event of cleavage crack advance, fracture of a grain (typically 30  $\mu\text{m}$  dia) would generate large amplitude signals, as would intergranular fracture along several grain facets. More generally there is likely to be a range of crack areas and velocities generating detectable emission. Scruby and Wadley [28] made an attempt to represent these (fig. 3) in the form of a map that visually indicates the likelihood of detectability. All the estimates assumed an isolated microcrack. Recent work [29] has shown that the effect of a precrack, which would be present in the practical case, is one of a "sounding-board" for the AE event, enhancing its apparent amplitude in the frequency range of observation. An "amplification factor" of about 10 has been determined by experiment, so that correspondingly smaller crack

increments should be detectable or the same sized events detectable from further away.

Turning now to the more usual forms of constructional steel fracture, it is necessary to distinguish two modes of ductile fracture. In material of low work-hardening capacity, for instance in the heat-affected zone of a weld, or following radiation embrittlement, fast shear of inter-inclusion ligaments may occur. This occurrence involves crack advances of 100  $\mu\text{m}^2$  or more and is likely to be detectable if the crack velocity exceeds  $\sim 50 \text{ ms}^{-1}$ . Such a source has been observed [30]. In material of higher work-hardening capacity, inter-inclusion and inter-carbide ligaments neck down until they finally part. This process occurs slowly and involves final separations over relatively small areas comparable with the inter-carbide spacing. The product  $a^2v$  is likely therefore to be below the detection threshold, and the quietness of this ductile dimple fracture has been confirmed experimentally many times [22].

It should be noted, however, that ductile crack growth is accompanied by the expansion of a plastic zone. Thus, although the crack advance mechanism itself may be quiet, there may be detectable AE from decohesion or fracture of inclusions as the plastic zone expands.

In service, sub-critical crack growth is most likely

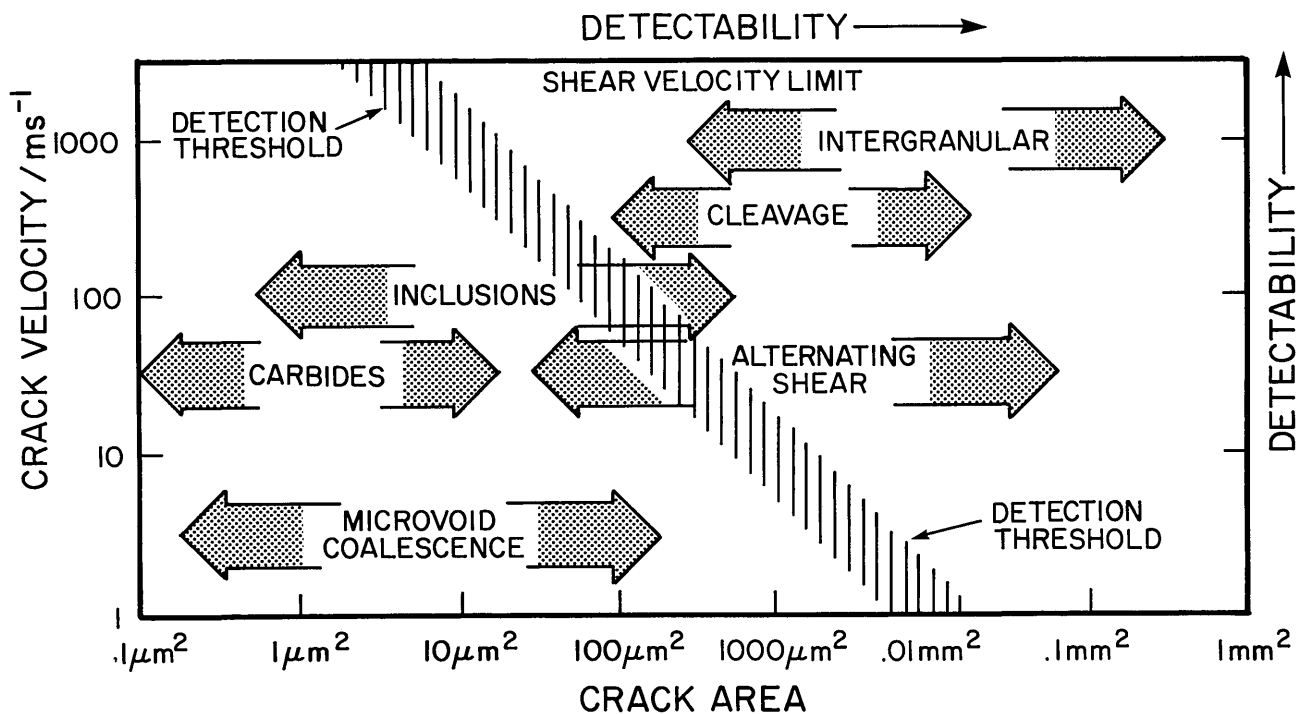


Figure 3—Detectability of fracture events in steels. Detection threshold assumes transducer compression wave sensitivity of  $10^{-13}$  m, source-transducer distance 0.1 m, stress  $500 \text{ MNm}^{-2}$ .

to occur under fatigue loading, possibly assisted by the environment, i.e., corrosion fatigue. During the fatigue of low alloy ferritic steels, crack advances as large as  $\sim 1 \mu\text{m}$  in a fatigue cycle are possible. Provided the advance takes place over at least  $10 \mu\text{m}$  of the crack front and at a velocity  $> 500 \text{ ms}^{-1}$ , detectable AE should be generated. Environmental effects and embrittlement by, for instance, hydrogen, in addition to possibly changing the fracture mode, also enhance the AE activity from crack growth. Under these conditions McIntyre and Green [31], for example, have shown that AE activity is proportional to crack extension.

In order to measure the reliability of flaw detection by AE, more experiments are required. Of particular importance are tests to determine the AE from fatigue and corrosion fatigue mechanisms in both base plate material and in and near weldments under realistic conditions of stress and temperature. Simultaneous, independent measurements of crack advance also must be made during these experiments.

## 4. Wave Propagation

### 4.1 Calculation of Elastic Wave Propagation in a Plate Specimen

The interpretation of source signatures requires a fully instrumented and well characterized laboratory experiment incorporating a structure whose wave propagation characteristics are known. The simplest geometry with practical relevance is a plate. Simmons et al. [32], and independently Pao et al. [33], thus set about the task of developing the mathematical and numerical framework for determining wave propagation in a plate; i.e., they calculated the dynamic elastic Green's tensor for an isotropic elastic plate.

Previously, only Green's tensor solutions for the elastic whole-space and half-space were available and experimental time records could only be compared with theory for short periods of time (a few microseconds for a convenient-sized test block) in geometries (plates) that resembled engineered structures. Two features of the solution for the plate were as follows:

1. The derived solution was a complete Green's tensor of an infinite plate in the sense that the vector displacement at an arbitrary point, due to any arbitrarily oriented point force with step function time dependence, could be numerically calculated.

2. It was in the form of an infinite series expansion, usually called a generalized ray expansion in geophysical applications where similar problems have been treated [34,35]. This series is not an approximation (like normal modes).

The objective was to develop usable representations for the response of an elastic plate to a point force with step function time dependence. Since no completely closed solution is possible, the approach had to be amenable to computation. Two approaches were feasible. The first, designated in the seismological literature as a "ray theory" method, explicitly takes account of each wave reflection and is useful for short times after the initial application of the force. The second approach is to study the normal modes of the plate and to find what mode combinations are excited by the given source. The first approach has been implemented at NBS.

Consider the problem defined by the equations of motion:

$$\frac{\partial \sigma_{ij}}{\partial x_j} + f_i \delta(x_1) \delta(x_2) \delta(x_3 - z) H(t) = \rho \frac{\partial^2 u_i}{\partial t^2} \quad -h < x_3 < h \quad (8)$$

and the boundary conditions:

$$\sigma_{i3} = 0 \quad x_3 = \pm h \quad (9)$$

where the stress  $\sigma_{ij}$  is related to the displacement gradient  $\partial u_i / \partial x_j$  by:

$$\sigma_{ij} = C_{ijkl} \frac{\partial u_k}{\partial x_l} \quad (10)$$

The summation convention is employed,  $\delta(x)$  denotes the Dirac delta function and  $H(t)$  is the Heaviside step function. The plate is assumed to be at rest until the instant  $t=0$ .

The solution of eqs (7) to (9), may be written in the form:

$$u_i = G_{ij}^H f_j \quad (11)$$

where the "Heaviside Green's tensor"  $G_{ij}^H$  represents the  $i^{\text{th}}$ -component of displacement produced by a unit point force  $H(t)$  applied in the  $j$ -direction. Thus,  $G_{ij}^H$  satisfies the equations:

$$C_{ijkl} \frac{\partial^2 G_{kp}^H}{\partial x_j \partial x_l} + \delta_{ip} \delta(x_1) \delta(x_2) \delta(x_3 - z) H(t) = \rho \frac{\partial^2 G_{ip}^H}{\partial t^2} \quad -h < x_3 < h \quad (12)$$

and

$$C_{\beta kl} \frac{\partial G_{kp}}{\partial x_i} = 0 \quad x_3 = \pm h. \quad (13)$$

The final task is to find explicit representations for  $G_{ij}^H$ . The ray approach represents  $G^H$  as the sum:

$$\mathbf{G}^H = \mathbf{G}^\infty + \mathbf{G}^{\text{im}} \quad (14)$$

where  $\mathbf{G}^\infty$  is the (readily calculable) infinite-body Heaviside Green's tensor, and  $\mathbf{G}^{\text{im}}$  is the "image" tensor induced by the free boundaries at  $x_3 = \pm h$ .  $\mathbf{G}^{\text{im}}$  is thus composed of all possible reflections of the waves generated by  $\mathbf{G}^\infty$ , and the ray method represents  $\mathbf{G}^{\text{im}}$  in this form.

The physical meaning of each ray is quite straightforward. If the initial source function is broken into its characteristic components—longitudinal (*P*), horizontal polarized shear (*SH*), and vertical polarized shear (*SV*)—then each of these components can be followed through a series of reflections at the top and bottom faces of the plate until the receiver is reached, at which time they can be recombined. One ray is the contribution of one such component followed through a particular series of reflections—taking into account mode conversion wherein longitudinal or vertical shear components split into each other at each reflection. All rays arriving at the same time at the receiver can be grouped together and classed by arrival time.

Although the derivation of the Green's function is based on an infinite plate, the solution is exactly applicable to a finite plate for a finite period. This period corresponds to the first arrival of the ray reflected from the sides of the plate or to the number of terms used in the ray expansion.

#### 4.2 Examples of Green's Function Components for Point Monopole and Dipole Sources in a Ferritic Steel Plate

The Green's tensors for a ferritic steel plate are used as input to both the forward and inverse AE problems; however, a great deal can be learned about wave propagation by inspection of the Green's tensors themselves. The tensor components of the Green's function are informative because they give the displacement-versus-time response of the structure due to a point force input. While this input may or may not represent some AE sources, the response indicates which surface displacement directions are active, how

the response changes relative to the source and sensor locations, how the source signal changes, and how much information is potentially available. The Green's function for a (double-force) dipole source, equal and opposite forces at a point, provides additional information on questions discussed above and information on how the surface displacements available for measurement change due to a change in source function. The dipole source also provides a simple model for some AE events.

As before, the Green's function tensor is designated by  $\mathbf{G}$  and the component functions, the displacements in a given direction due to a point-force source in a given direction, are designated by  $G$  with two subscripts, for example,  $G_{13}$  or  $G_{23}$ . As shown in figure 4, the subscript number 3 designates a direction normal to the plate surface; the subscripts 1 and 2 designate orthogonal directions in the plane of the plate surface. Thus,  $G_{13}$  describes the displacement in the plane of the plate due to a point force normal to the plate and  $G_{33}$  describes the normal displacement due to a normal force. We note that since the components represent displacements in the  $j$  direction due to a force in the  $i$  direction, the reciprocity theorem of elasticity applies and  $G_{ij} = G_{ji}$  so that, for example,  $G_{13} = G_{31}$ .

The displacement response due to a force *dipole* is designated by three subscripts on  $G$  for example,  $G_{31,1}$  which represents the displacement normal to the structure due to collinear equal but opposite forces in the plane of the structure.

Figures 4 to 10 are examples of displacements arising from point force step and force dipole step sources at the top and bottom of a nominal 2.5 cm plate of A533B pressure vessel steel. A complete set of responses was calculated using measured wave speeds for an A533B plate specimen:

$$\begin{aligned} \text{longitudinal speed} &= 3.18825 \times 10^3 \text{ ms}^{-1} \\ \text{shear speed} &= 5.85000 \times 10^3 \text{ ms}^{-1} \end{aligned}$$

Here, we present examples of these calculated responses. The first of the figures (fig. 4) exhibits the geometry and the notations for the remainder of the plots. We summarize some of the principal observations from these curves as follows:

1. Each geometrical configuration of the source (its type, orientation, and location), plate thickness and transducer (its position, directionality, and sensitivity) produce characteristic signatures which permit determination of source location and orientation, especially source depth, with improved resolution

### Case (1) Epicenter

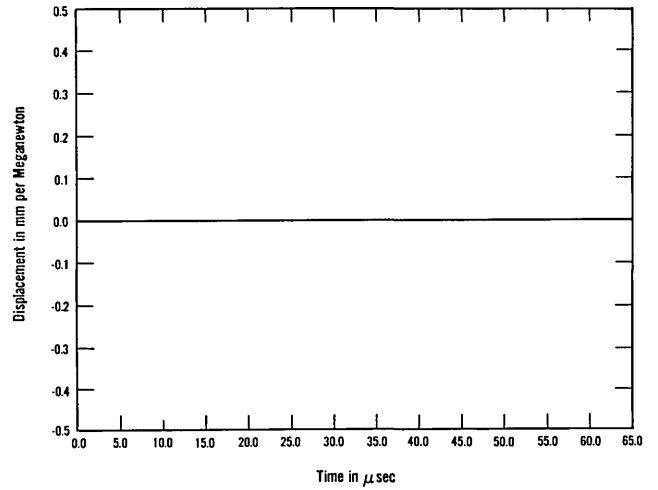
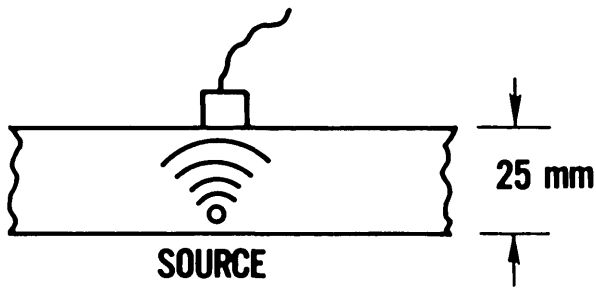


Figure 6-Displacement response  $G_{13}$  due to a point force step for case 1.

### Case (2) Top at two thicknesses

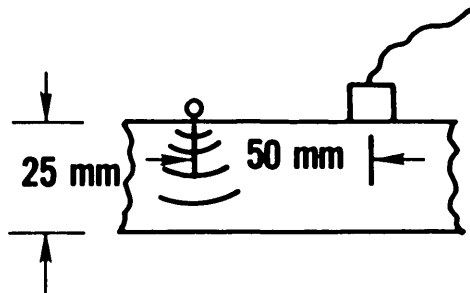


Figure 4-Source-plate-transducer configurations.

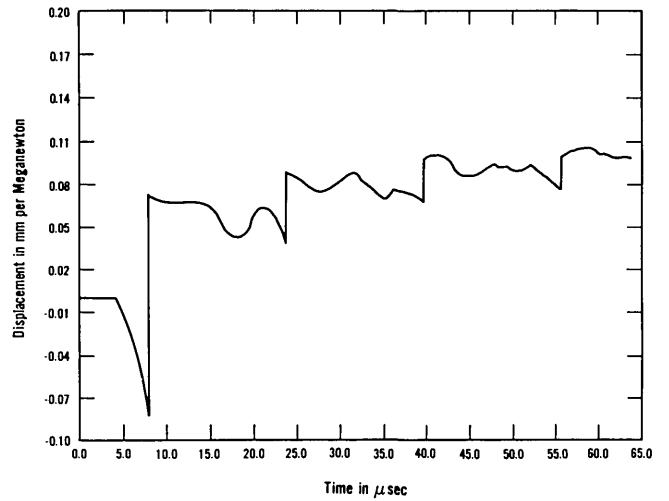


Figure 7-Displacement response  $G_{22}$  due to a point force step for case 1.

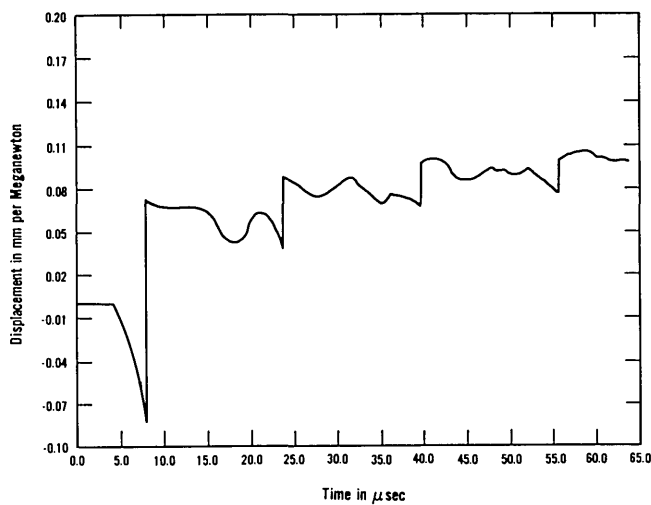


Figure 5-Displacement response  $G_{11}$  due to a point force step for case 1.

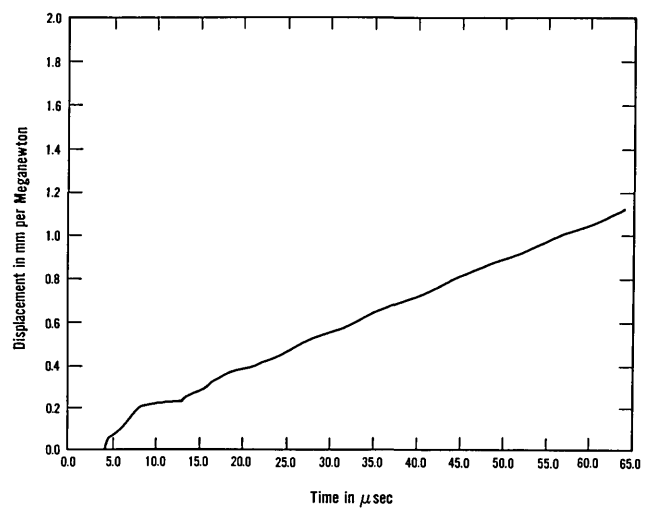


Figure 8-Displacement response  $G_{33}$  due to a point force step for case 1.

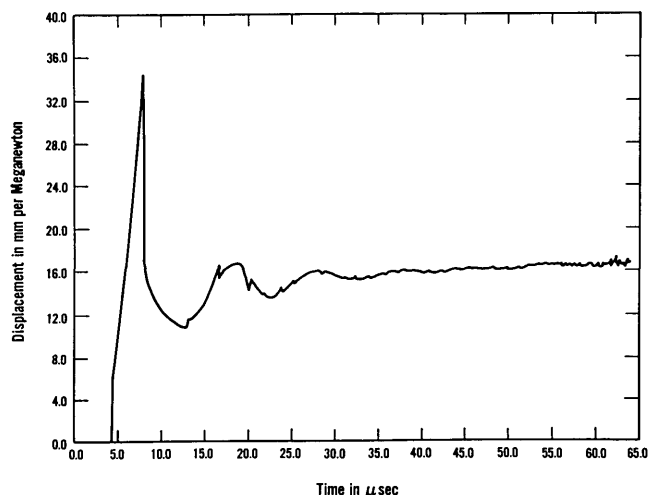


Figure 9—Displacement response  $G_{33,1}$  due to a point force step for case 1.

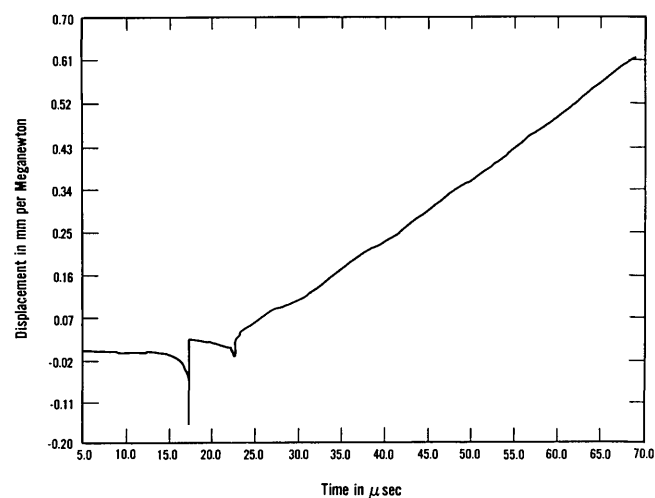


Figure 10—Displacement response  $G_{33}$  due to a point force step for case 2.

over conventional source location techniques [2]. These signatures contain many characteristic features and thus demonstrate the crudity of attempting to select a single feature, such as amplitude of the curves, especially after these undistorted curves have passed through a resonating transducer as was done in the instruments of the mid-1970's for source characterization. The spikes in the curves generally result from the arrival of wavefronts that have traveled over multiple paths so that, if their arrival times are to be used for source location, a more detailed analysis of their significance is required than is currently the case.

2. This leads to a related observation concerning the multi-axial (or vector) nature of displacements. A transducer with sensitivity to displacement in a single direction may not "see" displacements in other directions. Thus, source location, in which it is assumed that only waves with the Rayleigh velocity are observed may be grossly inaccurate. In addition, unless the vector calibration of a sensor is known, i.e., its sensitivity to displacement in each orthogonal direction, it is *not* possible to characterize the vector properties of the source. These two points underscore the importance of multi-axial (vector) transducer calibration [36,37].

## 5. Transduction

Transducers are used to convert dynamic surface displacements of transient elastic waves into electrical signals. The electrical signal resulting from the transient displacements of an AE event depends critically on the transduction process. The majority of transducers used in acoustic emission are piezoelectric crystals. Other types have been used; e.g., capacitors, laser interferometers, EMATs, etc., but these are normally too insensitive. Those used in field applications are similar in design to the transducers used in pulse/echo ultrasonic testing. To develop better instruments we must be able to characterize the measurement system. System characterization in turn leads to an understanding and improvement of the action of the transducers.

In the mid-1970's, AE transducers were not optimally designed. One part of the NBS program has centered around the use of calibration systems for the design of advanced AE transducers that are now beginning to appear commercially. The second area of transduction research at NBS has focused on the calibration/standardization itself. The numerical values of traditionally measured parameters of AE signals (e.g., event or ring-down count) depend very much upon the sensitivities, directivities, and frequency response of the transducer used. In addition, if the individual transducers of a source-locating array are of unequal sensitivity or respond differently to a particular kind of wave motion, the deduced location may be in error.

Standardization provides a basis for transducer comparison making it possible to compare the results of different tests. The need for a standard method of calibrating transducers has been stressed by the American Society for Nondestructive Testing, the

American Society for Testing and Materials, the American Society of Mechanical Engineers, and other technical organizations concerned with using acoustic emission techniques.

Many people hold strong opinions that a calibration be expressed in terms of absolute physical quantities such as open circuit volts of output per unit of surface motion at the transducer face,<sup>3</sup> the motion being that which would occur in the absence of the transducer. Another choice could be to base it on the dynamic stress resulting from the interaction of the transducer and the body on which it is mounted, but with no transducer present this surface would be traction free. However, the problem with the latter approach is that two transducers having the same sensitivity to stress, but which present different loads to the surface, would give a different output to the same mechanical input. The definition in terms of a free surface has thus been the preferred one.

In order to improve data interchangeability and to improve extraction of information from AE signals through signal processing, the NBS AE program undertook to develop:

1. An AE transducer calibration and standardization system.
2. An optimal AE transducer using the calibration facility.

### 5.1 AE Transducer Calibration System

After consulting with practitioners and researchers in the AE community it was decided first to implement a transducer calibration system using the so-called "surface-pulse" method. The development of the basic principles that make the calibration possible owes to Breckenridge, Tschiegg, and Greenspan [38].

The surface-pulse transducer calibration system [39] functions in the following way: A step-function force event is generated on the plane surface of a large elastic block by the sudden release of a nearly static force applied through a glass capillary which is released when the capillary breaks. The resulting dynamic displacements of all points on this surface can be expressed in closed form by elastic theory (Section 4) up until the arrival time of reflections from the other boundaries of the block.

The normal component of the dynamic displacement is measured using a capacitive transducer [40]

<sup>3</sup>For example, the attendees of the U.S. Acoustic Emission Working Group, San Antonio, TX, April 1975, arrived at a consensus on this point.

which is described below. Figures 11 and 12 show the theoretically calculated displacement and the average of 10 measured displacement waveforms. Satisfactory agreement between theory and measurement is observed. To perform a calibration, the capacitive transducer (standard) and the transducer to be calibrated (unknown) are placed on the plane surface of the steel block equally distant from the source. The transient electrical outputs of both the standard and the unknown transducers are recorded digitally and computer processed (deconvolved) to extract the response of the unknown transducer relative to that of the standard capacitive transducer.

Figure 13 indicates the basic arrangement. A glass capillary, B, (~0.2 mm diameter), is squeezed between the top of the loading screw, C, and the upper face of the large steel transfer block, A. When the capillary breaks, the sudden release of force is a step function, whose risetime is of the order of 0.1 μs. The magnitude of this force step is measured by the combination of the PZT disc, D, in the loading screw and a charge amplifier, E, connected to a storage oscilloscope, F. The standard capacitive transducer, G, and the transducer under test, H, are equally

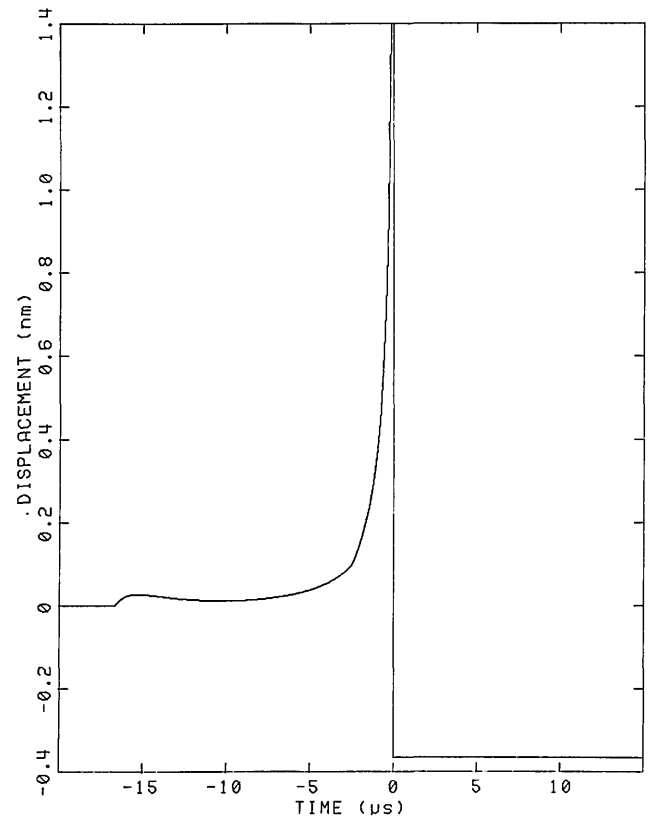


Figure 11—Calculated surface-pulse waveform for the steel block at the location of the transducer (101 mm from the source).

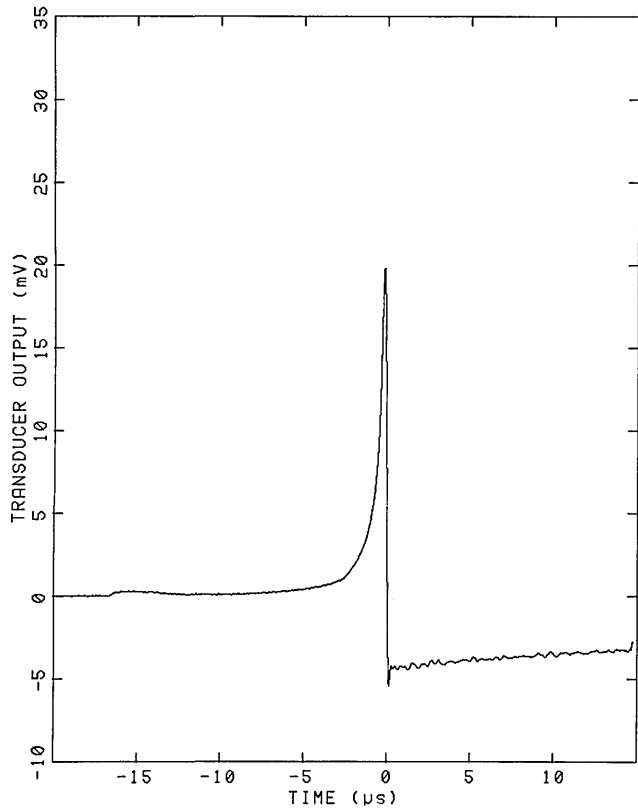


Figure 12-Experimental surface-pulse waveform obtained by averaging 10 waveforms from the transducer.

distant and on opposite sides of the source. It is obvious from the symmetry that the surface displacements would be the same at the two transducer locations if it were not for the loading effects of the transducers. The loading effect of the standard capacitive transducer is negligible and the loading effect of the unknown transducer is part of its calibration. Voltage transients from the two transducers are recorded simultaneously by digital recorders, I, and the information stored for processing by computer, J.

With this system it is possible to compare the signal from the unknown transducer with either that of the standard transducer or the calculated displacement waveform using a value for the magnitude of the step function force measured with a piezoelectric force transducer attached to the capillary loading device. The comparisons produce similar results. In either case, it is the free motion of the surface that is determined, the reference capacitive transducer providing essentially no loading [40]. The unknown transducer interacts with and loads the surface, the interaction also being dependent on the block material. These interactions are considered to be part of the calibration and so, in principle, the interpretation of the transducer output would be affected if used on a material with elastic properties different from those of the steel transfer block A.

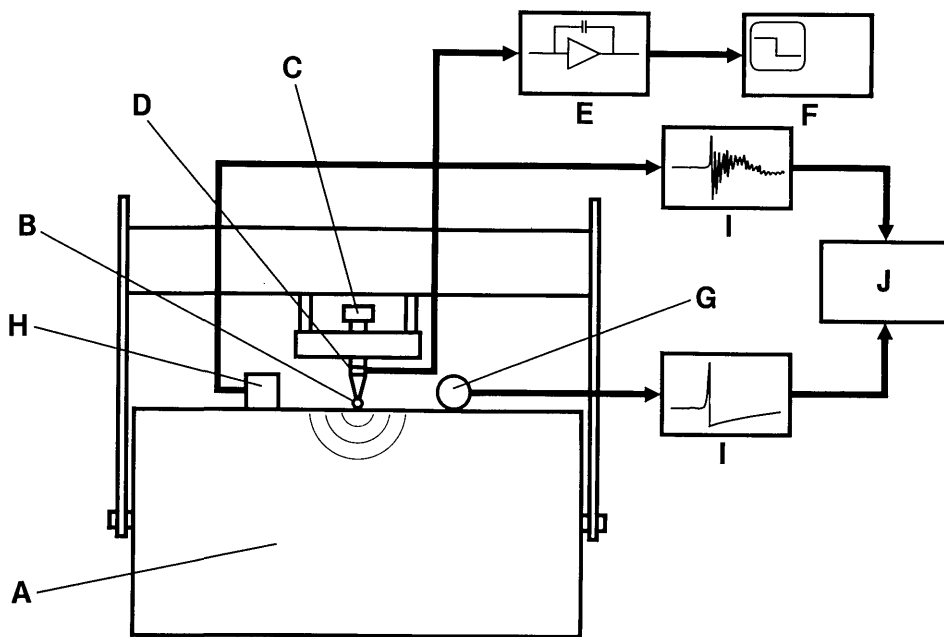


Figure 13-Schematic of the apparatus.

The frequency range for the calibration of acoustic emission transducers is nominally from 100 kHz to 1 MHz. In order to deal with frequencies as low as 100 kHz, 100  $\mu$ s of sample time is necessary to avoid computation errors. This dictates that a large transfer block be used so that sidewall reflections are delayed 100  $\mu$ s or more. The block, donated by Bethlehem Steel, is 90 cm in diameter and 43 cm thick. It weighs about 4000 kg, and is made of A508 Class 2 steel. Both faces of the block were lapped in the NBS optical shop to be spectral reflectors in order to satisfy the surface smoothness requirements of the capacitive transducer and to eliminate surface roughness or surface work-hardening effects on wave propagation.

The standard capacitive transducer (figs. 14 and 15) has three cylindrical parts separated by insulators. The center cylinder is the active electrode and the ends are electrical guards. The ends are driven by a special unity gain amplifier, whose input is connected to the center part. The sensitivity of the transducer may be calculated with an error of at most 0.6% on the basis that the active portion is part of an infinitely long cylinder. This sensitivity is one-half the polarization voltage divided by the air gap. The air gap, nominally 4  $\mu$ m, can be independently deduced from a measurement of static capacitance using a three-terminal capacitance bridge. The transducer also features built-in compliant elements remote from the active portion to minimize loading of the block. The

sensitivity limit (noise level) of the standard transducer is about  $4 \times 10^{-12}$  m.

There is a measure of redundancy built into the calibration system—provided the displacement as measured by the standard capacitive transducer agrees with the calculated displacement. Experiments to check this agreement were performed (see fig. 16) and adequately establish this redundancy in the determination of displacements.

A typical captured waveform from the standard transducer is shown in figure 17, and, for the same force event, the waveform from an unknown transducer is shown in figure 18. An FFT is performed on both of these waveforms and the resulting frequency spectra are divided, frequency by frequency. The result yields the frequency response of the unknown transducer relative to that of the standard. The results of this calibration are presented with a logarithmic scale in figures 19 and 20.

## 5.2 An Optimal Acoustic Emission Sensor

The typical response of commercially available AE transducers to transient surface displacement is shown in figure 18. Such devices have two drawbacks:

1. They tend to be sensitive to a combination of mechanical inputs (displacement, velocity, or acceleration) rather than only a single

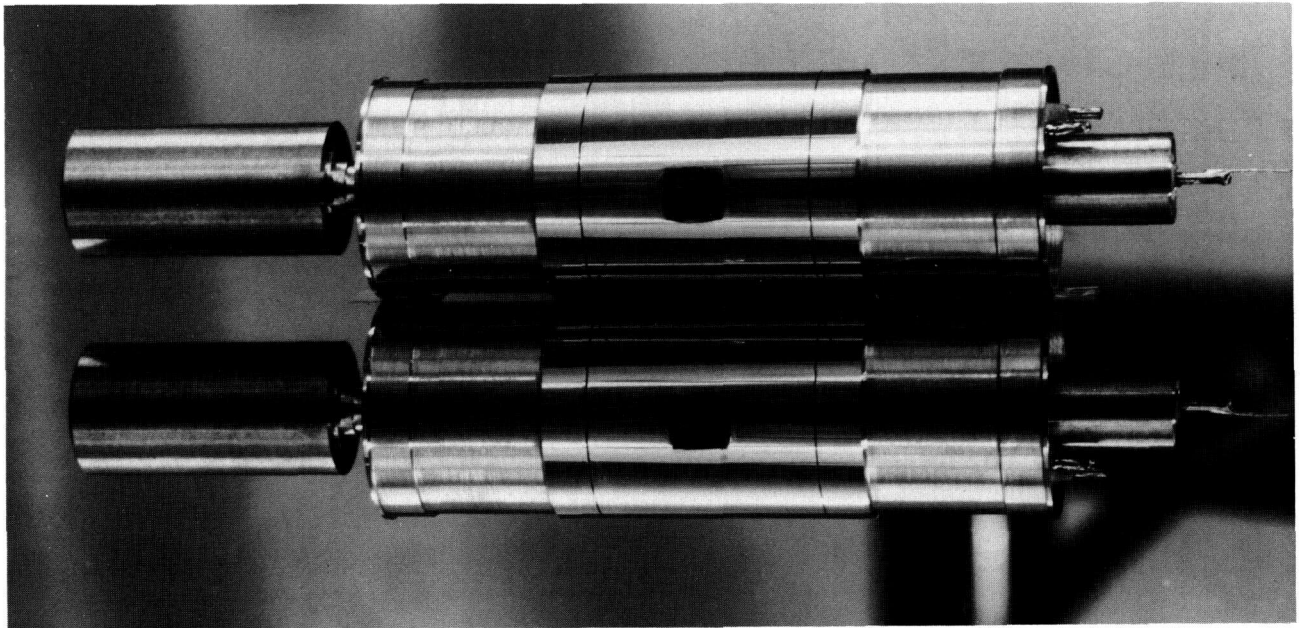


Figure 14—Photograph of the transducer and its reflection.

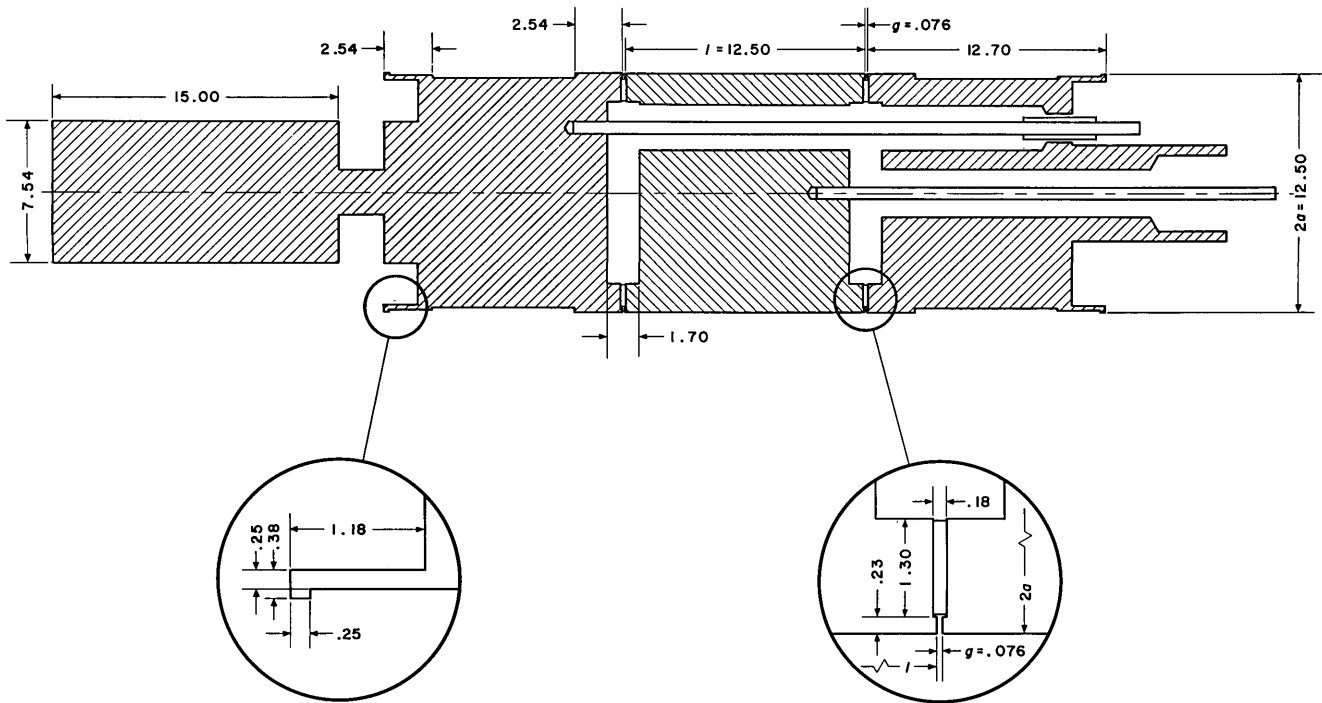


Figure 15—Longitudinal section through the transducer. All dimensions are given in millimeters. Here  $l$  is the length of the active electrode,  $2a$  is its diameter, and  $g$  is the width of the guard gap.

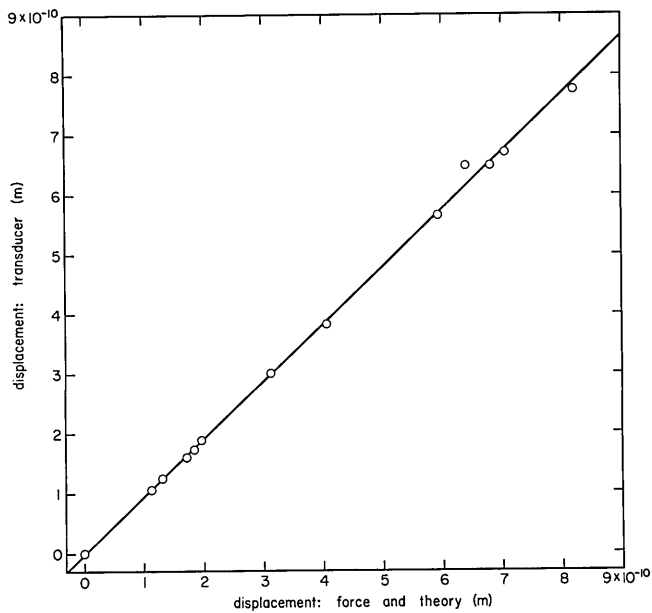


Figure 16—Comparison of the displacement measured by the capacitive transducer (ordinate) and that determined by elastic theory from measurements of applied force (abscissa): steel block. The line is a linear least-squares fit to the data shown.

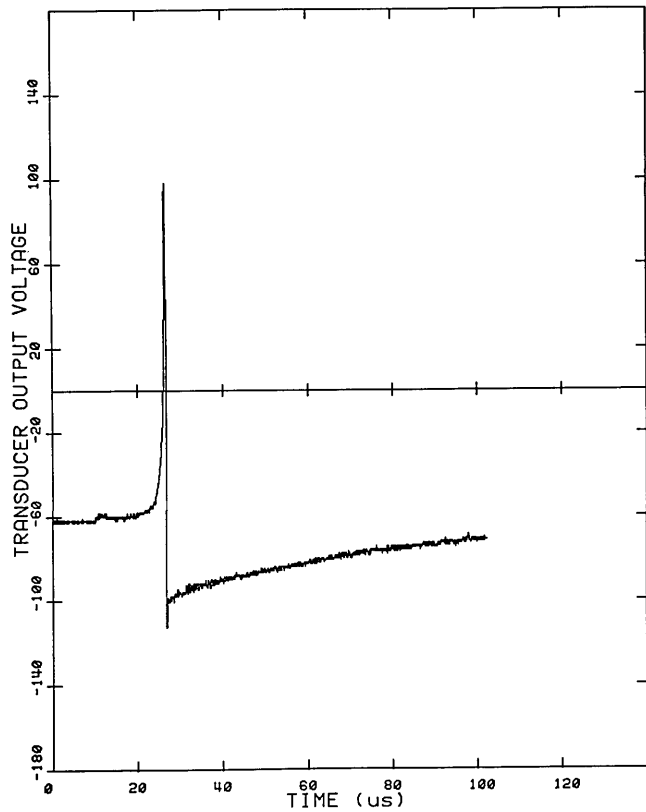


Figure 17—A typical calibration: voltage versus time waveform from the standard transducer as captured by the transient recorder.

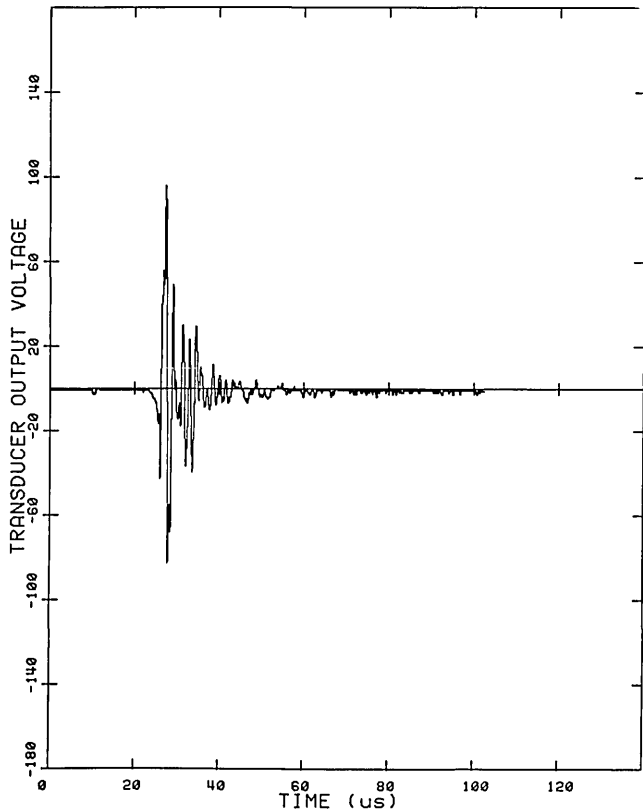


Figure 18—The same calibration: voltage versus time waveform from the unknown transducer as captured by the transient recorder.

physical quantity. As will become clear in the later discussion of source characterization, this leads to difficulties in the conceptual design and implementation of AE source determination.

2. They also tend to have large variations in sensitivity over the frequency range of interest. Regaining the information filtered out in the regions of sensitivity minima is, at best difficult, because of the poor signal-to-noise ratio at these frequencies.

The capacitive transducer described above has a flat frequency response over a wide frequency range, making possible a faithful reproduction of dynamic surface displacement. It is, however, directional, of low sensitivity, and requires a highly polished mounting surface. While it is an excellent transducer for laboratory calibration work, a need for a transducer without these limitations was evident.

The NBS conical transducer was developed in response to these needs [41–44]. One of the first models is shown in figure 21. It is a simple two-piece device consisting of a small conical piezoelectric element and a large backing, usually of brass.

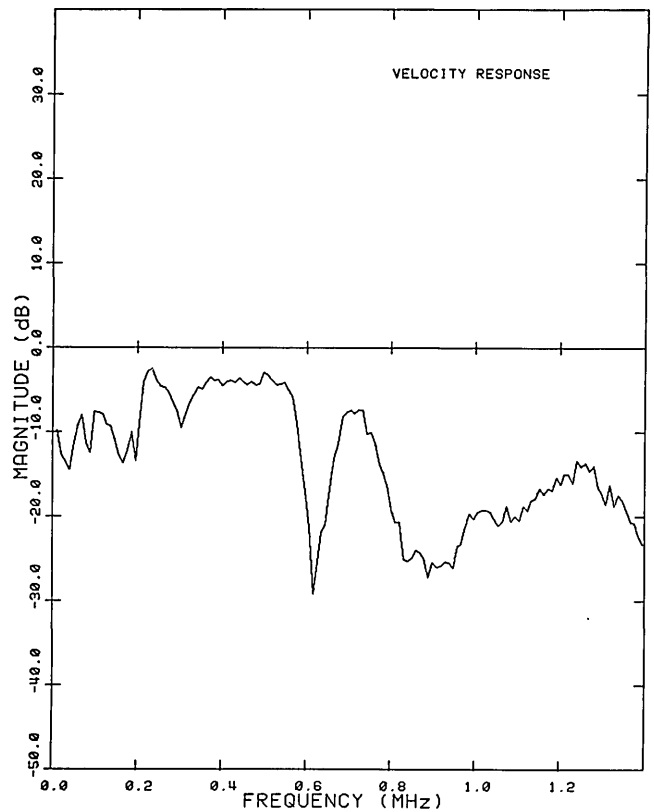


Figure 19—Magnitude response of the unknown transducer.

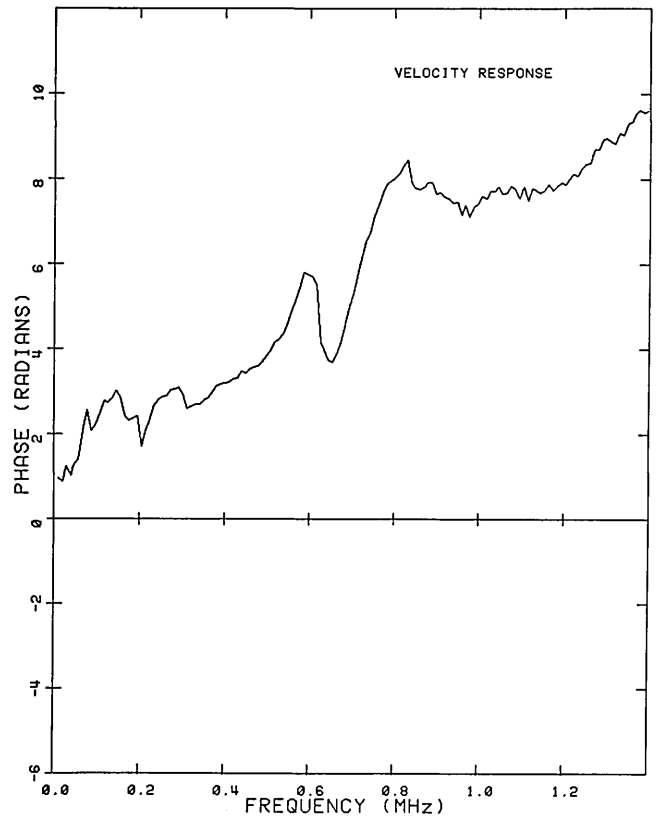


Figure 20—Phase response of the unknown transducer.

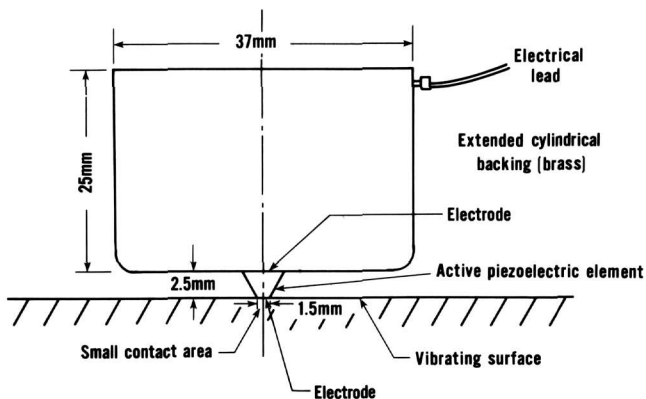


Figure 21—Schematic of one version of the NBS conical transducer.

By design, this transducer has a contact area which is small relative to Rayleigh wavelengths in the working range, nominally 0.1–1 MHz. This eliminates the aperture effect, evident in most commercial transducers, which changes transducer directionality and reduces bandwidth. The brass backing block is so large and so lossy that waves entering it via the conical element are largely dissipated by the time they reflect back to the element. Thus the backing block may be approximated as a solid elastic half-space. On this basis, it can be shown that for low frequencies the transducer functions as a displacement sensor.

The surface-pulse response of the NBS conical transducer (fig. 22) shows a little undershoot after the Rayleigh wave arrival and some backing reflections but compares favorably both with the theory and with the capacitive transducer response as shown in figure 17. It also compares very advantageously with the typical response of a commercial transducer to the same waveform as shown in figure 18. It follows dynamic normal displacements nearly as well as the standard capacitive transducer but it is more rugged,

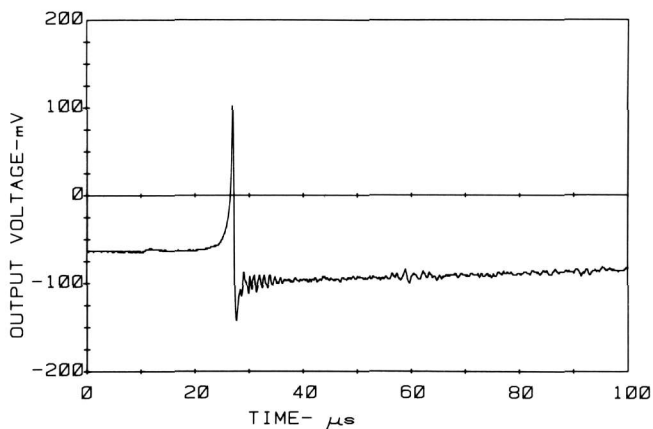


Figure 22—Measurement of surface pulse using the NBS conical transducer.

one to two orders of magnitude more sensitive (about as sensitive as commercial AE transducers), and it is broad band.

Figure 23 shows two views of a newer model of the transducer which produces the most faithful waveform of any piezoelectric transducer we have encountered. The idea behind the complex geometry is to smear out the reflections to the element by the backing; it does this by delaying them because of their different transit times.

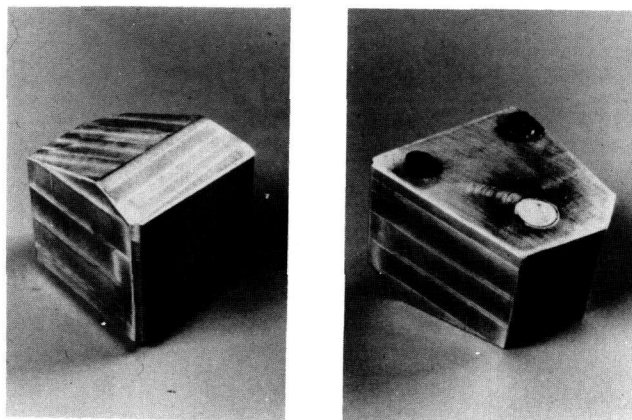


Figure 23—Version of NBS conical transducer which produces most faithful measurement of dynamic displacement by means of a piezoelectric transducer.

An example of the response of this model of the NBS conical transducer is shown in figure 24. The dashed curve gives the theoretically predicted normal displacement of a plate at a location three thicknesses away from, and on the same side of a plate as, a point-force step function input. The solid curve is the voltage-time output of the transducer shown in figure 23 on a glass plate with the transducer located two plate thicknesses away from a breaking glass capillary event [44]. Current plans call for making available for purchase the model shown in figure 23 through the NBS Standard Reference Materials Program. Other models have been designed to be more rugged or smaller but with almost the same fidelity.

## 6. Simulated AE Sources

A long-term weakness with the development of acoustic emission for materials testing and structural monitoring has been the absence of a well characterized simulated source that can be used for system evaluations. Such a source should result in a short duration stress pulse, similar to actual sources, of known characteristics at any arbitrarily-chosen location. Referring back to figure 1, a simulated AE

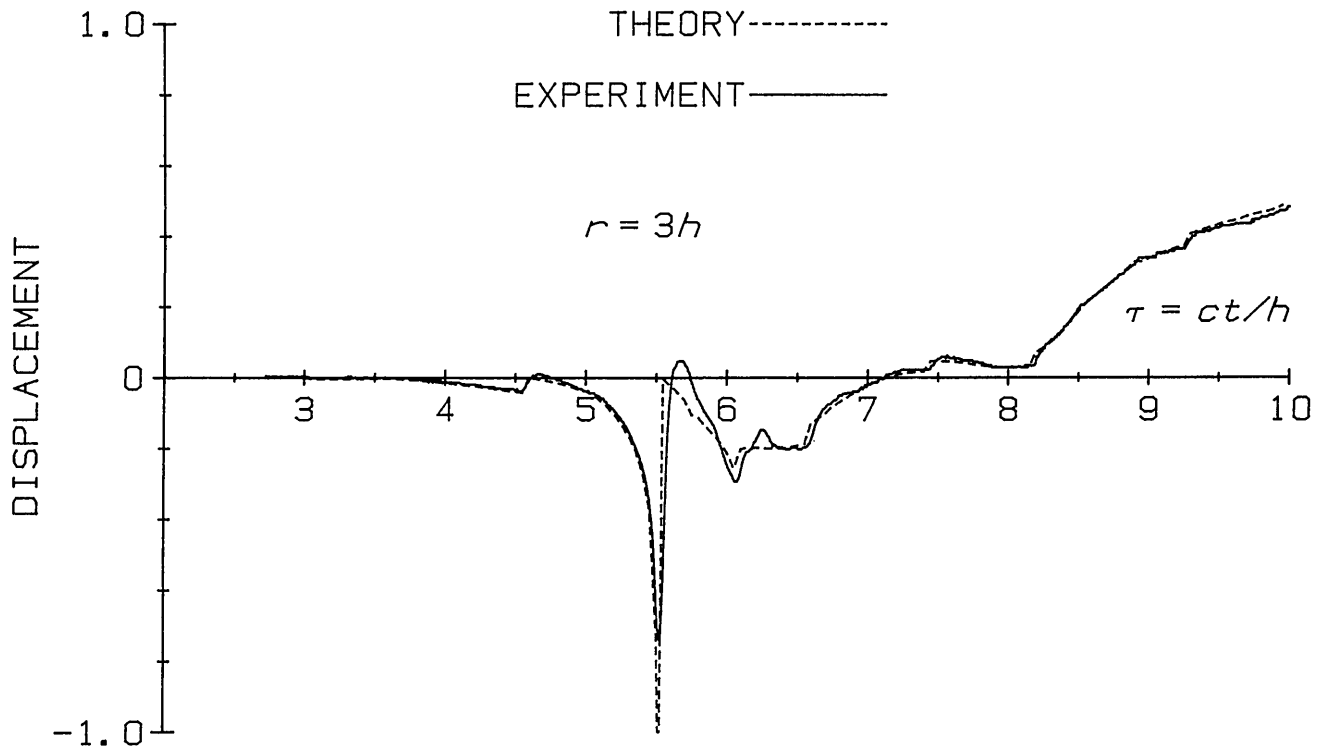


Figure 24—Theoretically predicted and measured displacement of a plate due to step-function force input. The transducer used is that shown in figure 22.

source is critical to calibrating AE transducers (defining Link III) in conjunction with a structure with known wave propagation characteristics, to determining unknown wave propagation characteristics of structures (defining Link II) in conjunction with a calibrated transducer of high fidelity, and to aiding the development and testing of appropriate signal processing schemes (Link IV) for determining source significance. This latter function includes facilitating the making of instrument settings and the verification of performance, for example, of source location systems. A simulated source should be; 1) repetitive, 2) reproducible with a known source mechanism, 3) of similar characteristics to “real” AE, and 4) relatively easy to implement.

The first simulated AE source developed, the breaking capillary source, already has been described briefly. Some additional details are given by Breckenridge [39]. The technique has proved an extremely good laboratory tool. Hsu [45] has extended the approach with a technique based on the breaking of a pencil lead. A self-contained push-button type mechanical pencil with high quality pencil leads replaces the glass capillary. A piece of lead of specific length is projected from the pencil. As the tip of the lead is pressed, at steadily increasing pressure, against the structure; this increasingly loads the structure until

the lead breaks, thereby generating a step function force unloading on the structure. The magnitude of the force can be selected by the choice of pencil lead as shown in figure 25. This simple technique has become the standard method throughout the world for checking instrument calibrations. It is being adopted as a calibration tool by AE standards groups in the United States, Europe, and Japan.

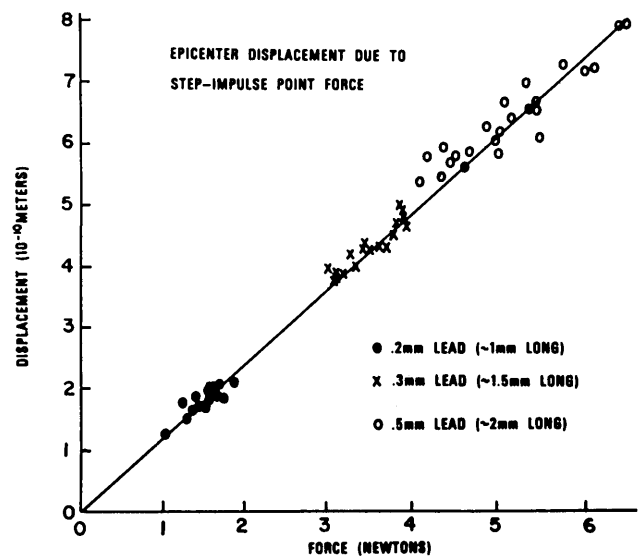


Figure 25—Typical calibration results.

The pencil lead technique has also been implemented as an absolute input force [2]. Figure 26 shows such a device. As the pencil is pushed against the structure by turning a loading screw, the force is transmitted through a previously calibrated load cell which pivots the pencil to load the structure. The load cell output is connected to a peak-hold device and displays the peak force which is the magnitude of the force-step. The waveform shape of each lead-break event is very similar to the others; the exact amplitude cannot be controlled since it linearly scales with force magnitude. Provided this is determined through the technique above, absolute calibration is possible, however.

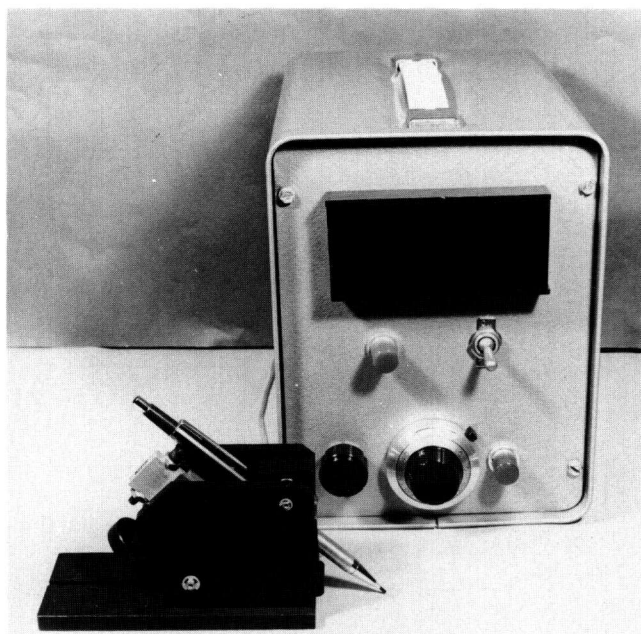


Figure 26—Mechanical AE simulator.

More recently a Nd:YAG pulsed laser has been used to produce predictable, repetitive, thermoelastic dipole sources to generate elastic waves (simulated AE) in a structure [46]. A large plate has been used to implement this source to permit comparisons with theory. The elastic displacements due to a force dipole combination representing the thermal expansion for a laser source have been calculated for an isotropic elastic plate. Figure 27 shows the excellent agreement between experiment and theory for this source. An advantage of this source is the wide range of source strengths that can be activated merely by varying laser pulse energy. The source is also dipolar in nature, like defect sources. It is, however, a very costly simulated source with certain safety limitations.

Comparisons have been made between more economical and safe electrical spark impact sources

and pulsed laser sources. The laser source is effective but the spark source has advantages which include portability, simplicity, and low cost. The charging, switching, and triggering circuits have been perfected so that a brief (few nanosecond), high-voltage current pulse with very low jitter can be discharged between electrodes. The simulated AE waveforms that result are essentially identical one to another.

The mode of the spark source which is controlled by the configuration of the electrodes effects the signal generated. We have emphasized the configuration in which the plate or structure is one electrode with the second just above the plate surface. The stress wave generated in the structure can be modeled as evolving from local surface plasma heating, the same mechanism as when using a pulsed laser source for radiation heating. Figure 28 shows a detected signal due to sparking onto a 1.5 in thick plate. In figure 28, (a) corresponds to the sensor located at the epicenter and (b) to the sensor located on the same surface as the source, and two plate thicknesses away from the source. From such experiments we conclude that: the source is extremely reproducible; the detected signals agree well with theoretical predictions for a dipole source; the surface normal motion has a well-defined negative pulse whose arrival is easily detected, a fact that could be exploited for precise measurements of ultrasonic wave speed measurements; the rise time for the stress wave is less than one-half microsecond; and, although the source generates electromagnetic signals, these can be isolated easily in the time domain. A comparison of these various sources has recently been completed by Jones, Green, and Hsu [47].

A different approach to producing a known source is to induce actual AE events in a material in a controlled way [16]. The method we have used involved indentation, i.e., local loading, of a plate so that the location can be chosen. The number and size of defects can be controlled by the loading rate. By using surface-hardened steel plates and diamond pyramid indenters, subsurface microcracks can be reproducibly created and sized later using destructive metallography. Correlations can then be made between the signal from the defect, signals from non-defect (simulated) sources such as those discussed above, and the crack microstructure. Indentation is not a new method of producing surface cracks, but it is new in combination with AE.

In using the indentation source, acoustic emission signals were monitored at the epicenter as well as on the same surface as the source. A sample of O2 tool steel, 2.54 cm thick and 7.62 cm in diameter, was

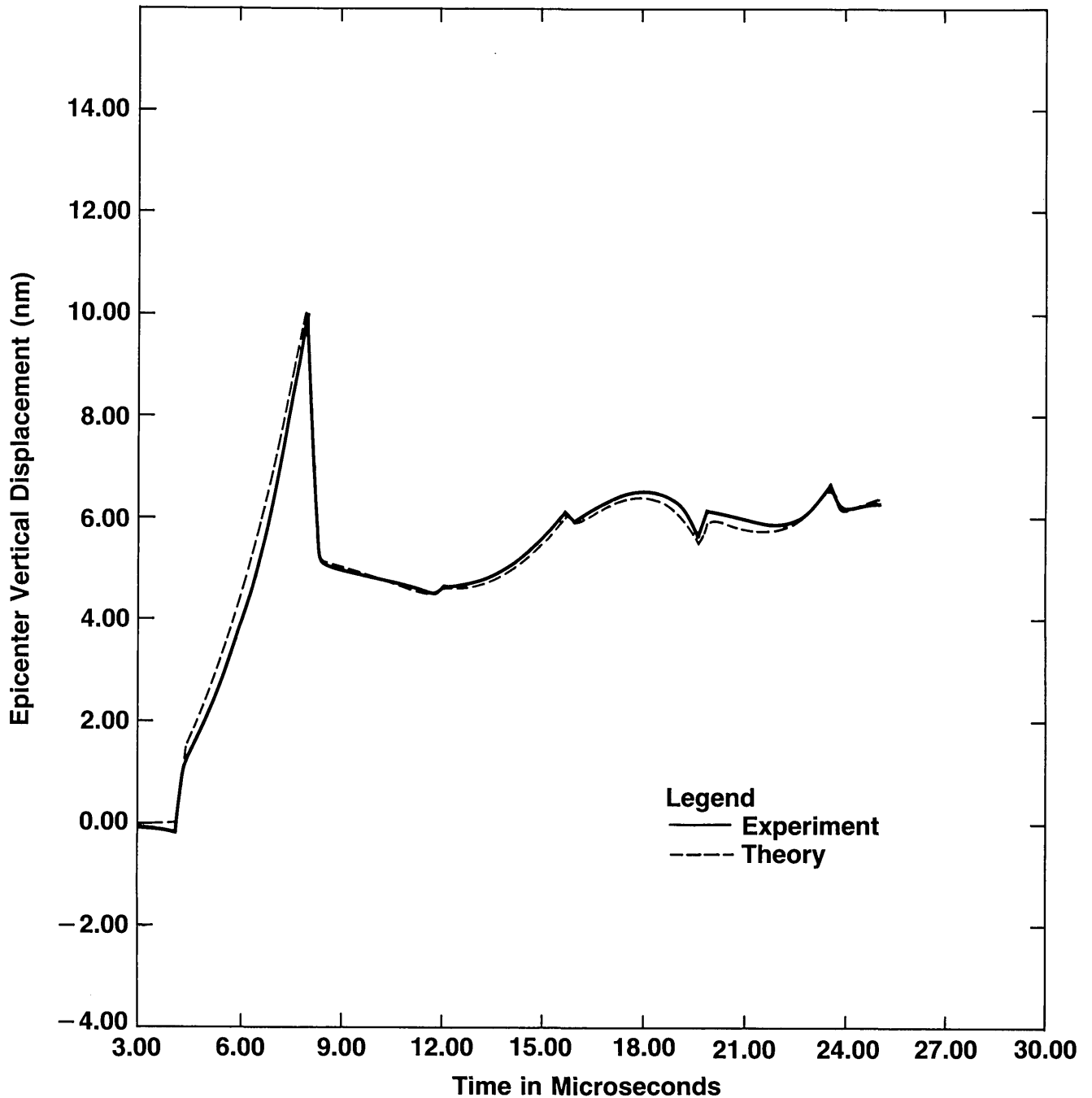


Figure 27—Comparison of experiment and theory for laser generated AE in 2024-T6 Aluminum.

prepared by austenitizing at 865 °C, and water quenching, following which the surfaces were ground and metallographically polished with care to avoid surface damage.

Examples of the very reproducible epicenter signals which were generated are shown in figure 29. In figure 30, one of these signals (A) is compared with that produced by very fast (~0.3 μs) step function unloading due to breaking of a glass capillary, while

another signal (B) is obtained by replacing the glass capillary with a piece of commercially available plastic labeling tape. Here the load, in excess of 50 kg, is approximately that needed for indentation AE, and the signal is of the same order of magnitude (-76 dB) as the signal from the microcracks. The glass capillary signal is at a much higher level, -20 dB. The similarity of these signals suggests that the epicenter signal from the crack looks very much like an unloading signal

consistent with the notion that cracking relaxes the elastic stress distribution.

### 7. Source Characterization (the Inverse Problem)

One of the most important objectives of current AE research is development of signal analysis methods to

explicitly characterize the AE source from remotely measured AE signals alone. This general problem, common to fields such as seismology and radar, is as yet an unsolved one, and one that will require complex processing of many independent channels of information. However, for sources which can be represented by a point force of unknown magnitude and time dependence but known direction, normal to

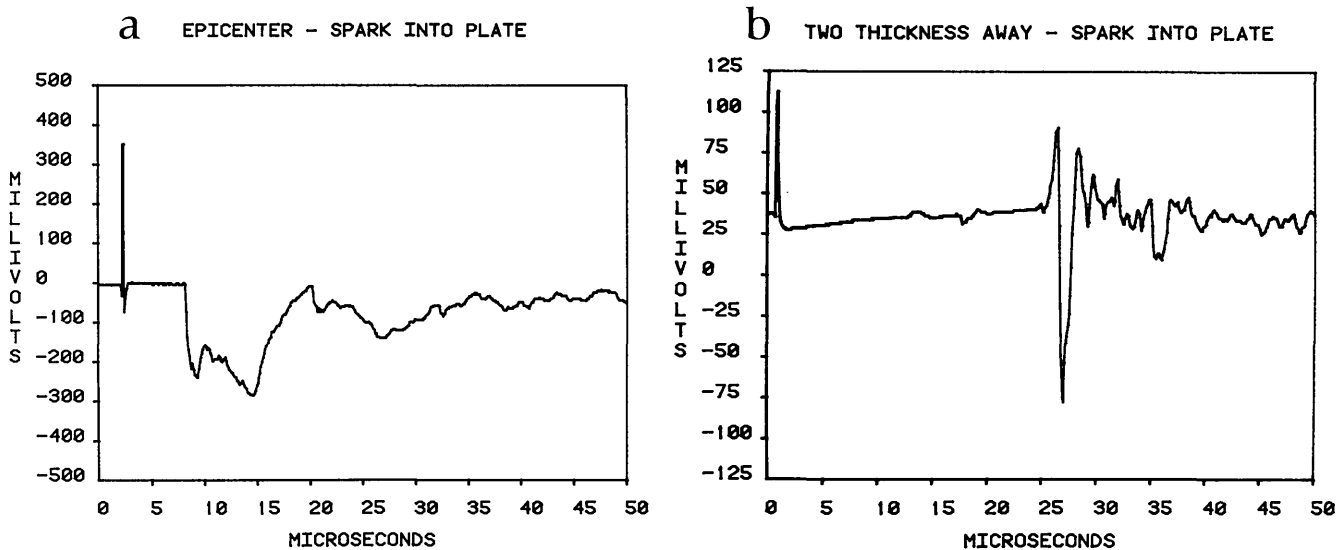


Figure 28—Detected AE signals due to a spark source for sensor (a) at epicenter and (b) on the same surface as the source and two plate thicknesses away.

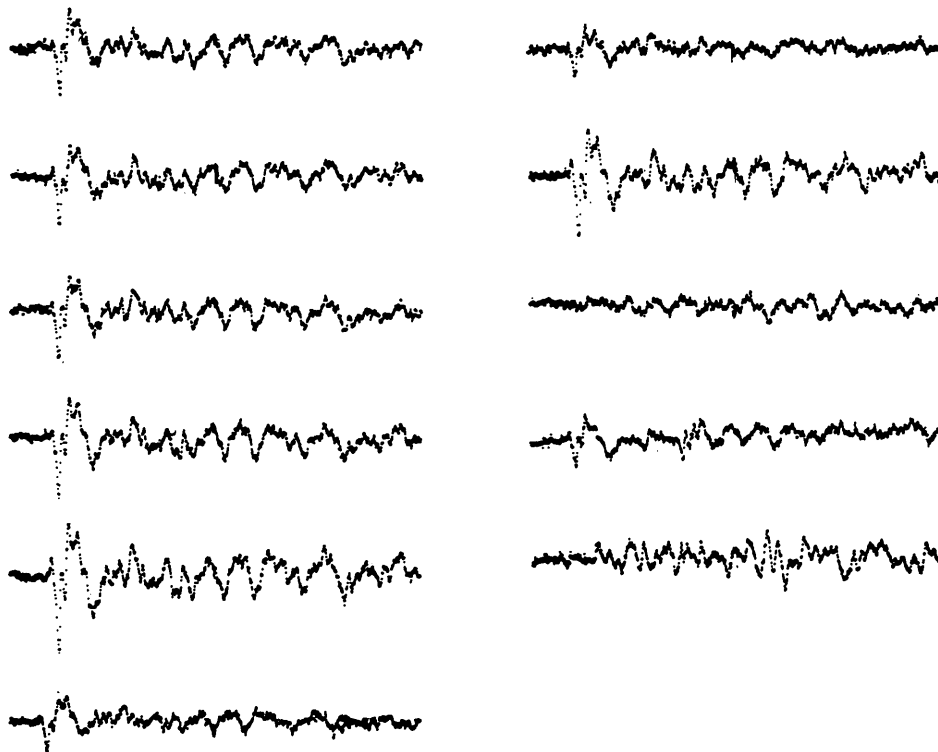


Figure 29—Reproducible signals at epicenter from indentation in an embrittled 02 tool steel (Rockwell C hardness, 69). The duration of the signal is 102  $\mu$ s and the amplitude after 76 dB amplification is about  $\pm 50$  mV. Two of the signals near the end are included to show some of the occasional nonreproducible signals that occurred during this test.

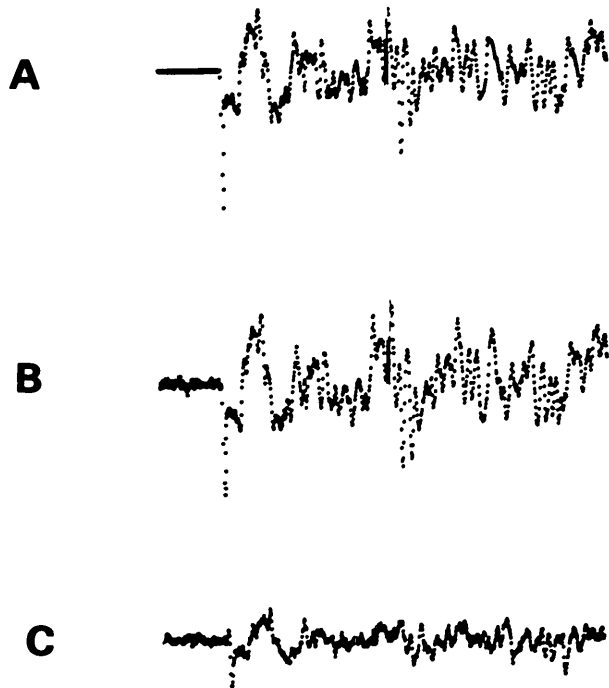


Figure 30—Epicenter signals through plate of embrittled 02 tool steel (Rockwell C hardness, 69). The signal duration is 102  $\mu\text{s}$  and the amplitude is about  $\pm 50$  mV. (A) Ball-tipped indenter breaking glass capillary (20 dB amplification). (B) Ball-tipped indenter fracturing plastic labeling tape (76 dB amplification). (C) Vickers indenter directly contacting plate (76 dB amplification).

the surface, for example, explicit determination of the source by deconvolution has been accomplished for two source-receiver configurations.

One geometry used for deconvolution of the received signal is that of a large plate with a point source on one surface and the receiver centered directly over the source on the opposite surface (epicenter). In this case, the Heaviside Green's function  $G^H$  can be calculated exactly. It is also assumed that the sensor measures the normal surface displacement,  $u_3$ . Practically this is accomplished by using either a capacitive transducer or the NBS conical transducer. For this case of a point source applied to a surface, it can be readily shown that eq (1) reduces to a one dimensional convolution integral:

$$u_3(t) = \int_0^t G_{33}^H(t-t') \Delta \dot{\sigma}_3(t') dt', \quad (15)$$

where  $G_{33}^H$  is the Heaviside Green's function and  $\Delta \dot{\sigma}_3$  is the history of the time rate change in the point force. Following the procedure detailed by Hsu and Hardy [18], the differentiated source function can be obtained as a convolution integral,

$$\Delta \dot{\sigma}_3 = \int_0^t u_3(t') H(t'-t) dt' \quad (16)$$

where  $H = (G^H)^{-1}$ . Shown in figures 31 and 32 are plots of  $G^H(t)$  and  $H(t)$  corresponding to an aluminum plate with a shear wave speed to longitudinal wave speed ratio of 0.487. The vertical scale is relative.  $G^H(t)$  is computed using the geometric ray method and  $H(t)$  is obtained by the matrix inversion technique outlined in [19]. The step curve shown in figure 33 is the convolved function  $G^H(t) * \dot{H}(t)$  plotted to show the numerical stability of the computations.

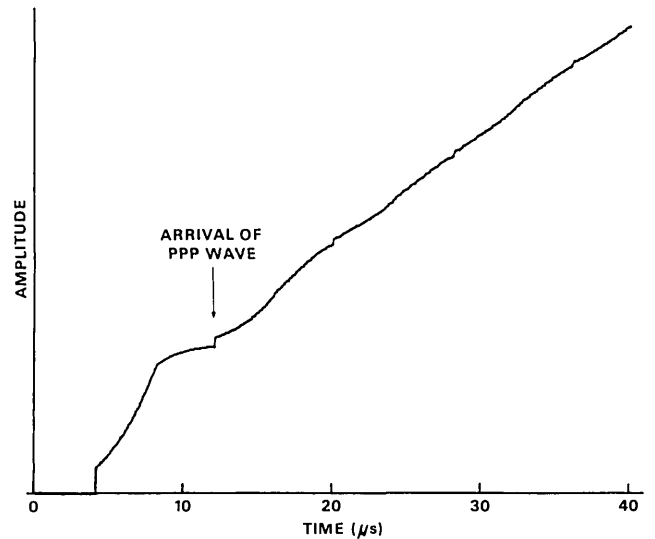


Figure 31—Theoretical vertical displacements at the epicenter.  $G^H(t)$ —due to a vertical force of step-function time dependency.

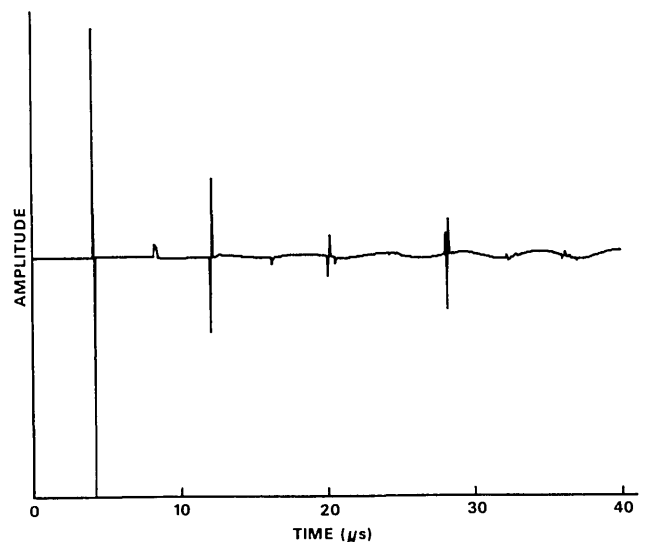


Figure 32— $H(t)$ —inverse function of  $G^H(t)$ .

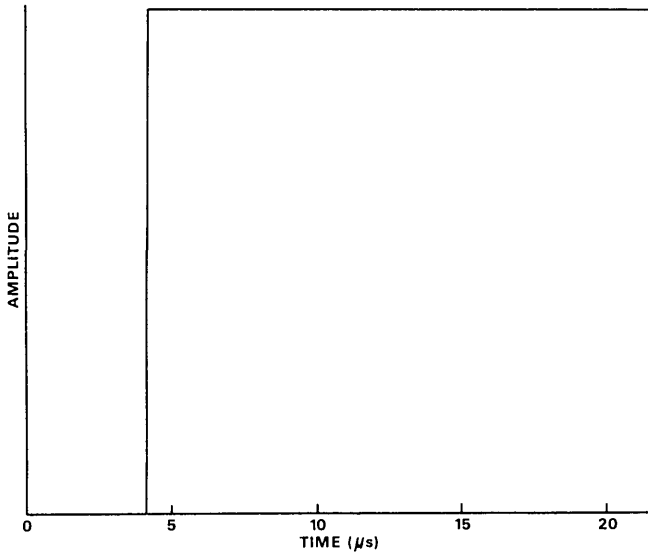


Figure 33—Convolution of the step-function response curve  $G^H(t)$  with the inverse function  $H(t)$ , the impulse response.

Two key elements of the procedure are being able to 1) measure a physical quantity such as normal displacement (uncorrupted by horizontal displacements), and 2) determine the inverse Heaviside Green's function. We have shown how, with care, this displacement can be accurately measured. In the case of the plate with source and receiver at epicenter, the computation of the inverse Green's function is rather straightforward. In general, however, not every time series has an inverse with respect to convolution; whether a specific time series, in our case a specific Green's function, has an inverse or not cannot be answered in general and it is this problem on which much of the ongoing research is focused. We have found, however, that in a second configuration, where the sensor and source are on the same surface and are sufficiently close, the inverse function can again be computed. But it is necessary to resort to the trick of reversing the time, computing the inverse, and reversing the time again. Examples of such computations are shown as figures 34 and 35.

Having established the validity of the theoretical calculation and experimental devices, we may substitute unknown components one at a time into the experiment, and determine their characteristics. Thus this procedure may be used to determine the source function, Green's tensor or transducer response. The data processing outlined above and detailed in [18,19] was used to determine simulated AE sources. Results are shown in figures 36 through 38 [18]. The inserts in the figures are the actual epicenter displacements detected by a capacitive transducer for various

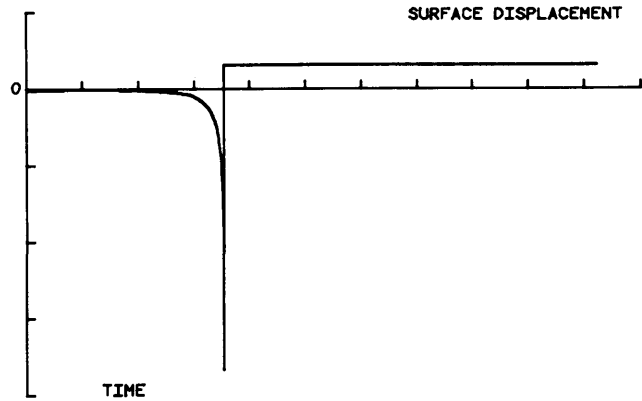


Figure 34—Theoretical vertical surface displacement for a point nearby and on the same surface as the source.  $G^H(t)$ —due to a vertical step-function force.

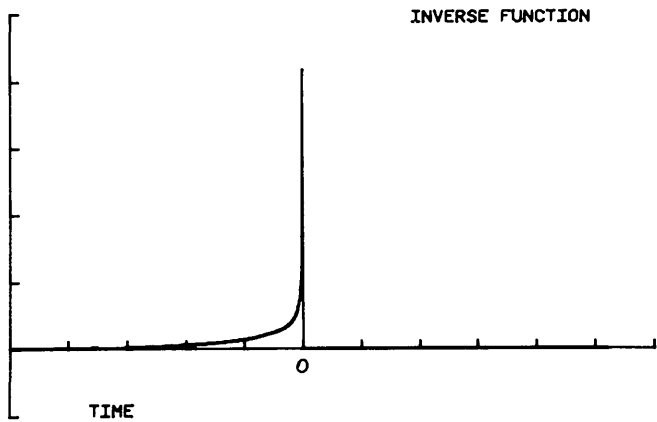


Figure 35— $H(t)$ —inverse function for  $G^H(t)$  for a point on the same surface as the source.

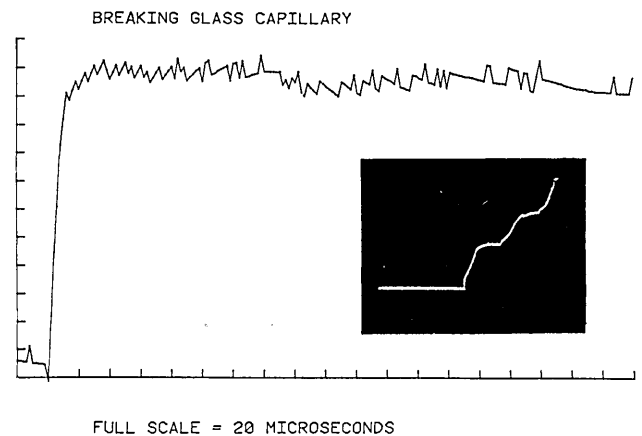
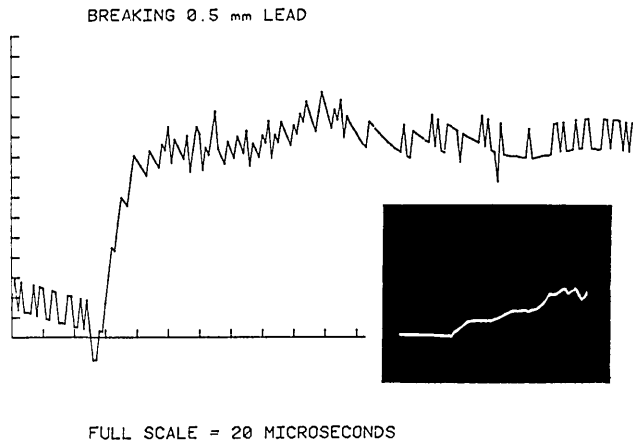
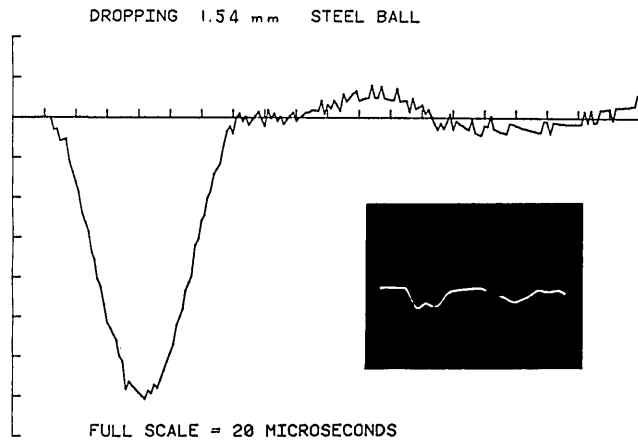


Figure 36—Source force-time function of breaking glass capillary obtained by time domain deconvolution of recorded epicenter displacement. Insert trace is the recorded epicenter displacement.



**Figure 37**—Source force-time function of breaking 0.5 mm pencil lead. Insert trace is the recorded epicenter displacement.



**Figure 38**—Force-time function for a source produced by dropping a 1.5 mm steel ball from a height of 5 cm onto a plate.

sources. A theoretically computed impulse response for the plate was used in this computation. It is found that the force time history produced by a breaking glass capillary is, indeed, a step-function with a rise time  $< 0.5 \mu\text{s}$ . The source function for the breaking pencil lead has a small yet noticeable dip before the step. This is interpreted as due to the reflection of the fracture wave at the contact point. The remotely measured displacement and deconvolved force-time history shown in figure 38 was produced by dropping a steel ball onto a plate. The dropping ball contact source function deduced compares well with elasticity theory. Deconvolution was also performed on displacements measured during an actual cracking event. Acoustic emission signals induced by indenting a glass plate were recorded and deconvolved (see fig. 39). The source signatures of such brittle fractures

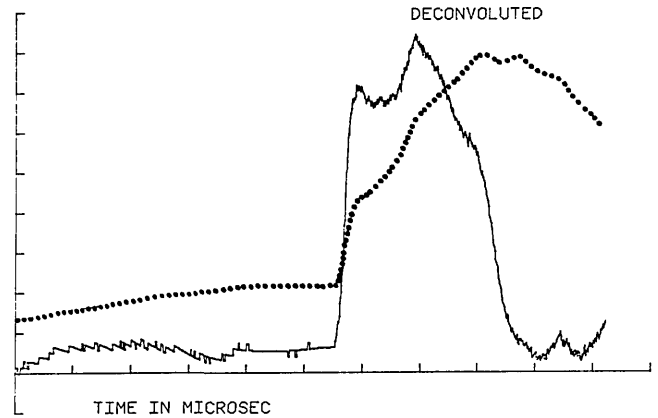


**Figure 39**—Source function for a brittle crack opening produced by indenting a glass plate.

resemble a step function at least for the initial part of the waveform.

No data smoothing procedure was used for the computations; thus noise sources introduced by the measurement and deconvolution procedures could be investigated. As was expected, the limited resolution (8-bit) of the analog/digital conversion process during waveform recording caused noise in these computations, especially when the full dynamic range of the A/D was not utilized. The usual noise suppression scheme for repetitive signals of summing and averaging is inappropriate for AE source characterization because each is a unique event. However, it can be used for determining the other unknowns in an AE system. The signal averaging technique has been used, for example, for characterizing the force-time function of a wideband piezoelectric transducer excited by a short-duration electrical pulse [1]. This application offers a possible absolute calibration technique for ultrasonic transducers used as ultrasound generators for nondestructive testing.

While considerable success has been achieved in deconvolution of the waveforms shown above, the same cannot be said for the waveforms encountered in practice using sensitive, but narrow-band resonant receivers located remotely from the source. The requirement to deconvolve these complicated signals in the presence of noise has stimulated ongoing research into the development and application of inverse methods.

Simmons [20] and Simmons and Leary [21] have developed two new methods for inverse modeling. One technique is based upon the singular value decomposition method. The second is based upon z-transforms. The algorithms developed from this work have proved to have sufficient flexibility to

optimize filtering in such a way as to use only the data with acceptable signal:noise value. These techniques show promise that many more source-detector geometrical arrangements may be amenable to deconvolution. However, they are complicated and require excessive computing capacity to implement. They are useful for laboratory studies but more simple techniques may be called for in field applications.

## 8. Summary

In the mid-1970's it was realized that acoustic emission techniques possessed great potential for determining and monitoring structural integrity. Acoustic emission signals were thought to contain potentially useful information about the location and identity of defects and about the criticality of the defects in a structure under load. However, the signal reception methods failed to preserve much of this information, and signal processing techniques used then, such as threshold counting, RMS recording, energy measurement, peak detection, and spectral analysis, did not extract the remaining information unambiguously. Acoustic emission was thus unable to fulfill its early promise, in part because of the inherent complexity of 1) the generating mechanisms, 2) the transient wave propagation details, and 3) the physics of the mechanical-to-electrical conversion process of the sensor. In other words, there was insufficient basic understanding of the acoustic emission phenomenon in solids.

The reviewed research program along with parallel efforts elsewhere have done much to remedy the situation. Particularly noteworthy contributions which help remove the impediments to the optimal application of acoustic emission techniques have included the development of:

1. A theoretical framework for investigating and analyzing the acoustic emission process.
2. Theoretical methods for predicting the surface motion due to an acoustic emission event.
3. Calibration methods and standards that currently are being adopted on a worldwide basis and are leading to data interchangeability and improved reliability of field data.
4. A transducer for measuring the normal component of surface motion with high sensitivity and fidelity, a tool necessary for advanced signal processing; and finally, the development of
5. Inverse techniques for processing the remotely measured signals to extract maximum

information about the acoustic emission source.

These and other developments are now being embodied in laboratory and field studies and in test methods, instruments, and analysis methods used in field applications. Acoustic emission is becoming, by NDE standards, a relatively well understood phenomenon. But research needs are far from satisfied. It is becoming increasingly apparent that:

1. Signal analysis methods should be developed for field applications where only limited, noisy data are available and source significance must be determined quickly.
2. Inverse techniques for more complex geometries and materials must be developed.
3. More realistic models of the sources themselves, going beyond those of a microcrack under uniform loading, are required.
4. Additional transducer developments, e.g., for transverse surface motion, are required. The calibration methods already developed provide the essential tools for this.

It is hoped that such research, in conjunction with increasing practical experience, will result in a successful transition from adolescence to maturity for this important NDE technique.

---

We wish to acknowledge the help and encouragement of our colleagues, F. Breckenridge, N. Hsu, T. Proctor, R. Clough, J. Simmons, and C. B. Scruby in preparing this review of their contributions to acoustic emission of the past decade. We also acknowledge J. Willis (University of Bath) who made important contributions to the NBS program on AE while visiting the Bureau.

## References

- [1] Hsu, N.; Simmons, J. A.; Hardy, S. An approach to acoustic emission signal analysis—Theory and experiment. *Matls. Eval.* **35**: 100-106; 1977.
- [2] Eitzen, D.; Breckenridge, F.; Clough, R.; Fuller, E.; Hsu, N.; Simmons, J. Fundamental developments for quantitative acoustic emission measurements. Electric Power Research Institute Report EPRI NP-2084. Palo Alto, CA; 1981. 1-219.
- [3] Green, A. T.; Lockman, C. S.; Steele, R. K. *Modern PLastics.* **41**: 137; 1964.
- [4] Kaiser, J. *Arkiv fur das Eisenhüttenwesen.* **24**: 43; 1953.
- [5] Spanner, J. C. *Advances in acoustic emission.* Dunhart: U.S.A.; 1981. p. 1.

- [6] Sachse, W.; Hsu, N. Ultrasonic transducers for materials testing and their characterization, in *Physical acoustics*, Vol. 14. W. P. Mason and R. Thurston, eds. New York: Academic Press; 1979. 277–406.
- [7] Nabarro, F. R. N. The synthesis of elastic dislocation fields. *Philos. Mag.* **42**: 1224–1231; 1951.
- [8] Mura, T. Continuous distributions of moving dislocations. *Philos. Mag.* **8**: 843–857; 1963.
- [9] Malen, K.; Bolin, L. A theoretical estimate of acoustic emission stress amplitudes. *Phys. Stat. Sol. (b)* **61**: 637–645; 1974.
- [10] Freund, L. B. The analysis of elastodynamic crack tip stress fields, in *Mechanics today*, Vol. 3. S. Namat-Nasser, ed. New York, NY: Pergamon Press; 1976. 55–91.
- [11] Aki, K.; Richards, P. G. *Quantitative seismology*. San Francisco: W. H. Freeman; 1980.
- [12] Rice, J. R. The mechanics of earthquake rupture. Proc. Int. School of Physics “Enrico Fermi,” Italian Physical Society, Course LXXVIII (Varenna on Lake Como, Italy, 1979) on *Physics of the Earth’s Interior*, E. Boschi, ed. North-Holland Publ. Co. (expected publication 1980–81).
- [13] Stephens, R. W. B.; Pollock, A. A. Waveforms and frequency spectra of acoustic emission. *J. Acoust. Soc. Am.* **50**: 904–910; 1971.
- [14] Tatro, C. A. Design criteria for acoustic emission experimentation, in *Acoustic emission*, ASTM STP 505, Philadelphia, PA: American Society for Testing and Materials; 1972.
- [15] Simmons, J. A.; Clough, R. B. Theory of acoustic emission, in Proc. Int. Conf. Dislocation Modeling Physical Systems. J. Hirth and M. Ashby, eds. Scripta Metall.; 1981.
- [16] Clough, R. B.; Simmons, J. A. Reproducible acoustic emission signatures by indentation in steels. *Mater. Eval.* **39**: 1026–1031; 1981.
- [17] Wadley, H. N. G.; Scruby, C. B.; Shrimpton, G. Quantitative acoustic emission source characterization. *Acta Metall.* **29**: 399; 1981.
- [18] Hsu, N.; Hardy, S. C. Experiments in acoustic emission waveform analysis for characterization of AE sources, sensors, and structures, in *Elastic waves and non-destructive testing of materials*, AMD-Vol. 29. Y. H. Pao, ed. New York: The American Society of Mechanical Engineers; 1978. 85–106.
- [19] Hsu, N.; Eitzen, D. AE signal analysis—Laboratory experiments examining the physical processes of acoustic emission. Proc. Fifth Int. Acoustic Emission Symp., Tokyo: Japanese Society for NDI; 1980. 67–78.
- [20] Simmons, J. New methods for deconvolution and signature analysis of causal and transient time series. Submitted to IEEE, 1984.
- [21] Simmons, J.; O’Leary, D. *SIAM J. Sci. Stat. Comput.* **2**: 474–489; 1981 December.
- [22] Wadley, H. N. G.; Scruby, C. B.; Speake, J. *Int. Metall. Rev.* **3**: 41; 1980.
- [23] Scruby, C. B.; Jones, C.; Titchmarsh, J. M.; Wadley, H. N. G. *Metall. Sci.* **15**: 241; 1981.
- [24] Scruby, C. B.; Wadley, H. N. G.; Sinclair, J. E. *Philos. Mag.* **A44**: 240; 1981.
- [25] Titchmarsh, J. M.; Bartlett, A. F.; Druce, S. G. AERE-R9674. 1980.
- [26] Wadley, H. N. G.; Scruby, C. B.; Lane, P.; Hudson, J. A. AERE-R9945. 1981.
- [27] Gopal, R.; Smith, J. R.; Rao, C. U. *Proc. Inst. Mech. Eng.* c194/76, p. 1; 1976.
- [28] Scruby, C.; Wadley, H. An assessment of acoustic emission for nuclear pressure vessel monitoring. *Nucl. Eng.* **11**: 275–297; 1983.
- [29] Wadley, H. N. G.; Scruby, C. B. AERE-R10351. 1981.
- [30] Wadley, H. N. G.; Furze, D. C.; Scruby, C. B.; Eyre, B. L. *Metal Sci.* **13**: 451; 1979.
- [31] McIntyre, P.; Green, G. Br. *J. NDT* **20**: 135; 1978.
- [32] Simmons, J. A.; Willis, J. R.; Hsu, N. N. The dynamic Green’s tensor for an elastic plate. In preparation.
- [33] Pao, Y. H.; Gajewski, R. R.; Ceranoglu, A. N. Acoustic emission and transient waves in an elastic plate. *J. Acoust. Soc. Am.* **65**: 96–105; 1979.
- [34] Muller, G. Theoretical seismograms for some types of point-sources in layered media. Part II: Numerical calculations. *Z. fur Geophysik* **34**: 147–162; 1968.
- [35] Pao, Y. H.; Gajewski, R. R. The generalized ray theory and transient responses of layered elastic solids, in *Physical acoustics*, R. N. Thurston, ed. Vol. XIII: New York, NY: Academic Press; 1977.
- [36] Hsu, N.; Breckenridge, F. Characterization and calibration of acoustic emission sensors. *Mater. Eval.* **39**: 60–68; 1981.
- [37] Simmons, J. A.; Wadley, H. N. G. Vector transducer calibration. Review of progress in quantitative NDE. Santa Cruz. 1983. To be published.
- [38] Breckenridge, F. R.; Tschiegg, C. E.; Greenspan, M. Acoustic emissions: Some applications of Lamb’s problem. *J. Acoust. Soc. Am.* **57**: 626–631; 1975.
- [39] Breckenridge, F. Acoustic emission transducer calibration by means of the seismic surface pulse. *J. Acoustic Emission* **1**: 87–94; 1982.
- [40] Breckenridge, F.; Greenspan, M. Surface-wave displacement: Absolute measurements using a capacitive transducer. *J. Acoust. Soc. Am.* **68**: 1177–1185; 1981.
- [41] Proctor, T. Improved piezoelectric transducer for acoustic emission reception. *J. Acoust. Soc. Am. Suppl. 1*, **68**: 568; 1980.
- [42] Proctor, T. An improved piezoelectric acoustic emission transducer. *J. Acoust. Soc. Am.* **71**: 1163–1168; 1982.
- [43] Proctor, T. Some details on the NBS conical transducer. *J. Acoustic Emission* **1** 173–178; 1982.
- [44] Proctor, T. Breckenridge, F.; Pao, Y. Transient waves in an elastic plate: Theory and experiment compared. *J. Acoust. Soc. Am.* **75**(1): 1984.
- [45] Hsu, N. Acoustic emission simulator. U.S. Patent 4018084 assigned to Lockheed Aircraft Corporation, Burbank, CA, May 1976.
- [46] Wadley, H. N. G.; Simmons, J. A. Review of progress in quantitative NDE, Santa Cruz; 1983; to be published.
- [47] Jones, M.; Green, R.; Hsu, N. Comparison of simulated acoustic emission sources. *Proc. Ultrasonics Int.* 1983.